

University of Windsor

Scholarship at UWindsor

Electronic Theses and Dissertations

Theses, Dissertations, and Major Papers

3-10-2021

Advanced Ignition Strategies for Future Internal Combustion Engines with Lean and Diluted Fuel-Air Mixtures

Zhenyi Yang
University of Windsor

Follow this and additional works at: <https://scholar.uwindsor.ca/etd>

Recommended Citation

Yang, Zhenyi, "Advanced Ignition Strategies for Future Internal Combustion Engines with Lean and Diluted Fuel-Air Mixtures" (2021). *Electronic Theses and Dissertations*. 8581.
<https://scholar.uwindsor.ca/etd/8581>

This online database contains the full-text of PhD dissertations and Masters' theses of University of Windsor students from 1954 forward. These documents are made available for personal study and research purposes only, in accordance with the Canadian Copyright Act and the Creative Commons license—CC BY-NC-ND (Attribution, Non-Commercial, No Derivative Works). Under this license, works must always be attributed to the copyright holder (original author), cannot be used for any commercial purposes, and may not be altered. Any other use would require the permission of the copyright holder. Students may inquire about withdrawing their dissertation and/or thesis from this database. For additional inquiries, please contact the repository administrator via email (scholarship@uwindsor.ca) or by telephone at 519-253-3000ext. 3208.

ADVANCED IGNITION STRATEGIES FOR FUTURE INTERNAL
COMBUSTION ENGINES WITH LEAN AND DILUTED FUEL-AIR
MIXTURES

by

Zhenyi Yang

A Dissertation

Submitted to the Faculty of Graduate Studies

through the Department of Mechanical, Automotive and Materials Engineering

in Partial Fulfillment of the Requirements for

the Degree of Doctor of Philosophy at the

University of Windsor

Windsor, Ontario, Canada

2021

© 2021 Zhenyi Yang

Advanced Ignition Strategies for Future Internal Combustion Engines with
Lean and Diluted Fuel-Air Mixtures

by

Zhenyi Yang

APPROVED BY:

C. R. Koch, External Examiner
University of Alberta

X. Xu
Department of Civil and Environmental Engineering

J. Tjong
Department of Mechanical, Automotive and Materials Engineering

G. Reader
Department of Mechanical, Automotive and Materials Engineering

M. Zheng, Co-Advisor
Department of Mechanical, Automotive and Materials Engineering

D. S-K Ting, Co-Advisor
Department of Mechanical, Automotive and Materials Engineering

19 January 2021

DECLARATION OF ORIGINALITY

I hereby certify that I am the sole author of this thesis and that no part of this thesis has been published or submitted for publication.

I certify that, to the best of my knowledge, my thesis does not infringe upon anyone's copyright nor violate any proprietary rights and that any ideas, techniques, quotations, or any other material from the work of other people included in my thesis, published or otherwise, are fully acknowledged in accordance with the standard referencing practices. Furthermore, to the extent that I have included copyrighted material that surpasses the bounds of fair dealing within the meaning of the Canada Copyright Act, I certify that I have obtained a written permission from the copyright owner(s) to include such material(s) in my thesis and have included copies of such copyright clearances to my appendix.

I declare that this is a true copy of my thesis, including any final revisions, as approved by my thesis committee and the Graduate Studies office, and that this thesis has not been submitted for a higher degree to any other University or Institution.

ABSTRACT

The main objective of this research was to study the mechanisms of the spark ignition process of lean or diluted fuel-air mixtures under enhanced gas flow conditions for applications in future internal combustion engines. Various spark ignition strategies were deployed by controlling the spark discharge process via different spark ignition hardware configurations. Modulated spark discharge parameters, such as enhanced discharge power, prolonged discharge duration, and boosted discharge current were facilitated in the research. The impact of gas flow on the spark discharge process in air was investigated under varying air flow conditions with a range of flow velocities from 0 m/s to 60 m/s. The ignition performance of the spark strategies was investigated with lean or diluted fuel-air mixtures under controlled gas flow conditions in an optical constant volume combustion chamber test platform. The mixture flow velocity across the spark gap ranged from 0 m/s to 35 m/s during the combustion tests.

Experiments were carried out with air as the background media. Short circuits and restrikes were observed under air flow conditions. The frequency of these occurrences increased with increased air flow velocity. The length of the spark plasma increased, due to the stretch of the plasma channel by the air flow. The plasma was stretched at a speed similar to the air flow velocity across the spark gap. The maximum length of the spark plasma was affected by the air flow velocity and the spark gap size. The spark discharge duration reduced with increased air flow velocity.

To enhance the ignition of a lean or diluted fuel-air mixture under quiescent conditions, high spark discharge power or high spark discharge current were applied. With equivalent spark discharge energy, a larger flame kernel was achieved by the high-power spark whereas the impacts of spark discharge current level and discharge duration during the arc and glow phases were insignificant on the flame kernel growth. A transient high-current spark also generated a larger flame kernel, although with much higher spark energy as compared with that from a conventional spark. Under gas flow conditions, both the spark

discharge current magnitude and discharge duration were critical for the flame kernel growth. It is postulated that this kernel growth was the result of a prolonged spark discharge duration effectively increasing the interaction volume between the plasma channel and the combustible gas engulfed by the mixture flow. Consequently, a longer spark discharge duration proved beneficial in establishing a larger flame kernel, probably because the spark discharge current was sufficient to support the flame kernel growth. Indeed, it was observed that boosted spark current was advantageous for the flame kernel growth, especially at higher flow velocities. However, the high-power spark and transient high-current spark proved to be less effective with higher flow velocities, probably because of the short discharge duration.

Keywords: spark ignition, gas flow, spark plasma, flame kernel initiation, high-power spark, transient high-current spark, boosted-current spark, spark discharge duration, spark discharge energy, spark discharge current

DEDICATION

This thesis is dedicated to my family: my husband Weiyang Zeng, my mother Shumei Ran, my father Yuezhong Yang, my sister Aihua Yang, and my daughter Lucy Zeng.

ACKNOWLEDGEMENTS

I am deeply grateful to my advisor, Dr. Ming Zheng. The great research platforms and unconditional support provided by him make this work possible. I was able to improve my research ability under his guidance, which I considered a lifetime treasure for my professional development. I would also like to devote my sincere acknowledgment to my co-advisor, Dr. David, S-K Ting. His wisdom, open mind, and encouragement have inspired me always.

I would like to acknowledge the external examiner Dr. C. R. Koch and committee members for their valuable comments and suggestions to improve the quality of this work.

I would like to thank all my present colleagues – Dr. Meiping Wang, Dr. Xiao Yu, Hua Zhu, Linyan Wang, Navjot Sandhu, Simon Leblanc, and Li Liang. Acknowledgments are also sent to my past colleagues – Dr. Shui Yu, Dr. Xiaoye Han, Dr. Prasad Divekar, Dr. Tongyang Gao, Dr. Kelvin Xie, Dr. Marko Jeftić, Dr. Shouvik Dev, and Dr. Qingyuan Tan. I have received tremendous help from them. This work cannot be realized without their support. It is my honor to work with them and to be part of the team.

I would like to thank the research sponsors: NSERC Industrial Research Chair program, NSERC Collaborative Research and Development Program, Ford Motor Company of Canada Ltd., and the University of Windsor.

TABLE OF CONTENTS

DECLARATION OF ORIGINALITY	III
ABSTRACT	IV
DEDICATION	VI
ACKNOWLEDGEMENTS	VII
LIST OF TABLES	XIII
LIST OF FIGURES	XIV
LIST OF SYMBOLS AND ABBREVIATIONS	XXIII
PREFACE	1
Motivation and objective.....	1
Structure of the thesis.....	3
CHAPTER 1 INTRODUCTION.....	6
1.1 Energy sources for automotive application	6
1.2 Spark ignition engine development for clean combustion	11
1.3 Challenges in the spark ignition process	17
1.4 Chapter summary.....	18
CHAPTER 2 TECHNICAL BRIEFING AND LITERATURE REVIEW	20
2.1 Basic spark discharge process from an inductive ignition system	20
2.2 Spark ignition systems.....	24
2.2.1 High-power ignition system.....	24
2.2.2 High-energy ignition system.....	26

2.2.3	Ignition systems with controlled spark discharge current and duration.....	27
2.3	Spark ignition strategies for ignition of lean and diluted fuel-air mixtures.....	27
2.3.1	High-power ignition strategy	28
2.3.2	High-energy ignition strategy	29
2.3.3	Spark strategies with controlled spark current and voltage profiles	29
2.4	Spark discharge process under gas flow conditions	31
2.5	Chapter summary	32
CHAPTER 3 RESEARCH METHODOLOGY		34
3.1	Constant volume combustion chambers	34
3.1.1	Gas supply systems of the optical constant volume chamber	37
3.1.2	Imaging systems of the optical constant volume chamber	42
3.1.3	Measurement instruments of the optical constant volume chamber	43
3.2	Controlled air flow test bench.....	44
3.3	Hardware setup of ignition systems.....	45
3.3.1	Multi-coil ignition system.....	49
3.3.2	High-power ignition system.....	53
3.3.3	Boosted-current ignition system	56
3.3.4	Transient high-current ignition system	59
3.4	Data analysis methods	63
3.4.1	Ignition energy calculation	63
3.4.2	Pressure data analysis	65
3.4.3	Imaging processing	66
3.5	Experimental conditions	67

CHAPTER 4	FLAME KERNEL INITIATION WITH DIFFERENT IGNITION STRATEGIES UNDER QUIESCENT CONDITIONS	70
4.1	Effects of spark discharge current profiles on the ignition process.....	70
4.1.1	Spark generated by a conventional inductive coil system	70
4.1.2	Spark generated by a multi-coil simultaneous discharge.....	73
4.1.3	Spark generated by multi-coil offset discharge.....	75
4.2	Effects of breakdown power on the ignition process.....	78
4.2.1	High-power spark with air as background media	79
4.2.2	Impact of high-power spark on ignition of lean mixtures.....	83
4.2.3	Impact of high-power spark on ignition of diluted mixtures	85
4.3	Effects of transient high-current on the ignition process.....	88
4.3.1	Transient high-current spark with air as background media.....	88
4.3.2	Impact of transient high-current spark on ignition of lean mixture	89
4.3.3	Impact of transient high-current spark on ignition of diluted mixtures	92
4.4	Chapter summary.....	93
CHAPTER 5	IMPACT OF AIR FLOW ON SPARK DISCHARGE PROCESS.....	95
5.1	Characteristics of the spark discharge under air flow conditions	96
5.1.1	Pre-breakdown and breakdown phases	96
5.1.2	Arc and glow phases	98
5.1.3	Waveform analyses	100
5.1.4	Detection of short circuit and restrike.....	102
5.1.5	Electric parameters affected by air flow	103
5.1.6	Section summary.....	106

5.2	Effects of the magnitude of air flow velocity on spark discharge	107
5.2.1	Plasma stretching rate and maximum plasma length	110
5.2.2	Spark discharge energy and duration	112
5.2.3	Section summary	116
5.3	Effects of background pressure on spark discharge channel shape and electric waveforms	117
5.4	Effects of spark gap size on spark discharge channel shapes and electric waveforms	120
5.5	Effects of air flow on spark discharge process with different discharge current levels	124
5.5.1	Spark discharge energy and discharge duration.....	125
5.5.2	Short circuit and restrike frequency	126
5.5.3	Plasma length and stretching rate.....	127
5.6	Impact of air flow on the effective control of different ignition strategies	131
5.6.1	High-power and transient high-current spark	131
5.6.2	Multi-coil offset spark.....	133
5.6.3	Boosted-current spark	134
5.7	Chapter summary	138
CHAPTER 6 DIFFERENT IGNITION STRATEGIES ON FLAME KERNEL INITIATION UNDER GASEOUS MIXTURE FLOW CONDITIONS		139
6.1	Effects of gas flow on flame kernel initiation	139
6.2	Effects of enhanced breakdown power on flame kernel initiation	145
6.2.1	High-power spark with air as background media	146
6.2.2	Impact of high-power spark on ignition of lean mixtures.....	147

6.3	Effects of transient high-current spark on flame kernel initiation	151
6.3.1	Transient high-current spark with air as background media.....	151
6.3.2	Impact of transient high-current spark on ignition of lean mixtures.....	153
6.3.3	Energy release profile on ignition of lean mixtures.....	157
6.3.4	Effects of spark discharge energy levels of the transient high-current and conventional spark on the ignition of lean mixtures	161
6.4	Effects of spark glow phase current profile on flame kernel development	165
6.4.1	Effects of varied spark glow phase current profile with equivalent spark energy	166
6.4.2	Effects of glow phase current level on the flame kernel development	171
6.4.3	Effects of glow phase duration on the flame kernel development.....	175
6.4.4	Further considerations of the spark discharge current level and duration	179
6.5	Chapter summary	181
CHAPTER 7 CONCLUSION		182
7.1	Conclusions.....	182
7.2	Contributions made to the study of spark ignition mechanisms.....	184
7.3	Recommendations for future work	185
REFERENCES		187
VITA AUCTORIS		200

LIST OF TABLES

Table 3-1	Specifications of the optical constant volume combustion chamber	36
Table 3-2	Specifications of the Environics 4040 gas dilution system [116]	38
Table 3-3	Specifications of the high-speed cameras	42
Table 3-4	Specifications of the current probe, voltage probe, and oscilloscope	44
Table 3-5	Characteristics of the spark ignition systems	46
Table 3-6	Parameters of the spark plugs.....	49
Table 3-7	Estimation of flame propagation speed at different engine speed	68
Table 3-8	Summary of experimental conditions	69
Table 5-1	Time scale of the spark discharge events of different spark strategies	131
Table 6-1	Characteristics of the spark ignition systems	162

LIST OF FIGURES

Figure P-1	Structure of the thesis.....	4
Figure 1-1	Highway fuel consumption for vehicles (Adapted from US Federal Highway Administration [17]).....	6
Figure 1-2	Gravimetric and volumetric energy densities of various portable energy sources [21–23]	8
Figure 1-3	Variation of fuel consumption with vehicle weight (Adapted from The National Academies Press [24]).....	9
Figure 1-4	Vehicle weight and battery pack/fuel weight (Adapted from Yu <i>et al.</i> [19]) .	9
Figure 1-5	Charging time and traveling time of electric vehicles [17].....	10
Figure 1-6	Passenger automobile fuel economy standards [32–34]	11
Figure 1-7	Efficiency improvement by cooled EGR (Adapted from Takaki <i>et al.</i> [2]) .	14
Figure 1-8	EGR loop configurations in turbocharged SI engines.....	15
Figure 1-9	Operational modes of a gasoline direct injection engine (Adapted from Blank <i>et al.</i> [67])	16
Figure 1-10	Challenges for the ignition in modern SI engines	19
Figure 2-1	Inductive coil ignition system (Adapted from Zheng <i>et al.</i> [16])	21
Figure 2-2	Waveforms during the charging and discharging processes of an inductive coil ignition system (Adapted from Yu <i>et al.</i> [74,79]).....	22
Figure 2-3	Phases in the spark discharge process under quiescent conditions (Adapted from Maly <i>et al.</i> [84]).....	23
Figure 2-4	High-power ignition systems	25
Figure 2-5	Plasma jet ignition system (Adapted from Murase <i>et al.</i> [99])	26

Figure 2-6	Multi-coil ignition system represented by two coils (Adapted from Alger <i>et al.</i> [95]).....	27
Figure 3-1	Photos of constant volume combustion chamber test platform	35
Figure 3-2	Experimental setup of the constant volume combustion chamber.....	37
Figure 3-3	Demonstration of the flow field near the spark gap.....	38
Figure 3-4	Flow chart of the procedure during the experiment	39
Figure 3-5	Architecture of the CompactRIO system	40
Figure 3-6	Signal sequence during the experiments	41
Figure 3-7	Flow velocity near the spark gap.....	42
Figure 3-8	Experimental setup of the flow test bench	45
Figure 3-9	Conventional inductive coil ignition system.....	47
Figure 3-10	Flow chart of the spark process based on an inductive coil ignition system	48
Figure 3-11	Multi-coil ignition system (represented by a dual-coil configuration)	49
Figure 3-12	Multi-coil simultaneous spark discharge.....	51
Figure 3-13	Multi-coil offset spark discharge	52
Figure 3-14	High-power ignition system.....	53
Figure 3-15	Working principle of the high-power ignition strategy.....	54
Figure 3-16	Voltage and current waveforms with increased levels of add-on parallel capacitors.....	54
Figure 3-17	Spark discharge current, voltage, and power during the breakdown phase with different levels of add-on parallel capacitors	55
Figure 3-18	Spark discharge current and voltage during the arc and glow phases with different levels of add-on parallel capacitors	56
Figure 3-19	Boosted current ignition system.....	57

Figure 3-20	Working principle of the boosted-current ignition system	58
Figure 3-21	Modulation of the spark discharge current by the boosted-current strategy .	59
Figure 3-22	Transient high-current ignition system	61
Figure 3-23	Illustration of the transient high-current spark discharge process.....	61
Figure 3-24	Current and voltage waveforms of transient high-current spark (different voltage).....	62
Figure 3-25	Current and voltage waveforms of transient high-current spark (different capacitance).....	62
Figure 3-26	Demonstration of the pressure trace.....	65
Figure 3-27	Image processing method for flame area calculation.....	66
Figure 3-28	Image processing method for plasma length calculation	66
Figure 3-29	In-cylinder pressure at the spark timing in a production engine (Adapted from Yu <i>et al.</i> [127])	67
Figure 4-1	Spark discharge current and voltage waveforms with low to conventional discharge energy.....	71
Figure 4-2	Effect of spark discharge energy on flame kernel formation under quiescent conditions	72
Figure 4-3	Effects of different spark discharge energy on combustion.....	73
Figure 4-4	Spark discharge current and voltage waveforms from multi-coil simultaneous discharge	74
Figure 4-5	Effects of the spark discharge current profiles on combustion with a similar spark discharge energy level	75
Figure 4-6	Command signal for the dual-coil offset spark	76
Figure 4-7	Continuous spark discharge current profiles.....	77

Figure 4-8	Effects of spark discharge current profiles on combustion	77
Figure 4-9	Voltage and current waveforms with increased levels of add-on parallel capacitors.....	78
Figure 4-10	Effects of background pressure on the breakdown voltage and current	80
Figure 4-11	Effects of add-on parallel capacitance and background pressure on the breakdown energy	81
Figure 4-12	Shadowgraph images of the thermal-induced density field by high-power spark in air under quiescent conditions	83
Figure 4-13	Effects of high-power spark on flame kernel growth of lean mixture under quiescent conditions	84
Figure 4-14	Effects of high-power spark on the combustion of lean mixtures under quiescent conditions	85
Figure 4-15	Effects of high-power spark on the combustion of CO ₂ diluted mixtures under quiescent conditions	87
Figure 4-16	Current and voltage waveforms of transient high-current spark.....	88
Figure 4-17	Shadowgraph images of the thermal-induced density field by transient high-current spark in air under quiescent conditions	89
Figure 4-18	Effect of transient high-current spark on the flame kernel growth of lean mixture under quiescent conditions	90
Figure 4-19	Flame areas with transient high-current spark discharge under quiescent conditions	91
Figure 4-20	Effects of transient high-current spark on the combustion of lean mixtures under quiescent conditions	92
Figure 4-21	Effects of transient high-current spark on combustion of CO ₂ diluted mixtures under quiescent conditions	93

Figure 4-22	Comparison of different ignition strategies for lean combustion under quiescent conditions	94
Figure 5-1	Comparison of spark plasma and flame kernel formation under quiescent and air flow conditions	95
Figure 5-2	Spark discharge waveforms during the breakdown phase under various air flow conditions	97
Figure 5-3	Effect of cross-flow velocity on the breakdown process	97
Figure 5-4	Plasma channel structure and electric waveforms of the spark discharge process	99
Figure 5-5	Spark discharge current and voltage during short circuit and restrike	101
Figure 5-6	Detection of the plasma short circuit and restrike from the spark discharge voltage profile	103
Figure 5-7	Spark discharge waveforms under quiescent and air flow conditions	104
Figure 5-8	Impact of plasma resistance on the spark discharge parameters	106
Figure 5-9	Spark discharge current and voltage waveforms (quiescent conditions)	108
Figure 5-10	Plasma stretch by the air flow	109
Figure 5-11	Spark discharge current, voltage, and plasma length under different cross-flow velocities	110
Figure 5-12	Plasma stretching rate under different cross-flow velocities	111
Figure 5-13	Maximum plasma length under different cross-flow velocities	112
Figure 5-14	Effects of air flow velocity on the spark discharge energy and duration	113
Figure 5-15	Effect of air flow velocity on the spark discharge voltage	114
Figure 5-16	Average spark discharge voltage under different cross-flow velocities	114

Figure 5-17 Average short circuit and restrike frequency under different cross-flow velocities	115
Figure 5-18 First plasma holding period, spark discharge voltage, and current at the first short circuit or restrike under different cross-flow velocities.....	116
Figure 5-19 Spark plasma images under different background pressures	118
Figure 5-20 Effects of background pressure on the spark current and voltage.....	119
Figure 5-21 First plasma holding period and voltage at the first short circuit under different background pressures	120
Figure 5-22 Spark plasma images with varied spark gap size under 20 m/s air flow.....	121
Figure 5-23 Effects of spark gap size on the discharge current, voltage, and plasma length under 20 m/s air flow	122
Figure 5-24 Effect of spark gap size on maximum plasma length.....	123
Figure 5-25 Effect of spark gap size on plasma stretching rate	123
Figure 5-26 Effects of spark gap size on the spark discharge energy and duration.....	124
Figure 5-27 Spark discharge current waveforms with increased current levels	125
Figure 5-28 Effects of air flow velocity on spark discharge energy and duration with different discharge current levels	126
Figure 5-29 Short circuit and restrike frequency with different current level under varied cross-flow velocities.....	127
Figure 5-30 Spark plasma images with different spark discharge current level under 20 m/s and 50 m/s air flow	128
Figure 5-31 Plasma length under 20 m/s and 50 m/s air flow	129
Figure 5-32 Plasma stretching rate at different spark discharge current levels	130
Figure 5-33 Maximum plasma length at different spark discharge current levels.....	131

Figure 5-34	Electric waveforms of high-power spark under air flow conditions.....	132
Figure 5-35	Electric waveforms of transient high-current spark discharge under air flow conditions.....	133
Figure 5-36	Effect of air flow on the dual-coil offset spark discharge	134
Figure 5-37	Spark discharge current and voltage waveforms of a boosted-current spark under quiescent conditions	135
Figure 5-38	Spark discharge current of a boosted-current spark under 20 m/s air flow.	136
Figure 5-39	Improved spark discharge process of the boosted-current spark with a higher module voltage.....	137
Figure 5-40	Effect of air flow velocity on the spark discharge energy of high-voltage current-boosting module	137
Figure 6-1	Demonstration of enhanced flame propagation by gas motion.....	140
Figure 6-2	Effects of gas flow on spark plasma and flame kernel.....	142
Figure 6-3	Flame kernel formation under quiescent and gas flow conditions.....	143
Figure 6-4	Effects of cross-flow velocity on the combustion of lean mixtures.....	145
Figure 6-5	Effect of cross-flow velocity on the high-power spark ignition strategy during the arc and glow phases	146
Figure 6-6	Shadowgraph images of the thermal-induced density field by the high-power spark in air under 25 m/s air flow	147
Figure 6-7	Shadowgraph images of flame propagation under 25 m/s gas flow with the high-power spark.....	149
Figure 6-8	Flame area with the high-power spark under 25 m/s gas flow.....	149
Figure 6-9	Flame area at 5 ms after the breakdown event with the high-power spark under varied cross-flow velocities.....	150
Figure 6-10	Current and voltage waveforms of transient high-current spark.....	152

Figure 6-11 Shadowgraph images of the thermal-induced density field by the transient high-current spark discharge in air under 25 m/s air flow	153
Figure 6-12 Shadowgraph images of flame propagation under 25 m/s gas flow with the transient high-current spark.....	155
Figure 6-13 Flame area with the transient high-current spark under 25 m/s gas flow ...	156
Figure 6-14 Spark discharge current and voltage waveforms of the transient high-current spark discharge	158
Figure 6-15 Current and voltage waveforms of the long-duration spark discharge	159
Figure 6-16 Shadowgraph images of the transient high-current and long-duration spark strategies for the flame kernel development under 35 m/s gas flow	160
Figure 6-17 Flame area at the completion of the spark discharge process under different cross-flow velocities.....	161
Figure 6-18 Flame area of 3 ms after breakdown under different cross-flow velocities	161
Figure 6-19 Spark discharge current waveforms of the conventional and transient high-current spark	163
Figure 6-20 Flame area at the completion of spark discharge by the conventional spark and the transient high-current spark under 25 m/s gas flow	164
Figure 6-21 Flame area comparison between 8 ms post breakdown and the completion of spark discharge.....	165
Figure 6-22 Spark discharge current and discharge energy waveforms	166
Figure 6-23 Shadowgraph images of the flame kernel initiation under 35 m/s gas flow with different spark glow current profiles.....	167
Figure 6-24 Definition of flame propagation distance in the gas flow direction and perpendicular to the gas flow direction	168
Figure 6-25 Flame propagation distances in different directions and flame areas	169

Figure 6-26 Flame kernel growth under gas flow conditions for different glow energy levels	170
Figure 6-27 Spark discharge current waveforms at different current levels.....	172
Figure 6-28 Shadowgraph images of the flame propagation with different spark discharge current levels under 25 m/s gas flow	173
Figure 6-29 Images of plasma channel with different spark discharge current levels under 25 m/s gas flow	174
Figure 6-30 Length of the plasma channel at different spark discharge current levels ..	175
Figure 6-31 Impact of spark discharge duration on flame kernel development (50 mA discharge current).....	176
Figure 6-32 Impact of spark discharge duration on flame kernel development (250 mA discharge current).....	177
Figure 6-33 Effects of spark discharge current level and discharge duration on flame kernel development	178
Figure 6-34 Equivalent crank angle of different spark discharge duration under varying engine speeds	180
Figure 6-35 Spark gap resistance and energy transfer at different spark discharge current levels	180

LIST OF SYMBOLS AND ABBREVIATIONS

Symbols

τ	inductive discharge time constant	[ms]
λ	excess air ratio	[-]
l	length of the plasma channel	[mm]
Δl	increased plasma length	[mm]
s	spark gap size	[mm]
t	time	[ms]
$t_{discharge}$	spark discharge duration	[ms]
$t_{discharge_quiescent}$	spark discharge duration under quiescent conditions	[ms]
$\overline{t_{discharge}}$	normalized spark discharge duration	[%]
ρ	density of air	[kg/m ³]
u	air flow velocity	[m/s]
μ	dynamic viscosity of air	[kg/(m·s)]
d	tube inner diameter	[mm]
Δt	time duration of a stretching process	[ms]
C_{add-on}	add-on parallel capacitance	[pF]
$C_{parasitic}$	parasitic capacitance of spark plug	[pF]
$C_{storage}$	energy storage capacitance	[μ F]
F_{AD}	aerodynamic drag	[N]
F_{RR}	rolling resistance	[N]
F_{ACC}	acceleration force	[N]
F_{RG}	slope force	[N]
$E_{arc/glow}$	spark discharge energy during the arc and glow phases	[mJ]
$E_{breakdown}$	spark discharge energy during the breakdown phase	[mJ]
E_{coil}	energy stored in the secondary coil	[mJ]
E_{total}	total spark discharge energy from the ignition coil	[mJ]
$E_{total_quiescent}$	total spark discharge energy under quiescent conditions	[mJ]
$E_{high-current}$	spark energy from the transient high-current module	[mJ]

\bar{E}	normalized spark discharge energy	[%]
I	spark discharge current	[mA]
L_{coil}	inductance of the secondary coil	[H]
N	number of short circuits and restrikes	[-]
R_{cable}	resistance of ignition cable	[k Ω]
R_{coil}	resistance of the secondary coil	[k Ω]
Re	Reynolds number	[-]
R_{plug}	resistance of the spark plug	[k Ω]
R_{plasma}	resistance of the spark plasma	[k Ω]
$V_{breakdown}$	spark gap voltage during the breakdown phase	[kV]
V_{DC}	voltage of the transient high-current module	[kV]
V	spark gap voltage	[kV]

Abbreviations

AC	alternating current
CEI	controlled electronic ignition
CH ₄	methane
CI	compression ignition
CO	carbon monoxide
CO ₂	carbon dioxide
CMI	coupled multi-charge ignition
DC	direct current
EGR	exhaust gas recirculation
FPGA	field-programmable gate arrays
GDI	gasoline direct injection
HC	hydrocarbons
HCCI	homogeneous charge compression ignition
HPL	high-pressure loop
H ₂ O	water
IC	internal combustion
IGBT	insulated-gate bipolar transistor
LPL	low-pressure loop
MFB	mass fraction burnt
N ₂	nitrogen
NEDC	new European driving cycle
NO _x	oxides of nitrogen
PFI	port fuel injection
RPM	revolutions per minute
RT	real-time
SI	spark ignition
TWC	three-way catalytic converter
VVT	variable valve timing

PREFACE

Motivation and objective

Internal combustion engines have been used to power on-road and off-road vehicles for over a century. Despite the recent development in electric vehicles, internal combustion engines will continue to be one of the main propulsion systems for the automotive industry in the foreseeable future because of the high energy density of hydrocarbon fuels. Presently, new researches on internal combustion engines are mainly propelled by the strict emission regulations and the continuous requirement for engine efficiency improvement.

Lean burn and inert gas dilution are considered effective in improving the efficiency of spark ignition (SI) engines [1–4]. The lean burn is commonly achieved by providing air that is more than the amount required for meeting the fuel-air stoichiometry. The dilution is often deployed by exhaust gas recirculation (EGR). The effectiveness of lean burn and dilution is produced from different prospects. First, the lean-burn or dilution reduces the gas exchange pumping loss [2], especially under partial load operations [3]. Moreover, the combustion temperature is reduced by the excess air or dilution, which is beneficial for both the knocking suppression and the heat transfer loss reduction [1]. The lower knocking tendency facilitates the application of a higher compression ratio, which can greatly increase the thermal efficiency. Additionally, the lean burn can potentially improve combustion efficiency. On the other hand, the combustion of a lean or EGR diluted fuel-air mixture tends to be much slower as compared with that of a stoichiometric mixture, which adversely affects the engine thermal efficiency [5]. To speed up the combustion process, in-cylinder air motions are often intentionally introduced to promote flame propagation [6–9]. The combinations of these new strategies have imposed great challenges on the conventional spark ignition systems.

In conventional spark-ignition systems, the ignition energy is usually in the range of 30 mJ to 100 mJ [10], which is sufficient to ignite the homogeneous stoichiometric mixture with

moderate gas motion. However, for the lean or diluted fuel-air mixture, higher ignition energy is required because of the reduced mixture reactivity [11]. Additionally, the intensification of the in-cylinder air motion makes the ignition process even more difficult [11,12]. The interactions between the spark plasma and the air motion involve complicated physical, electrical, and chemical processes, which further affects the spark ignition process. An unstable ignition process may result in higher cyclic variations or even misfires that are detrimental to engine operation. The successful ignition depends on the matching between the reactivity of the fuel, the intensity of the air motion, and the scheduling of the ignition energy [6]. Under these circumstances, the investigation of the ignition strategies, especially in presence of the air motion, becomes crucial for the application of advanced combustion strategies in internal combustion engines.

In comparison, compression ignition (CI) engines generally have higher efficiency than spark-ignition engines [13]. However, the lack of cost-effective after-treatment devices for the lean-burn engine system makes emission reduction the main challenge for CI engines. NO_x and soot emissions generated from the locally high-temperature combustion regions can be reduced by lowering the combustion temperature with EGR [13]. Nevertheless, there is often a trade-off between emission reduction and efficiency improvement [13,14]. The low-temperature combustion may result in longer combustion duration and incomplete combustion, which impairs the thermal efficiency. The homogeneous charge compression ignition (HCCI) is a preferred combustion mode through which high efficiency and low emissions can be obtained simultaneously [15]. However, the lack of direct control over the ignition process makes it difficult to apply HCCI in production engines. An effective ignition source is thus helpful for the broader application of HCCI combustion.

Considering the trend and the challenges in the development of advanced internal combustion engines, the research on new ignition technologies and strategies is of vital importance. Though the ignition can be improved by many advanced technologies, such as laser ignition, corona ignition, and microwave ignition [16], the inductive coil ignition

systems will continue to be the most feasible way to initiate the combustion in IC engines because of the low cost, robustness, and reliability of inductive coil ignition systems [16].

This research aims to contribute to the advancement of spark ignition in future internal combustion engines. The objectives of this research are listed as follows:

- 1 To configure spark discharge strategies with independently controlled spark discharge parameters via various ignition hardware configurations. The impact of air flow on the discharge of the different spark strategies will be empirically studied.
- 2 To characterize the spark discharge parameters from different spark ignition strategies under various air flow conditions. The correlation between the spark discharge parameters and the air flow velocities will be established from the experiments.
- 3 To empirically study the ignition and flame propagation of a lean or diluted fuel-air mixture under independently controlled mixture flow conditions in constant volume combustion chambers that are comprehensively instrumented as the test platforms.
- 4 To improve the understanding of spark parameters on the flame kernel formation and early flame development under various mixture flow velocities. The effective spark strategies for the ignition of a lean or diluted mixture will be identified under various mixture flow velocities.

The results can potentially contribute to the understanding of the interactions between the flame kernel and the flowing gaseous mixture so that an ignition source with optimum spark discharge parameters can be designed for specific operating conditions. Detailed documentation of the control algorithms and electric circuits for various spark ignition strategies is to be produced, along with illustrations of their strength and limitations under various operating conditions, which can be used as a reference for practical applications in the future.

Structure of the thesis

The dissertation includes 7 chapters. The structure of the dissertation is shown in Figure P-1.

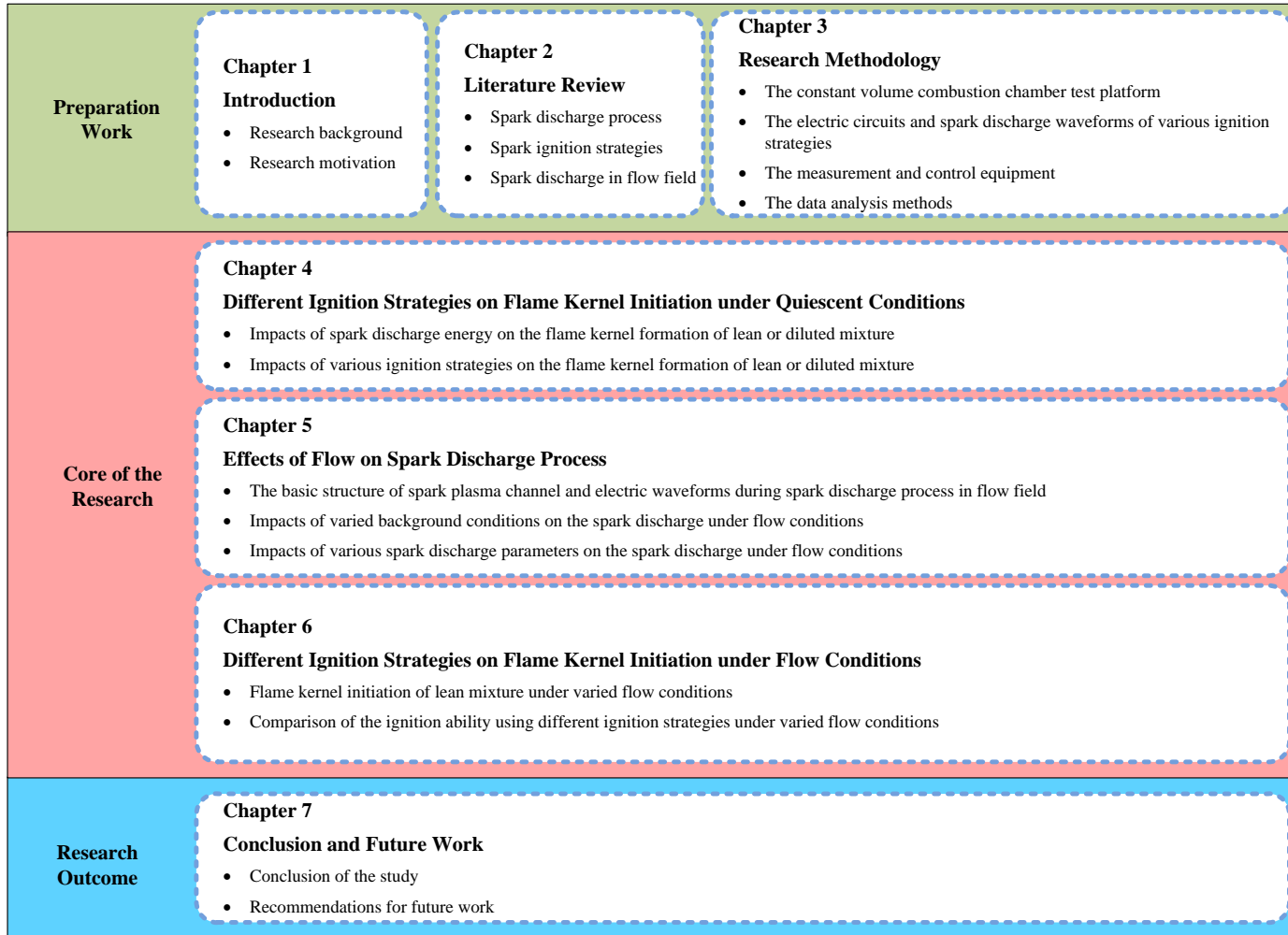


Figure P-1 Structure of the thesis

The research background of this study is introduced in Chapter 1. The current status and challenges in clean combustion engine development are described in this chapter. The importance of this study in achieving engine efficiency targets is emphasized in this chapter.

The literature review is summarized in Chapter 2. The previous research on different ignition strategies is introduced in this chapter. The direction of this research is identified based on the survey of the relevant research activities in the world.

Descriptions of the research methodology can be found in Chapter 3. This research is primarily based on the empirical work which is conducted in a set of constant volume combustion chambers that are instrumented comprehensively as the test platforms. The experimental setup of the combustion chamber test platform is shown in this chapter. A detailed introduction on the electric circuits and control algorithms of different ignition strategies is also provided in this chapter, along with the spark discharge current and voltage waveforms obtained from the experiments. The data analysis methods including the image and pressure processing methods, as well as equations for spark energy calculations, can also be found in this chapter.

In Chapter 4, the impact of spark discharge parameters on the flame kernel formation with lean or diluted mixtures is investigated under quiescent conditions.

The empirical study on the spark discharge under air flow conditions is presented in Chapter 5. The effects of air flow on the spark discharge with varied spark discharge parameters and backpressure are investigated under different air flow velocities. The influences of air flow on the discharge process of different spark strategies are also reported in this chapter.

The impact of the spark strategies on the flame kernel initiation with a lean fuel-air mixture is studied under various mixture flow velocities in the optical combustion chambers. The results and analysis can be found in Chapter 6.

The conclusions of this research are provided in Chapter 7.

CHAPTER 1 INTRODUCTION

1.1 Energy sources for automotive application

Internal combustion (IC) engines have been the primary power source for automotive vehicles for more than a century. Over the years, the efficiency of IC engines, along with the efficiency of automotive vehicles, has been extensively improved [17] (Figure 1-1), while the engine-out harmful emissions are continuously reduced [18]. Nevertheless, the recent development in electric vehicles has raised significant attention. Battery electric vehicles use onboard battery packs as an energy source. The battery can be charged from electric charging stations or other on-board power systems such as the IC engine burning hydrocarbon fuels in some hybrid vehicles. As the energy storage unit in a vehicle, one of the major challenges for batteries is the relatively low energy density.

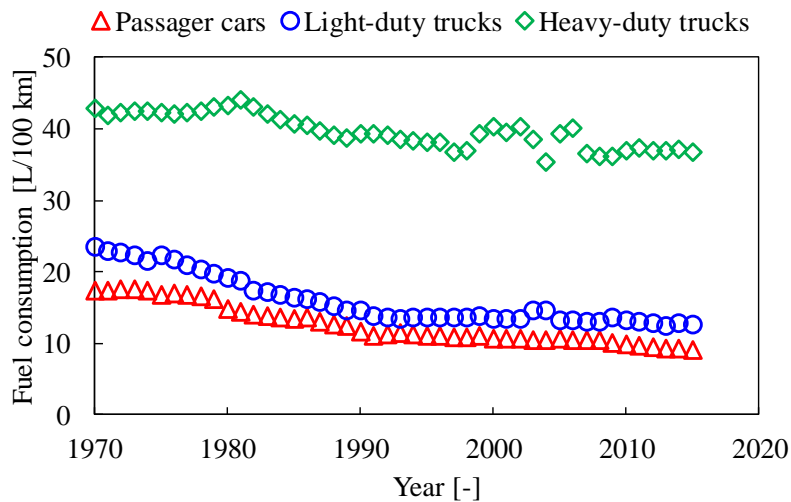


Figure 1-1 Highway fuel consumption for vehicles (Adapted from US Federal Highway Administration [17])

The volumetric and gravimetric energy densities of different portable energy sources are shown in Figure 1-2. Though the energy densities of batteries have increased substantially over the years, their maximum achievable energy densities are still confined by the fact that batteries need to contain all the reactants on-board for the electrical and chemical

reactions [19]. The scenario of reactants fully contained in a concealed pack is similar to the case of explosives. The energy densities of explosives are also shown in Figure 1-2 as references. In contrast, the combustion of fuel in automotive applications only requires partial reactants, the fuel, to be on-board. The other part of the reactants, the air, is readily available in the atmosphere. For this reason, the on-board energy densities of hydrocarbon fuels are intrinsically higher than the energy densities of batteries. Even compared with explosives, hydrocarbon fuels alone are much higher in energy density.

One of the major issues with the combustion of hydrocarbon fuels is the production of CO₂ which is a greenhouse gas. The use of renewable fuels can partially circumvent this issue by creating a carbon-neutral condition in the whole life cycle of the fuel. The energy densities of several renewable fuels are also shown in Figure 1-2.

The overall force required to drive a vehicle depends on many factors, such as the weight of the vehicle, the structural design, as well as the driving conditions. The total resistance of the vehicle that needs to be overcome by the powertrain can be quantified by 1-1 [20].

$$F_{Total} = F_{AD} + F_{RR} + F_{ACC} + F_{RG} \quad 1-1$$

Where, F_{AD} represents the aerodynamic drag that is determined by the aerodynamic shape of the vehicle, the projected frontal area of the vehicle, and the vehicle velocity. F_{RR} is the rolling resistance that is dependent on the velocity and the mass of the vehicle, in addition to the road surface and tire conditions. F_{ACC} denotes the acceleration force that increases with the vehicle's mass. F_{RG} is the slope force that can be directly affected by the road gradient and the vehicle's mass [20].

The composition of the total resistance suggests that the weight of the vehicle has a pronounced impact on the resistance that needs to overcome to drive a vehicle. The resistance will affect the energy required to drive the vehicle. As shown in Figure 1-3, the fuel consumption of vehicles generally increases with vehicle weight.

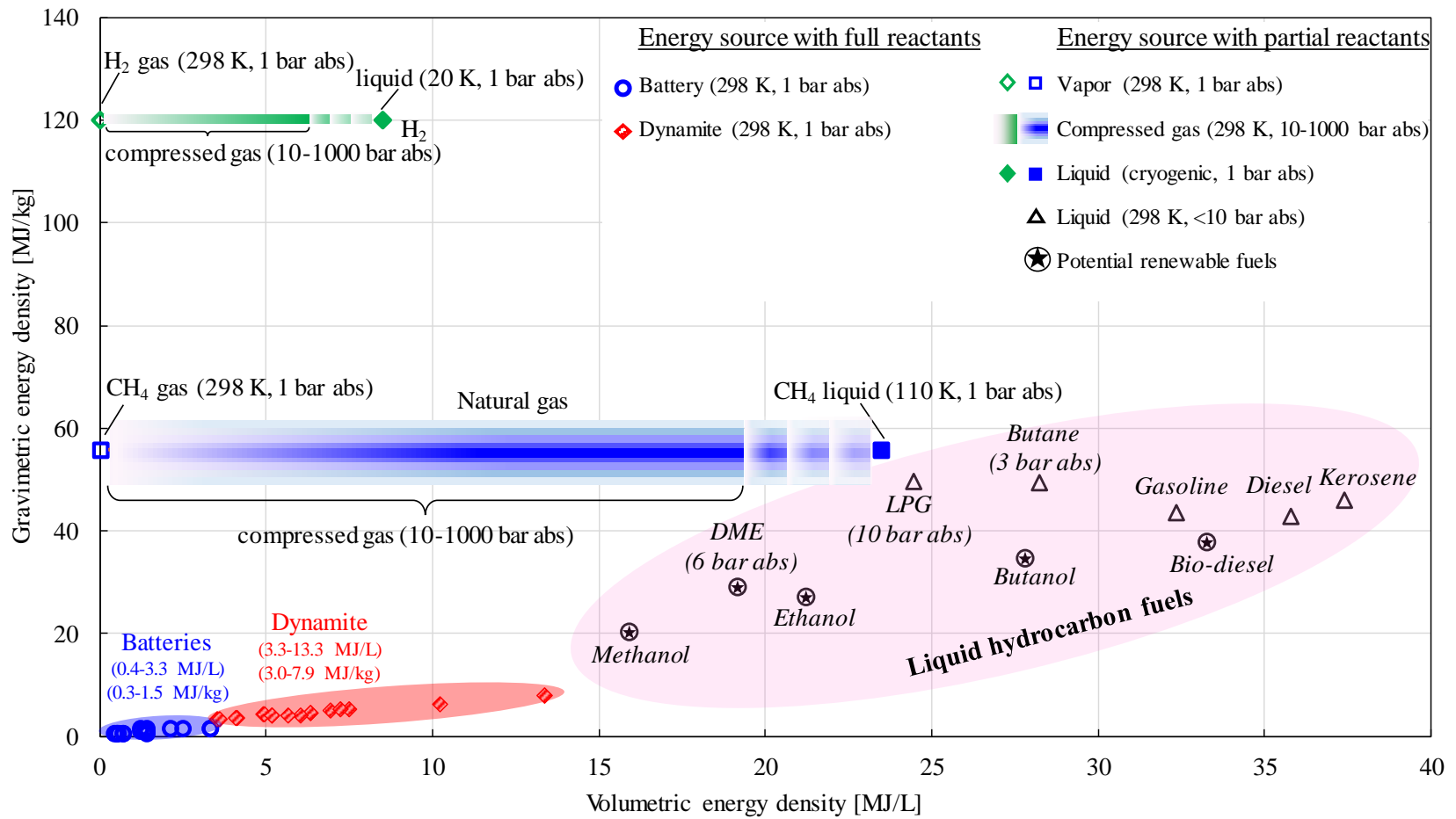


Figure 1-2 Gravimetric and volumetric energy densities of various portable energy sources [21–23]

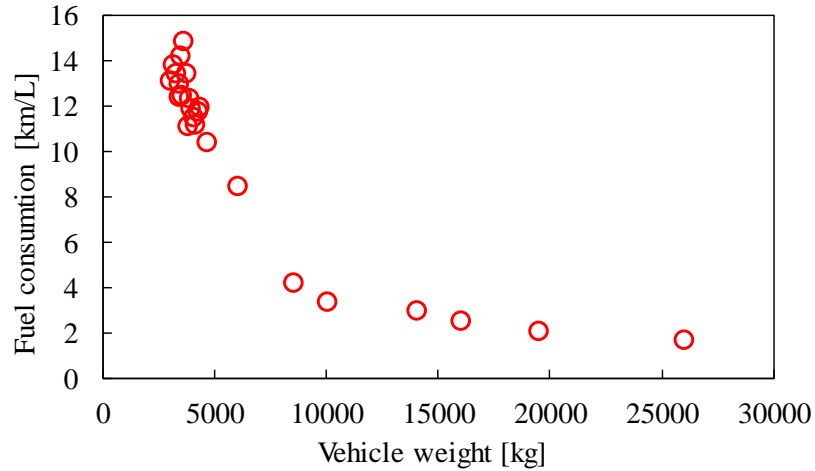


Figure 1-3 Variation of fuel consumption with vehicle weight (Adapted from The National Academies Press [24])

One of the greatest challenges for battery electric vehicles is that the battery weight contributes a substantial percentage to the weight of the whole vehicle as compared with the fuel weight in IC engines, as shown in Figure 1-4. The limitation in battery energy density can significantly hinder the application of battery-powered electric vehicles in heavy-duty transportation or long-distance traveling.

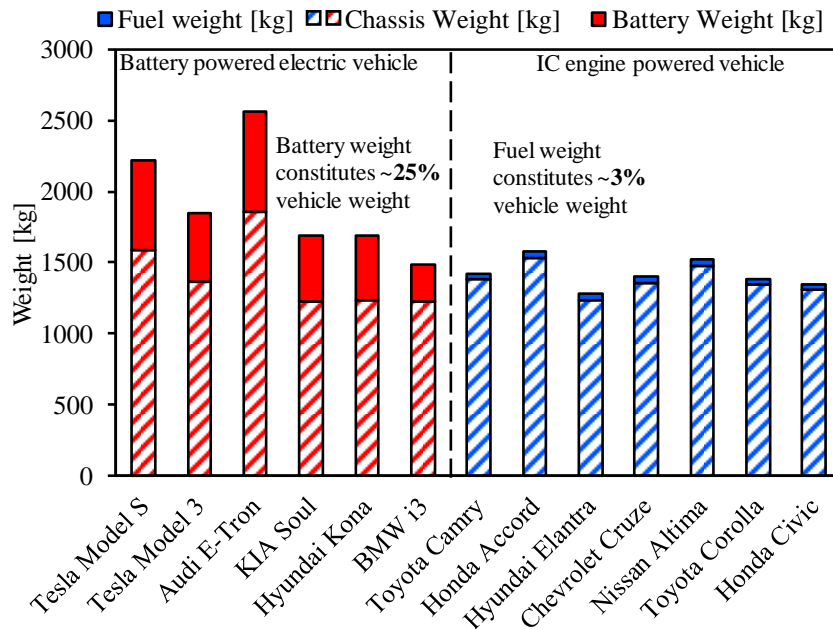


Figure 1-4 Vehicle weight and battery pack/fuel weight (Adapted from Yu *et al.* [19])

For traveling long-distances, if the battery to vehicle weight ratio is relatively low, the vehicle needs frequent charging. The long charging duration is a problem under this circumstance. The charging time and traveling time of some battery electric car models are plotted in Figure 1-5 [17]. The charging time constrain can be somewhat circumvented by increasing the charging power [25,26]. The time to charge a light-duty car can be reduced from 1.5 hours to 20 min for 90 miles drive when the charging power is increased from 19.2 kW (AC Level 2 charging station) to 90 kW (DC Fast charging station) [26]. However, fast charging often reduces the lifespan of batteries [27]. Besides, with the aging of batteries, the charging efficiency decreases, while the safety hazard increases due to the imbalance between the different cells of a battery pack [27].

Though the challenges to the electric powertrains are not part of the research work, it is important to emphasize that electric vehicles cannot fully replace IC engine-powered vehicles, at least not with the currently available technology, especially for commercial trucks, air crafts, and marine boats. The innovative research and advancement in IC engine vehicles are still of paramount importance for the transportation sector.

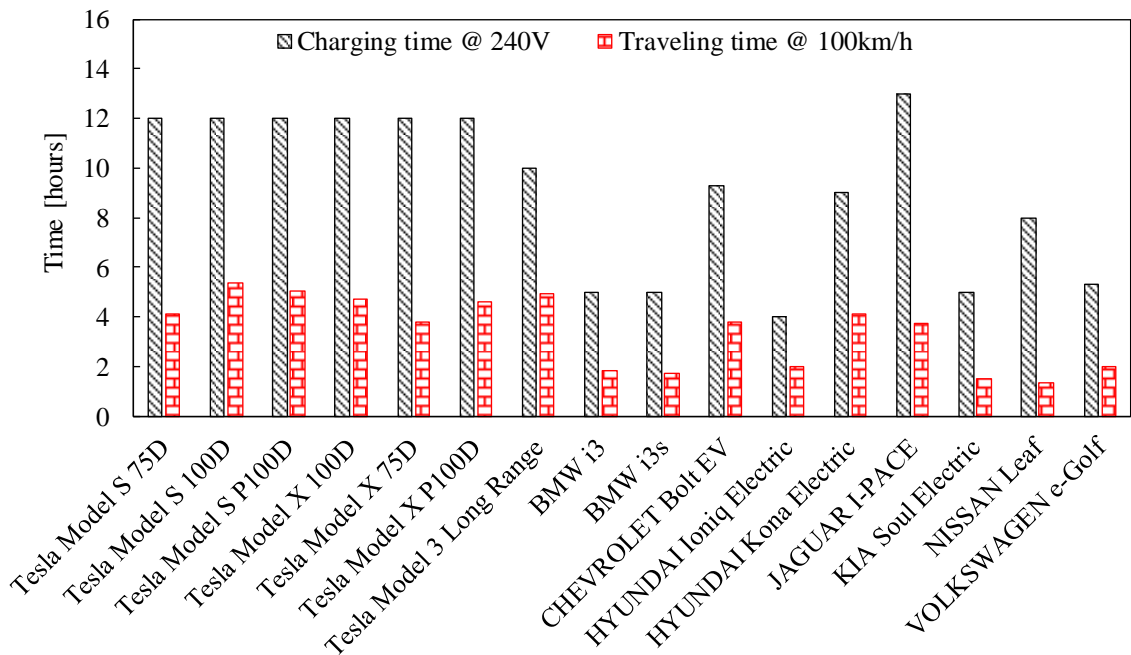


Figure 1-5 Charging time and traveling time of electric vehicles [17]

1.2 Spark ignition engine development for clean combustion

Between the two types of IC engines, spark ignition (SI) engines have been widely used in light-duty vehicles [28]. For conventional spark-ignition engines, the homogeneous combustion normally results in minimum soot emissions [29]. Other emissions, such as oxides of nitrogen (NO_x), carbon monoxide (CO), and unburned hydrocarbons (HC) can be effectively converted to nitrogen (N₂), water (H₂O), and carbon dioxide (CO₂) by the three-way catalytic converter (TWC) [30,31]. Though the toxic emissions of SI engines are easier to reduce as compared with that of the compression ignition engines, owing to the TWC, the efficiency of spark-ignition engines is generally lower than that of its compression ignition counterpart [28]. In line with the lower efficiency, more CO₂ gas is released. CO₂ gas is a major contributor to the greenhouse effect [32]. Thus, the CO₂ emission regulation has been gradually tightened by environmental protection authorities, as shown in Figure 1-6, which urges the automotive manufacturers to continuously improve engine efficiency.

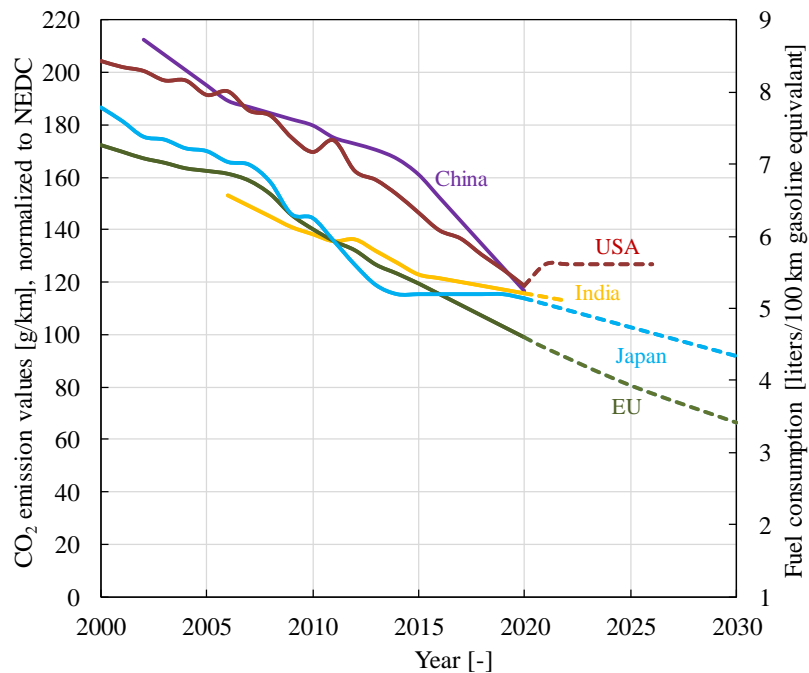


Figure 1-6 Passenger automobile fuel economy standards [32–34]

The relatively low efficiency of SI engines stems from different aspects. Conventional SI engines operate with fuel-air mixtures locked at nearly stoichiometric air-fuel ratios. The adjustment of engine load is accomplished by controlling the opening of a throttle valve in naturally aspirated engines, or the combination of the throttle valve opening and the boost pressure in turbocharged engines [3]. A smaller opening of the throttle valve at partial load conditions restricts the intake air flow, along with the fuel flow, i.e., the work output. Consequently, the engine efficiency suffers from increased pumping loss during the gas exchange process [3,35,36]. Moreover, the homogeneous and stoichiometric mixture in SI engines confines the range of the compression ratio because of the knocking limit [3,37,38]. Furthermore, under high speed and full load conditions, fuel enrichment could be applied to limit the engine and catalyst temperatures for safety and engine system protection [39], which also increases the fuel consumption. Different strategies have been deployed to improve the efficiency of SI engines, such as the application of variable valve timing (VVT) [3,28,40,41], engine downsizing [28,39,42], gasoline direct injection (GDI) [43–45], and the EGR dilution [2,35,37,46].

The application of VVT is effective in improving engine efficiency by reducing the gas exchange pumping loss [40]. Instead of using a throttle, an early or late inlet valve closing can be devised to moderate the amount of fuel-air mixture that flows into the cylinder [40]. Moreover, the effective expansion ratio can be adjusted by controlling the exhaust valve opening time [41]. Additionally, the change in the valve timing affects the in-cylinder pressure and temperature, which may affect the combustion process [47].

Engine downsizing is another widely used technique for efficiency improvement. A downsized engine with a smaller swept volume has the advantage of reduced engine mass and size. With a smaller displacement, the engine can operate at a comparatively higher load to achieve the same power output, which reduces the frequency for low load operation and hence results in less gas exchange pumping loss [37,48]. To maintain the same power with a downsized engine, intake boosting is often used to increase the density of air that flows into the cylinder [2,48]. The increased intake air density results in higher temperature

during the compression stroke, which promotes the pre-ignition and the knocking tendency [49]. Strategies such as retarding the spark timing or decreasing the compression ratio can be used to suppress the knocking and pre-ignition tendency [48,50]. However, these operational necessities tend to compromise the gain in engine efficiency improvement. These conflicts can be mitigated by the application of lean burn and diluted combustion [37,48,49,51].

The knocking suppression with lean burn and dilution can be attributed to both the reduced end gas temperature and the lower end gas reactivity [7,49]. Cooled EGR is generally used for the purpose of knocking suppression [38]. The reactivity of the in-cylinder fuel-air mixture is reduced by the exhaust gas or the extra air, resulting in a lower flame propagation speed [37,38,52]. The decreased flame propagation speed leads to a longer combustion duration and a lower combustion pressure [53]. The lower combustion pressure has reduced compression effects on the end gas, which is beneficial for the knocking suppression [53]. On the other hand, the inert dilution gas increases the amount of the total in-cylinder mixture that acts as a heat sink for the combustion process [7,49]. Consequently, a larger amount of in-cylinder gas results in lower end-gas temperature [7,49].

EGR is also beneficial for engine efficiency improvement [2,54]. The exhaust gas replaces a part of the fresh air. Consequently, under the same load level, the throttle needs to be opened wider to let more fresh air flow into the cylinder [55]. The wider opening of the throttle results in lower gas exchange pumping loss. Moreover, the heat transfer loss is decreased due to the reduced combustion temperature enabled by the dilution effect of the exhaust gas [56]. The reduced combustion temperature alleviates the knocking tendency, which facilitates an advanced spark timing to place the combustion period in a window with better thermal efficiency [57]. Another benefit of EGR is that it reduces the exhaust temperature so that the frequency of fuel enrichment can be reduced, which also contributes to the fuel economy improvement, especially under high load conditions [2,54]. The aspects for efficiency improvement with cooled EGR are summarized in Figure 1-7.

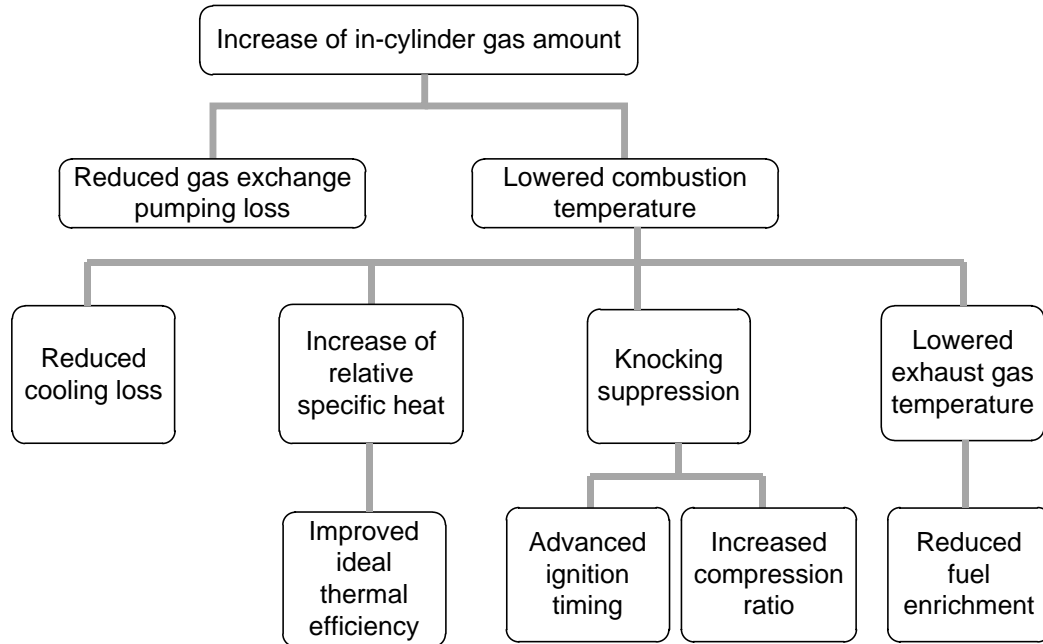
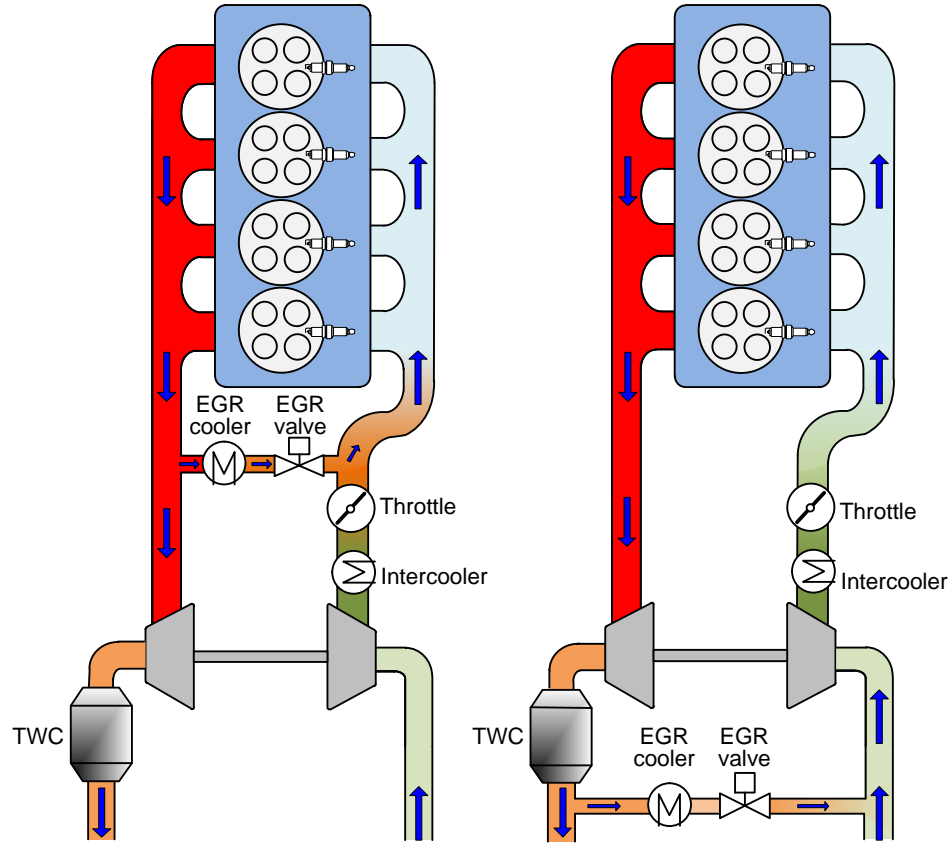


Figure 1-7 Efficiency improvement by cooled EGR (Adapted from Takaki *et al.* [2])

Two commonly used EGR loop configurations in turbocharged engines are the high-pressure loop EGR and the low-pressure loop EGR [37,52,58], as illustrated in Figure 1-8. The high-pressure loop (HPL) EGR works by recirculating a portion of the exhaust gas upstream of the turbine back to the intake pipe downstream of the compressor (Figure 1-8 (a)). The low-pressure loop (LPL) EGR reroutes a part of the exhaust gas downstream of the turbine back to the upstream of the compressor, as shown in Figure 1-8 (b). The selection of the HPL EGR and LPL EGR depends on the engine operating conditions. The combination of the two configurations has also been used to realize an improved engine performance in the full load range [59,60].



(a) High-pressure loop EGR

(b) Low-pressure loop EGR

Figure 1-8 EGR loop configurations in turbocharged SI engines

The lean-burn is another viable combustion strategy for efficiency improvement in SI engines [61–63]. Lean burn strategy is normally realized by supplying air that is more than the amount required for meeting the fuel-air stoichiometry [51,64]. Similar to the dilution effects of EGR, the lean-burn strategy can also increase the thermal efficiency by reducing the gas exchange pumping loss, increasing the specific heat ratio, and reducing the heat transfer loss by lowering the combustion temperature [51,65].

The lean-burn strategy is often used together with EGR, along with the gasoline direct injection (GDI) for engine efficiency improvement [43–45], as shown in Figure 1-9. When the engine is running at low load conditions, a stratified fuel-air mixture with an overall lean air-fuel ratio can be used to reduce the gas exchange pumping loss [36,66]. The

combustion instability can be alleviated and the ignition process can be improved by creating a fuel-rich condition close to the spark gap with a background of overall lean mixtures [36,66]. At higher load conditions, the injection timing is advanced to create an overall homogeneous stoichiometric mixture, which is similar to the condition when a port fuel injection (PFI) is used [67].

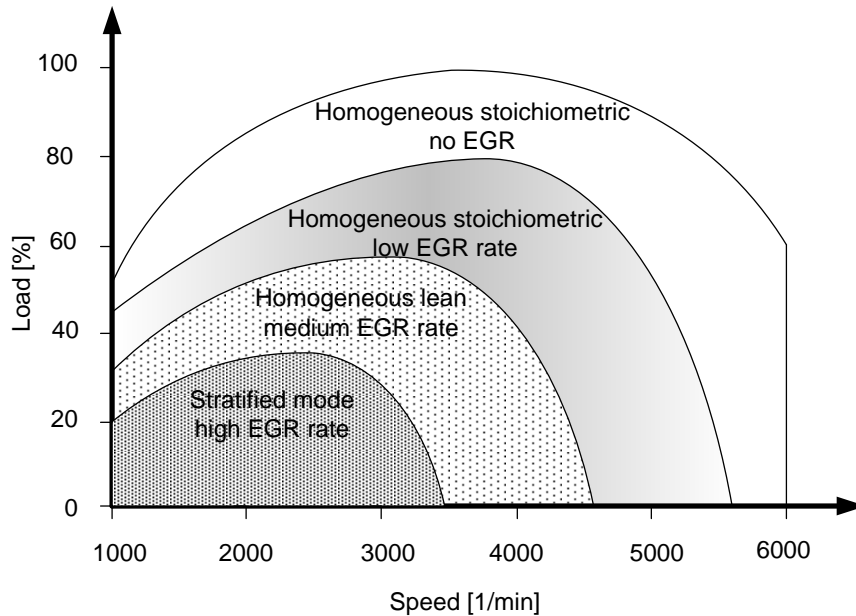


Figure 1-9 Operational modes of a gasoline direct injection engine (Adapted from Blank *et al.* [67])

One of the major disadvantages of lean burn and diluted combustion is the reduced combustion speed of the in-cylinder fuel-air mixture, which results in longer combustion duration and lower combustion efficiency [68]. Combustion instabilities are increased due to the slow-burning process [68]. Enhanced in-cylinder gas motion is often applied to improve the combustion speed [6,8,9].

Modern advanced spark-ignition engines often use a combination of the above-mentioned technologies to achieve better efficiency gain [69]. Some common features of the new combustion systems include higher boost pressure, enhanced gas motion, diluted in-cylinder fuel-air mixture, and a wider spectrum of fuel-air ratios. Although these techniques

are effective in improving engine efficiency, they also raise challenges for the ignition and the following combustion process, which will be elucidated in the next section.

1.3 Challenges in the spark ignition process

The combustion of a lean or diluted in-cylinder fuel-air mixture is more unstable as compared with the stoichiometric combustion in conventional SI engines, which limits the potential for efficiency enhancement [6,9,68,70]. The reasons for the unstable combustion include the increased breakdown difficulties from the higher gas density with EGR dilution and higher boost pressure, the unstable flame kernel growth, and the longer combustion duration of the diluted mixture [71].

Intensified gas motions are proposed to improve the combustion process [6,8,9]. The gas motion is effective in enhancing the in-cylinder turbulence level and the flame propagation speed, resulting in a shorter combustion duration [5,6]. However, the intensified gas motion further increases the difficulties in the ignition process with the conventional spark ignition system [5,6]. The minimum ignition energy increases with the dilution of the mixture [72,73]. The gas motion makes the scenario even worse as suggested by Huang *et al.* [72]. Their research showed that the minimum ignition energy (MIE) increased sharply with the increased turbulence intensity [72]. Though the ignition mainly affects the initial stage of the flame kernel formation, the insufficient ignition abilities manifest later in the combustion process as increased variability and poor combustion controllability [5,74,75].

The direct injection SI engines also encounter challenges in the ignition process. The combustion instability partially originates from the convective flow fluctuations caused by the direct fuel injection, as well as the reduced flame speed of a leaner mixture [51]. In the spray-guided stratified-charge SI engines, the spark plug is located close to the injector which induces strong air motion during the injection. The injection-induced strong air motion and the in-cylinder gas motion can greatly stretch the spark plasma channel. The resistance of the plasma channel is increased due to the stretch [76]. The plasma breaks off when it is stretched to a certain extent. The spark discharge becomes unstable, and the

discharge duration gets shorter. The reduced spark duration can potentially affect the flame kernel formation [77].

1.4 Chapter summary

The application of lean burn and EGR diluted combustion has great potential in improving the efficiency of SI engines. However, the new combustion strategies have also mandated higher requirements on the spark ignition system. These challenges are summarized in Figure 1-10. Ignition systems that can operate under a higher background density, tolerate lower reactivity of the mixture, and sustain the ignition source with stronger gas motion, need to be developed for the advanced combustion strategies.

Among the multiple challenges for the ignition process, the increased gas density often raises difficulties for the breakdown process, where a higher voltage is essential to ensure the breakdown event. The heterogeneity of the in-cylinder mixture advocates the necessity of higher ignition energy, as the minimum ignition energy increases when the mixture gets either lean or rich [78]. Moreover, challenges for the ignition process come from the enhanced gas motion, especially with lean or diluted mixtures. The gas motion not only affects the flame kernel but also alters the spark discharge process. The interactions among the electric discharge, heat transfer, and chemical reaction make the ignition process much more complicated as compared with the case under quiescent conditions. The focus of the present research is thus on the ignition process under gas flow conditions.

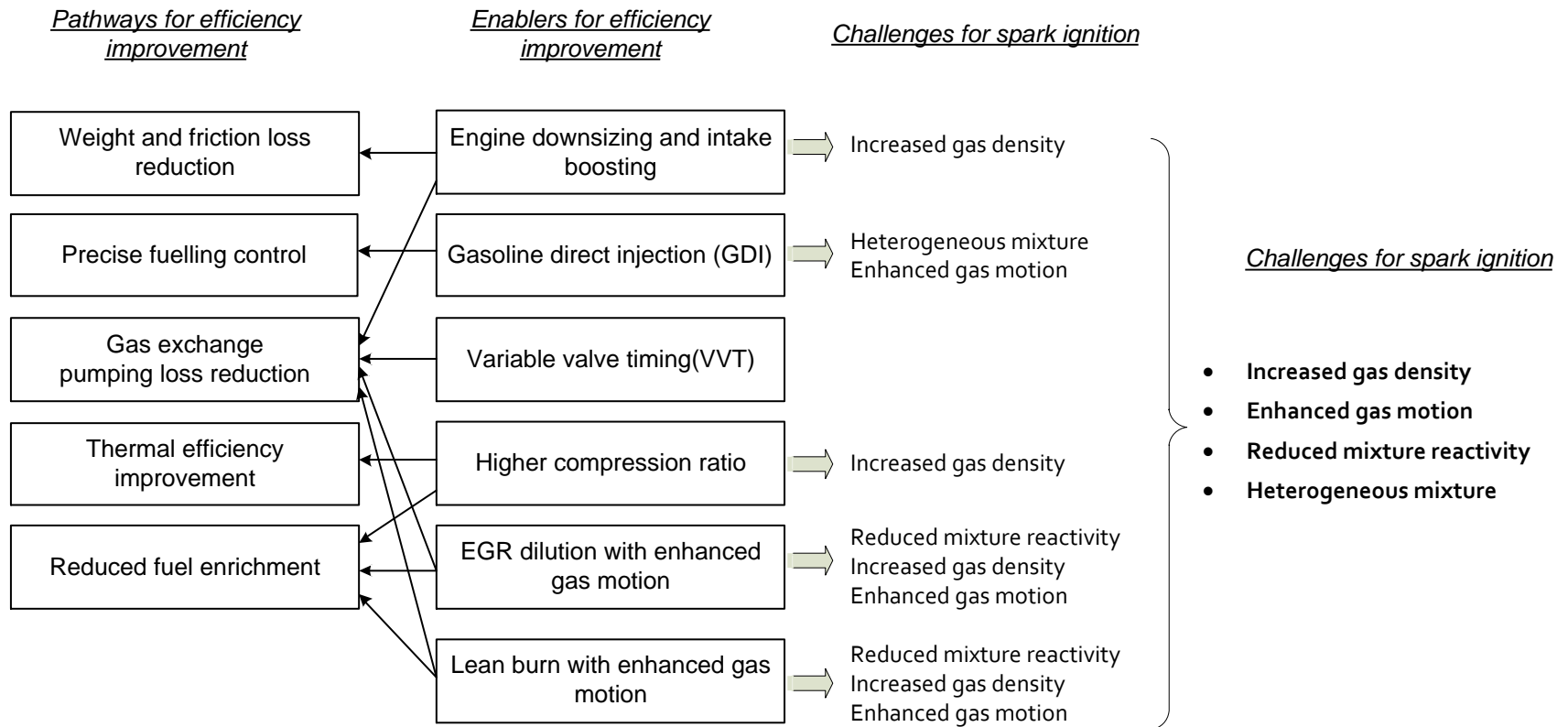


Figure 1-10 Challenges for the ignition in modern SI engines

CHAPTER 2 TECHNICAL BRIEFING AND LITERATURE REVIEW

In this chapter, a literature review about different spark ignition strategies is presented. The review focuses on the ignition strategies that are based on conventional inductive ignition coils. The emphasis is on the application of the spark ignition strategies for the ignition of fuel-lean or EGR diluted fuel-air mixtures. The second part of the review provides an overview of the characteristics of spark discharge under gas flow conditions.

2.1 Basic spark discharge process from an inductive ignition system

The inductive coil ignition system has been considered the most reliable and cost-effective solution for production engine applications [16]. The ignition coil pack works based on the transformer principle [79]. The coil pack consists of a primary coil with a smaller number of windings and a secondary coil with a larger number of windings. A schematic diagram of the inductive coil ignition system is shown in Figure 2-1. Batteries of 12 V and 24 V are widely used in passenger cars and natural gas trucks, respectively. The voltage of the battery should be maintained within an appropriate range. For instance, the lower voltage limit of a lead-acid 12 V automotive storage battery is 7.2 V to pass the Cold Cranking Test as required by the SAE J537 standard for storage batteries [80]. One end of the primary ignition coil is connected to the positive terminal of the battery. The other end of the primary coil is connected to an insulated-gate bipolar transistor (IGBT) which is then connected to the negative terminal of the battery [81]. The negative terminal of the battery is normally connected to the metal frame of a vehicle as the common ground. In the secondary circuit, one terminal of the secondary coil is connected to the central electrode of the spark plug. The other terminal of the secondary coil is connected to the ground electrode of the spark plug and the common ground of the ignition circuit.

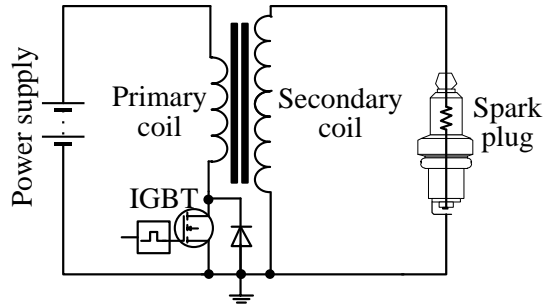
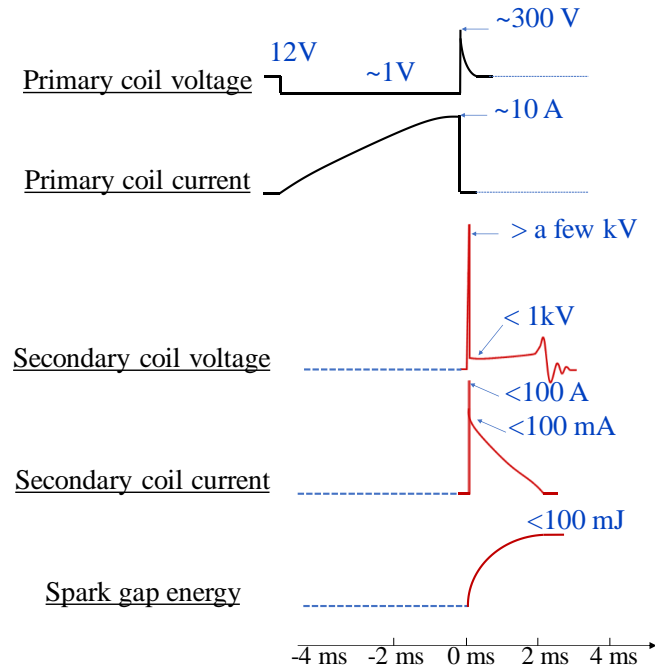


Figure 2-1 Inductive coil ignition system (Adapted from Zheng *et al.* [16])

For a typical conventional inductive coil ignition system, the electric current and voltage waveforms of the charging and discharging processes are shown in Figure 2-2. The primary circuit can be switched ON or OFF by the IGBT following the ignition control signal. The charging process is started in the primary coil when the primary circuit is switched on. The primary current gradually increases, usually to several amps in a duration up to approximately 5 ms. This time stage is usually termed as the charging duration [79]. A magnetic field is generated due to the increased current in the primary coil. The electric energy of charging is transformed to the magnetic field of the coil in this process. The dynamic charging process finishes when the primary circuit is switched off prior to saturating the coil current. Thereby, the primary current drops drastically to a value close to 0 amps. The abrupt change in the primary current results in the transformation of the magnetic field to a transient inductive voltage of several hundred volts in the primary coil. Correspondingly, in the secondary circuit, a voltage of often higher than a couple of thousands volts is generated in the secondary coil due to the abrupt voltage change of the primary coil. The ratio between the primary voltage and the secondary voltage in this process depends on the ratio between the number of windings in the primary coil and the number of windings in the secondary coil [82]. The high voltage from the secondary coil results in the gas ionization process across the spark gap. The secondary circuit is closed once the ionized channel is formed in the spark gap. The energy stored in the magnetic field is gradually released to the spark gap in a few milliseconds, which initiates a flame kernel by heating the surrounding combustible mixtures and activating the gas molecules. The time stage for the spark discharge process is termed as the spark discharge duration [16].

The spark discharge current gradually decreases during the inductive discharge process. Concurrently, the spark discharge voltage drops rapidly until resumes to about a few hundred volts [74,79].



Note: Values in this figure represents spark discharge from a typical spark gap (~1 mm) under quiescent and atmospheric conditions

Figure 2-2 Waveforms during the charging and discharging processes of an inductive coil ignition system (Adapted from Yu *et al.* [74,79])

The spark discharge from the secondary coil can be divided into four phases: pre-breakdown, breakdown, arc, and glow [83–86], as shown in Figure 2-3. During the pre-breakdown phase, the secondary coil voltage increases rapidly in receiving the energy of the magnetic field that is transformed from the current collapse of the primary coil. In accordance, the parasitic capacitance in parallel to the spark gap is charged. In the meantime, the spark gap voltage increases until the gaseous media in between the gap is electrified to become conductive, i.e. the onset of the breakdown phase. Once the conductive channel is formed between the gap, the energy held in the secondary coil and

the parasitic capacitance (typically around 5-15 pF) of the spark plug, is released through the channel [83].

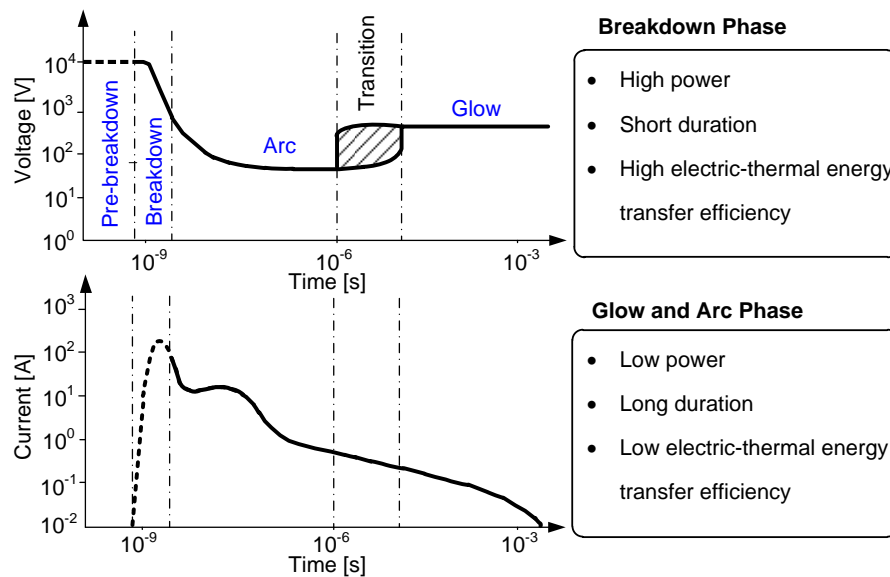


Figure 2-3 Phases in the spark discharge process under quiescent conditions (Adapted from Maly *et al.* [84])

The breakdown phase is characterized by high power and short duration, often more than tens of kilowatts in several nanoseconds. The transient spark discharge current during the breakdown phase can exceed hundreds of amps, depending on the equivalent impedance of the secondary circuit [87]. The dropping of high breakdown voltage and the surging of high discharge current are in step, which concurs an extensively high discharge power. Within the brief duration of the breakdown phase, the temperature and pressure in the plasma channel also increase drastically. The overpressure in the plasma may generate audible shock waves that propagate outwards. The electric energy is transferred to the gas across the vicinity of the spark gap for thermal heating and kinetic activation. The electrical-to-thermal energy transfer efficiency during the breakdown phase is reported as high as 94% in air with 300 K background temperature and 1 bar background pressure [84].

Following the breakdown phase, the gaseous plasma arcing is accompanied by the thermionic emissions from the molten hot spots on the cathode [87]. The current level is

typically over 100 mA [84]. The electrical-to-thermal energy transfer efficiency is reported about 50% [84]. The current level further drops in the glow phase to below ~100 mA. Unlike in the arc phase, the electrons during the glow phase are obtained mostly from the cold cathode via ion impact without the assistance of thermionic emissions from otherwise molten hot spots [87]. The electrical-to-thermal energy transfer efficiency during the glow phase is reported to be the lowest, about 30% in the air at 300 K background temperature and 1 bar background pressure [84].

Based on the configuration of the conventional inductive coil ignition systems, different ignition strategies were investigated to modify the spark discharge process, such as the high-power spark, the high-energy spark, and the boosted current spark. These ignition systems are discussed in the following sections.

2.2 Spark ignition systems

The ignition strategies can be categorized based on their control and operating principles, such as the high-power spark, the high-energy spark, and the long-duration spark. Different hardware can be used to realize these spark strategies. A few representative ones are summarized in this section.

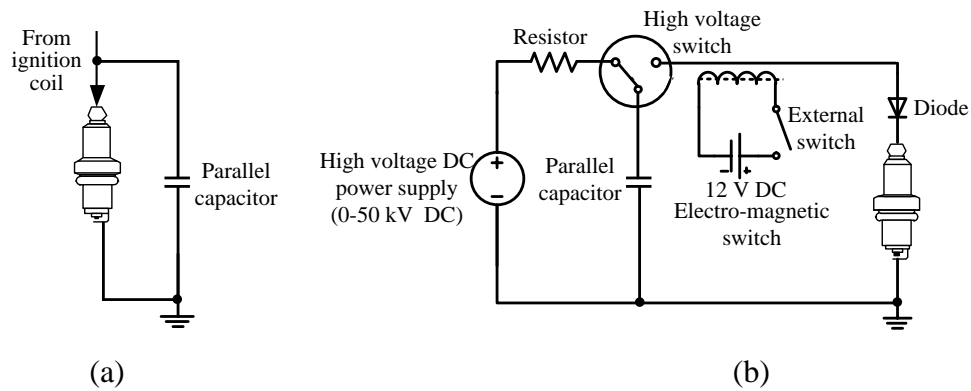
2.2.1 High-power ignition system

The high-power ignition system features a higher spark discharge power and a short spark discharge duration [88–93]. The high power can be achieved by adding a capacitor in parallel to the spark gap in a conventional inductive ignition system [88,89,92], as shown in Figure 2-4 (a). The capacitance of the add-on high voltage complying capacitor is typically much higher than the structural capacitance of the spark plug. The add-on capacitor receives electrical charging during the pre-breakdown phase.

Alternatively, an external high-voltage power supply is used to pre-charge the added parallel capacitor [94], as shown in Figure 2-4 (b). During the breakdown, the voltage drop

of the central electrode allows the energy stored in the capacitors to be released through the gap plasma channel quickly. The added parallel capacitor can therefore increase the transient spark discharge current during the breakdown phase. The high power is realized when the high discharge current is in step with the high discharge voltage during the breakdown event [88–93].

Small loop resistance is preferred to ensure a swift discharge process of the energy stored in the capacitor so that the high spark discharge current can meet the high voltage during the breakdown to concur a high spark discharge power. A non-resistive spark plug is usually used for this reason [89,92]. Alternatively, the embedded resistor of the spark plug should be placed upstream of the parallel capacitor so that it does not affect the capacitive discharge during the breakdown phase [88].



(a) Peak capacitor coupled with ignition coils (Adapted from Anderson *et al.* [92]),

(b) Peak capacitor coupled with external power supply (Adapted from Cho *et al.* [94])

Figure 2-4 High-power ignition systems

Previous studies reported that the peak spark discharge current was increased dramatically in a high-power ignition system. Anderson [91] reported a peak spark discharge current of 700 A with the high-power ignition system when using a 250 pF parallel capacitor. A peak spark discharge current of 800 A was generated by Cho *et al.* using their high-power ignition system [94]. Corresponding to the low parallel capacitance, the high current spark discharge was generally very fast, within 100 ns [91,94].

2.2.2 High-energy ignition system

The high-energy ignition systems refer to ignition systems that can provide higher spark discharge energy to the spark gap. The high-energy ignition systems generally involve extra energy supply hardware in addition to the original ignition coil. The additional energy supply hardware can be more ignition coils [71,95], or can be supplementary power supply and energy storage systems [96–98]. The spark discharge energy can range from several hundred millijoules to as high as several joules [5,97,99–102]. The different energy supply hardware results in different energy release processes. The stored energy can be released by a transient high discharge current, which is released in several microseconds, such as in the plasma jet and rail plug ignition systems [100,101]. An exemplary electric circuit of a plasma jet ignition system is shown in Figure 2-5. Alternatively, the high energy ignition system can deliver extra energy to the spark gap in the form of a long-duration spark discharge [95,102].

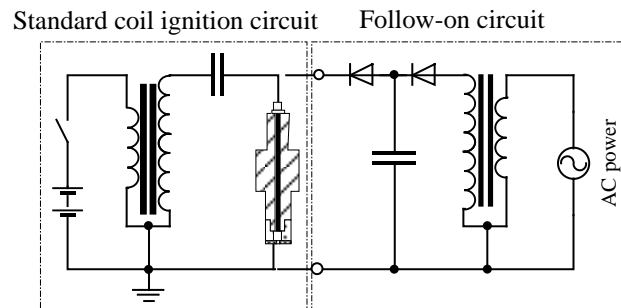


Figure 2-5 Plasma jet ignition system (Adapted from Murase *et al.* [99])

The ignition systems with transient high spark discharge current often feature thermal expansion of the plasma due to the abrupt release of energy, which is different from the long-duration spark discharge whose performance is related to both the spark discharge duration and the spark discharge current level.

In a plasma jet ignition system, the breakdown event is triggered by a conventional inductive coil ignition system. Once the ionization channel is formed after the breakdown event, the energy stored in the external energy storage element, usually a capacitor with a

capacitance of several microfarads (μF), will be released, resulting in a high spark discharge current [97].

2.2.3 Ignition systems with controlled spark discharge current and duration

More ignition systems are designed to accommodate the requirement of controlling the spark discharge process. The multi-coil ignition system is such a kind of ignition system that is frequently used to generate different spark discharge profiles. A representative circuit of a dual-coil ignition system is shown in Figure 2-6. More coils can be added in a similar configuration. With multiple coils connected to the same spark plug, the coils can be charged and discharged simultaneously or alternately so that different spark discharge current profiles are created. Other ignition systems with modulated spark discharge current such as the Controlled Electronic Ignition (CEI) and the Coupled Multi-charge Ignition (CMI) have also been proposed [103].

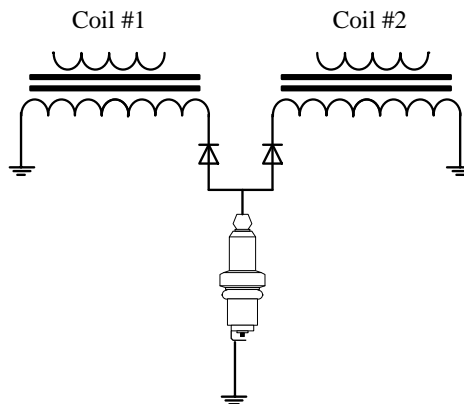


Figure 2-6 Multi-coil ignition system represented by two coils (Adapted from Alger *et al.* [95])

2.3 Spark ignition strategies for ignition of lean and diluted fuel-air mixtures

Realized by the aforementioned ignition systems, the spark discharge energy can be released with different features. For instance, a high current is in step with the high voltage as in the case of high-power spark; a very high current can be achieved transiently as in the

case of plasma jet and rail plug ignition system; multiple sparks or a long duration spark can be generated by the multi-coil system. Studies have been carried out to investigate the effectiveness of the different spark discharge strategies for the ignition of lean and diluted fuel-air mixtures.

2.3.1 High-power ignition strategy

The performance of the high-power ignition strategy was studied on spark ignition engines [88,89,91–93], and constant volume test facilities [94,104]. Experiments conducted by Yu *et al.* [104] on constant volume combustion chamber proved that the lean ignition limit of methane-air mixtures under quiescent conditions was extended from an excess air ratio of 1.7 to 1.9 by a high-power spark.

Jacobs *et al.* [88] compared the high-power spark with a spark from the “base” ignition system (conventional inductive ignition coil system) in a GDI engine running under low load conditions. Their results showed that the high-power spark reached a lean operation limit with an excess air ratio of $\lambda=1.4$ compared with $\lambda=1.25$ when the base ignition system was used. The combustion stability was also improved with the high-power spark. However, the authors did not report the spark discharge energy levels from the two spark strategies.

Anderson *et al.* [92] found the high-power, which they termed as the “blast wave” ignition strategy, outperformed both the normal and the long duration spark strategies in reducing the 0-10% burning duration and the combustion instability of a gasoline engine operated under lean conditions [92].

Nevertheless, some other research results demonstrated that the high-power ignition strategy was not as effective under certain operating conditions. According to Pischinger *et al.*[93], the high-power spark did not shorten the flame initiation period in an SI engine under very lean conditions when higher turbulence was present inside the cylinder.

Pischinger *et al.* [93] commented that the engine design and operating conditions might affect the performance of different ignition strategies.

Cho *et al.* [94] studied the performance of the high-power spark ignition strategy in a constant volume combustion chamber with different turbulence levels. They found the high-power spark was less effective under high turbulence and high dilution conditions.

2.3.2 High-energy ignition strategy

Many researchers reported better ignition capability of the plasma jet ignition strategy as compared with a conventional ignition strategy from an inductive coil ignition system [99,100,105]. The experiments were carried out in both combustion chambers [100] and research engines [105], under both quiescent conditions and with turbulence [100]. The plasma jet ignition strategy delivered a much higher level of spark discharge energy in the experiments.

Murase *et al.* [99] carried out combustion experiments in a chamber configured to generate swirl motion. They found that a conventional spark resulted in a faster pressure rise in comparison to a plasma jet ignition under a swirl velocity of 10 m/s, albeit with the much lower spark discharge energy from the conventional spark as compared with that of the plasma jet ignition. The authors stated that the flow velocity had a great impact on the ignition process and needed further in-depth investigation.

2.3.3 Spark strategies with controlled spark current and voltage profiles

The ignition performances of spark with controlled discharge current and voltage profiles during the arc and glow phases were also reported [5,6,71,95,103,106–110]. The studies often focused on the impact of spark discharge current level and duration on the ignition performance.

Jung *et al.* [6] used ten inductive ignition coils connected in parallel to the same spark plug to realize different spark discharge current profiles by changing the offset between each

coil. They found that a spark discharge with low-current and long-duration was incapable of maintaining a stable operation under lean conditions, probably due to the insufficient spark discharge energy. The performance of a high-current short-duration spark was not satisfactory as well, possibly because of the inadequate spark discharge duration. The spark discharge strategies with medium current level and duration demonstrated the best results with respect to lean limit extension and engine stability improvement.

Ogata *et al.* [71] studied the impact of different ignition strategies on the EGR dilution limit under varying engine speeds. They found that a boosted spark discharge current level extended the EGR dilution limit.

Alger *et al.* [95] investigated the impact of different ignition strategies on EGR diluted combustion in engine test systems. Their results showed that the dual coil continuous spark discharge was most effective in shortening the combustion duration and extending the dilution limit, especially at low-load or high-speed engine operating conditions. The authors commented that the better performance of the dual coil continuous discharge was mainly due to the continuous nature of the spark discharge current, rather than the higher spark discharge energy. However, the energy they referred to was the coil-out energy instead of the energy delivered to the spark gap.

Suzuki *et al.* carried out a study on the ignition performance in an engine with a tumble ratio of 3.5 [107]. They found that there was a limit in extending the spark discharge duration, beyond which minimal benefit was observed in promoting the flame kernel growth. The limit was related to the spark discharge current level as well, where a longer duration was required for a lower current level. The impact of spark discharge energy was not discussed in detail in their research.

Other published results also demonstrated the superior performance of the continuous spark discharge in extending the lean and dilution limit or improving engine operation stability, whereas the authors had different opinions on the impact of spark discharge energy level on the ignition ability [109,110]. Wallner *et al.* commented that the spark discharge energy

level had minimal impact on the ignition performance [109], which was contradictory to Pilla *et al.* [110]'s results.

2.4 Spark discharge process under gas flow conditions

The air motion not only affects the flame propagation but also changes the spark discharge process, including varied spark discharge energy levels and altered plasma channel shape [12,103]. This is unlike the spark ignition of a quiescent mixture, where the flame kernel is normally generated along a line the shortest distance of the spark gap. With the impact of air flow, the flame kernel can be formed at different locations, depending on the plasma shape and distribution [12,103].

The research on the spark plasma and flow interactions was dated back to the 1930s when Lindvall [111] found that the change in glow discharge voltage was correlated to the air flow velocity. The feature of the glow discharge voltage in correlation with the flow field was used as an anemometer for air velocity measurement. Later on, more research work was carried out [86,112–114]. Based on the research results, with specific assumptions, researchers derived equations to describe the relationships between the flow, the spark discharge parameters, and the spark gap dimension [86,113].

Kim *et al.* [113] measured the spark discharge current and voltage waveforms under atmospheric pressure and with an air flow velocity up to 15 m/s. They found the spark discharge voltage demonstrated a “saw-toothed” shape with multiple restrikes. The voltage rise rate increased with the air flow velocity.

Pashley *et al.* [86] carried out experiments under a gauge pressure of up to 12 bar and air flow velocity of less than 20 m/s. They reported a rise in the spark discharge voltage and a reduction of the spark discharge duration with the increased air flow velocity.

In both studies [86,113], without simultaneous optical recording of the plasma channel, the authors simplified the plasma profile as a piecewise rectangle shape and correlated the increase in the plasma length to the air flow velocity. The relationships between the spark

discharge voltage, discharge current, spark gap size, air flow velocity, and the background pressure were summarized to form empirical models.

Shiraishi *et al.* [115] conducted experimental research on the spark discharge under air flow conditions with flow velocity changing from 0 m/s to 8 m/s under a background pressure from 1 bar abs to 10 bar abs. From the images of the spark plasma, they found the plasma length before the first restrike increases with both the air flow velocity and the background pressure. They also calculated the convection velocity of the spark channel tip from the images. The convection velocity of the spark channel tip was lower than the air flow velocity, especially under low background pressure.

2.5 Chapter summary

From the published literature, various ignition strategies were used for lean or diluted combustion. Each of the strategies showed some beneficial effects under certain conditions. However, in summary of the literature, the mechanisms of how different ignition strategies performed under gas flow conditions were not studied thoroughly.

The engine test results demonstrated the capability of certain ignition strategies under specific operating conditions. However, the boundary conditions, such as the background pressure, temperature, and gas flow velocity were not controlled or specified in most of the experiments. The indefinite boundary conditions made it difficult to perceive the critical influential factor in the ignition process and to expand the research findings obtained from one test system to another test system. Moreover, ignition strategies under comparison in previous studies were often coupled with different igniter configurations and supplied with different spark energy levels. The reported spark energy values were mostly the energy supplied to the spark plug instead of the energy that was delivered to the spark gap.

Moreover, in many of the research, the spark discharge current level and the spark discharge duration were both improved to achieve better ignition performance [95,103,106–110], whereas the impact of each parameter was not differentiated.

For the study of the spark discharge under air flow conditions, existing literature demonstrated some general impact of the air flow velocity on the spark discharge process, such as the increase in the spark discharge voltage, decrease in the discharge duration, and the occurrence of restrike events. However, existing research results covered a limited range of air flow velocities. The impact of the air flow on the spark discharge parameters, such as the discharge energy and the discharge duration, was not investigated in a comprehensive manner. Moreover, there was insufficient research on spark and air flow interactions with varied spark parameters, such as spark gap size and spark current. Furthermore, the mechanisms on how the interactions between spark plasma and air flow would affect the flame kernel initiation were not studied in detail.

CHAPTER 3 RESEARCH METHODOLOGY

The literature review in the previous chapter has demonstrated the key effects of different spark ignition strategies on the ignition of lean and diluted fuel-air mixtures. The mechanisms of the ignition process under gas flow conditions need further investigation. The behaviors of the spark plasma under gas flow conditions also need to be studied to better understand the ignition process. In order to characterize the spark ignition process under gas flow conditions, extensive empirical research has been carried out in this dissertation.

Various spark ignition strategies have been deployed to modulate the spark discharge parameters by setting up different hardware configurations. Thus, the spark discharge parameters, such as the spark discharge current amplitude and profile, the discharge duration, and the discharge power, can all be adjusted by the in-house developed control algorithms and ignition circuits. A set of constant volume combustion chambers have been used as the major research platform to study the flame kernel formation with different ignition strategies. One of the constant volume combustion chambers is configured to generate a cross-flow of gaseous fuel-air mixtures in the vicinity of the spark gap through a tube jet flow set up under various background pressures. Additionally, an air flow test bench has been utilized to generate controlled flow velocities for the study of the spark plasma behavior under air flow conditions with atmospheric pressure and temperature.

3.1 Constant volume combustion chambers

Two constant volume combustion chambers are used in the study. An all-metal chamber is used to carry out combustion experiments under quiescent conditions. An optical constant volume combustion chamber is configured to operate with controlled mixture flow. The photos of the optical combustion chamber test system are shown in Figure 3-1.

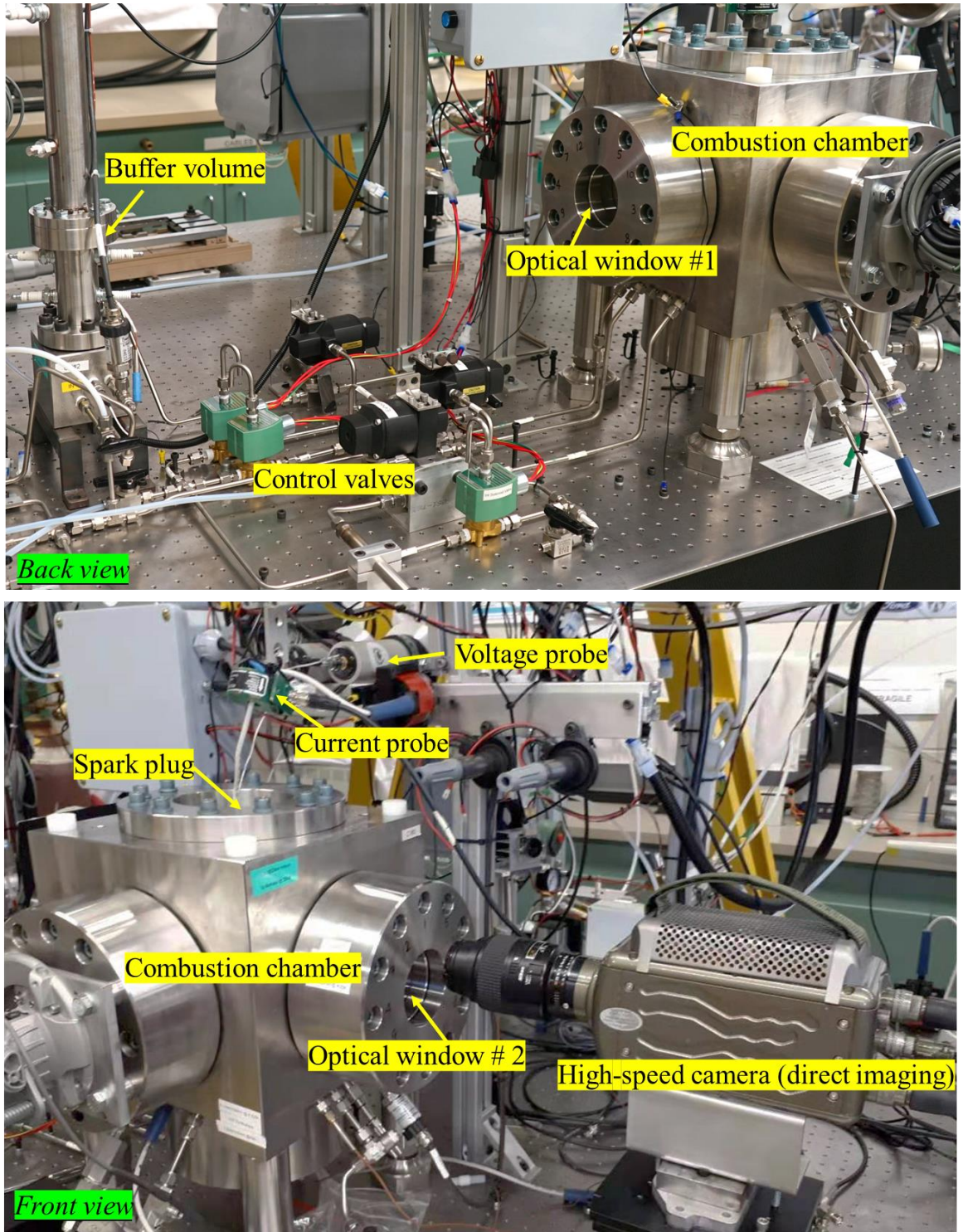


Figure 3-1 Photos of constant volume combustion chamber test platform

The specifications of the optical chamber are listed in Table 3-1.

Table 3-1 Specifications of the optical constant volume combustion chamber

Maximum block heating temperature	200 °C
Designed maximum pressure	200 bar abs
Chamber body material	SS 304
Chamber dimensions	Width 300 mm × Depth 300 mm× Height 300 mm
	Chamber inside volume: 2.6 liters
Optical windows	Synthetic quartz (max. 5) Φ120 mm, thickness 100 mm
	Optical access: Φ 80 mm
	Surface accuracy: $\lambda/10$ (λ is the wavelength of the testing light source, typically 632.8 nm)
Maximum view ports	5

A schematic diagram of the optical constant volume combustion chamber test platform is illustrated in Figure 3-2. The test platform is configured with gas supply systems, imaging systems, and measurement systems. The imaging systems include a shadowgraph imaging system and a direct imaging system. The measurement instruments include current and voltage probes and pressure transducers. The all-metal chamber is configured similarly, except that the flowing gas line and the imaging systems are not set up with the all-metal chamber. The volume of the all-metal chamber is 102 ml. Repeated combustion experiments under quiescent conditions have been primarily carried out in the metal chamber.

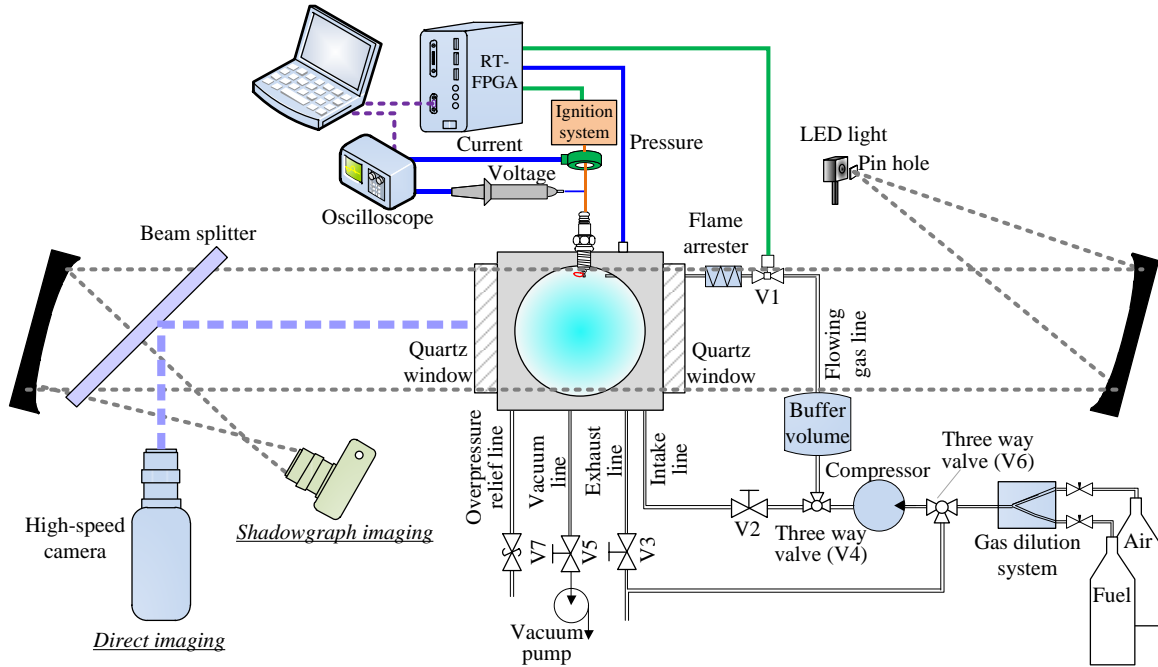


Figure 3-2 Experimental setup of the constant volume combustion chamber

3.1.1 Gas supply systems of the optical constant volume chamber

The gas supply system of the optical chamber is composed of an Environics 4040 computerized gas dilution system, an oil-free compressor, an intake line, and an exhaust line. An overpressure relief line is also connected to the chamber for safety precautions.

The specifications of the Environics 4040 computerized gas dilution system are listed in Table 3-2. The computerized gas dilution system can produce gas concentrations from percent to ppb levels. Eight mass flow controllers are configured in the gas dilution system to control the concentration and flow rate of mixing gases.

The gas dilution system can operate at different modes. When the gas dilution system operates at the concentration mode, a blend gas can be created by entering target gas concentrations for each source gas cylinder, and the desired total output flow for the gas mixture. When it operates at the flow mode, the flow rate of each gas cylinder can be

specified by the user. In the experiments carried out in this study, the concentration mode is applied to create gas mixtures with precisely controlled compositions.

Table 3-2 Specifications of the Environics 4040 gas dilution system [116]

Accuracy	Concentration mode: $\pm 1.0\%$ setpoint Flow mode: $\pm 1.0\%$ setpoint
Operating Pressures at inlets	1.67 – 6.04 bar abs
Dilution ratios	Up to 10000:1
Performance temperatures	15-35°C

Both quiescent and flow conditions can be provided during the experiments in the optical chamber. The flow conditions are achieved by introducing a jet flow produced cross flow near the spark gap, as shown in Figure 3-3.

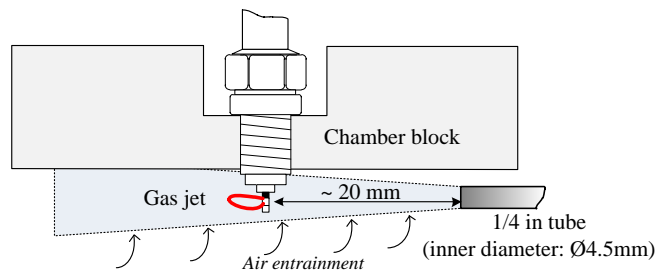


Figure 3-3 Demonstration of the flow field near the spark gap

To create a jet flow, the gas mixture is supplied to a 400 ml buffer volume that is pressurized to a higher pressure than the pressure in the optical chamber. The jet flow is generated by releasing the gas mixtures in the buffer volume to the optical chamber. A solenoid valve (V1 in Figure 3-2) that is connected between the buffer volume and the optical chamber is used to control the timing and duration for releasing the flowing gas. A flame arrester is connected to the flowing gas line to prevent the flame from propagating back to the buffer volume. The composition of the flowing gas and the background gas is the same in the experiments. The procedure of operation during the experiment is demonstrated in the flow chart shown in Figure 3-4.

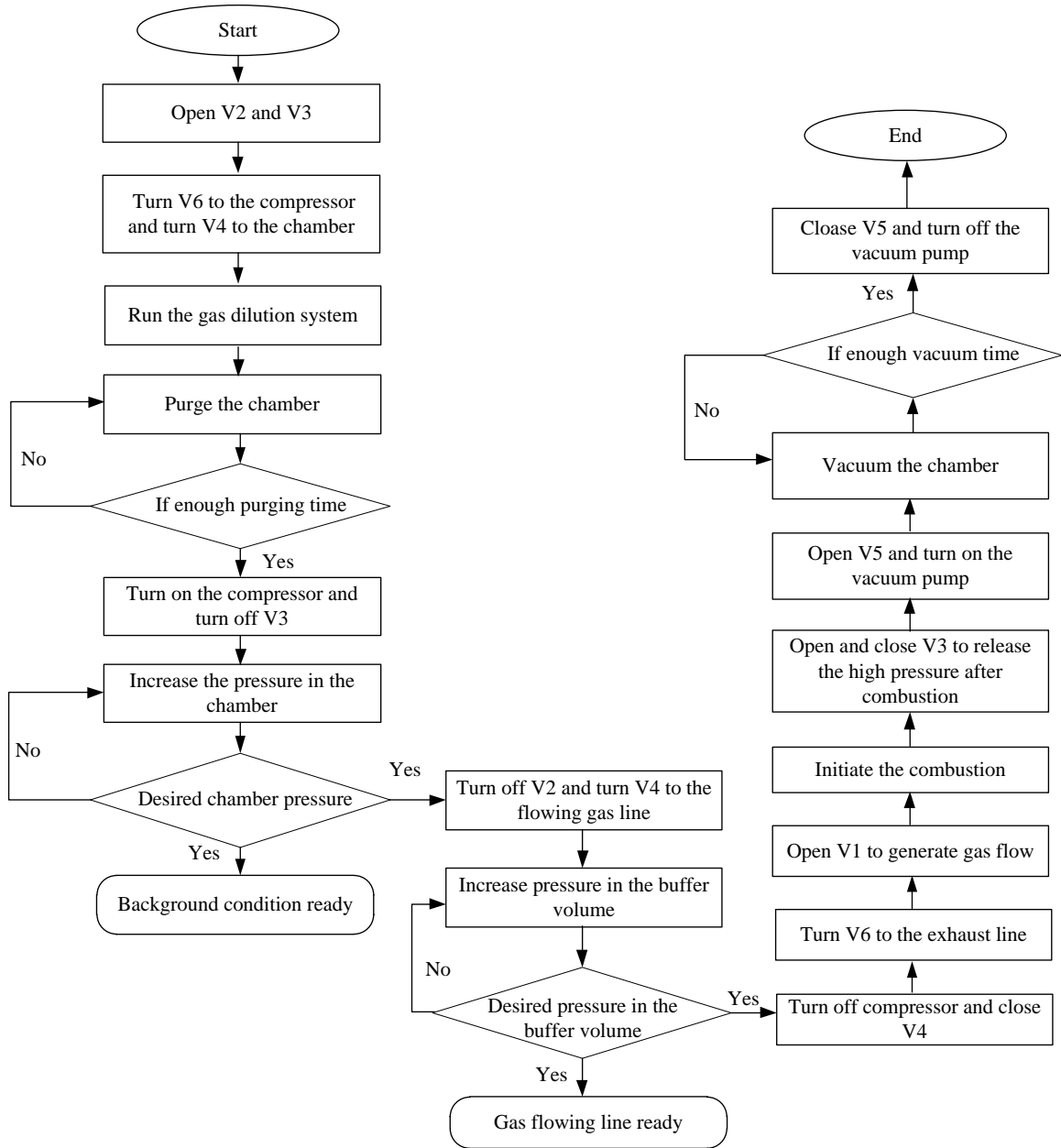


Figure 3-4 Flow chart of the procedure during the experiment

The velocity of the flowing gas at the spark timing can be controlled by adjusting: (1) the pressure difference between the optical chamber and the buffer volume, or (2) the time offset between the valve opening and the spark initiation. Once a proper pressure difference between the combustion chamber and the buffer volume is decided, the flow velocity is mainly controlled by adjusting the time offset between the valve command and the spark

command through the control program to minimize the impact of pressure change on the ignition and combustion process.

The control algorithm is implemented on a set of National Instruments™ CompactRIO systems. The architecture of the control hardware is shown in Figure 3-5. A real-time (RT) controller (cRIO-9002) is connected to a cRIO-9102 chassis with embedded field-programmable gate arrays (FPGA) modules. The RT controller and FPGA devices are connected to a host computer via an ethernet cable. A user interface is configured on the host computer based on the National Instruments™ LabVIEW software so that the command signals can be adjusted conveniently.

The RT controller features high-speed floating-point real-time computation while the FPGA handles precisely the critical timing events. The control programs are deployed in the hierarchical architecture of the RT-FPGA system. The RT controller sends the commands of the duration and timing of each control signal to the FPGA through high-speed inter-target communication. The execution of the low-level FPGA program generates precisely the TTL control signals. The FPGA features a 40 MHz single-cycle timed loop, which enables the execution of the programmed code in a 25 ns timing interval. The FPGA is connected to multiple digital input and output modules that transmit signals to the spark ignition circuits and solenoid valves. The output module (cRIO-9474) for the spark signal command has an output delay time of up to 1 μ s at full scale [117]. The output module (cRIO-9472) drives the actuation relays of the solenoid valves with an output delay time of up to 100 μ s at full scale [118].

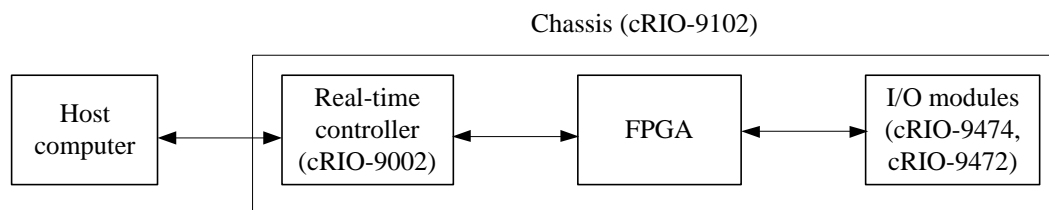


Figure 3-5 Architecture of the CompactRIO system

The solenoid valve opens upon receiving the control signal from the FPGA output module to generate a momentum air jet crossing the spark gap. Then a command signal to trigger the spark event is sent out by the FPGA output module when the gas flow at the spark gap reaches the desired flow velocity. The time dwell between the valve command and the spark command is pre-calibrated to ensure the gas flow velocity near the spark gap is the required flow velocity at the spark timing. The measurement of current, voltage, camera, and pressure all started simultaneously with the spark triggering. The sequence of the command signals is shown in Figure 3-6.

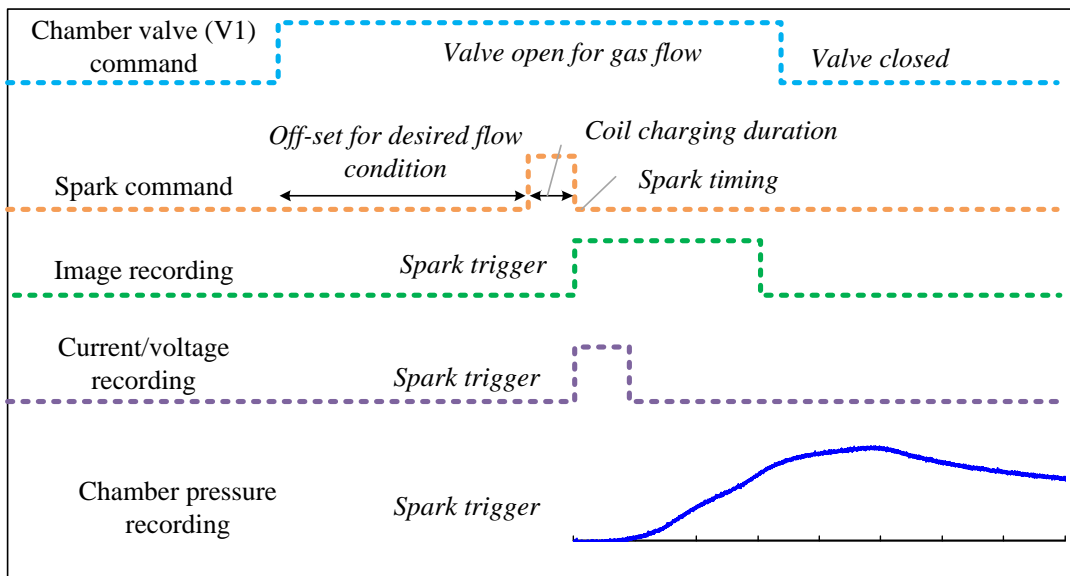


Figure 3-6 Signal sequence during the experiments

The flow velocity across the spark gap is estimated from the movement of seeding particles captured by high-speed images. In general, the flow process is unsteady, because the pressure in the buffer volume reduces gradually once the valve is opened to release the flowing gas. However, within a very short time window of several milliseconds during the spark discharge, the gas flow can be considered quasi-steady flow. The transient velocity after the valve opening is shown in Figure 3-7.

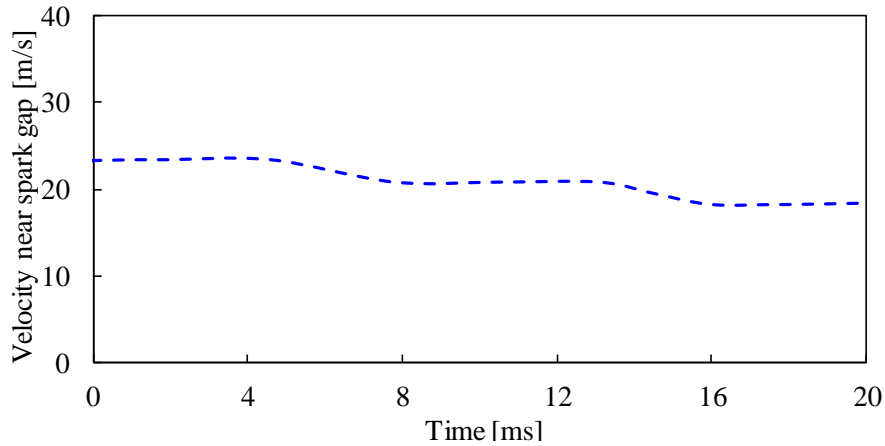


Figure 3-7 Flow velocity near the spark gap

3.1.2 Imaging systems of the optical constant volume chamber

Two imaging systems are set up with the chamber, including a shadowgraph imaging system and a direct imaging system. The shadowgraph imaging system is composed of a “z-type” light path, a high-speed camera, and two 6-inch f/8 precision parabolic mirrors. The shadowgraph imaging is set up to observe the density change of the media inside the chamber during the spark event and the combustion process. For the direct imaging system, the camera is placed directly in front of the optical window of the chamber. Alternatively, the direct imaging system can be used together with the shadowgraph imaging system when a beam splitter is set up in the light path to split light for both systems. The specifications of the high-speed cameras are listed in Table 3-3.

Table 3-3 Specifications of the high-speed cameras

Camera	Sampling frequency	Lens
Vision Research TM Phantom v7.3	6688 fps @ 800 × 600 pix 190476 fps @ 32 × 32 pix	Nikon 105 mm f/2.8 FX AF MICRO-NIKKOR
IDT TM MotionXtra	4000 fps @ 512 × 512 pix	Nikon Ray fact PF10545MF-UV

3.1.3 Measurement instruments of the optical constant volume chamber


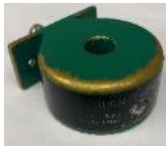
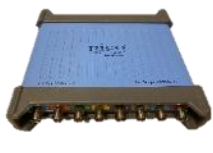
The spark plug is centrally located at the ceiling of the combustion chamber. A Tektronix 6015 high voltage probe, a Pearson 411 current probe, and a PicoScope 4824 oscilloscope are set up to measure the electrical waveforms during the spark discharge process. The voltage and current probes are connected to the spark plug terminal nut. A Swagelok PTI-S-NG5000-15AQ standard industrial pressure transducer is connected to the combustion chamber to measure the pressure during the combustion process.

The Tektronix P6015A is a ground-referenced high voltage probe with 1000X attenuation. The input resistance is 100 M Ω and the input capacitance is 3 pF. The spark discharge voltage during both the breakdown and the glow and arc phases can be measured with the voltage probe.

The Pearson 411 current probe is a current transformer. The rated bandwidth is 20 MHz and the rising time is approximately 20 ns. The bandwidth is fast enough for measuring the discharge current during the arc and glow phases. The measurement of the discharge current during the breakdown phase is less accurate. The breakdown phase occurs in a time duration of several nanoseconds, which is beyond the bandwidth of the current probe.

The specifications of the Tektronix P6015A voltage probe, the Pearson 411 current probe, and the PicoScope 4824 oscilloscope are listed in Table 3-4. The sampling frequency for the current and voltage signals during the breakdown phase and the arc and glow phases is set to be 40 MHz and 1 MHz, respectively.

Table 3-4 Specifications of the current probe, voltage probe, and oscilloscope

	Tektronix P6015A	Pearson 411	PicoScope 4824
Rated bandwidth	75 MHz	20 MHz	20 MHz (50 mV to 50 V range) 10 MHz (10 mV to 20 mV range)
Rise time	~4 ns	~20 ns	17.5 ns (50 mV to 50 V range) 35.0 ns (10 mV to 20 mV range)
Measurement range	1.5 kV- 20 kV (DC + peak AC), impulses up to 40 kV peak	Up to 5000 A	10 mV-50V
Photo			
Reference	[119]	[120]	[121]

3.2 Controlled air flow test bench

An air flow test bench is set up to generate controlled air flow with steady flow velocities. A schematic diagram of the test bench is shown in Figure 3-8. A free jet air flow is generated from a Dantec Dynamics™ StreamLine Pro Automatic Calibrator flow controller. The flow controller operates under atmospheric background with air as the working fluid. The input pressure can be set between 7 bar g to 9 bar abs [122]. A range of velocities from 0 to 60 m/s, created by a nozzle with a diameter of 12.4 mm, are used in this research. The spark gap is placed approximately 20 mm away from the nozzle outlet. The direct image of the plasma channel is captured by the Phantom V7.3 high-speed camera. The spark discharge current and voltage are also measured during the experiments.

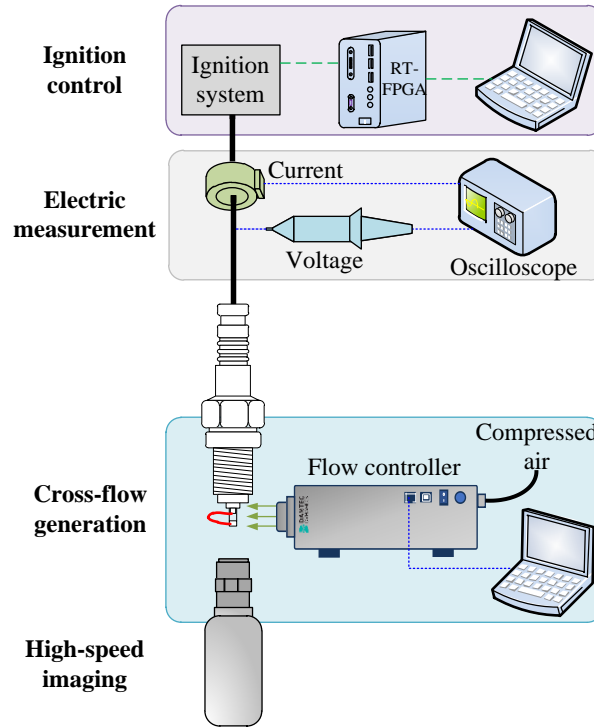


Figure 3-8 Experimental setup of the flow test bench

3.3 Hardware setup of ignition systems

Five types of ignition systems have been developed in-house and applied in this research, including a conventional inductive coil ignition system, a multi-coil ignition system, a boosted current ignition system, a high-power ignition system, and a transient high-current ignition system. All the ignition systems are based on a conventional inductive coil ignition system, albeit with hardware modifications to change the spark discharge parameters. The capabilities and operational range of the different ignition systems are summarized in Table 3-5.

Table 3-5 Characteristics of the spark ignition systems

	Spark discharge duration	Peak spark discharge current	Peak power
Conventional inductive coil (base system for all other ignition systems)	0.1–5 ms	Breakdown phase: ~10 A Arc and glow phases: 10–150 mA	~10 kW
Multi-coil	on demand	Breakdown phase: ~10 A Arc and glow phases: 10–200 mA	~10 kW
High-power	< 1 μ s during the high-power spark discharge	Breakdown phase: ~100 A Arc and glow phases: 10–150 mA	0.1–2 MW
Transient high-current	5–40 μ s during the transient high-current spark discharge	Breakdown phase: ~10 A Arc and glow phases: 100–1500 A	~10 kW
Boosted-current	on demand	Breakdown phase: ~10 A Arc and glow phases: 200–4000 mA	~10 kW

Note: The values are based on 1 mm spark gap size and atmospheric pressure.

The electric circuit of a conventional inductive coil ignition system is shown in Figure 3-9. The charging process initiates when the IGBT in the primary circuit is switched ON. The primary current gradually increases in the charging process. The electric energy of charging is transformed to the magnetic field of the coil in this process. Then the IGBT is switched OFF at the end of the commanded charging duration (usually less than 5 ms). The primary current drops drastically to a value close to 0 amps due to the open circuit. The abrupt change in the primary current results in a transient inductive voltage of several hundred volts from the transformation of the magnetic field.

Corresponding to the voltage increase in the primary coil, the secondary coil voltage increases rapidly in receiving the energy of the magnetic field. In accordance, the structural parasitic capacitance in parallel to the spark gap is charged. This process is normally termed the pre-breakdown phase. In the meantime, the spark gap voltage increases until the gaseous media in between the gap is electrified to become conductive (breakdown phase). The secondary circuit is closed by the ionized channel. Upon the breakdown event, the

energy stored in the structural parasitic capacitance quickly released to the spark gap, resulting in a current surge. The energy stored in the magnetic field is gradually released to the spark gap in a few milliseconds. The spark discharge current gradually decreases during the inductive discharge process. Concurrently, the spark discharge voltage drops rapidly until resumes to about a few hundred volts.

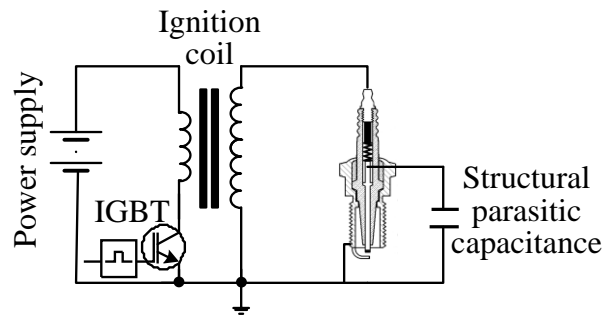


Figure 3-9 Conventional inductive coil ignition system

The breakdown event in all the systems is relying on the high voltage generated from the ignition coil. Once the breakdown is initiated, the advanced ignition systems function by changing the original spark discharge process through external hardware and control. A flow chart in Figure 3-10 demonstrates the spark process based on an inductive coil ignition system, with the high-power, boosted-current, and transient high-current spark strategies marked in the diagram as well.

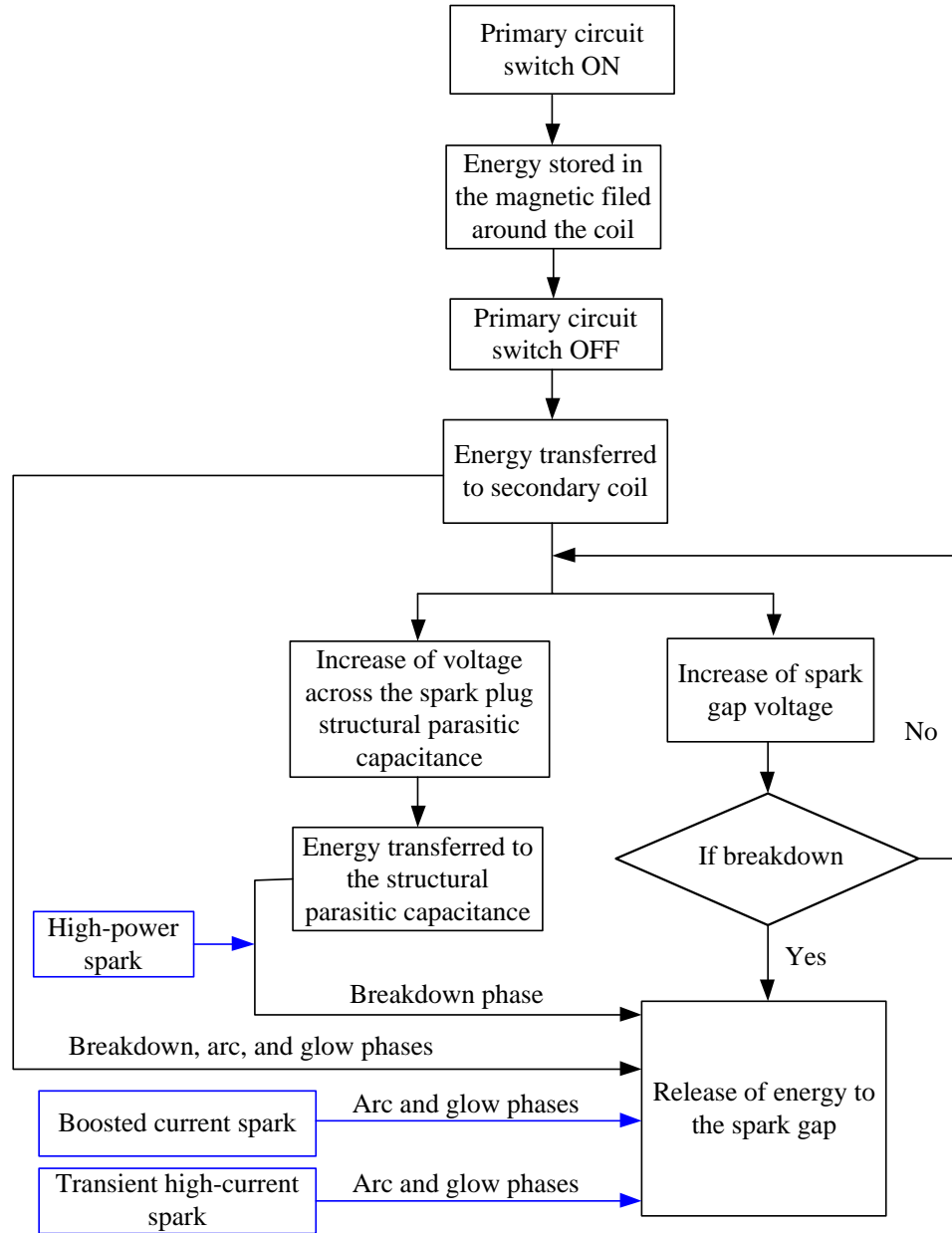


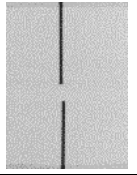


Figure 3-10 Flow chart of the spark process based on an inductive coil ignition system

Various spark plugs are also used in this study, as shown in Table 3-6. The spark plug is selected to meet the specific requirement of the test scenarios. For instance, the high-power and transient high-current ignition strategies demand non-resistive spark plugs for fast

spark discharge. The same spark plug has been used for the same set of experiments to minimize the impact of electrode shape on the ignition process.

Table 3-6 Parameters of the spark plugs

	Spark plug A	Spark plug C	Spark plug D
Photos			
Central electrode diameter (mm)	2.5	0.6	0.08
Resistance (kΩ)	0	4.5	0
Thread diameter and pitch sizes	M14 × 1.25	M14 × 1.25	M14 × 1.25

3.3.1 Multi-coil ignition system

The electric circuit of the multi-coil ignition system represented by a dual-coil configuration is shown in Figure 3-11. Two identical ignition coils are connected in parallel to the same spark plug. Two high-voltage diodes (D_1 and D_2) are connected in the circuit to avoid interference between the two coils during the charging and discharging processes.

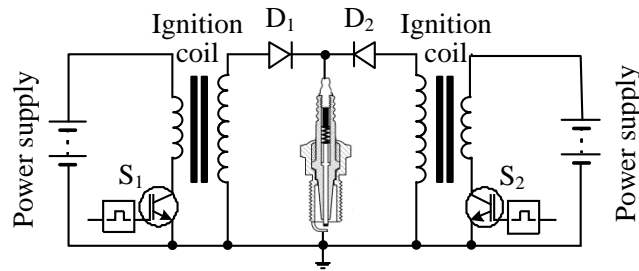


Figure 3-11 Multi-coil ignition system (represented by a dual-coil configuration)

The multiple coils can operate in different patterns to generate different spark discharge current profiles. When the multiple ignition coils are operating simultaneously, a higher spark discharge current can readily be obtained, as shown in Figure 3-12. When the multiple ignition coils operate in a time offset pattern, a continuous spark discharge event

with extended discharge duration can be realized, as shown in Figure 3-13. To generate a continuous spark discharge current profile, the time sequence should be properly arranged so that one coil discharges while the other coil is charging. The coil operating frequency can be modified by adjusting the offset duration of each coil. The first charging process is generally longer to ensure that enough energy is stored in the coil for the breakdown event.

The spark discharge current level of the multi-coil ignition system can be increased by enhanced primary voltage or prolonged charging duration to the primary coil. Still, the achievable current level is generally less than 200 mA with the hardware used in this study. To achieve a higher spark discharge current level, the boosted-current ignition system is deployed.

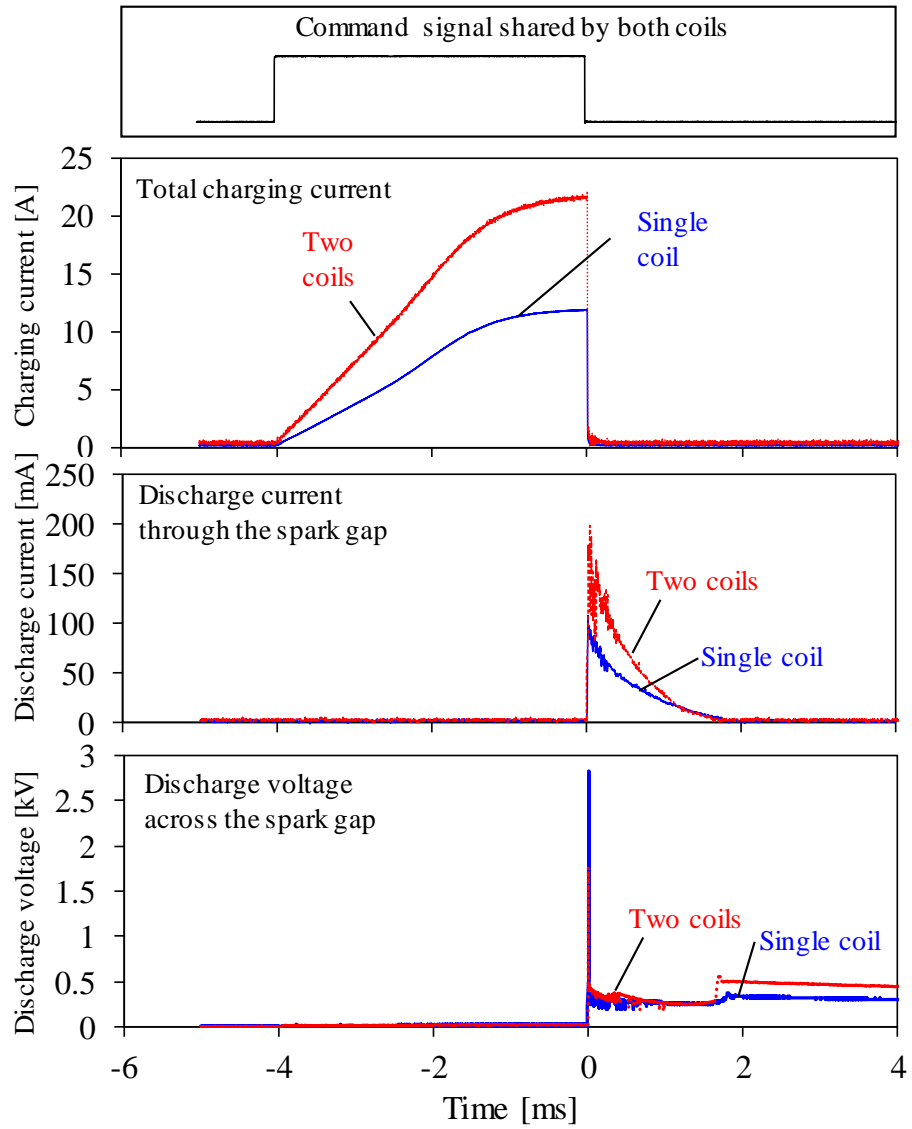


Figure 3-12 Multi-coil simultaneous spark discharge

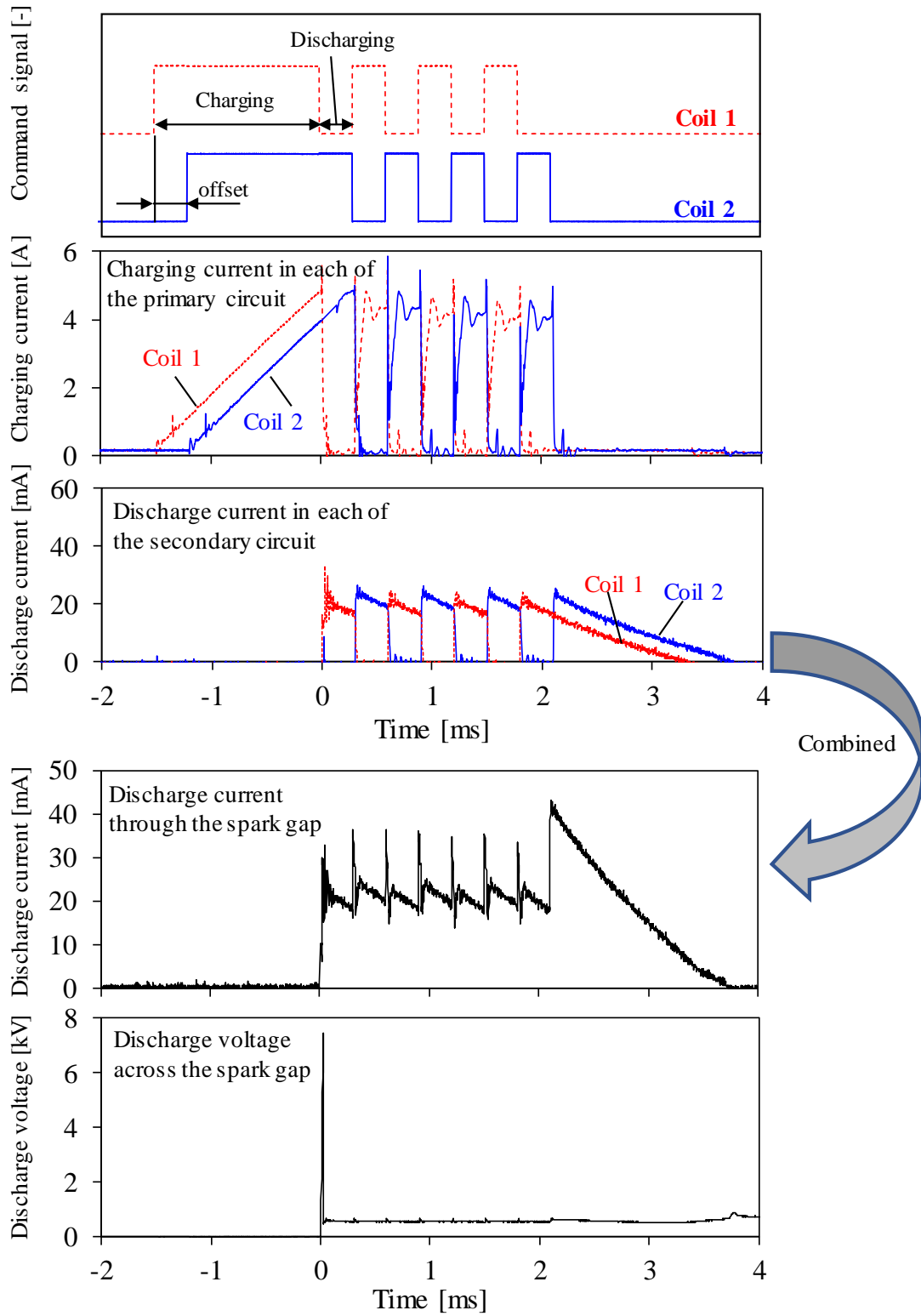


Figure 3-13 Multi-coil offset spark discharge

3.3.2 High-power ignition system

The electric circuit of a high-power ignition system is shown in Figure 3-14. The working principle of the high-power ignition system is demonstrated in Figure 3-15. A high-voltage capacitor of up to several hundred pF is added in parallel to the structural parasitic capacitor of the spark plug.

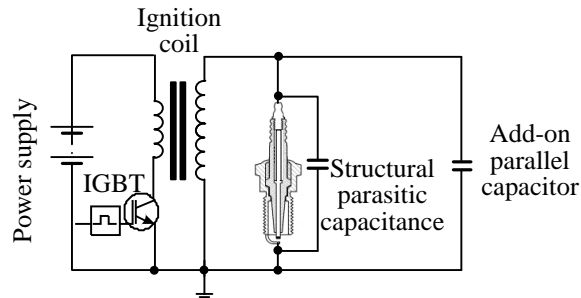


Figure 3-14 High-power ignition system

Under the same spark command, the breakdown event is delayed when the add-on capacitor is applied. A longer charging time is required by the coil to charge up the capacitor to the voltage threshold for the breakdown event, as shown in Figure 3-16. The added parallel capacitor does not affect the amplitude of the breakdown voltage. The breakdown voltage still depends on conditions at the spark gap, such as the properties of the gas media and the gap size.

More energy is stored due to the increased parallel capacitance so that the spark discharge current during the breakdown phase increases, as shown in Figure 3-17. The increased spark discharge current is jointly provided by the coil and the capacitors during the breakdown event. Consequently, the peak power of the breakdown phase can be greatly enhanced. This process can also be considered as a method to redistribute the spark discharge energy along the timeline, wherein more energy is placed to the breakdown phase and less energy is reserved for the later arc and glow phases. A shorter spark discharge duration during the arc and glow phases is therefore observed because of the lower energy for the arc and glow phases, as shown in Figure 3-18.

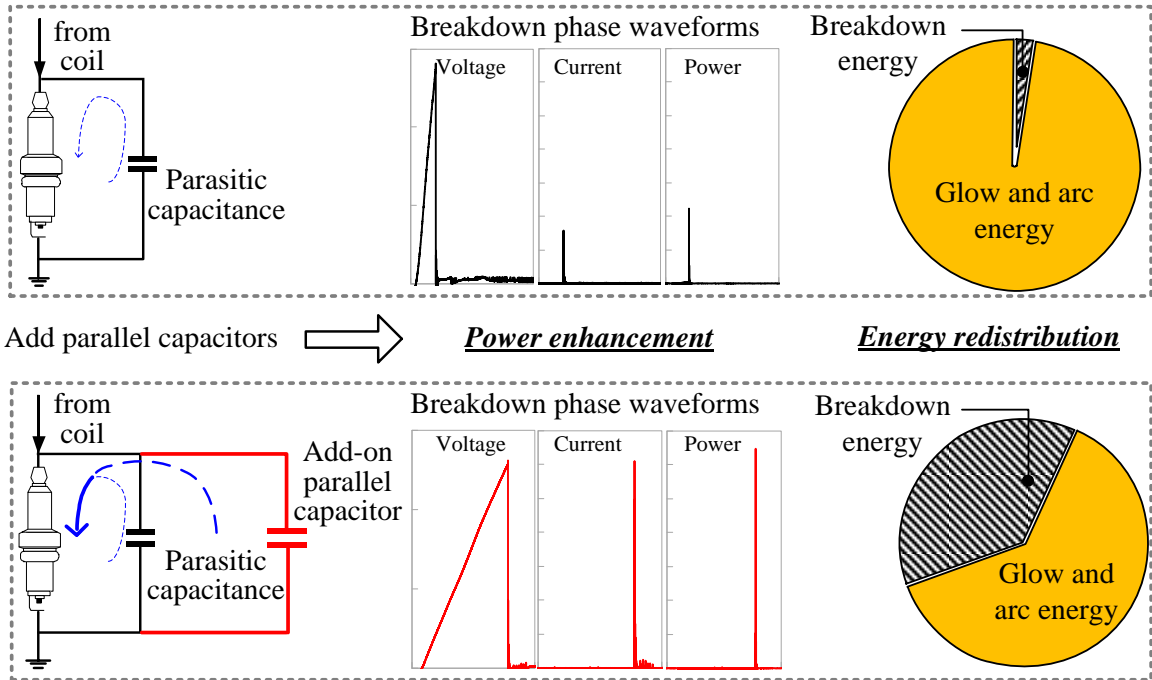


Figure 3-15 Working principle of the high-power ignition strategy

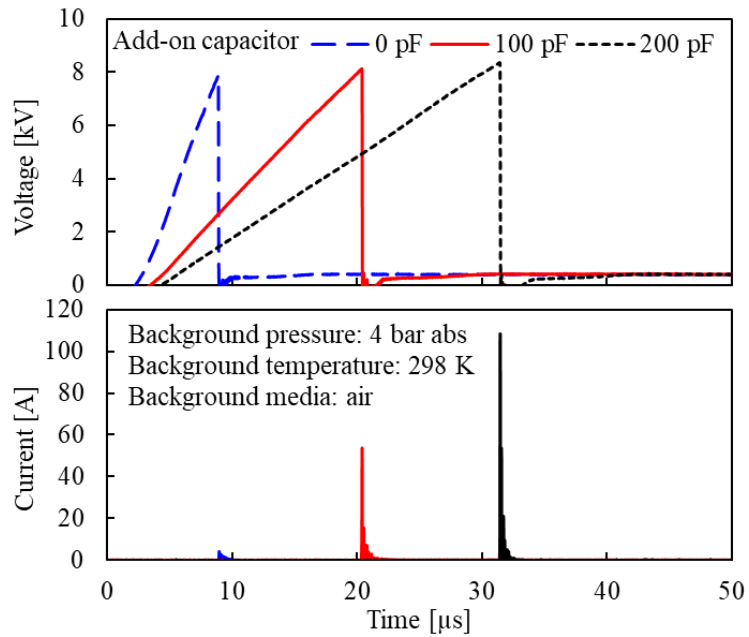


Figure 3-16 Voltage and current waveforms with increased levels of add-on parallel capacitors

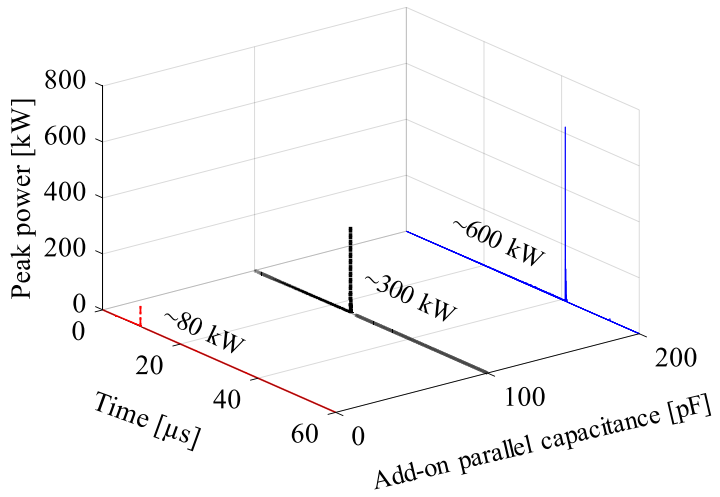
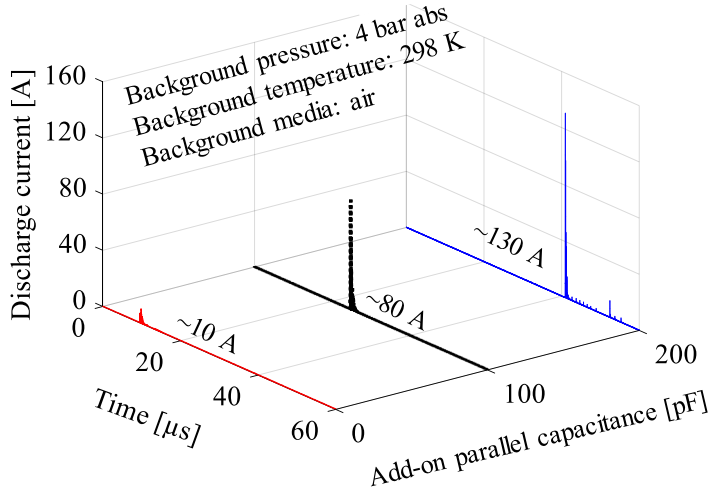
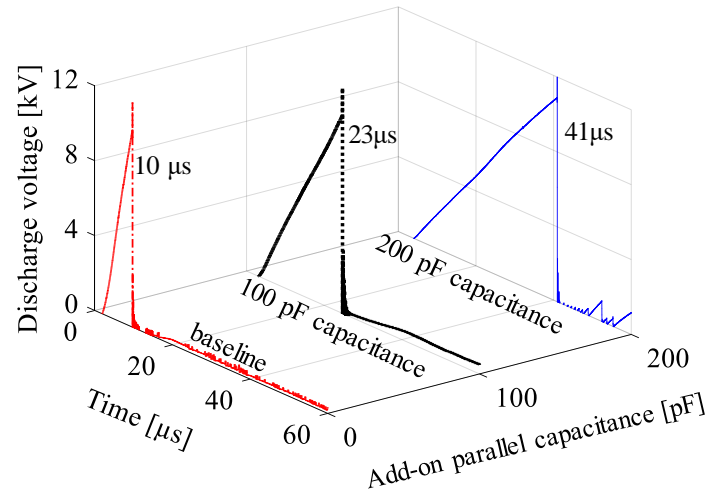


Figure 3-17 Spark discharge current, voltage, and power during the breakdown phase with different levels of add-on parallel capacitors

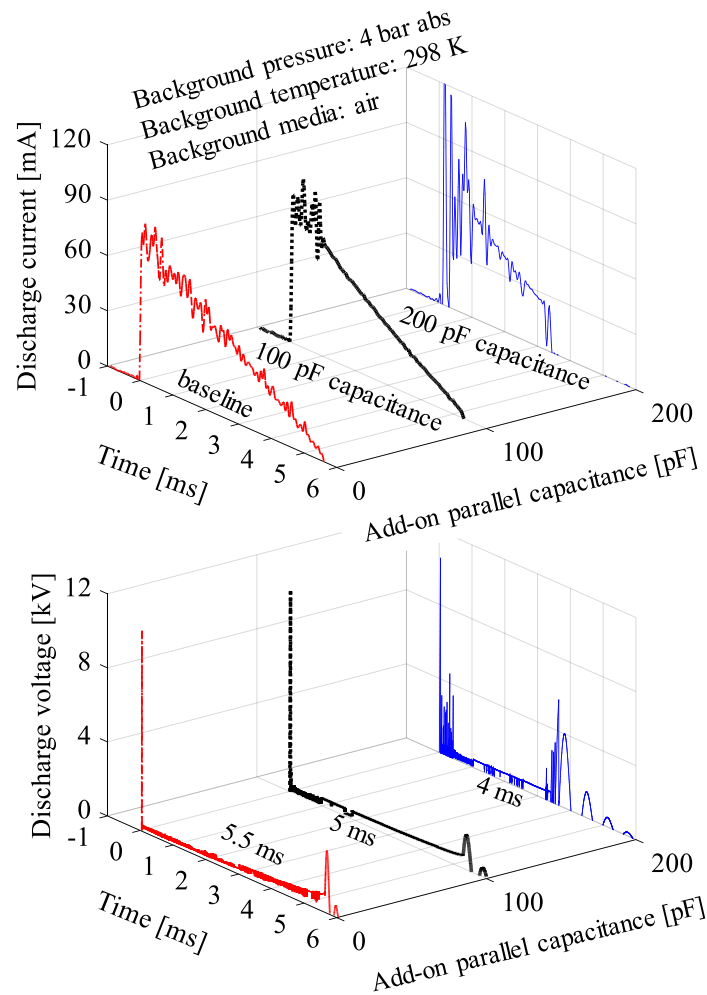


Figure 3-18 Spark discharge current and voltage during the arc and glow phases with different levels of add-on parallel capacitors

3.3.3 Boosted-current ignition system

The boosted-current ignition strategy can be realized through an electric circuit demonstrated in Figure 3-19. The boosted-current ignition system consists of a conventional inductive ignition coil, coupled with a boosted-current module. The inductive coil generates the breakdown event. The boosted current module reserves energy to be released for current boosting, jointly with the continued energy release from the inductive coil during the arc and glow phases.

The boosted-current module is composed of an isolated DC power supply, a high-voltage stabilizing capacitor, and a high-voltage switch (S_2). The voltage of the isolated DC power supply is set between 400V to 2000 V. Two sets of high-voltage diodes (D_1 and D_2) are used to avoid interference between the ignition coil and the boosted-current module during the charging and discharging processes.

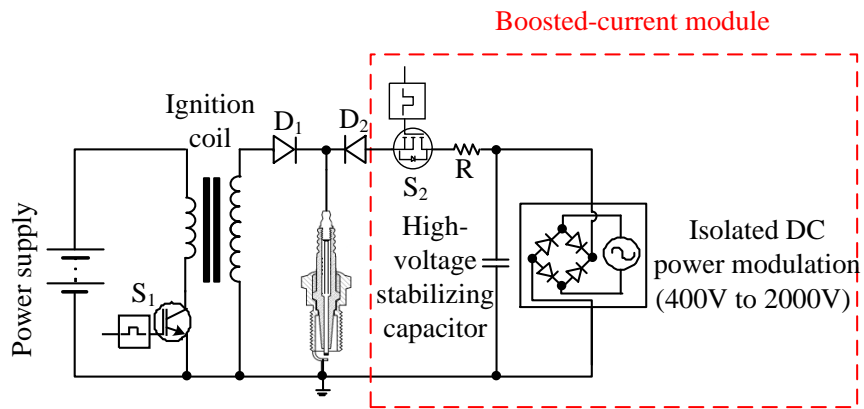


Figure 3-19 Boosted current ignition system

The working principle of the boosted-current ignition system is illustrated in Figure 3-20. Two command signals are required. The signal sent to switch S_1 controls the spark discharge process from the ignition coil. The command sent to switch S_2 controls the spark discharge process from the boosted-current module. Once the plasma channel is established, the boosted-current module starts to release energy to the spark gap. During the discharge process of the boost-current spark, the voltage of the boosted-current module needs to be higher than the spark gap voltage (~ 400 V under quiescent condition), otherwise, the current from the boosted-current module cannot flow to the spark gap.

Both the timing and duration of the boosted-current spark discharge can be controlled by the command signal sent to S_2 . The amplitude of the spark discharge current can be adjusted by the supply voltage level of the boosted-current module and the inline resistance. The modulation of the spark discharge current level, discharge duration, and discharge timing of the boosted-current spark discharge is demonstrated in Figure 3-21.

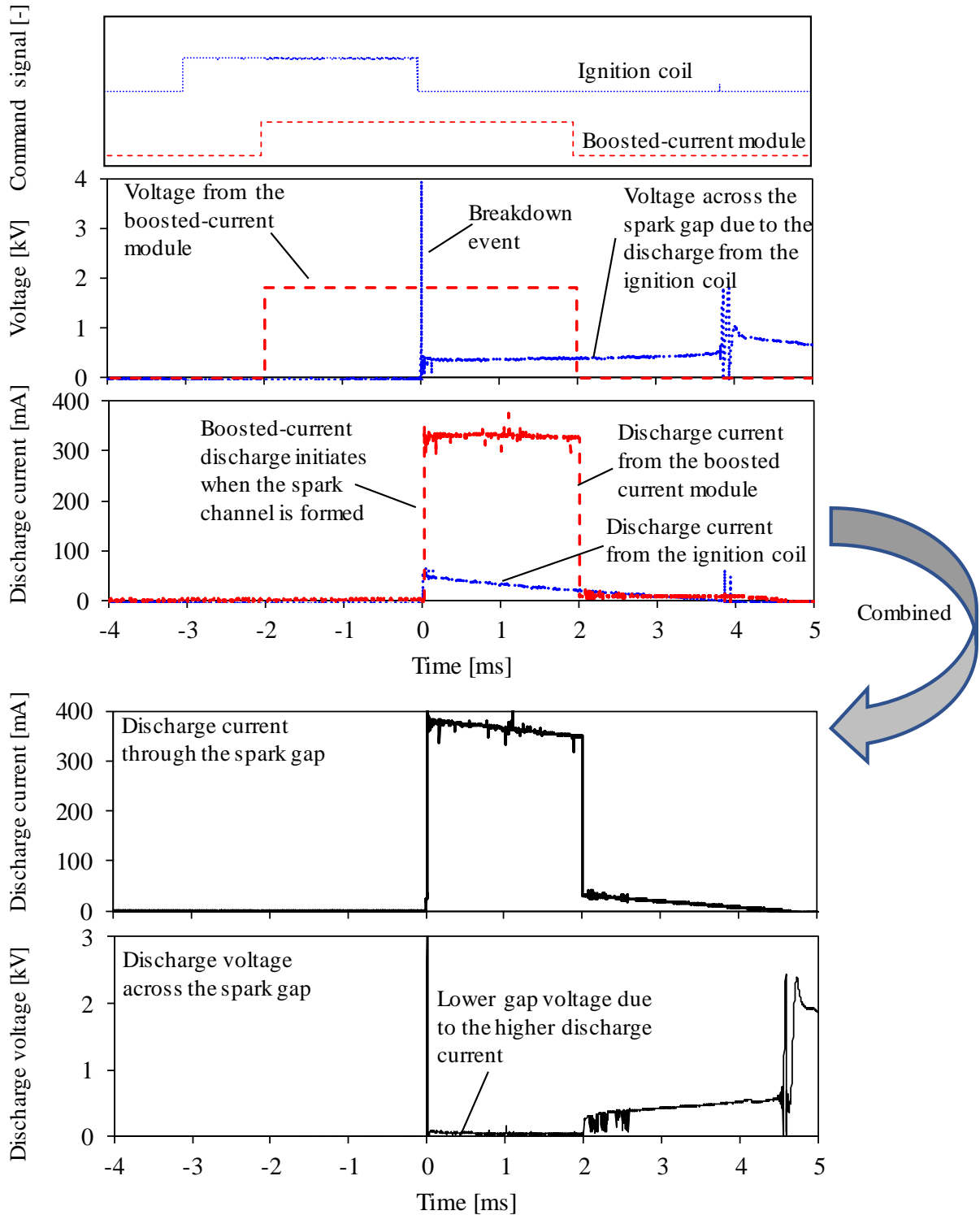


Figure 3-20 Working principle of the boosted-current ignition system

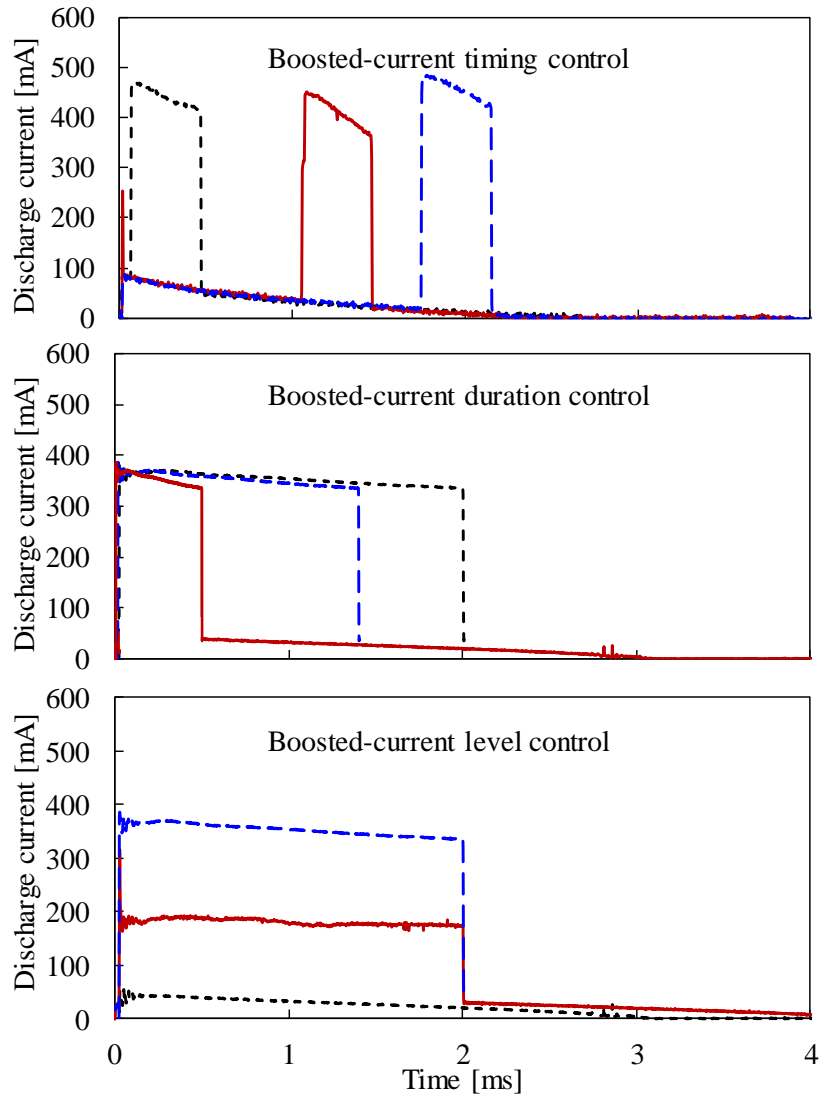


Figure 3-21 Modulation of the spark discharge current by the boosted-current strategy

3.3.4 Transient high-current ignition system

The electric circuit demonstrated in Figure 3-22 is used to generate a transient high-current spark. Two major systems are connected, an inductive ignition coil system and a transient high-current module. An energy storage capacitor is pre-charged by an external power supply to store a large amount of electric energy. To achieve appreciable thermal impact, the energy stored in the high voltage capacitor is usually much higher than the energy stored

in the ignition coil. The energy storage capacitor used in this study has a capacitance that varies from 1.5 μF up to 4.5 μF .

A sketch diagram in Figure 3-23 demonstrates the transient high-current spark discharge process. The spark discharge process relies on the ignition coil to initiate the breakdown event. Once a plasma channel is formed, the energy storage capacitor starts to release energy to the spark gap. The spark discharge process of the transient high-current is finished within tens of microseconds. The ignition coil releases energy concurrently in this process and continues for a couple of milliseconds. The energy of the transient high-current spark includes both the energy stored in the energy storage capacitor and the energy stored in the ignition coil.

Significant differences are observed in the magnitude and duration of the spark discharge current from the energy storage capacitor and the inductive ignition coil. In a later discussion, only the spark discharge current and voltage waveforms during the transient high-current spark discharge are shown to magnify the details of the magnitude and duration of the transient high-current spark discharge.

The magnitude of the transient high-current can be controlled by either adjusting the DC power supply voltage or by changing the capacitance of the energy storage capacitor, as shown in Figure 3-24 and Figure 3-25, respectively. It is noted that although both methods result in higher spark discharge current and energy levels, they have different impacts on the spark discharge duration. The elevated DC power voltage does not change the spark discharge duration significantly, as illustrated in Figure 3-24. The duration for the high-current spark discharge period is extended from 8 μs to 12 μs when the capacitance increases from 1.5 μF to 4.5 μF , as shown in Figure 3-25.

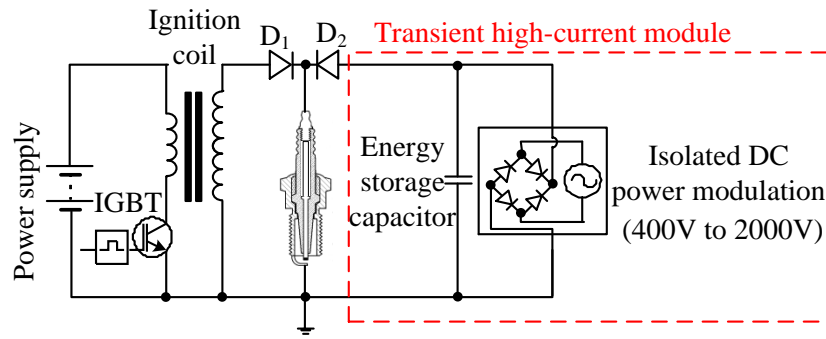
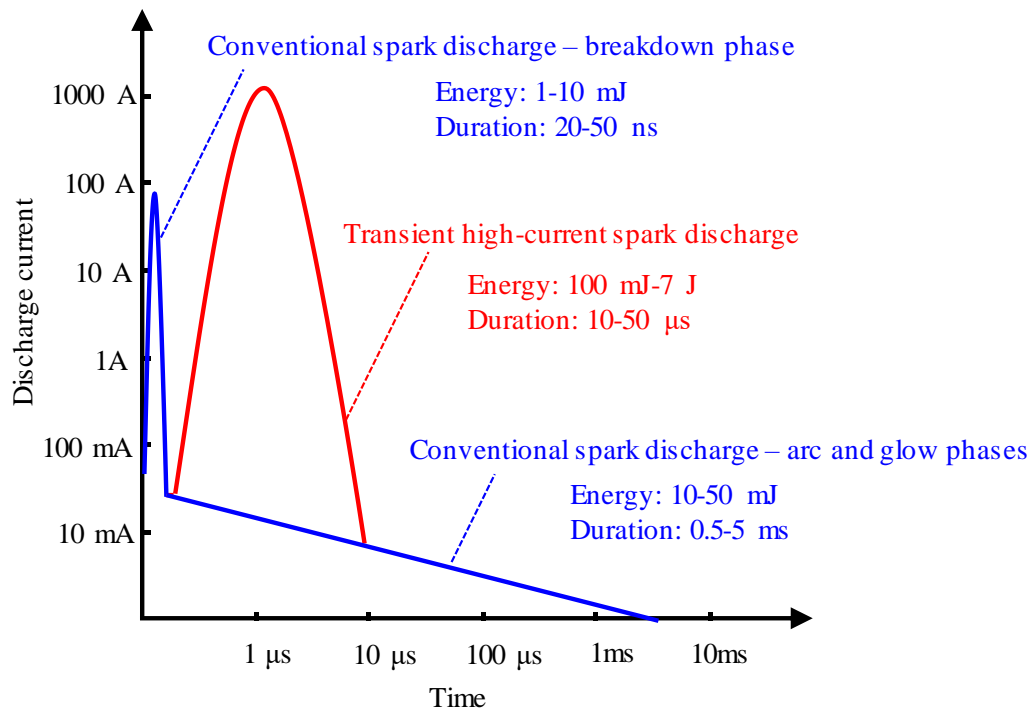


Figure 3-22 Transient high-current ignition system



Note: The values are based on the tested conditions in this study.

Figure 3-23 Illustration of the transient high-current spark discharge process

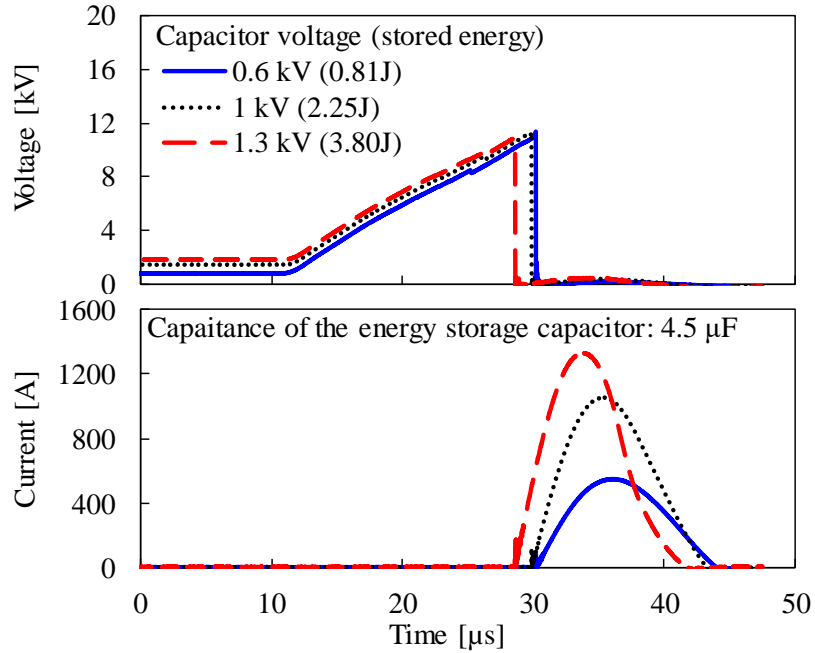


Figure 3-24 Current and voltage waveforms of transient high-current spark (different voltage)

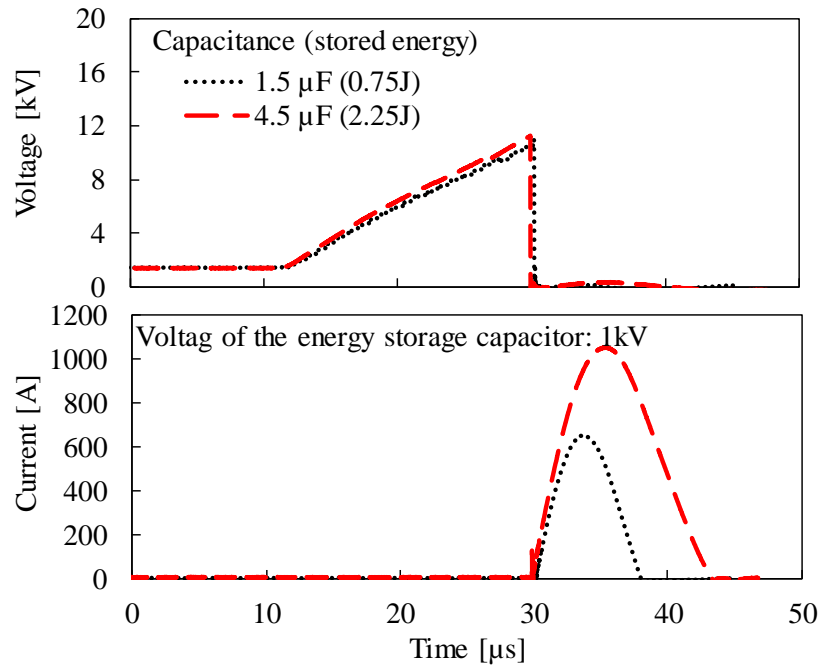


Figure 3-25 Current and voltage waveforms of transient high-current spark (different capacitance)

3.4 Data analysis methods

3.4.1 Ignition energy calculation

The spark discharge from a conventional inductive coil ignition system is composed of two components, capacitive discharge and resistive discharge [123]. Due to the short duration of the breakdown process, the discharge energy during the breakdown phase is mainly contributed by the capacitive discharge [124]. The energy can be estimated from the following equation [123]:

$$E_{breakdown} = \frac{1}{2} C_{parasitic} V_{breakdown}^2 \quad 3-1$$

Where $E_{breakdown}$ is the spark discharge energy during the breakdown phase, $C_{parasitic}$ is the structural parasitic capacitance of the spark plug, and $V_{breakdown}$ is the breakdown voltage. The values of the parasitic capacitance are measured with a Keysight Technologies E4990A impedance analyzer.

The energy released during the arc and glow phases is calculated as [123]:

$$E_{arc/glow} = \int_0^{t_{discharge}} V(t)I(t)dt \quad 3-2$$

Where $E_{arc/glow}$ is the spark discharge energy during the arc and glow phases, V is the voltage across the spark gap during the arc and glow phases at instantaneous time t , I is the spark discharge current during the arc and glow phases at instantaneous time t , and $t_{discharge}$ is the spark discharge duration. The total spark discharge energy from an ignition coil is the sum of the two parts [123]:

$$E_{total} = E_{breakdown} + E_{arc/glow} \quad 3-3$$

The energy reported in this study is the energy delivered to the spark gap. When a resistive spark plug is used, the spark gap voltage is acquired by subtracting the voltage reduction due to the spark plug's internal resistance from the voltage measured at the spark plug terminal nut. The spark discharge energy from the boosted current ignition strategy is also calculated from the above equations.

For the high-power spark, the capacitance that is in parallel to the spark plug is increased due to the add-on parallel capacitor. The energy from the resistive discharge during the breakdown phase is comparably low due to the short discharge duration. As such, the breakdown energy is calculated using 3-4.

$$E_{breakdown} = \frac{1}{2}(C_{parasitic} + C_{add-on})V_{breakdown}^2 \quad 3-4$$

Where $E_{breakdown}$ is the spark discharge energy during the breakdown phase, $C_{parasitic}$ is the parasitic capacitance from the spark plug, C_{add-on} is the add-on parallel capacitance, and $V_{breakdown}$ is the breakdown voltage.

For the transient high-current spark, the energy is composed of the energy delivered from the energy storage capacitor, as well as the energy delivered by the ignition coil. The two parts of the spark discharge energy are calculated separately. 3-1 to 3-3 are used to calculate the energy delivered from the ignition coil. While the energy delivered from the energy storage capacitor is calculated via 3-5.

$$E_{high-current} = \frac{1}{2}C_{storage}V_{DC}^2 \quad 3-5$$

Where $E_{high-current}$ is the energy delivered from the transient high-current module, $C_{storage}$ is the capacitance of the energy storage capacitor, and V_{DC} is the voltage of the transient high-current module. The assumption is that the energy stored in the energy storage capacitor is fully discharged during the transient high-current spark process.

3.4.2 Pressure data analysis

The pressure data is used to analyze the impact of different ignition strategies on the combustion process. The percentage of fuel consumption is approximated from the pressure curve on an effort to quantify the combustion process. The estimation method is based on the first law of thermodynamics under isochoric conditions, as shown in 3-6, with the assumption that the mixture in the chamber is an ideal gas and the heat transfer loss is negligible for simplicity in the estimation.

$$\text{mass fraction burnt (MFB)} = \frac{m(t)}{m_{total}} = \frac{p(t) - p_{initial}}{p_{max} - p_{initial}} \quad 3-6$$

Where $m(t)$ is the mass of the burnt fuel at instantaneous time t , m_{total} is the total mass of the burnt fuel, $p(t)$ is the pressure at instantaneous time t , $p_{initial}$ is the initial pressure before combustion, and p_{max} is the maximum pressure inside the chamber during the combustion process.

In this way, the time for reaching 5%, 50%, and 90% of the maximum pressure can be used to represent the time for consuming 5%, 50%, and 90% of the total fuel mass. The $t_{5-90\%MFB}$ is considered as the burning duration of the combustion. The pressure trace in Figure 3-26 is an example to demonstrate $t_{5\%MFB}$, $t_{50\%MFB}$, and $t_{5-90\%MFB}$.

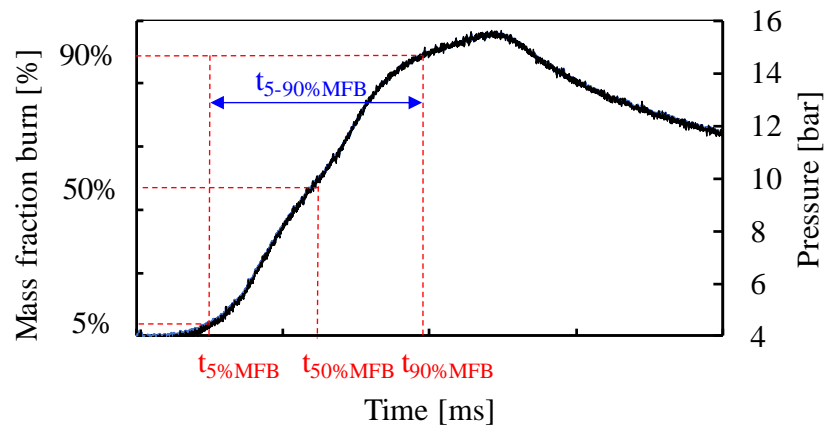


Figure 3-26 Demonstration of the pressure trace

3.4.3 Imaging processing

The spark plasma and the combustion process both release heat and hence result in density changes of the background media. These changes can be perceived from the shadowgraph or schlieren images [126]. The projected area can be calculated from the shadowgraph images, as shown in Figure 3-27. The grayscale images are first converted to binary images. Then, the area is calculated by counting the pixels.

The spark plasma is self-luminous. The stretch process of the plasma is captured by a direct imaging system. Then, the grayscale images are converted to binary images, as shown in Figure 3-28. The thickness of the plasma channel changes with the spark discharge current magnitude. Thus, the plasma image is thinned to get more accurate results of the length when different current levels are used. The plasma length is calculated by counting the pixels of the boundary of the thinned plasma profile.

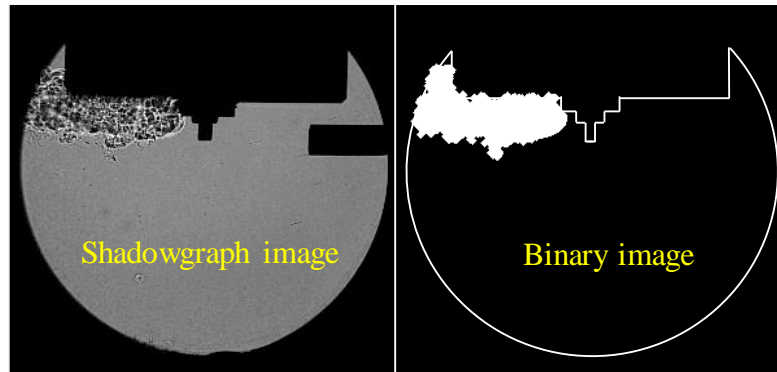


Figure 3-27 Image processing method for flame area calculation

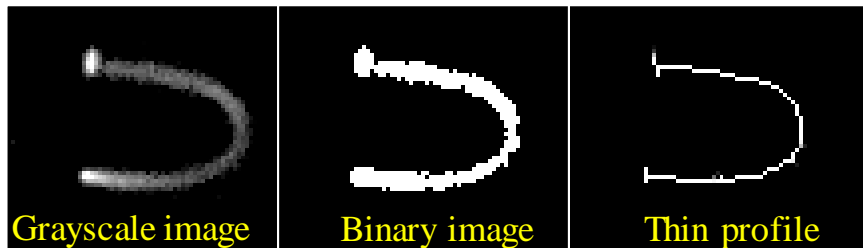


Figure 3-28 Image processing method for plasma length calculation

3.5 Experimental conditions

The experimental conditions in this study are stipulated with reference to the in-cylinder conditions during the spark event. The in-cylinder pressure at the spark timing in a typical production engine is shown in Figure 3-29. The in-cylinder pressure at the spark timing increases with the engine load level under fixed engine speed. On the other hand, the spark timing needs to be advanced with a leaner mixture owing to the prolonged combustion duration [127]. Consequently, the in-cylinder pressure at the spark timing often decreases with an increased excess air ratio under equivalent engine load.

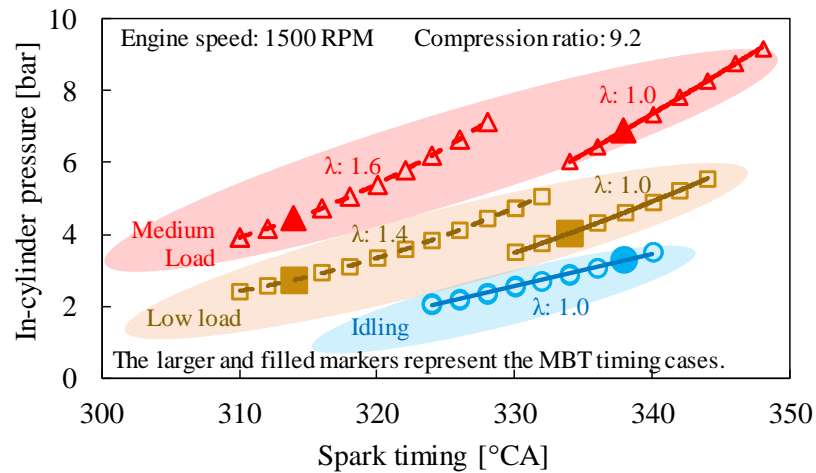


Figure 3-29 In-cylinder pressure at the spark timing in a production engine (Adapted from Yu *et al.*[127])

The suitable levels of lean-burn and dilution may be effective in engine efficiency improvement under partial load operating conditions, which also encounters more challenges during the ignition process. Therefore, by referencing these operating conditions, a background pressure of 2 bar abs and 4 bar abs are used for the combustion experiments in this research with an excess air ratio of about 1.6 in most of the experiments. Gaseous fuel methane (CH_4) is used in the experiments.

The flow velocity during the combustion tests varies between 0 m/s up to 35 m/s. This velocity range is decided by referencing multiple research results on the in-cylinder flow

measurements [107,128]. Additionally, the flame propagation speed under different engine speed is estimated by assuming a bore diameter of 80 mm and a combustion duration of 40°CA, as shown in Table 3-7. From this estimation, the flame propagation speed can be higher than 30 m/s under an engine speed of over 5000 RPM. The study on the spark discharge characteristics under gas flow conditions is thus carried out with a wider range of flow velocities varying from 0 to 60 m/s, considering the possible velocity range for engine running at higher engine speeds.

Table 3-7 Estimation of flame propagation speed at different engine speed

Engine speed (rpm)	Time per 1° CA (ms)	Combustion duration @ 40°CA (ms)	Flame propagation speed (m/s)
600	0.28	11.1	3.6
1500	0.11	4.44	9
5000	0.03	1.33	30
10000	0.011	0.44	60
Bore diameter: 80 mm			

The experimental conditions are summarized in Table 3-8

Table 3-8 Summary of experimental conditions

Background media	Ignition strategy	Background pressure (bar abs)	Gas flow velocity (m/s)	Section number	Remarks
CH ₄ -air	Conventional	2	0	4.1	Impact of spark energy and arc and glow phases current profiles
CH ₄ -air	High-power	2	0	4.2	Impact of breakdown power
CH ₄ -air	Transient high-current	2	0	4.3	Impact of peak current and spark energy
air	Conventional	1	0, 20	5.1	Characteristics of spark in gas flow field
air	Conventional	1	0-60	5.2	Impact of gas flow velocity on spark
N ₂	Conventional	6, 11, 15	40	5.3	Impact of background pressure on spark
air	Conventional	1	0-60	5.4	Impact of spark gap size on spark
air	Conventional	1	0-60	5.5	Performance of spark with different discharge current level
air	Boosted-current, High-power, Transient high-current, Dual-coil offset	1	0-60	5.5	Impact of gas flow on spark discharge strategies
CH ₄ -air	Conventional	4	0, 5, 15, 25 ,35	6.1	Impact of gas motion on spark ignition
CH ₄ -air	High-power	4	0, 5, 10, 25	6.2	Impact of breakdown power on spark ignition
CH ₄ -air	Transient high-current, conventional	4	5, 15, 25 ,35	6.3	Impact of transient high-current on spark ignition
CH ₄ -air	Boosted-current, Dual-coil, conventional	4	5, 15, 25 ,35	6.4	Impact of discharge current profiles on spark ignition

CHAPTER 4 FLAME KERNEL INITIATION WITH DIFFERENT IGNITION STRATEGIES UNDER QUIESCENT CONDITIONS

The ignition and flame kernel formation under quiescent conditions are discussed as a baseline for the evaluation of different ignition strategies. Started with the conventional spark discharge, the impact of spark discharge current level, duration, and profile during the arc and glow phases on the ignition is analyzed. Then the performance of the spark discharge with enhanced breakdown power is investigated. The last section reports the results with the transient high-current spark.

4.1 Effects of spark discharge current profiles on the ignition process

4.1.1 Spark generated by a conventional inductive coil system

The spark discharge energy from a conventional inductive coil ignition system can be adjusted by varying the charging duration of the primary coil when the same hardware configuration is applied. The waveforms in Figure 4-1 demonstrate the change in the spark discharge current and voltage profiles when different charging durations are commanded to the same ignition coil. Enhanced spark discharge energy, elevated peak spark discharge current, and prolonged spark discharge duration can be achieved by a longer charging duration, provided that the coil is not saturated. The corresponding ignition performance can be seen from the shadowgraph images from selected combustion tests, as shown in Figure 4-2. The images are recorded within 1.6 ms after the breakdown event. A misfired case is observed when the spark discharge energy is lowered to 1.4 mJ. The mixture is successfully ignited when the spark discharge energy is increased to 9 mJ. No significant improvements are observed in flame propagation when the spark discharge energy is further increased from 9 mJ to 45 mJ.

The flame kernel is initiated at the spark gap as can be seen from the shadowgraph images. The flame kernel grows, as the flame front propagates outwards. The region near the spark gap changes from an unburnt zone to a burnt zone with the flame propagation. With a longer

spark discharge duration, though the spark discharge process continues, the energy is discharged in the already burnt zone as the flame front propagates out of the spark gap vicinity. Therefore, under such quiescent conditions, the extra energy supplied through a longer spark discharge duration has minimal impact on flame propagation.

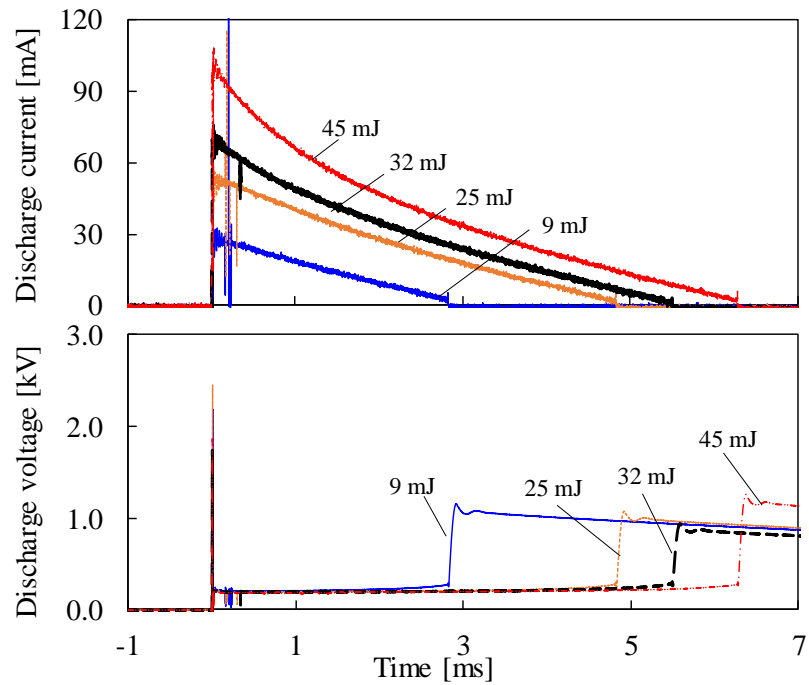


Figure 4-1 Spark discharge current and voltage waveforms with low to conventional discharge energy

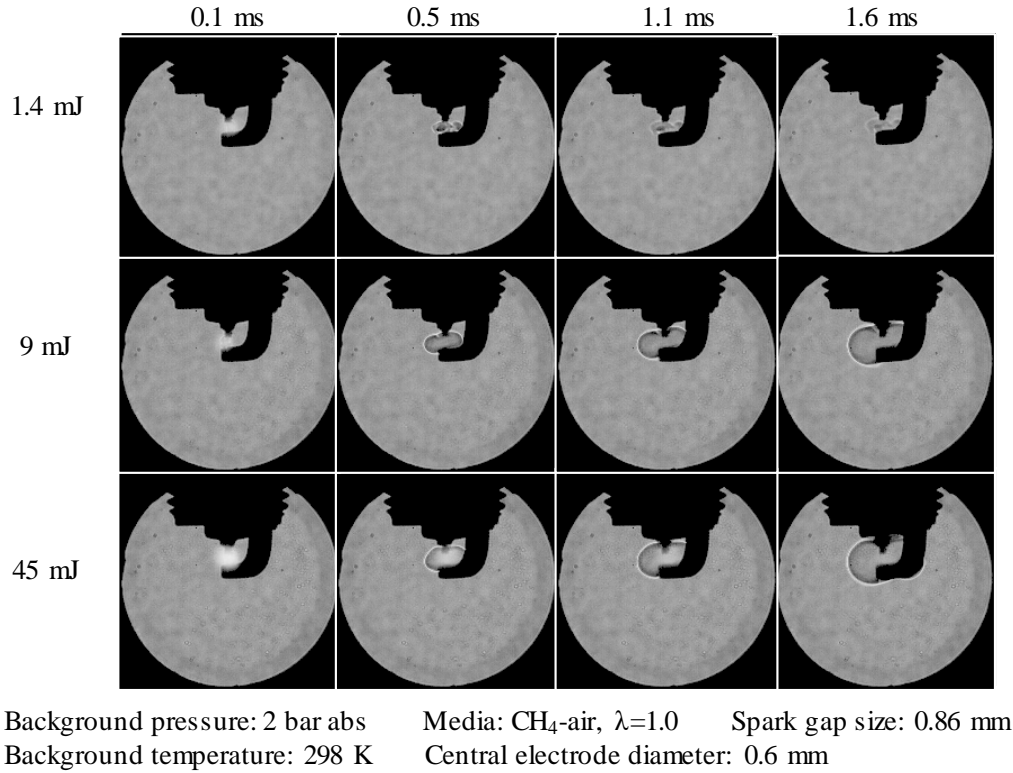


Figure 4-2 Effect of spark discharge energy on flame kernel formation under quiescent conditions

The impact of the low to conventional spark discharge energy levels on the combustion at different excess air ratios can be seen in Figure 4-3. The results are the averaged value from 10 repeated tests under each condition. The standard deviations of the test results are shown as error bars in the figure. With the stoichiometric mixture, neither the early flame propagation ($t_{5\%MFB}$) nor the combustion duration ($t_{5-90\%MFB}$) is significantly affected by the spark discharge energy, which is consistent with the observations from the shadowgraph images in Figure 4-2. A similar trend can be observed when the mixture strength is reduced to $\lambda=1.4$. The 9 mJ spark discharge energy is adequate to ignite the mixture under these conditions. Hence, further increases in spark discharge energy do not show noteworthy benefit to combustion. When the excess air ratio is further increased to $\lambda=1.8$, the $t_{5-90\%MFB}$ shortens slightly with increases in spark energy, albeit the $t_{5\%MFB}$ does not have a consistent

trend with further increase in the spark energy. The response to the changes in spark energy increase is less than 15% in $t_{5\%MFB}$ and less than 8% in $t_{5-90\%MFB}$ under such experiments.

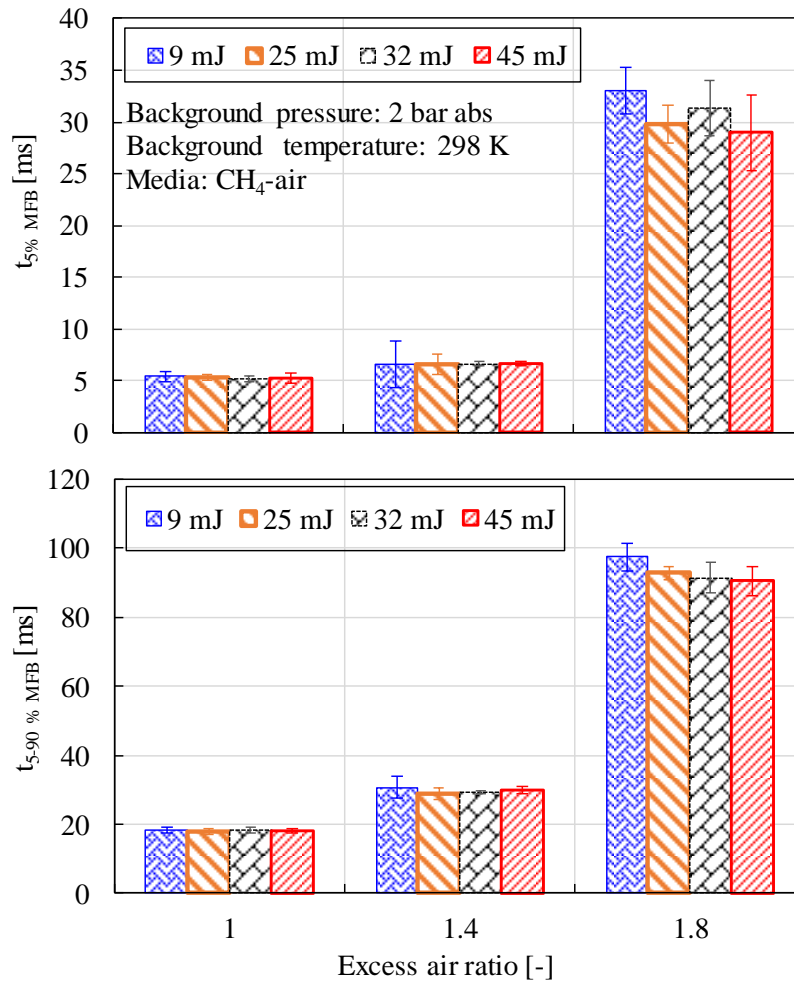


Figure 4-3 Effects of different spark discharge energy on combustion

4.1.2 Spark generated by a multi-coil simultaneous discharge

In the previous comparison, both the spark discharge current profiles and the spark discharge energy during the arc and glow phases are changed due to the different charging duration to the primary coil. The following experiments are carried out to investigate the impact of spark discharge profiles solely on the combustion process. In this comparison, the spark discharge energy is maintained at about 17 mJ while the spark discharge current and voltage waveforms have different peak values and durations, as shown in Figure 4-4.

These spark discharge waveforms are realized by the multi-coil simultaneous ignition strategy. A shorter charging duration of the multiple coil packs can achieve the same energy level as a single-coil pack with a longer charging duration. However, the multiple coil packs have quicker current discharging rates than a single-coil pack.

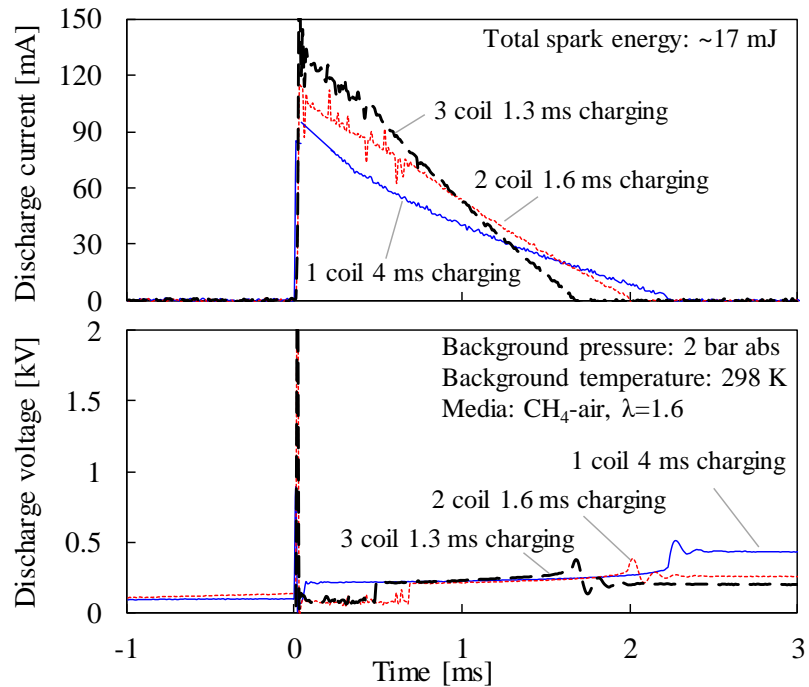


Figure 4-4 Spark discharge current and voltage waveforms from multi-coil simultaneous discharge

The combustion characteristics are analyzed from the pressure data and the results are shown in Figure 4-5. Negligible differences are observed in both the early stage of combustion ($t_{5\%MFB}$) and the combustion duration ($t_{5-90\%MFB}$).

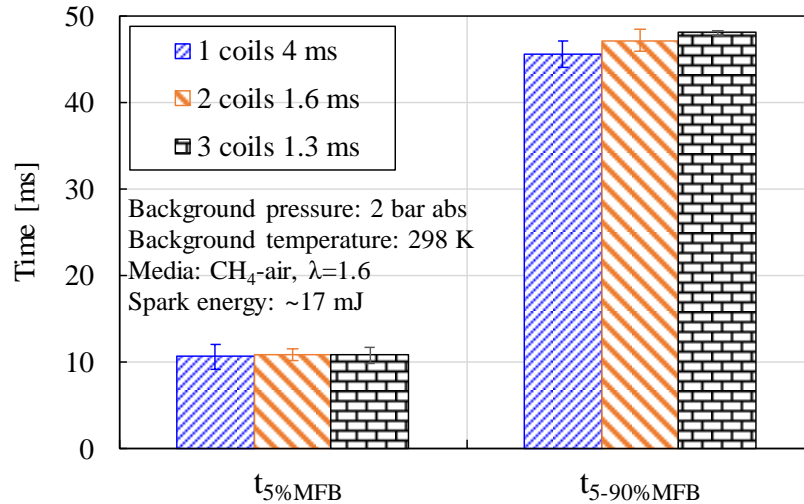
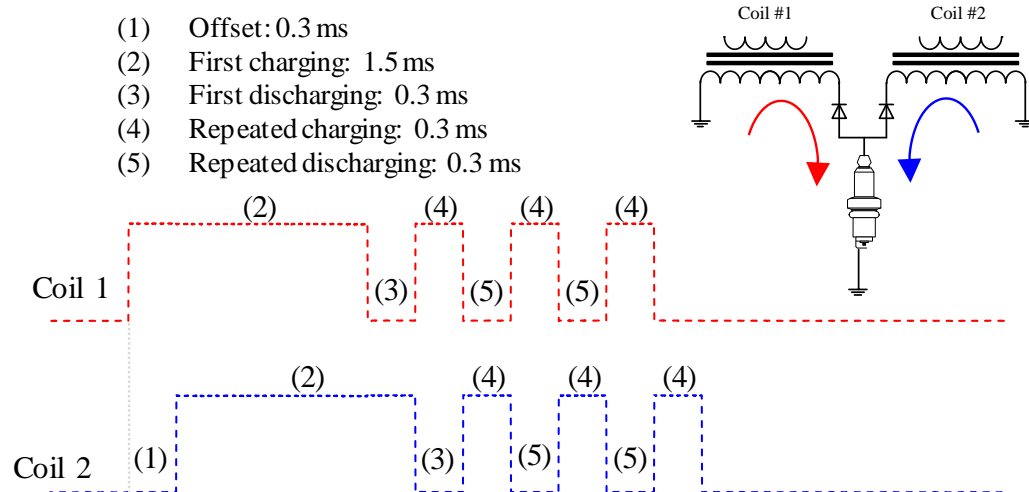


Figure 4-5 Effects of the spark discharge current profiles on combustion with a similar spark discharge energy level

4.1.3 Spark generated by multi-coil offset discharge

One more step is taken to further investigate the impact of the spark discharge current level on combustion. A stable spark discharge current with varying discharge duration during the arc and glow phases is realized by the multi-coil offset ignition strategy. Two coil packs are connected in parallel to the spark plug. To generate continuous discharge current and voltage profiles, the two coils are charging and discharging alternately. The command signals for the two coils are shown in Figure 4-6. The duration of the spark discharge is adjusted by controlling the number of repeated charging and discharging processes in each of the coils. The spark discharge current magnitude is controlled by changing the voltage of the power supply to the coil packs.



- The discharge duration is adjusted by changing the number of repeated pulses from each coil.
- The amplitude of discharge current is adjusted by changing the supply voltage to the primary coils.

Figure 4-6 Command signal for the dual-coil offset spark

The obtained spark discharge current profiles are shown in Figure 4-7. Among the three sets of spark discharge strategies, two of them have similar average spark discharge current levels (20 mA) while different spark discharge durations. The other two have similar spark discharge durations (8 ms) while different spark discharge current levels. The combustion results using the three spark strategies are compared in Figure 4-8. No evident discrepancies are observed among the three spark discharge strategies in $t_{5\%MFB}$, $t_{50\%MFB}$, and $t_{5-90\%MFB}$ under the tested conditions with 2 bar background pressure and methane-air mixture at $\lambda=1.8$.

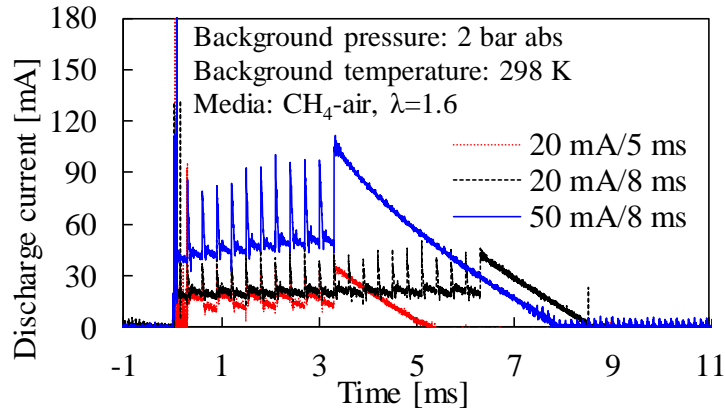


Figure 4-7 Continuous spark discharge current profiles

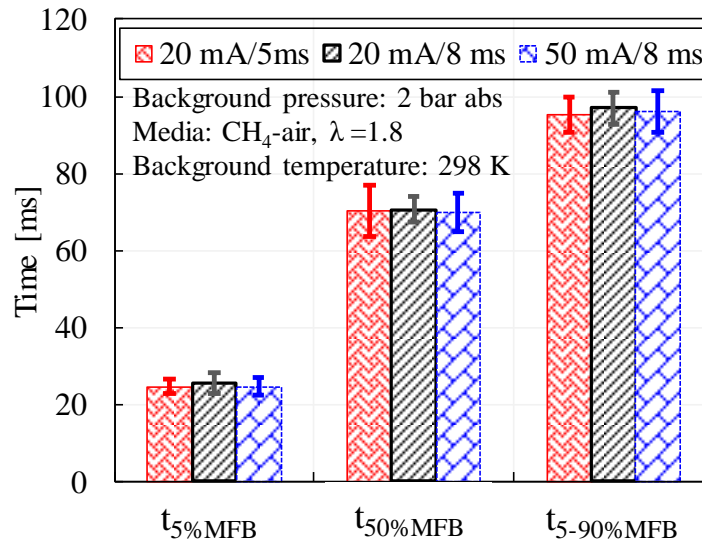


Figure 4-8 Effects of spark discharge current profiles on combustion

In summary of the experimental results, the changes in spark discharge current profile, discharge current level, discharge duration, and discharge energy have an insignificant impact on the combustion process, so long as the ignition energy is sufficient to ignite the mixture. However, it should be noted that the experiments in this section only involve the changes in spark discharge during the arc and glow phases, which is different from the change in spark discharge during the breakdown phase. The enhanced spark discharge power during the breakdown phase will be discussed in the following section.

4.2 Effects of breakdown power on the ignition process

The high-power ignition system shown in Figure 3-14 is applied to generate a spark discharge with enhanced breakdown power. Three capacitance levels (0 pF, 100 pF, and 200 pF) are deployed to enhance the peak spark discharge power. The current and voltage waveforms during the pre-breakdown and breakdown phases can be seen in Figure 4-9.

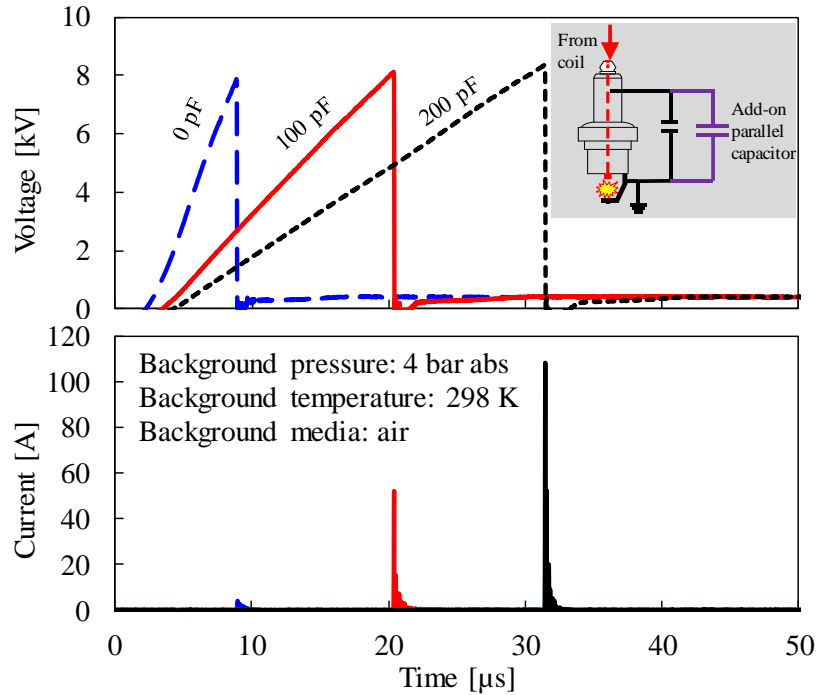


Figure 4-9 Voltage and current waveforms with increased levels of add-on parallel capacitors

It is preferred to report the values of the peak power that can be achieved when different parallel capacitance is added. However, as mentioned in section 3.1, it is difficult to have accurate measurements of the spark discharge current during the breakdown phase that appears to occur in the nanoseconds time scale with the Pearson 411 current probe. For this reason, the values of the energy discharged during the breakdown phase with different parallel capacitance are reported instead. The breakdown energy is estimated using 3-1.

4.2.1 High-power spark with air as background media

The experiments have been carried out with air under different background pressures to demonstrate the impact of pressure on the spark energy distribution to the different discharge phases. The background temperature remained constant at room temperature. The spark discharge current and voltage waveforms during the breakdown phase are shown in Figure 4-10. The spark discharge current values noted in Figure 4-10 are the measurement results from the Pearson 411 current probe. Although the magnitude of the current may not be accurately measured, it is still valuable to show the trend of increased spark discharge current with higher background pressure. The increased background pressure results in a higher density of the gas between the spark gap. Consequently, it takes a longer time to electrify the gas media. The spark discharge voltage keeps increasing by receiving the energy from the magnetic field generated from the current collapse of the primary coil until the breakdown event is initiated. An amount of energy is stored in the parallel capacitor during this process before breakdown. Once a conductive channel is formed, the energy stored in the parallel capacitor is released to the electric circuit that is completed by the spark gap. Higher energy storage in the parallel capacitor results in a higher amount of breakdown energy.

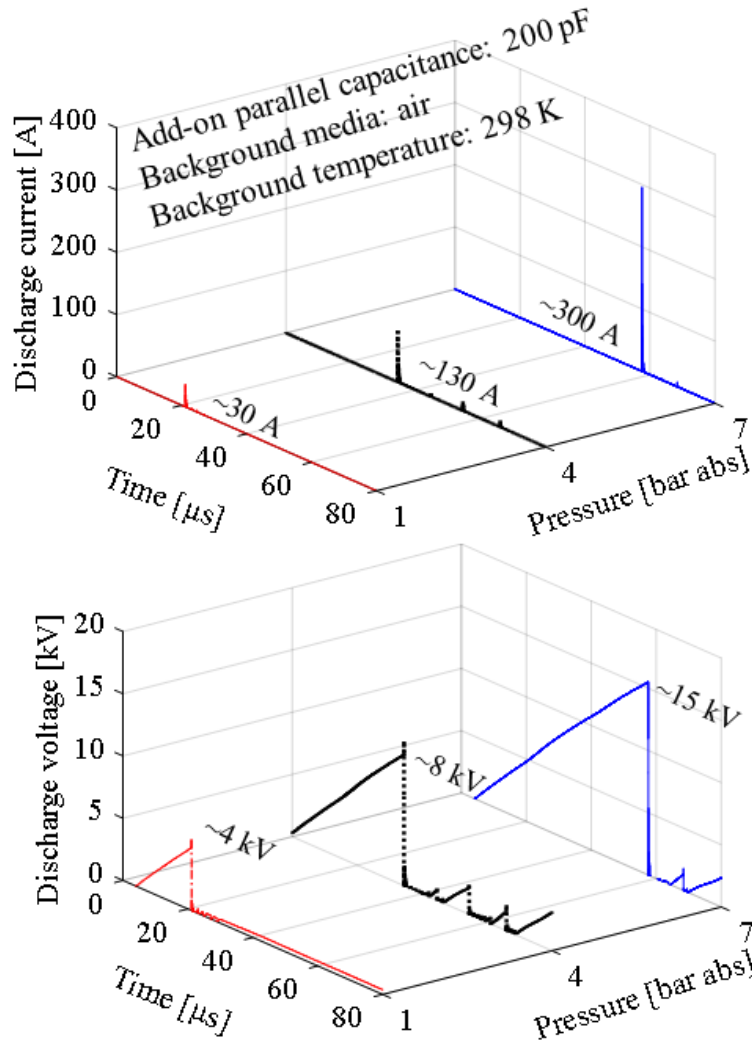


Figure 4-10 Effects of background pressure on the breakdown voltage and current

The spark energy discharged during the breakdown phase increases with the background pressure, due to the higher spark breakdown voltage with the elevated background pressure. The trend is more obvious with higher parallel capacitance, as shown in Figure 4-11. The energy value of 80 mJ as noted in the figure is the total spark discharge energy calculated using 3-3. The spark energy during the breakdown phase accounts for over 90% of the total spark energy when the background pressure increases to 7 bar and the parallel capacitance reaches 500 pF. Further increase in the background pressure or the parallel capacitance results in conditions with no breakdown event because the total spark energy is insufficient to charge the parallel capacitance to the breakdown voltage. The matching between the

spark discharge energy and the add-on parallel capacitance should be taken into consideration to ensure a successful spark discharge when the high-power spark ignition strategy is applied.

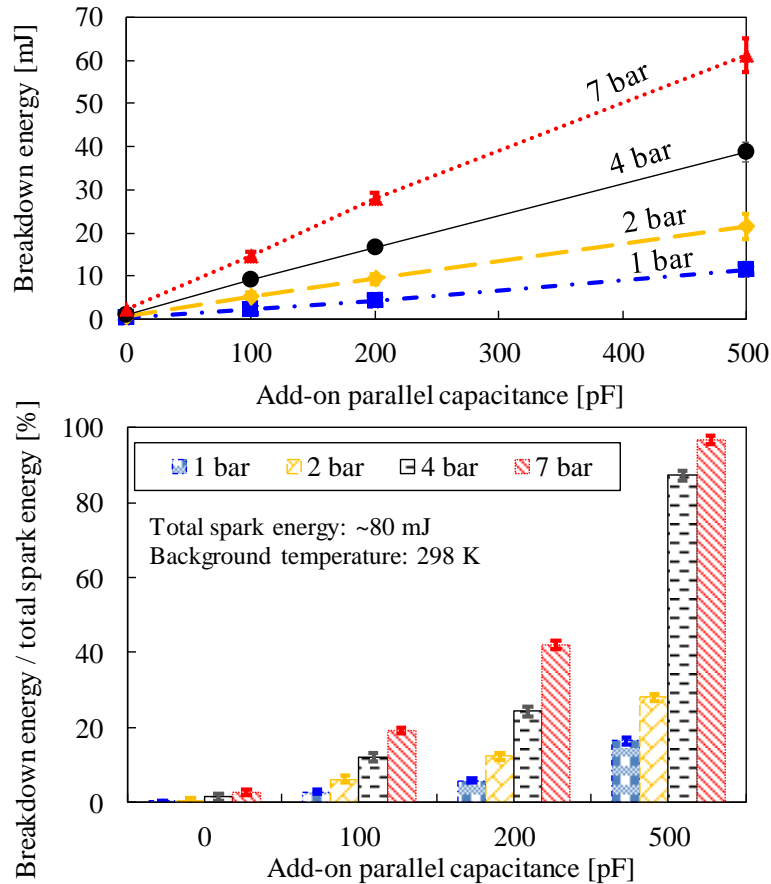


Figure 4-11 Effects of add-on parallel capacitance and background pressure on the breakdown energy

The impact of enhanced breakdown power is demonstrated in Figure 4-12. High-speed shadowgraph images are used to capture the density change induced by the hot spark plasma between a pair of opposite needle electrodes. Air is used as the background media in the experiment. A reference case of the conventional spark without added parallel capacitance is shown in the first row. Some distinct features of the high-power spark discharge can be observed qualitatively from the images.

Wrinkles in the density field near the spark gap are observed right after the breakdown event in all three cases. The wrinkles are caused by the abruptly increased temperature and pressure in the plasma channel during the breakdown phase. A temperature of about 60000 K and a pressure of over 200 bar could be achieved after the breakdown, as suggested by Maly *et al.* [10]. The rapid increase in pressure results in shock waves that generate turbulence. This phenomenon has been reported by previous researchers as “electric puff” [129].

Though turbulent areas are observed in all the cases, the size of the turbulent area is different in the three cases. The turbulent area is larger with higher parallel capacitance. The turbulence is mainly caused by the pressure wave during the breakdown phase. The high-power spark discharge produces a more powerful pressure wave owing to the higher breakdown energy. Therefore, the turbulent area is larger. On the contrary, for the conventional spark, most of the spark discharge energy is released during the arc and glow phases, resulting in thermal expansion from the spark gap without significant turbulence generation. Both the enhanced turbulence and the enlarged high-temperature area from the high-power spark may be beneficial for the flame kernel formation, as both can enlarge the surface area of the flame front.

The lifespan of the high-temperature area is longer than the spark discharge duration from the shadowgraph images. For instance, the electrically prompted turbulence continues for over 2 ms after the breakdown, though the spark discharge process finishes at 0.4 ms in the case of a 200 pF add-on capacitor. Whereas in the conventional spark, the high temperature persists for over 4 ms after the end of the spark discharge. The long-lasting high-temperature area is, however, trivial to the ignition, as the flame front propagates out of the spark gap, leaving the high-temperature gas in the burnt zone. For this reason, to better utilize the energy from the spark plasma, it is better to release the energy earlier to generate a larger initial flame kernel than reserve the energy to a later time when the flame front propagates away from the spark gap. The high-power spark should have better ignition ability from this point of view.

Spark in air (without combustion)

Add-on capacitance	0.1 ms	0.6 ms	1.1 ms	1.6 ms	2.1 ms	6.7 ms	Arc/glow duration
0 pF							2.7 ms
100 pF							2.3 ms
200 pF							0.4 ms
Media: air Spark gap size: 0.86 mm Total spark discharge energy: ~50 mJ				Background pressure: 4 bar abs Central electrode diameter: 0.08 mm Background temperature: 298 K			

Figure 4-12 Shadowgraph images of the thermal-induced density field by high-power spark in air under quiescent conditions

4.2.2 Impact of high-power spark on ignition of lean mixtures

The following combustion test results have verified the anticipated effects of the high-power spark discharge. As shown by the shadowgraph images in Figure 4-13, there are more wrinkles in the flame kernel. The development of the flame is faster with the increase in the parallel capacitance.

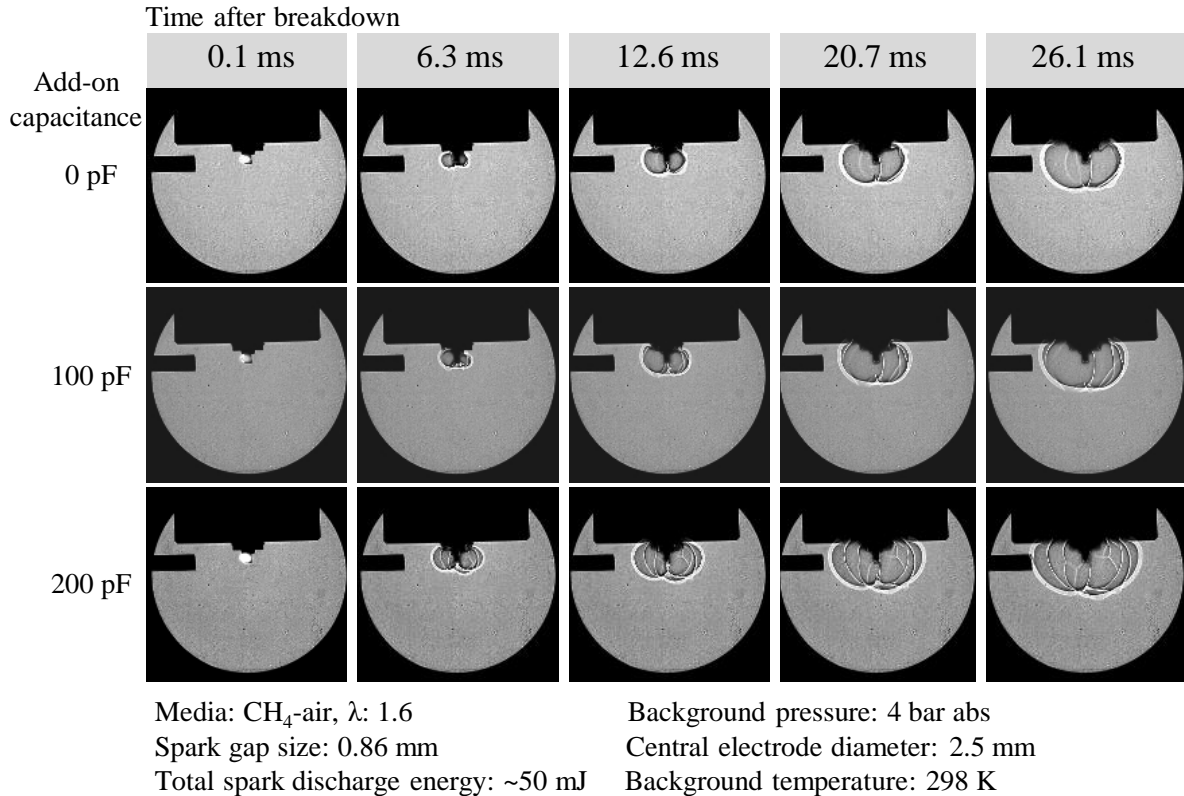


Figure 4-13 Effects of high-power spark on flame kernel growth of lean mixture under quiescent conditions

More tests are carried out to investigate the performance of the high-power spark under quiescent conditions. In the first set of tests, methane-air mixtures with excess air ratios ranging from $\lambda=1$ to $\lambda=1.8$ are used to investigate the effectiveness of the high-power spark with changing mixture reactivities. The results of $t_{5\%MFB}$, $t_{50\%MFB}$, and $t_{5-90\%MFB}$ are summarized in Figure 4-14.

The difference in the performance of the conventional spark and the high-power spark is more obvious when the mixture gets leaner, as shown in Figure 4-14. Negligible differences in the combustion process are observed when using the conventional spark and the high-power spark with the excess air ratio changing from 1 to 1.4. With a leaner mixture ($\lambda=1.6$ and $\lambda=1.8$), it is advantageous to use the high-power spark, especially for the initial stage of the combustion. $t_{5\%MFB}$ decreases by 50% when using the high-power spark with an

excess air ratio of 1.8. $t_{5\%MFB}$ and $t_{5-90\%MFB}$ are also shorter, though the difference is less significant as compared with the reduction in $t_{5\%MFB}$.

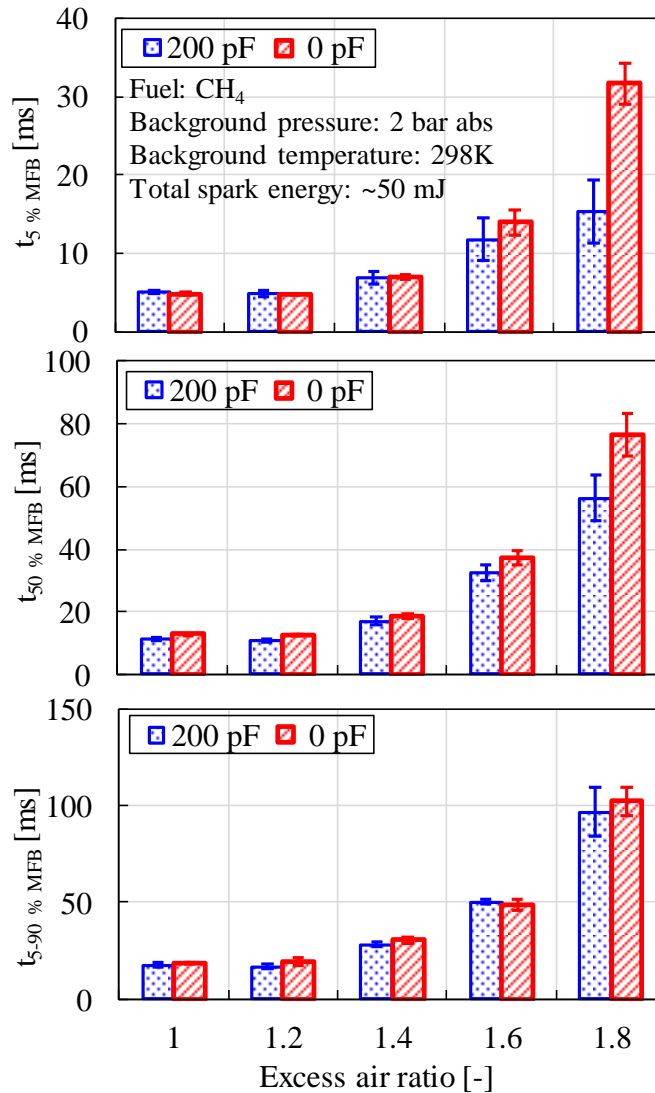


Figure 4-14 Effects of high-power spark on the combustion of lean mixtures under quiescent conditions

4.2.3 Impact of high-power spark on ignition of diluted mixtures

The second set of tests are performed with a CO₂ diluted stoichiometric methane-air mixture. Three different spark discharge energy levels, 10 mJ, 50 mJ, and 100 mJ, are used in these experiments to investigate the impact of the spark discharge energy level on the combustion

with the high-power spark ignition strategy. The results are illustrated in Figure 4-15. There is no significant benefit of using an add-on parallel capacitor when the spark discharge energy is as low as 10 mJ. Even some negative effects are observed when a higher capacitance is used with 10 mJ spark discharge energy. For example, when adding a 200 pF parallel capacitor, misfires are observed as the spark energy is insufficient to generate a breakdown event. However, when the spark discharge energy is higher, there is substantial improvement in the early stage of combustion by using the high-power spark, as can be seen from the smaller value of $t_{5\%MFB}$. The trend is that greater improvement in $t_{5\%MFB}$ can be achieved with higher parallel capacitance. $t_{50\%MFB}$ also gets shorter, yet the improvement is not as significant as in the early stage.

The impact of parallel capacitance and spark discharge energy level on the combustion duration ($t_{5-90\%MFB}$) is not significant in all cases. When the spark discharge energy is further increased to 100 mJ, there is no obvious improvement in the combustion as compared with the cases when 50 mJ spark discharge energy is used. It is thus suggested that a sufficient spark discharge energy level is required for the high-power ignition strategy to be effective. However, once the spark energy exceeds the requirement, further increasing the spark discharge energy has a trivial improvement on the combustion process.

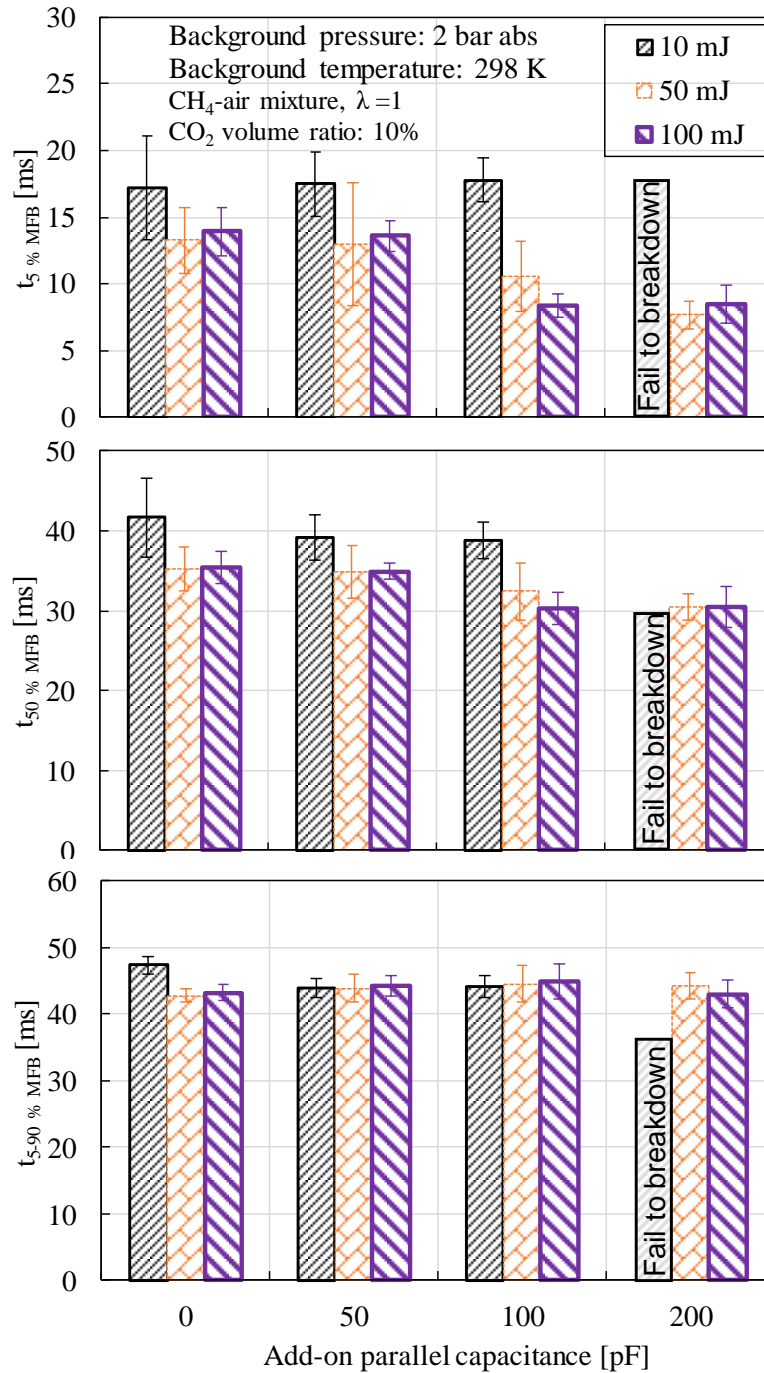


Figure 4-15 Effects of high-power spark on the combustion of CO₂ diluted mixtures under quiescent conditions

4.3 Effects of transient high-current on the ignition process

The performance of the transient high-current ignition strategy is analyzed in this section. The voltage and current waveforms during the transient high-current spark discharge are shown in Figure 4-16. The energy delivered from the energy storage capacitor is marked in the figure. The energy released from the ignition coil in the three cases is about 30 mJ.

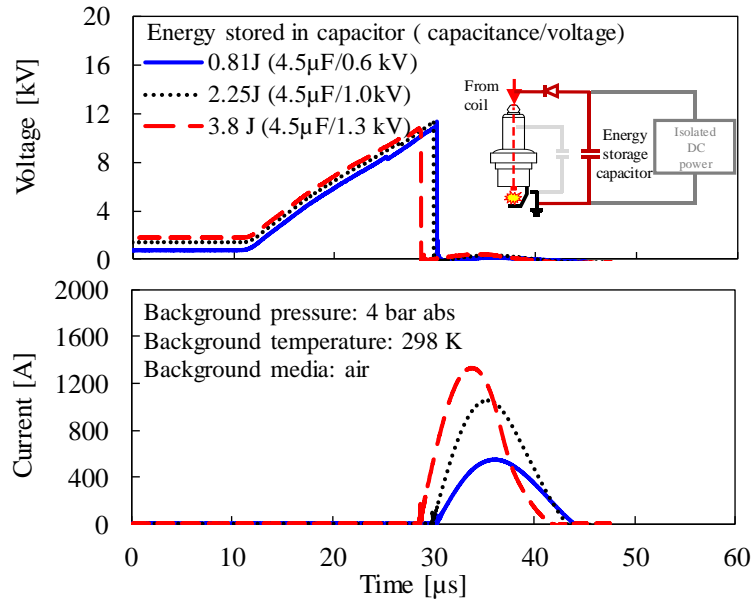


Figure 4-16 Current and voltage waveforms of transient high-current spark

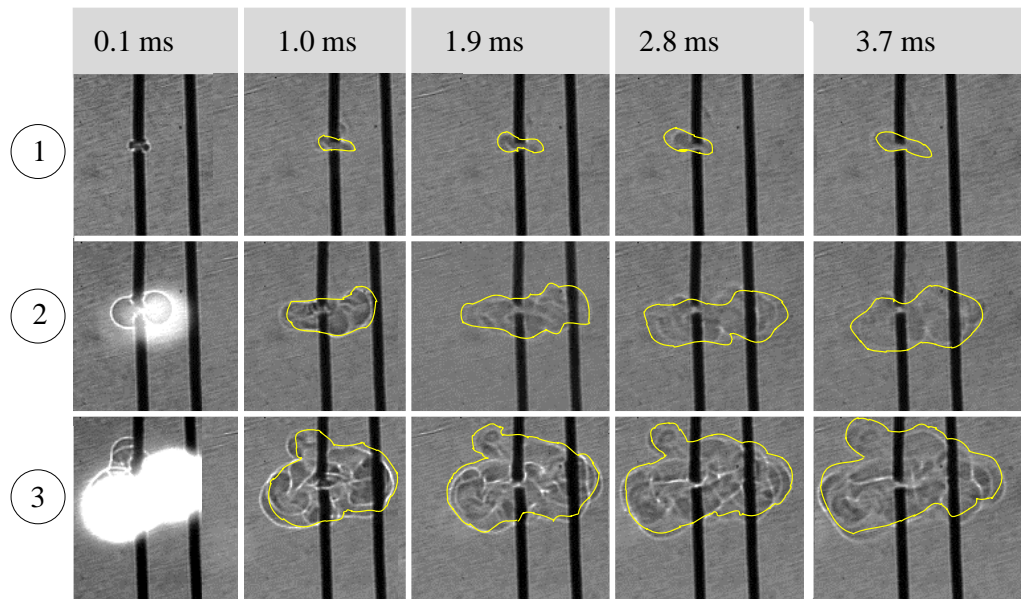
4.3.1 Transient high-current spark with air as background media

The transient high current can result in substantial thermal impact in the spark gap. Shadowgraph images in Figure 4-17 demonstrate the thermal expansion of the hot plasma in air. Comparisons are made between a conventional spark and a transient high-current spark with different spark discharge energy levels. A greater high-temperature area is observed when more energy is stored in the energy storage capacitor through a higher charging voltage.

Spark in air (Without combustion)

Case	Capacitance (μF)	DC supply voltage (kV)	Peak spark current (A)	Spark energy from the transient high-current module (mJ)	Spark energy from the coil (mJ)
1	0	0	0.05	0	30
2	4.5	0.6	550	810	30
3	4.5	1.3	1250	3800	30

Time after breakdown



Media: air Background pressure: 4 bar abs Background temperature: 298 K
 Central electrode diameter: 1.2 mm Spark gap size: 0.86 mm

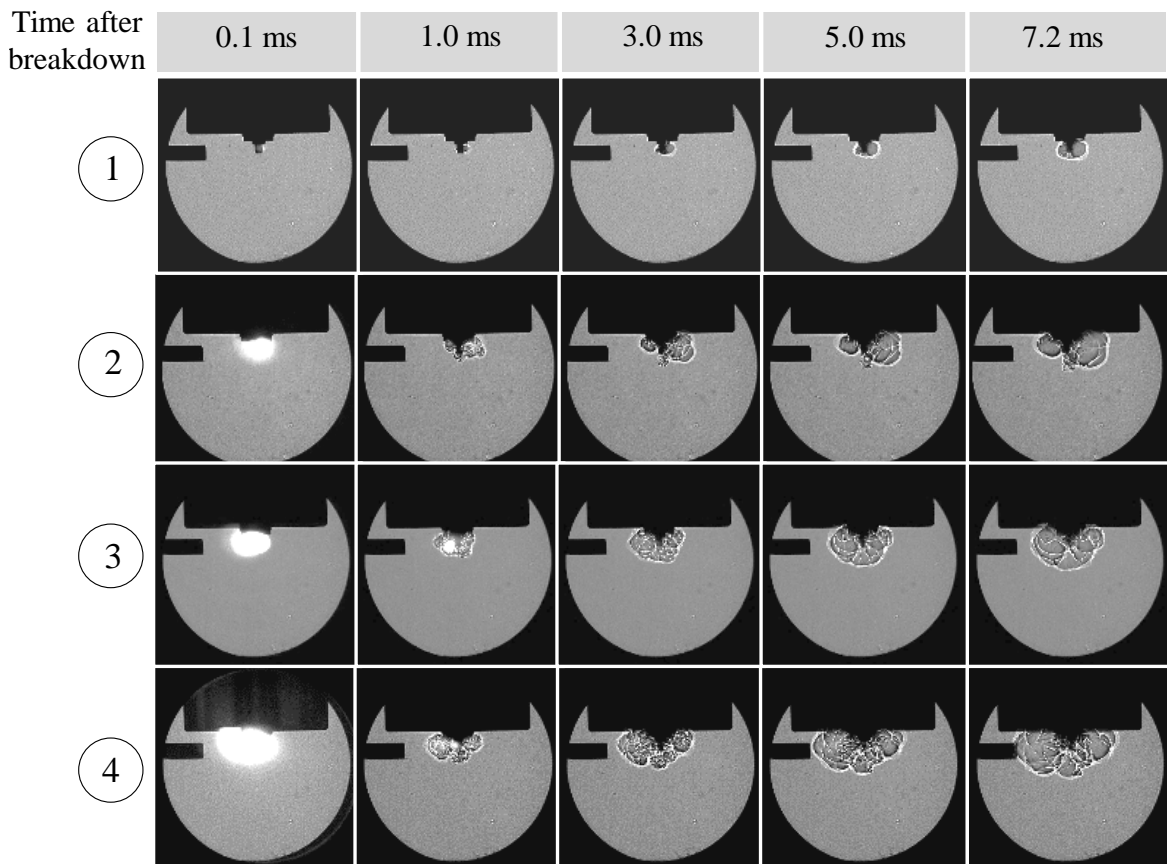
Figure 4-17 Shadowgraph images of the thermal-induced density field by transient high-current spark in air under quiescent conditions

4.3.2 Impact of transient high-current spark on ignition of lean mixture

The enlarged high-temperature area is beneficial for the flame kernel formation, which can be seen from the shadowgraph images of the flame in Figure 4-18. The corresponding flame areas calculated from the images are shown in Figure 4-19. A lean methane-air mixture with an excess air ratio of 1.6 is used in this experiment. The positive impact of the transient high current on the flame kernel formation is observed as early as the spark is initiated. Accelerated flame propagation is achieved due to the transient high-current spark, as can

be seen from the significantly larger flame area throughout the time duration when the flame is visible from the optical window.

Case	Capacitance (μF)	DC supply voltage (kV)	Peak spark current (A)	Spark energy from the transient high-current module (mJ)	Spark energy from the coil (mJ)
1	0	0	0.05	0	30
2	4.5	0.6	550	810	30
3	4.5	1	1100	2250	30
4	4.5	1.3	1250	3800	30



Media: CH_4 -air, λ : 1.6 Background temperature: 298 K Spark gap size: 0.86 mm
 Background pressure: 4 bar abs Central electrode diameter: 2.5 mm

Figure 4-18 Effect of transient high-current spark on the flame kernel growth of lean mixture under quiescent conditions

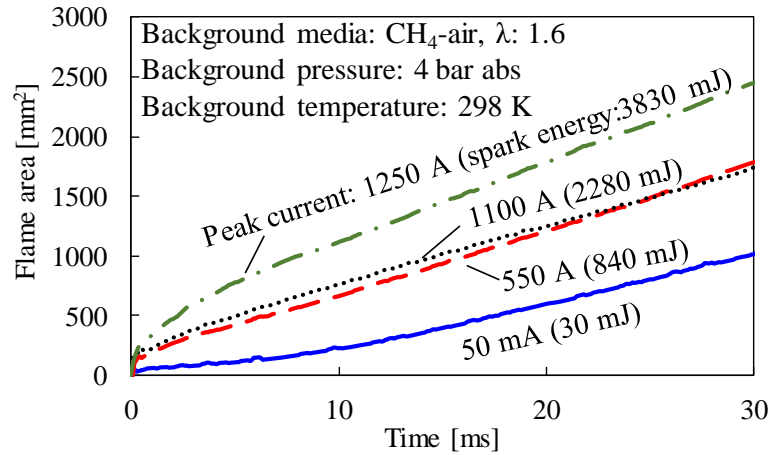


Figure 4-19 Flame areas with transient high-current spark discharge under quiescent conditions

The impact of the transient high current spark on the later stage of combustion can be observed from the results of the pressure measurement. The values of $t_{5\%MFB}$, $t_{50\%MFB}$, and $t_{5-90\%MFB}$ from the combustion of stoichiometric to lean mixtures are compared in Figure 4-20. Consistently faster combustion is observed throughout the tested range of the excess air ratios by using the transient high current spark discharge, especially with higher excess air ratios.

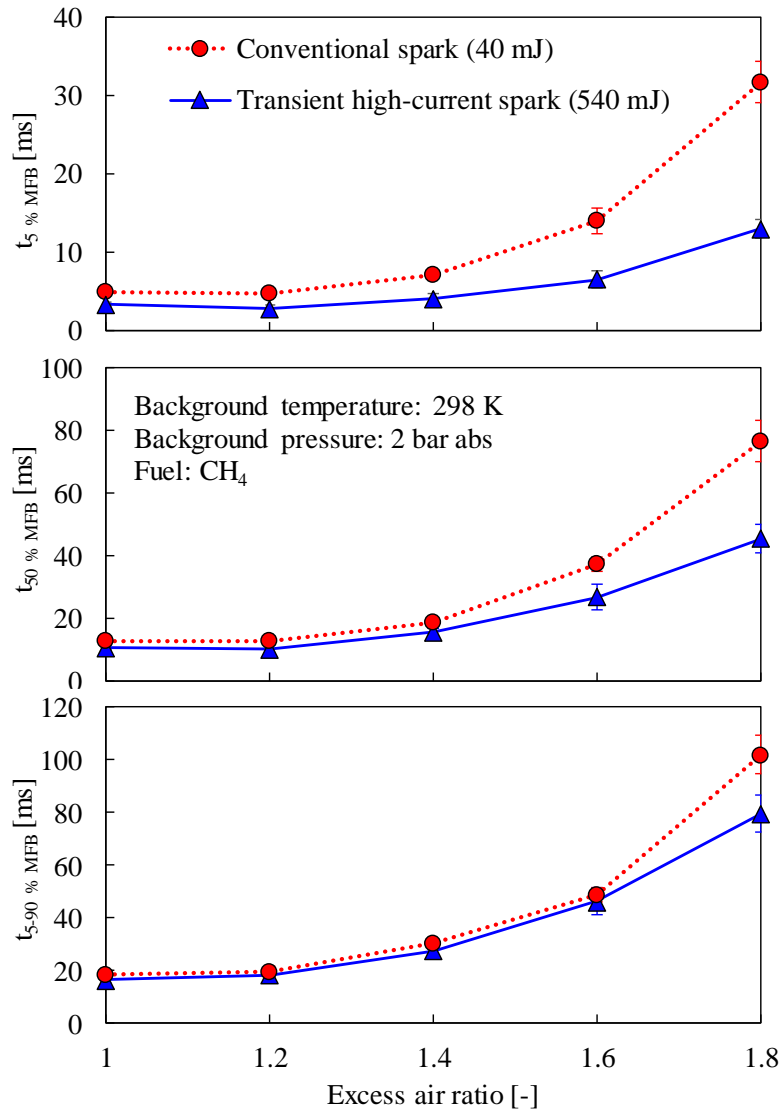


Figure 4-20 Effects of transient high-current spark on the combustion of lean mixtures under quiescent conditions

4.3.3 Impact of transient high-current spark on ignition of diluted mixtures

The values of $t_{5\% \text{MFB}}$, $t_{50\% \text{MFB}}$, and $t_{5-90\% \text{MFB}}$ from the combustion of CO_2 diluted mixtures are shown in Figure 4-21. The combustion initiated from a transient high-current spark is faster as compared with that generated by a conventional spark. The improvement is more significant under a higher dilution ratio.

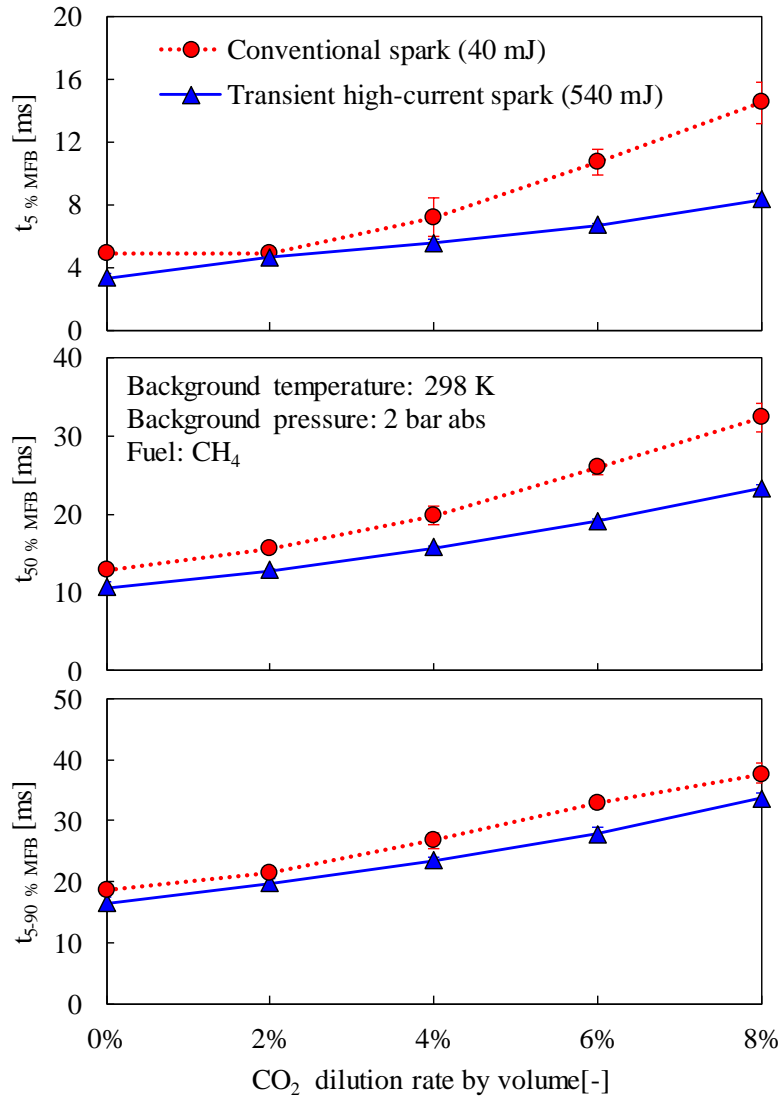


Figure 4-21 Effects of transient high-current spark on combustion of CO₂ diluted mixtures under quiescent conditions

4.4 Chapter summary

In summary of the experimental results, the initial flame kernel size is critical for the ignition under quiescent conditions. A faster combustion process can be achieved from a larger initial flame kernel. The spark discharge power is an important parameter to improve the initial flame kernel size under quiescent conditions. A summary of the spark discharge energy and peak power of different ignition strategies is provided in Figure 4-22. The

impact of ignition strategies on the early flame development in lean mixtures is compared in the bar chart. The high-power spark features higher peak spark discharge power than that of the conventional spark. The greater spark discharge power leads to an intense energy release in a short duration. The intense energy release results in a larger high-temperature area, consequently a bigger initial flame kernel. If the spark discharge energy is released in the form of lower power and longer duration, as in the case of the long-duration spark, it would have a minor impact on the flame kernel initiation.

From an effective ignition point of view, the high-power spark discharge is the most efficient strategy, as it consumes similar spark discharge energy to the conventional spark but improves the early combustion speed by 50%. Though the high transient discharge current is also effective in enhancing the flame propagation, the energy consumption of the transient high-current spark is much higher than that of a conventional spark.

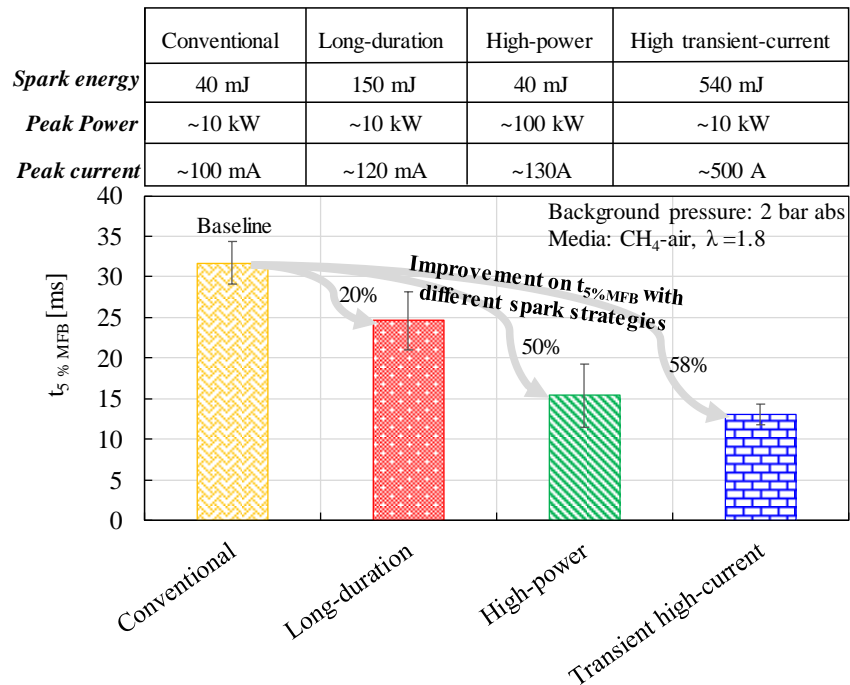


Figure 4-22 Comparison of different ignition strategies for lean combustion under quiescent conditions

CHAPTER 5 IMPACT OF AIR FLOW ON SPARK DISCHARGE PROCESS

The study of spark discharge processes under air flow conditions is presented in this chapter. The air motion not only affects the flame propagation and heat transfer during combustion but also changes the plasma shape and subsequently the energy transfer from the spark plasma to the combustible gaseous mixtures. As shown in Figure 5-1, the plasma channel is stretched away from the crossing line of the spark gap by the mixture flow. As a result, the plasma channel is elongated, and the location of the ignition is changed. These changes in the initial ignition process may significantly affect the initial stages of flame propagation and combustion. Therefore, it is important to investigate the plasma and air flow interactions.

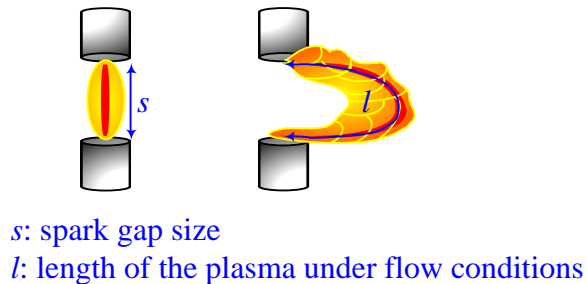


Figure 5-1 Comparison of spark plasma and flame kernel formation under quiescent and air flow conditions

Air is used as the background media in the experiments reported in this chapter. It is simpler and safer with background air to carry out the experiments under a broad range of velocities and background pressures. In combustible mixtures, air is also the major component in the mixture, especially under lean conditions. Thus, it is reasonable to use air as an approximation in the experiments.

The first section of this chapter is on the basic behaviors of the spark discharge under air flow conditions. The effects of air flow velocity, background pressure, spark gap size, and spark current level on the spark discharge under air flow conditions are reported in the

subsequent sections. Multiple types of ignition strategies are configured in this research. The impact of air flow on the performance of the different ignition strategies is also reported.

5.1 Characteristics of the spark discharge under air flow conditions

The characteristics of the spark plasma and the spark discharge parameters under gas air flow conditions are discussed in this section. The experiments are carried out with the controlled air flow bench under ambient background pressure and temperature.

5.1.1 Pre-breakdown and breakdown phases

Extensive experiments indicate that the formation of the plasma, which occurs during the breakdown phase, is not affected significantly by the air flow, as shown in Figure 5-2 and Figure 5-3. The breakdown voltage shows considerable variations, yet no apparent trend is observed on the variations of the breakdown voltage as the air flow velocity increases. The measurable breakdown event happens within several nanoseconds, while the air flow velocity ranges in tens of meters per second. Thus, the corresponding displacement of the gas within the spark gap is in the order of nanometers when the breakdown event happens, which appears to have very little impact on the onset of the spark plasma channel. For this reason, the discussions about the impact of the air flow on the spark discharge will be focused on the behaviors during the arc and glow phases.

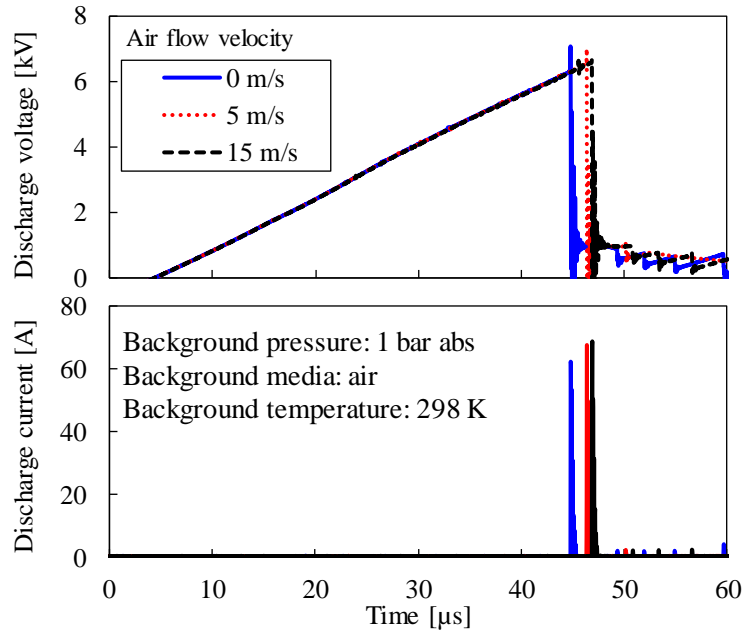


Figure 5-2 Spark discharge waveforms during the breakdown phase under various air flow conditions

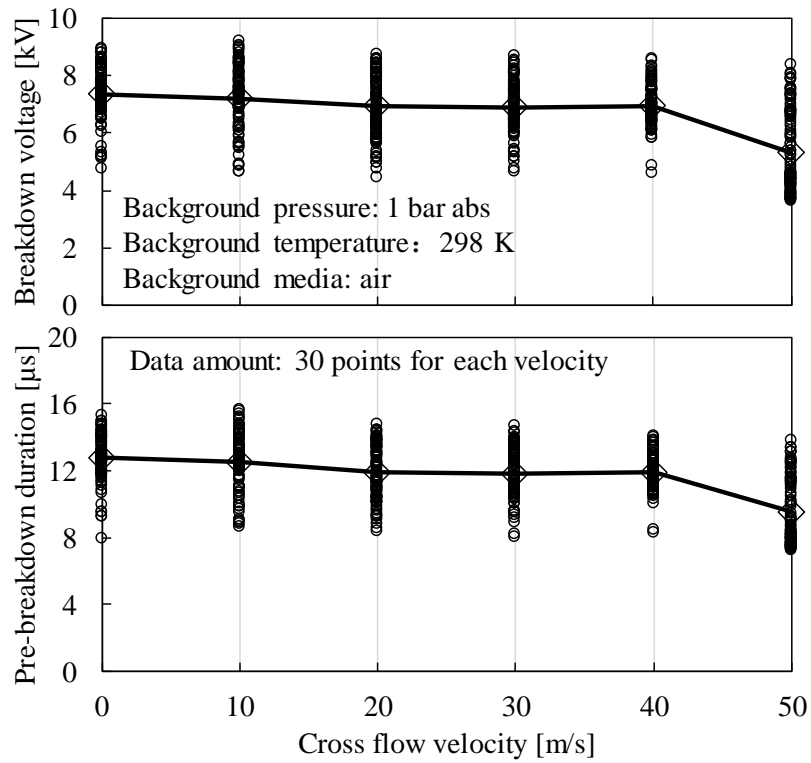


Figure 5-3 Effect of cross-flow velocity on the breakdown process

5.1.2 Arc and glow phases

The plasma during the arc and glow phases is subject to a greater impact of the air flow. The conductive particles generated during the spark discharge process are blown away from the spark gap by the air flow stream. Meanwhile, the two electrodes act as emitters and receivers of the plasma channel, appearing like anchors to form a closed electric circuit. Consequently, under a cross-flow, a U-shape stretched plasma channel can be observed visually, as shown in Figure 5-4.

The stretch results in an extensively prolonged plasma channel. The resistance of the plasma channel often increases due to the longer plasma length, which incurs a higher spark discharge voltage across the spark gap. As the length of the plasma keeps increasing under the effect of air flow, the voltage across the spark gap may keep increasing towards the coil potential voltage. During this process, the plasma may short circuit stochastically at some locations where the electric potential is adequately high to generate a new shorter electric path. The shorter plasma often has lower resistance and consequently results in a resurge in the spark discharge current and a drop in the spark discharge voltage. This phenomenon is termed a “short circuit” by some researchers [12,130,131]. The plasma stretch and short circuit can repeat several times during the spark discharge process, if the discharging energy sustains.

Flow velocity: 20 m/s Background media: air Background temperature: 298 K
 Spark gap size: 1 mm Central electrode diameter: 0.6 mm Background pressure: 4 bar abs

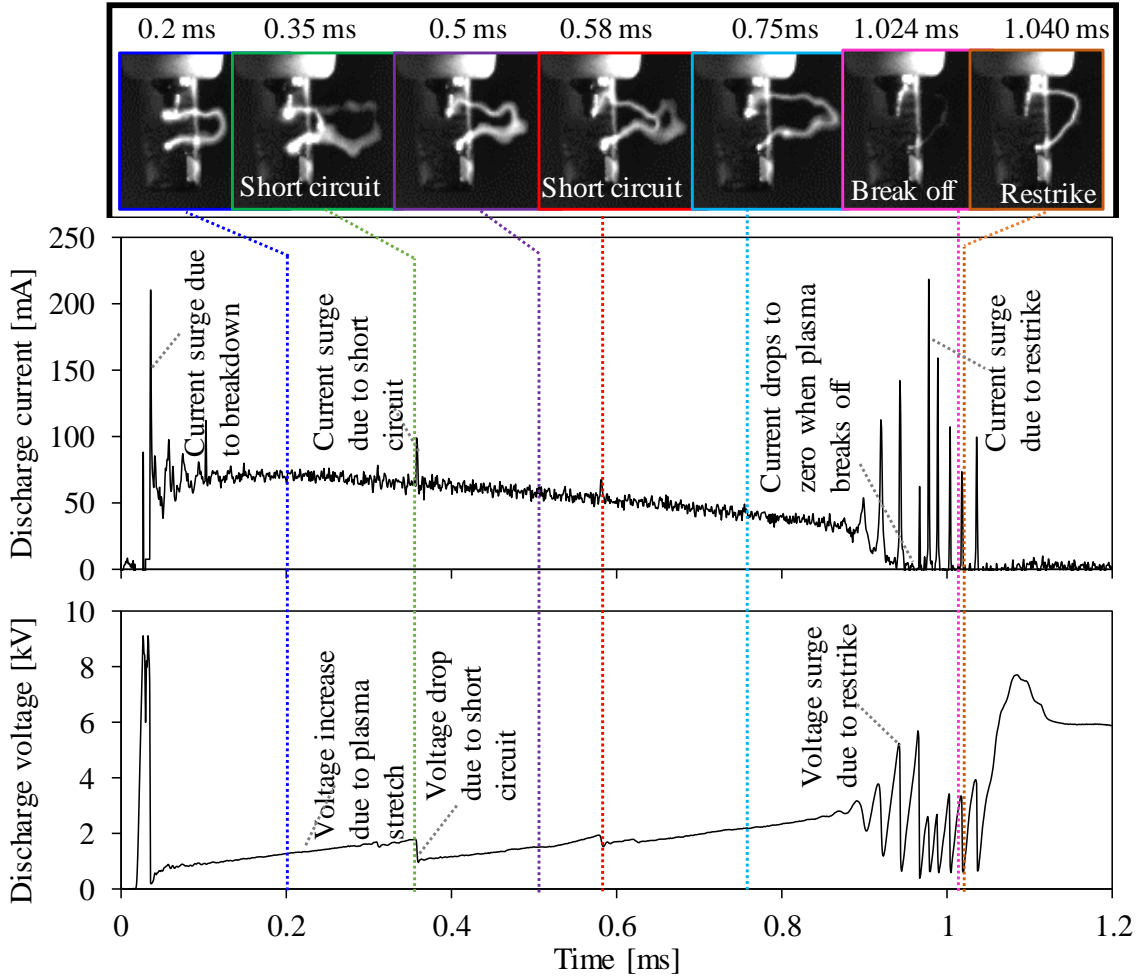


Figure 5-4 Plasma channel structure and electric waveforms of the spark discharge process

Towards the end of the spark discharge, the concentration of ions and electrons in the plasma channel reduces as the discharge energy depletes gradually. In the late stage of energy release, the plasma channel cannot be maintained, as shown in the flicking image suggests at 1.024 ms, in which the plasma channel disappears and restrikes, resulting in frequently open/close circuit oscillations. Eventually, the spark discharge current drops to zero.

However, the ignition coil is not completely discharged in the tail. The energy remaining in the ignition coil could be charged to the structural parasitic capacitance of the spark plug. Meanwhile, the voltage across the spark gap may increase again until the gas in the vicinity of the spark gap is ionized to form a new plasma channel. The process of restrike is similar to a breakdown event. A surge in the spark discharge current is observed once the new channel is formed, as shown in Figure 5-4. The newly formed plasma will take the path wherever the lowest electric potential is required for the electrons and ions to flow through.

According to the image taken at 1.04 ms in Figure 5-4, the plasma may have followed the same path as the previous plasma channel instead of the shortest path across the spark gap, probably due to the existence of some residual electrons and ions from the previous plasma channel so that the resistance of the path is low as compared with other locations. The new plasma channel exists for a very short time duration due to the insufficient energy supply. The phenomenon is different from the previous “short circuit” where the current never drops to zero. It is termed as the “restrike” phenomenon [12,130,131].

5.1.3 Waveform analyses

More detailed waveforms of short circuits and restrikes are shown in Figure 5-5. When a short circuit happens, the spark discharge current increases, and the voltage decreases, due to the reduced plasma resistance. When a restrike happens, the spark discharge current initially drops. The drop in the spark discharge current can either be attributed to reduced spark discharge current with the depletion of coil energy or loss of the ions and electrons in the air flow as reported by Sayama *et al.* [12]. They reported restrike phenomena due to the excessive diffusion loss of electrons in the air flow stream, where restrikes were observed at higher current levels. In this study, most of the restrike phenomena have been observed at a lower current level towards the end of the spark discharge. The voltage increases during the restrike, which eventually generates a new plasma channel, resulting in a surge in the spark discharge current, resembling the breakdown event.

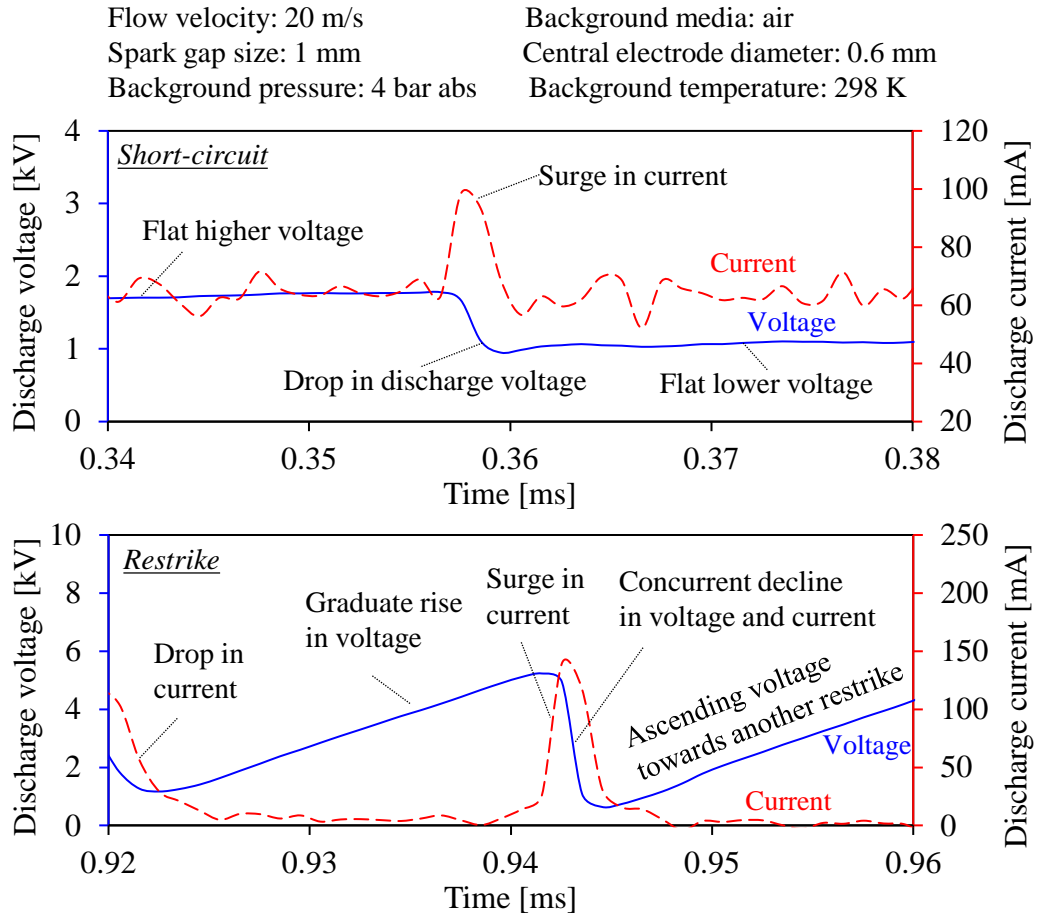


Figure 5-5 Spark discharge current and voltage during short circuit and restrike

The primary impact of the flicking in a short circuit or a restrike event on the ignition process is that the exact locations of the plasma heating and electrification are disrupted. Both phenomena result in the formation of a new path for the plasma. One of the differences between a short circuit and a restrike is that the spark discharge is continuous in the short circuit while the spark discharge is disrupted by the restrike. A new channel can be formed after a restrike if sufficient energy is available from the ignition coil. Generally, short circuit events are more frequently observed under this experimental setup. In this research, these two phenomena are not strictly differentiated in the later sections.

5.1.4 Detection of short circuit and restrike

The spark discharge current and voltage waveforms can be used to detect the occurrence of short circuits and restrikes. As shown in Figure 5-6, the spark discharge voltage profile shows a more distinctive response to the air flow effects as compared with the spark discharge current profile. Additionally, the spark discharge current profiles are more sensitive to the influence of electric fluctuations, as can be seen from the oscillations of current waveforms in the first 0.1 ms after the breakdown. From the frequency of repetitive oscillations, the fluctuations are likely resulted from the capacitive discharge after the breakdown, whereas not generated from short circuits and restrikes. These spikes in the spark discharge current are not equally reflected in the spark discharge voltage. Hence, the voltage waveforms can be analyzed to detect short circuits and restrikes.

To define a short circuit or restrike event, first, the average spark gap voltage during the spark discharge is calculated. For this experimental cases, a short circuit or restrike is counted when the voltage change rate is greater than 0.05 kV/ μ s. The threshold value is stipulated to ensure most of the significant plasma short circuit and restrike events can be considered.

The average short circuit and restrike frequency is defined in 5-1.

$$\text{Average short circuit and restrike frequency} = \frac{N}{t_{discharge} [ms]} \quad 5-1$$

Where N is the number of short circuit and restrike during the spark discharge, and $t_{discharge}$ is the discharge duration.

The timing interval from breakdown to the first short circuit or restrike event, termed as the first plasma holding period, as well as the spark discharge current and voltage at the first short circuit or restrike event, are also extracted in the analysis in the following section.

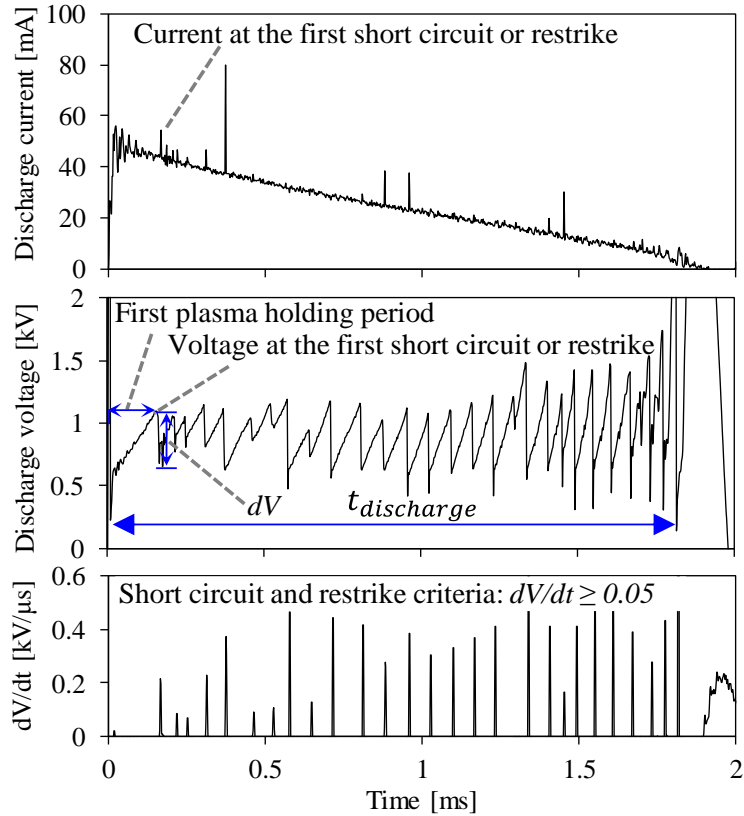


Figure 5-6 Detection of the plasma short circuit and restrike from the spark discharge voltage profile

5.1.5 Electric parameters affected by air flow

In addition to the short circuit and restrike phenomena, the spark discharge parameters are also altered due to the air flow. Comparisons of spark discharge current, voltage, spark plasma resistance, and discharge energy under a flow and a quiescent conditions are demonstrated in Figure 5-7. The spark in the two cases is generated by the discharge from a conventional inductive ignition coil with the same charging parameters. The differences in the discharge processes result from the impact of the air flow field.

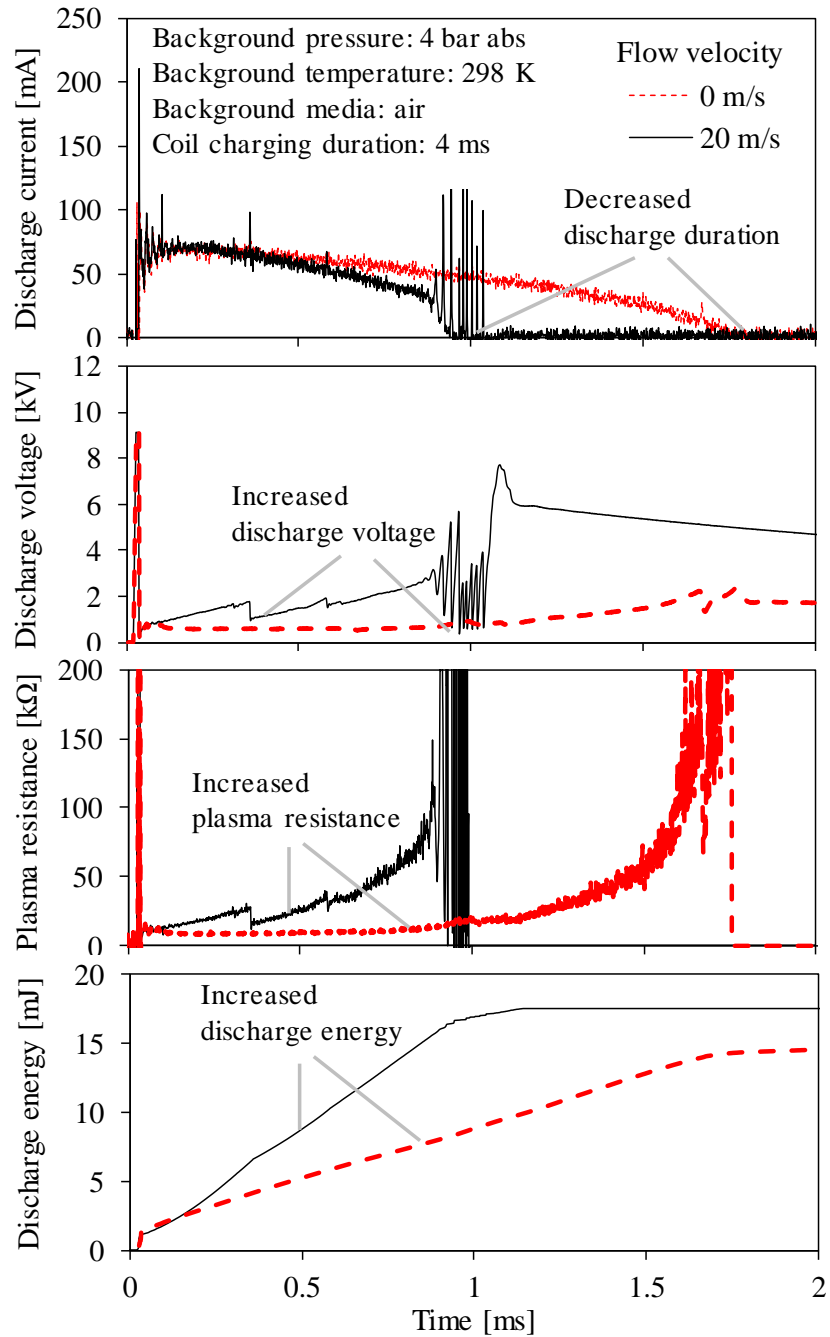


Figure 5-7 Spark discharge waveforms under quiescent and air flow conditions

The resistance of the plasma channel increases as the plasma is stretched longer by the air flow stream. The increased plasma resistance results in faster depletion of the energy stored in the ignition coil. The spark discharge duration is thus shorter under air flow conditions.

In this specific case, the spark discharge duration reduces from 1.7 ms under the quiescent condition to 1.0 ms when the spark discharge encounters an air flow velocity of 20 m/s. The energy is released at a faster rate, as can be seen from the larger increasing slope of the spark discharge energy profile under 20 m/s air flow. Moreover, the total spark discharge energy is increased, from 15 mJ under the quiescent condition to 17 mJ with 20 m/s flow. The spark discharge voltage increases under air flow conditions, whereas the spark discharge current level drops slightly under the air flow conditions.

The electric parameters in the secondary circuit of a conventional inductive ignition system are analyzed to assist the understanding of the impact of plasma stretch on the spark discharge parameters, as depicted in Figure 5-8. The plasma stretching results in increased plasma resistance. The higher resistance of the stretched plasma contributes to the higher total resistance of the secondary ignition circuit. The time constant reduces with the increased resistance, as shown in 5-2 [132]. Accordingly, the spark discharge current at the same time instant is lower (5-3) [132].

$$\tau(t) = \frac{L_{coil}}{R_{total}(t)} \quad 5-2$$

$$I(t) = (2 E_{coil}/L_{coil})^{0.5} e^{-t/\tau(t)} \quad 5-3$$

Where L_{coil} is the inductance of the secondary coil, E_{coil} is the energy stored in the secondary coil, R_{total} is the total resistance of the secondary circuit, τ is the inductive discharge time constant, I is the secondary discharge current.

The voltage across the spark gap generally increases with the increased plasma resistance, despite the decrease in the spark discharge current. Considering all the impacts, the spark discharge energy can increase or decrease, depending on the dominating parameter.

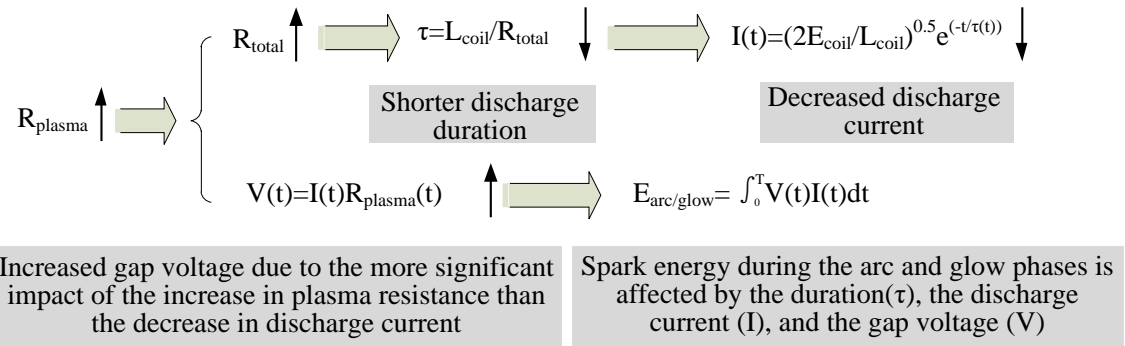
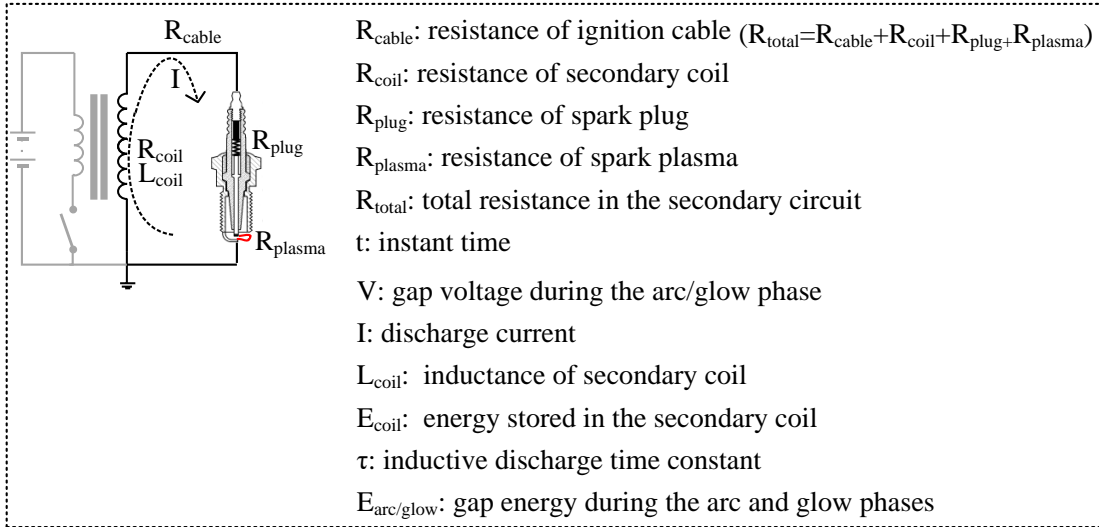


Figure 5-8 Impact of plasma resistance on the spark discharge parameters

5.1.6 Section summary

In summary, multiple effects of the air flow can be observed on the spark discharge process. The air flow stretches the plasma, extends its length, which causes higher spark discharge voltage, shorter discharge duration, and a change in the discharge energy. All these factors may affect the ignition ability of the spark.

In the case of combustible gaseous mixture, a shorter spark discharge duration may impair the ignition ability, as the time window for the energy transfer to the combustible gas becomes narrower. The extended plasma length may be beneficial for the ignition, as the ignition volume may increase due to the larger contact area between the hot plasma and the combustible gas. The displacement of the plasma away from the spark gap between the

electrodes may also result in a positive impact on the ignition, as the heat loss to the electrodes decreases.

The plasma length, spark discharge duration, and discharge energy are the main influential factors in the ignition process. Therefore, these parameters are further analyzed under varied air flow conditions. The short circuit and restrike phenomena are other important factors for ignition because they interrupt the energy transfer from plasma to a combustible gas. These phenomena will also be reported under various background conditions.

5.2 Effects of the magnitude of air flow velocity on spark discharge

In this section, a more detailed analysis is given on the impact of varied air flow velocities on the spark discharge characteristics during the arc and glow phases. The air flow test bench is used in the experiments, with a range of cross-flow velocities from 0 m/s to 60 m/s under ambient pressure and temperature.

Since the major purpose is to study the impact of air flow velocity on the plasma stretch, it is better to minimize the effects of the electrode shape on the plasma. For this reason, a pair of thin needles, with a needle diameter of 0.08 mm and gap size of 0.86 mm are used to form a spark gap. The details of the needle spark plug can be found as spark plug D in Table 3-6.

The spark discharge current and voltage waveforms provided in Figure 5-9 demonstrate the original spark discharge current and voltage profiles under quiescent conditions. The spark is generated from a conventional inductive coil system with a charging duration of 3 ms. The spark discharge energy, duration, and peak current under quiescent conditions are listed in Figure 5-9 as well. Then tests are carried out under various air flow velocities without any modifications to the hardware and control command of the ignition system.

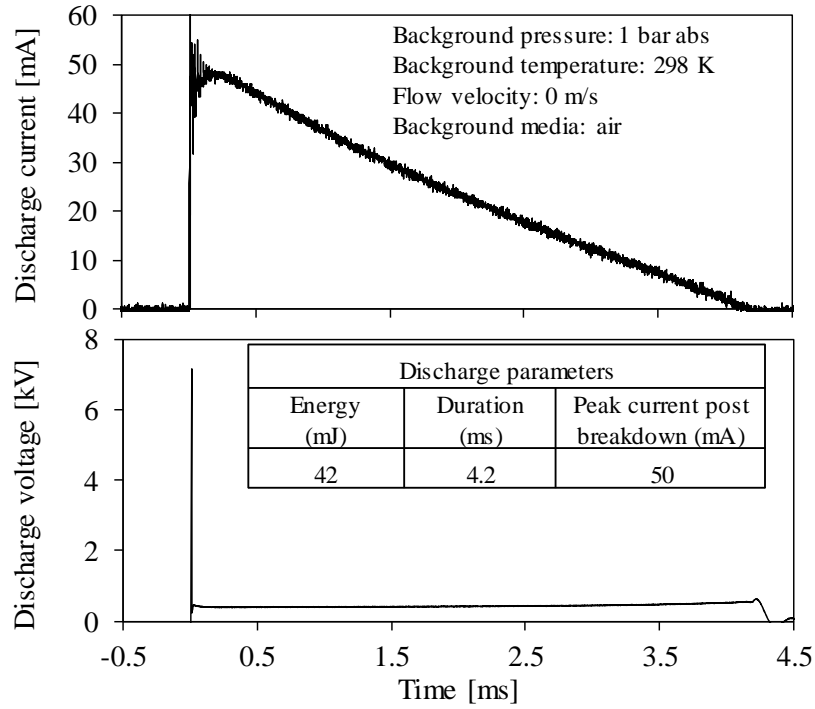


Figure 5-9 Spark discharge current and voltage waveforms (quiescent conditions)

The stretching of plasma in the flow field is recorded using the direct imaging system. The length of the plasma is calculated following the procedure introduced in section 3.4.3. The two ends of the plasma are attached to the two electrodes, while the central part of the plasma is stretched by the air flow. The stretch process generates a U-shape plasma channel, with the length increasing from both arms of the plasma. Half of the increased length is used to calculate the stretching rate. The stretching rate is defined by 5-4.

$$Stretching\ rate = \frac{\Delta l / 2 [mm]}{\Delta t_{stretch} [ms]} \quad 5-4$$

Where Δl is the increased plasma length in one stretch and $\Delta t_{stretch}$ is the time duration for the stretching process. Repeated stretches and short circuits can happen during the spark discharge so that multiple values of stretching rate can be calculated during one spark event. In data analysis, a linear regression procedure is applied to get the values of stretching rates.

A demonstration case under 10 m/s air flow is shown in Figure 5-10. Four major plasma stretching processes are observed in this case, the corresponding stretching rates in each process are listed in Figure 5-10 as well. In this example, repeated plasma stretching processes are observed during the discharge process. The maximum length that can be reached by each stretch decreases progressively whereas the restrike frequency increases, due to the decreasing spark discharge current. Overall, the calculated stretching rates agree with the setting velocity of 10 m/s. The first stretch process is used to represent the impact of flow velocity on the plasma stretching in the following analysis since the repeated stretches generally follow a similar pattern.

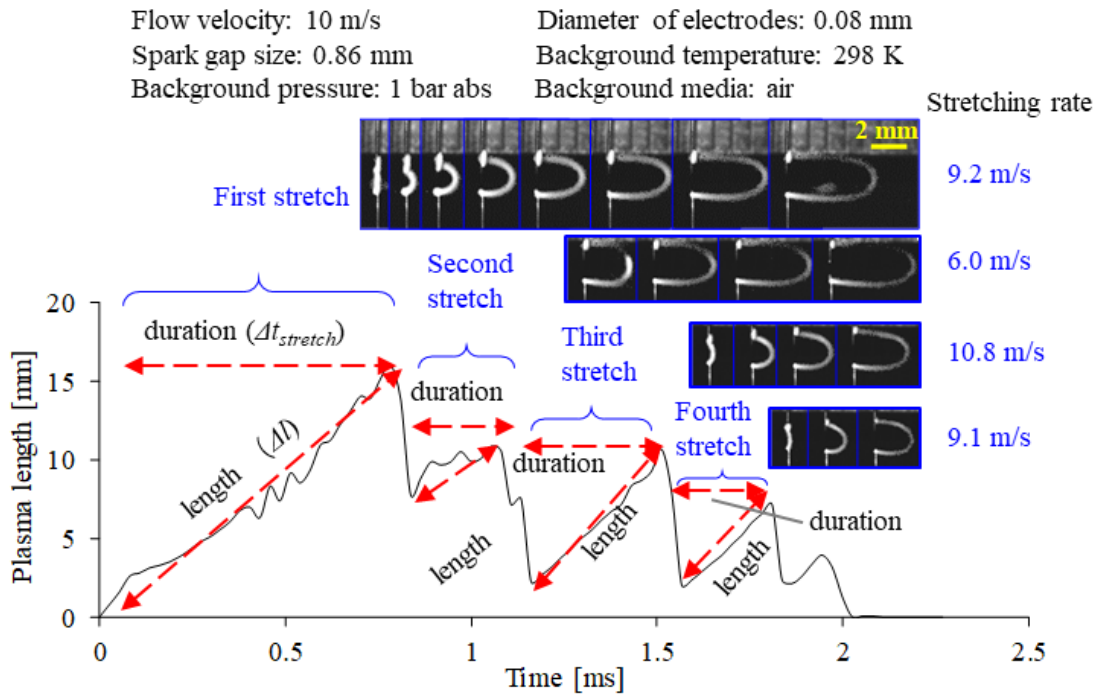


Figure 5-10 Plasma stretch by the air flow

The spark discharge current and voltage waveforms, along with the plasma length under air flow velocities of 10 m/s, 20 m/s, and 50 m/s are plotted in Figure 5-11. A slight drop in spark discharge current is observed with the increased air flow velocity. More significant changes are observed in the plasma length and the spark discharge voltage waveforms. The stretching rate of the plasma increases with the increased air flow velocity. Though the

plasma stretching rate changes with the air flow velocity, the maximum length of the stretched plasma is less affected by the air flow velocity. The maximum plasma length with 10 m/s air flow is merely slightly shorter as compared with the 20 m/s and 50 m/s cases.

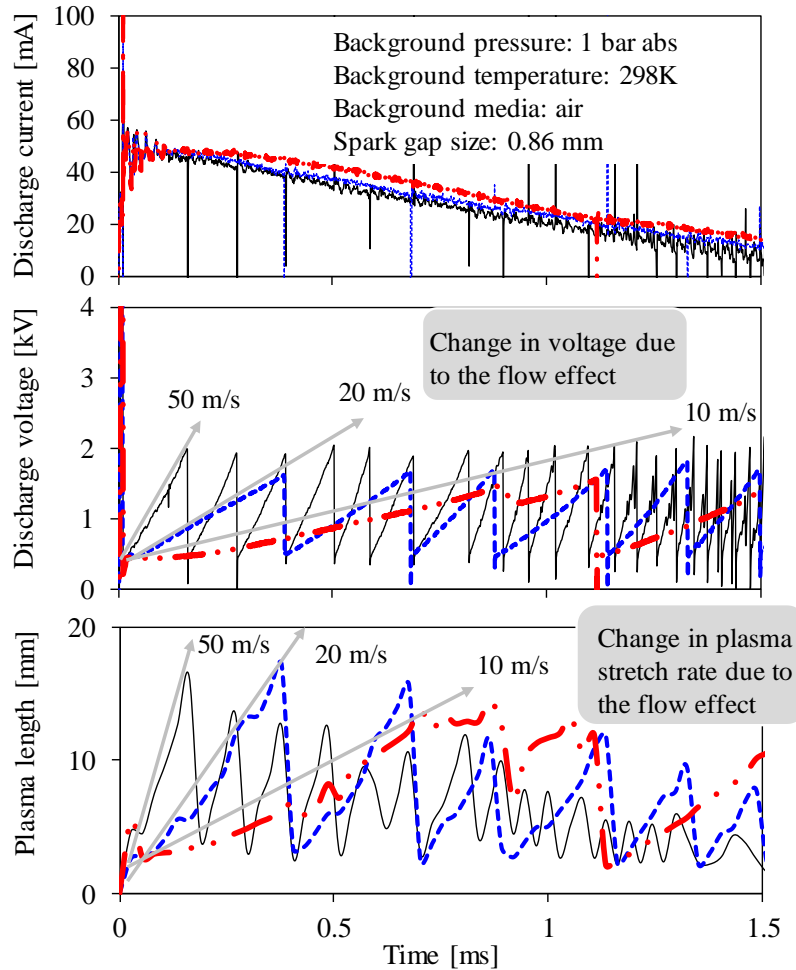


Figure 5-11 Spark discharge current, voltage, and plasma length under different cross-flow velocities

5.2.1 Plasma stretching rate and maximum plasma length

For benchmarking, the setting of air flow velocity across the spark gap varies between 0 to 50 m/s. The plasma stretching rates under different air flow velocities are summarized in Figure 5-12. Each value shown in the figure is the averaged result from 6 repeated tests under fixed conditions. The standard deviations are shown as error bars. The stretching rate

is calculated from the first stretch in the spark discharge process. The stretching rate is about 10-20% slower than the air flow velocity under the test conditions.

The averaged values of maximum plasma length under different air flow velocities are illustrated in Figure 5-13. The averaged value of maximum plasma length increases from 12.2 mm to 14.1 mm when the air flow velocity increases from 10 m/s to 20 m/s. When the air flow velocity further increases from 20 m/s to 50 m/s, the maximum plasma length does not have a significant change, remaining at approximately 14 mm.

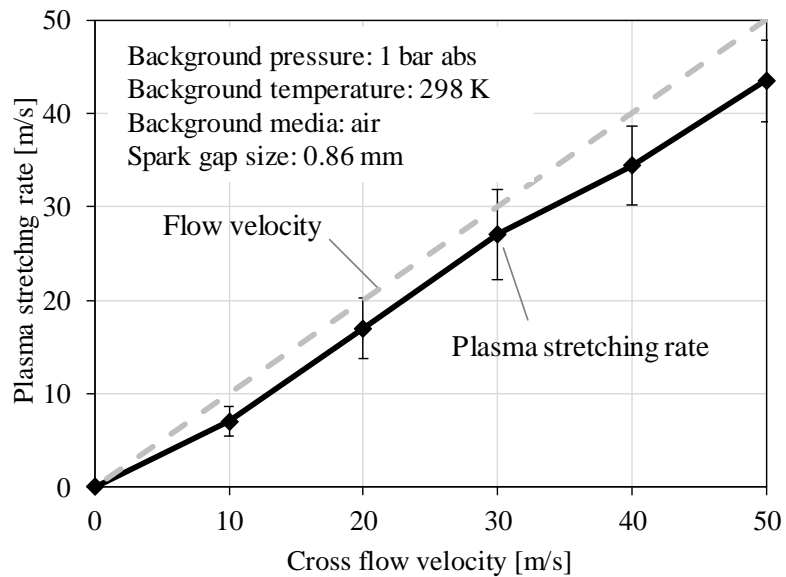


Figure 5-12 Plasma stretching rate under different cross-flow velocities

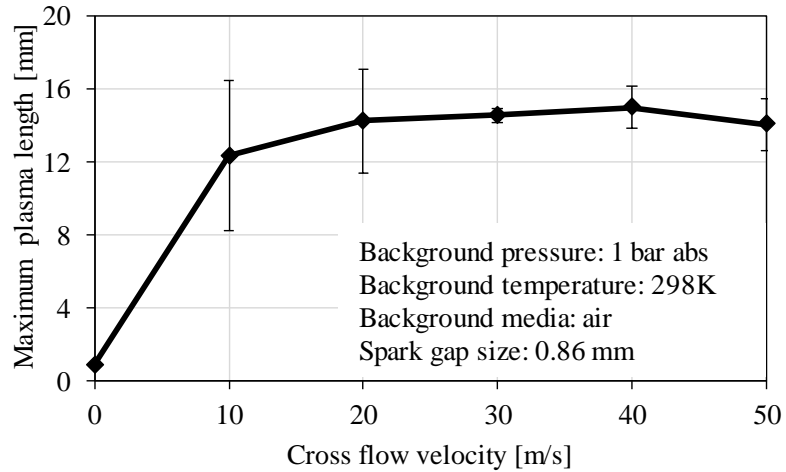


Figure 5-13 Maximum plasma length under different cross-flow velocities

5.2.2 Spark discharge energy and duration

The impact of air flow velocities on the spark discharge energy and duration is shown in Figure 5-14. The spark discharge energy increases, while the discharge duration decreases with the increased air flow velocity. These values are averaged results from 30 repeated tests. The standard deviations are shown as error bars in the figure. The standard deviation is generally less than 5% with respect to the mean value.

The gain in spark discharge energy is most significant when the air flow velocity increases from 0 m/s to 20 m/s, with an increase of 14%. Negligible changes are observed in spark discharge energy when the velocity further increases from 20 m/s to 60 m/s. The spark discharge duration reduces drastically to about 50% of the original value when the air flow velocity increases from 0 m/s to 10 m/s. Further increasing the air flow velocity from 10 m/s to 60 m/s results in an additional deduction of about 5%.

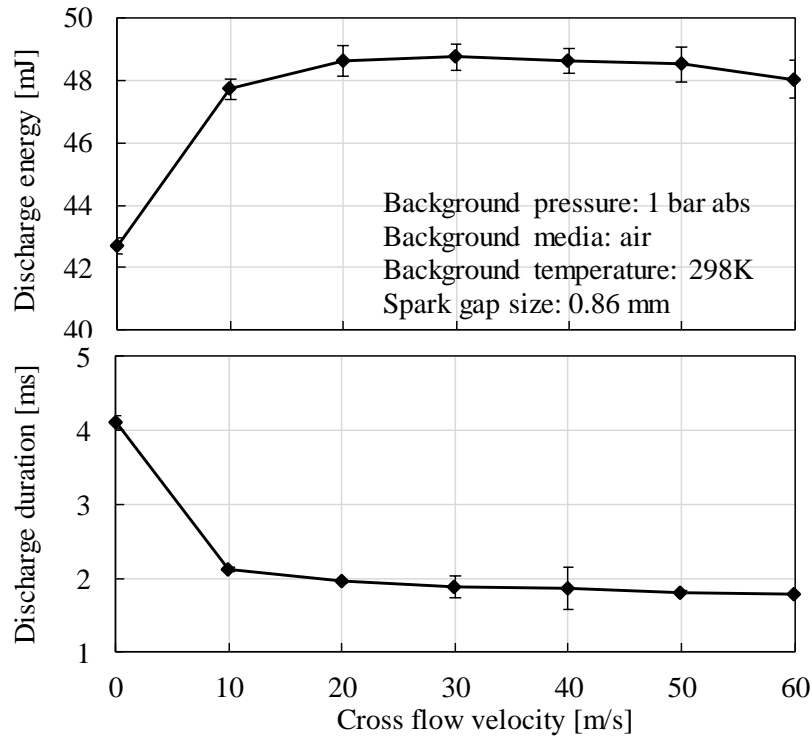


Figure 5-14 Effects of air flow velocity on the spark discharge energy and duration

Several data points are selected from the experimental results to discuss the trend of the change in the spark discharge energy with the air flow velocity. The discharge voltage waveforms are shown in Figure 5-15.

The average discharge voltage in the spark discharge process is plotted as a reference. The spark discharge voltage increases with the plasma stretch. However, when a short circuit occurs, the voltage drops to a much lower value. The hatched areas in the figure indicate the lower instantaneous spark discharge voltage as compared with the average spark voltage during the entire discharge process. Higher velocity results in higher short circuit frequency so that the drop in voltage due to the plasma short circuit partially negates the increase in voltage due to the plasma stretch, as can be seen from the increased hatched areas. Eventually, the average spark discharge voltage reaches a stable condition, as shown in Figure 5-16. Correspondingly, the spark discharge energy does not change significantly with increased air flow velocity once the average spark discharge voltage is stable.

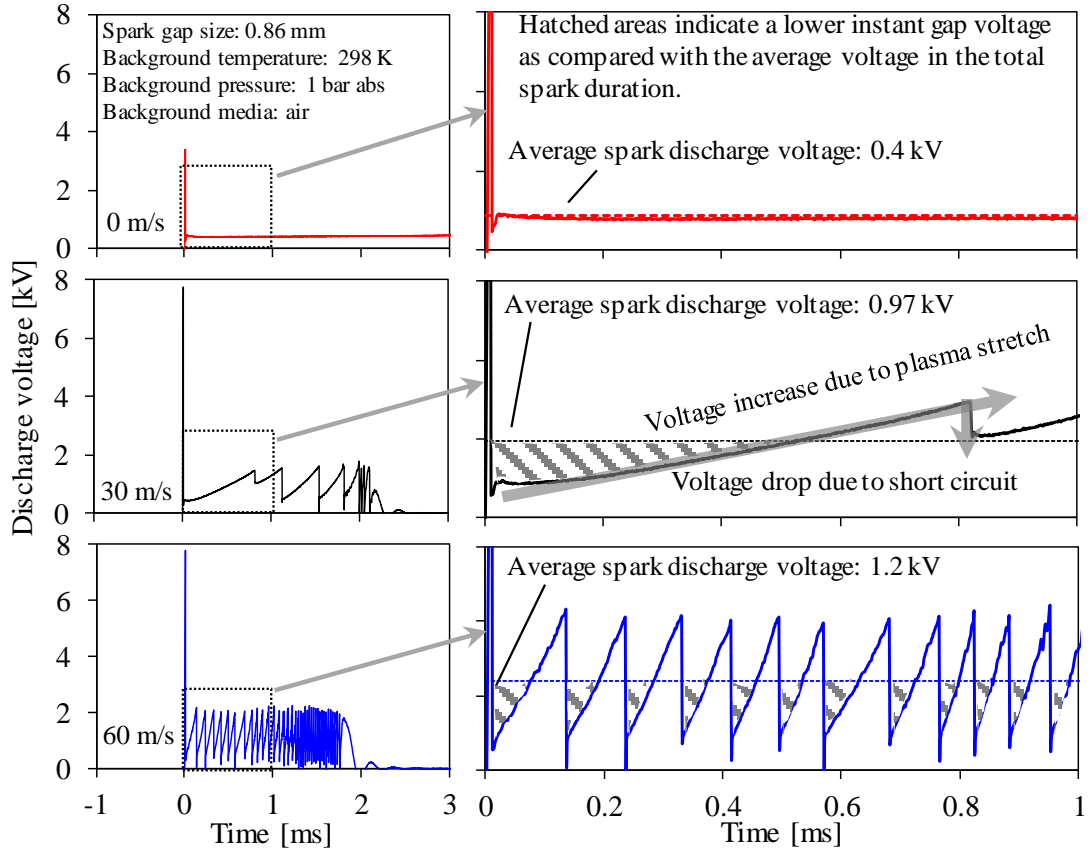


Figure 5-15 Effect of air flow velocity on the spark discharge voltage

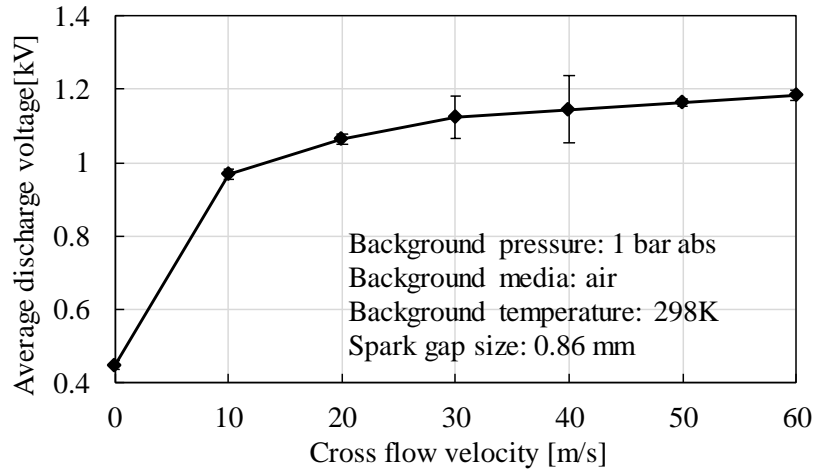


Figure 5-16 Average spark discharge voltage under different cross-flow velocities

The average short circuit and restrike frequency under different air flow velocities is shown in Figure 5-17. No short circuits or restrikes are observed when the air flow velocity is less than 10 m/s under the tested conditions. The average short circuit and restrike frequency increases almost linearly with the increased air flow velocity.

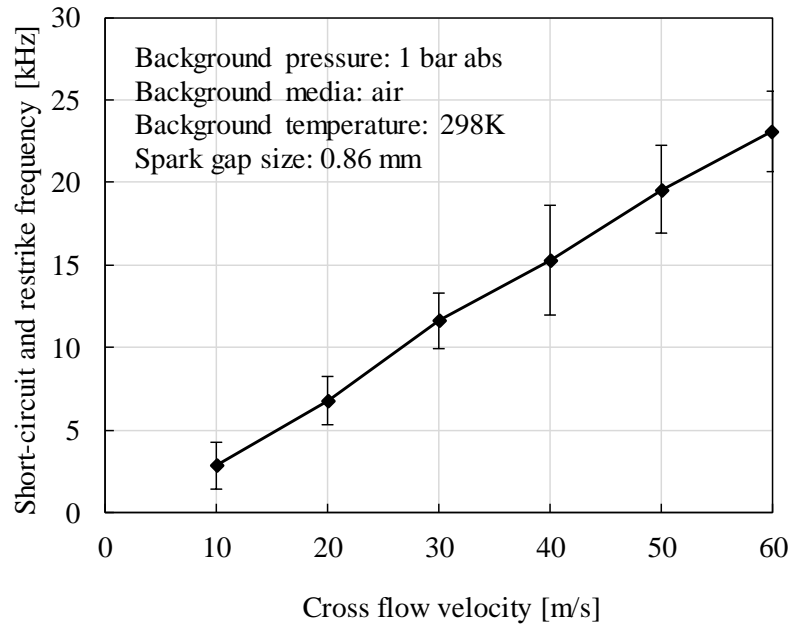


Figure 5-17 Average short circuit and restrike frequency under different cross-flow velocities

The first short circuit or restrike for each of the progressively increased flow cases is analyzed in more detail. The timing between spark breakdown and the first short circuit or restrike, which is termed as the first plasma holding period, along with the current and voltage at the first short circuit or restrike, is shown in Figure 5-18. With the increase of air flow velocity, the first plasma holding period progressively becomes shorter, suggesting an earlier timing for the short circuit or restrike. The spark discharge voltage and current at the first short circuit or restrike increase with the air flow velocity.

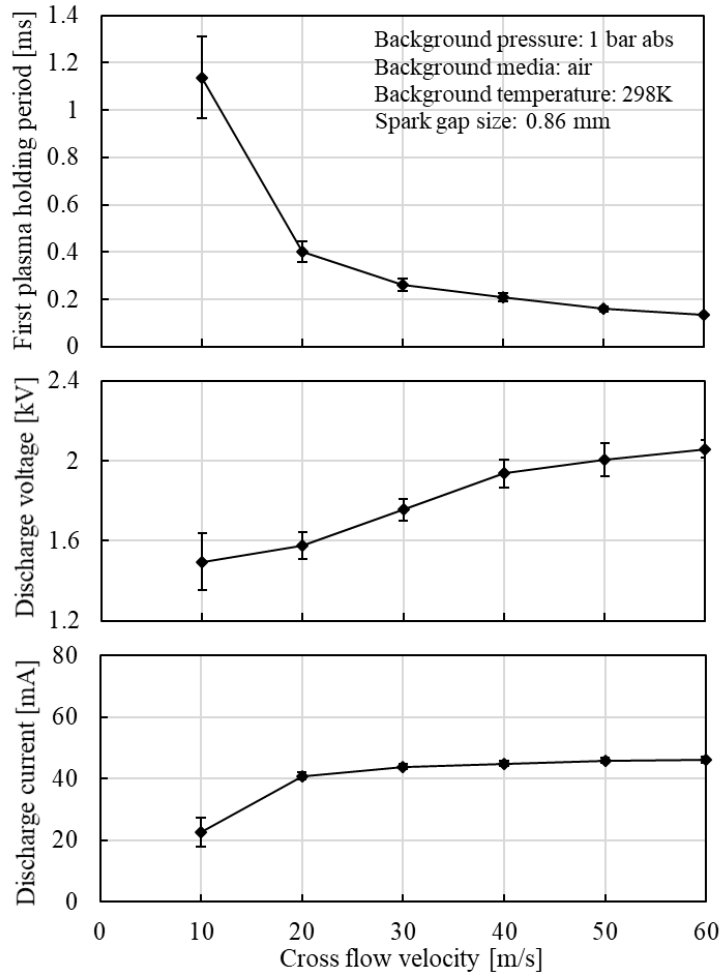


Figure 5-18 First plasma holding period, spark discharge voltage, and current at the first short circuit or restrike under different cross-flow velocities

5.2.3 Section summary

In summary of the behaviors of the spark discharge under different air flow velocities, several findings are listed below:

- (1) The short circuit and restrike frequency increases with the increased air flow velocity.
- (2) The spark discharge duration decreases with the increased air flow velocity.
- (3) The first plasma holding period decreases with the increased air flow velocity.

- (4) The plasma stretching rate increases with the increased air flow velocity. The value of the stretching rate is similar to the air flow velocity
- (5) The maximum plasma length is not affected significantly by the air flow velocity.

5.3 Effects of background pressure on spark discharge channel shape and electric waveforms

The impact of air flow on the spark discharge is also studied under different background pressure conditions. The experiments are performed in the constant volume combustion chamber system with a pressurized background. A free jet flow is generated from a tube with an inner diameter of 4.5 mm. The details of the experimental setup of the chamber test system can be found in section 3.1.

Images in Figure 5-19 demonstrate the selected cases with different background pressures. The plasma is twisted and wrinkled, which can be a result of enhanced turbulence intensity. The Reynolds number can be calculated from 5-5 [133]. With the same mean air flow velocity and tube diameter, and similar air dynamic viscosity under the same ambient temperature, the Reynolds number increases with the increased gas density.

$$Re = \frac{\rho u d}{\mu} \quad 5-5$$

Where ρ is the density of air, u is the air flow velocity, d is the tube inner diameter, and μ is the dynamic viscosity of air. The Reynolds numbers from the nitrogen jet are approximately 68200, 124600, and 169700 with the background pressure of 6 bar abs, 11 bar abs, and 15 bar abs under the test conditions.

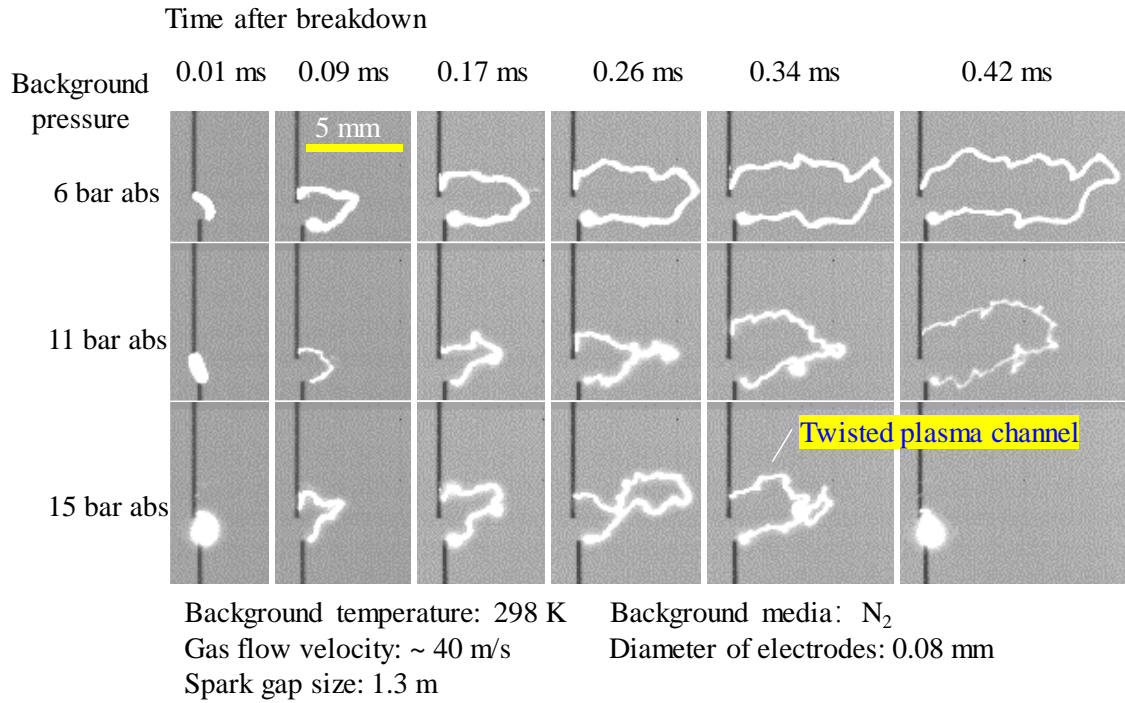


Figure 5-19 Spark plasma images under different background pressures

The spark discharge current, voltage, and plasma length are shown in Figure 5-20. Under the same air flow velocity, the spark discharge current and discharge duration decrease, while the discharge voltage increases with the increased background pressure. The calculation of the plasma length is more challenging from 2-D imaging analysis, as the plasma is twisted. The averaged plasma length and stretching rate are thus not reported for these cases.

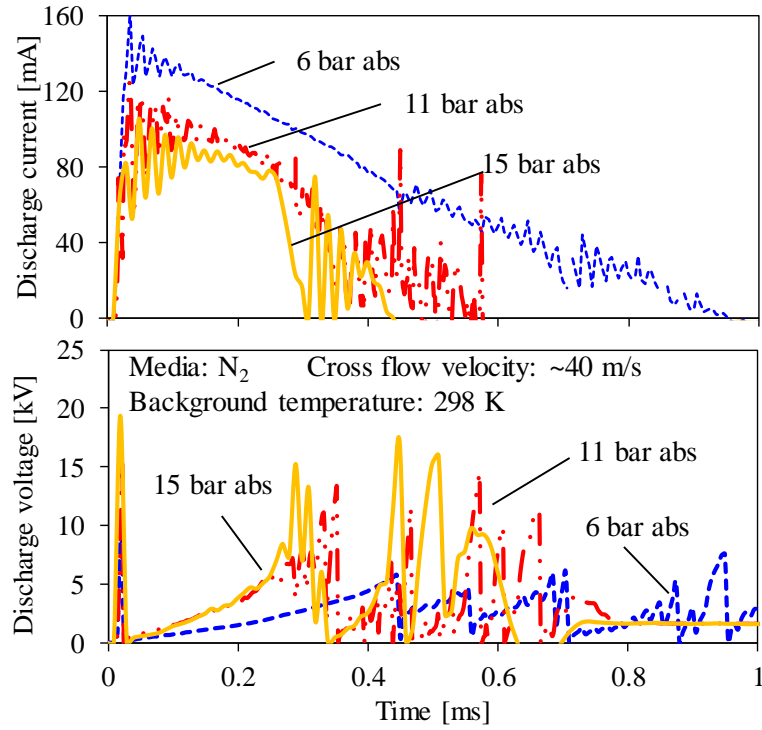


Figure 5-20 Effects of background pressure on the spark current and voltage

The first plasma holding period and the spark discharge voltage at the first short circuit or restrike are shown in Figure 5-21. With the increased background pressure, the first plasma holding period is shorter and the voltage is higher.

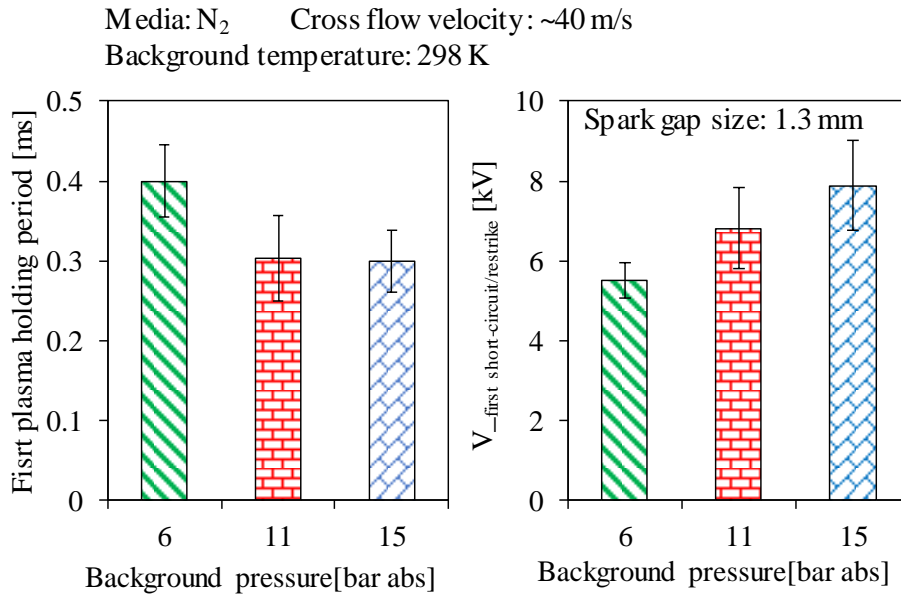


Figure 5-21 First plasma holding period and voltage at the first short circuit under different background pressures

5.4 Effects of spark gap size on spark discharge channel shapes and electric waveforms

The effects of spark gap size on the spark discharge, under air flow conditions, are discussed in this section. The experiments are performed with the controlled air flow test bench under ambient background pressure and temperature. Two spark gap sizes are used in the experiments, 2 mm and 0.86 mm. The same ignition system is used in the experiments. The commanded charging parameters, such as the coil supply voltage and the charging duration of the primary coil are also the same. The images in Figure 5-22 demonstrate the plasma stretching process under the effect of air flow in the first 0.58 ms after the breakdown event. With a 2 mm spark gap size, a longer plasma channel is observed visually.

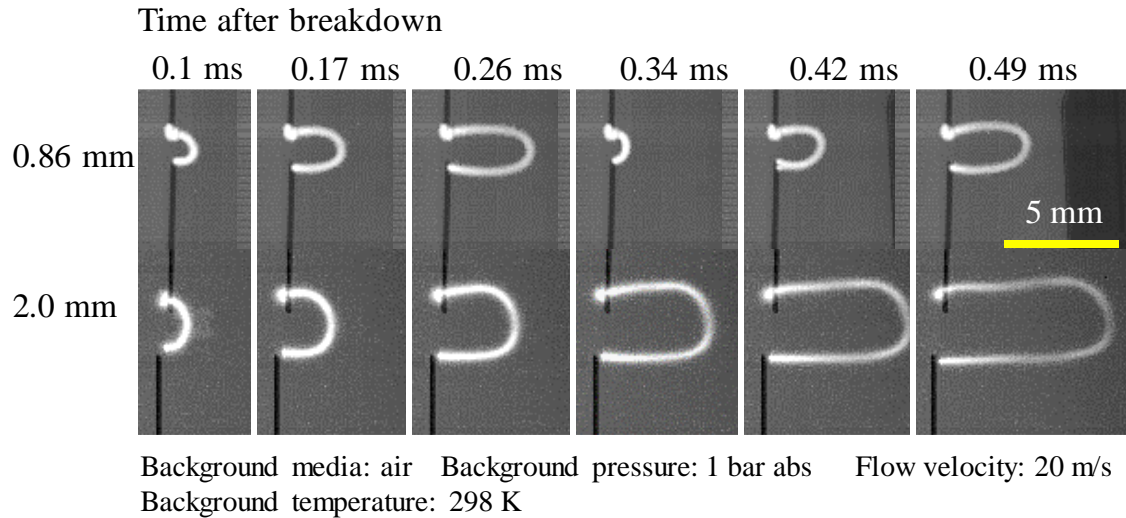


Figure 5-22 Spark plasma images with varied spark gap size under 20 m/s air flow

The corresponding waveforms for the plasma channel images of Figure 5-22 are shown in the early segments of Figure 5-23. The spark discharge current drops with the increased spark gap size, while the spark discharge voltage increases with the spark gap size. The spark discharge duration is shorter when the spark gap size is increased. The 2 mm spark gap size also facilitates a prolonged plasma channel in the flow field. In this case, the maximum length of the plasma is achieved in the first plasma stretch in both cases. A maximum length of 13 mm is achieved when the spark gap size is 0.86 mm, whereas the value increases to 28 mm when the spark gap size is increased to 2 mm.

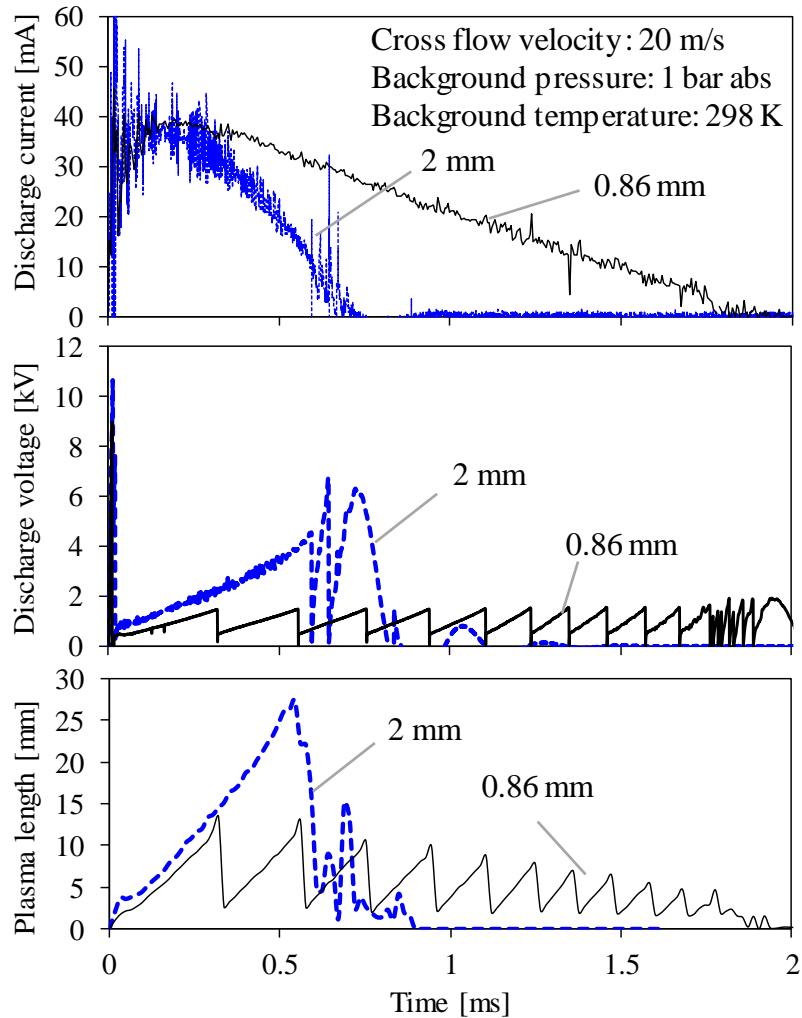


Figure 5-23 Effects of spark gap size on the discharge current, voltage, and plasma length under 20 m/s air flow

The values of maximum plasma length under air flow velocities from 0 m/s to 50 m/s are summarized in Figure 5-24. These values are averaged results from 6 repeated tests for each test condition. The maximum plasma length with a 2 mm spark gap is consistently larger than the maximum plasma length with a 0.86 mm spark gap.

Counting the first stretch, i.e., the longest stretch, the plasma stretching rate is also calculated and plotted in Figure 5-25. The change in spark gap size has an insignificant

impact on plasma stretching rates. The plasma stretching rates increase almost linearly following the air flow velocity, irrespective of the gap differences.

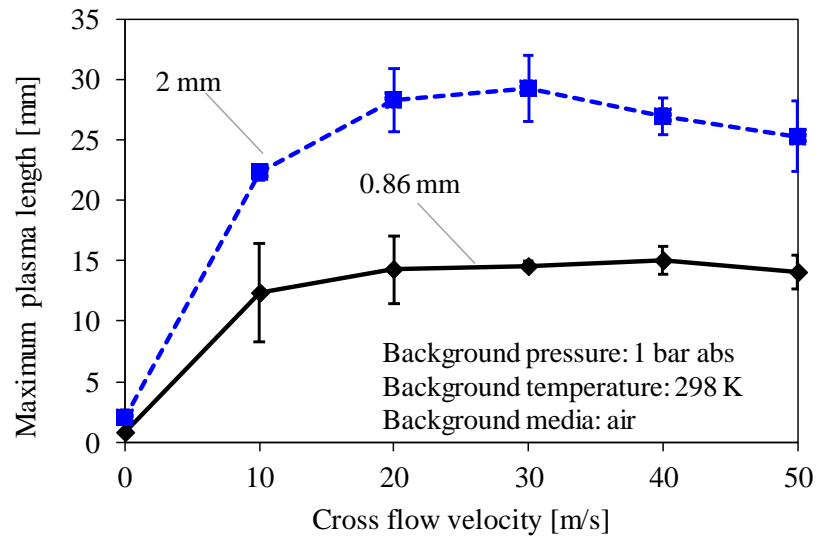


Figure 5-24 Effect of spark gap size on maximum plasma length

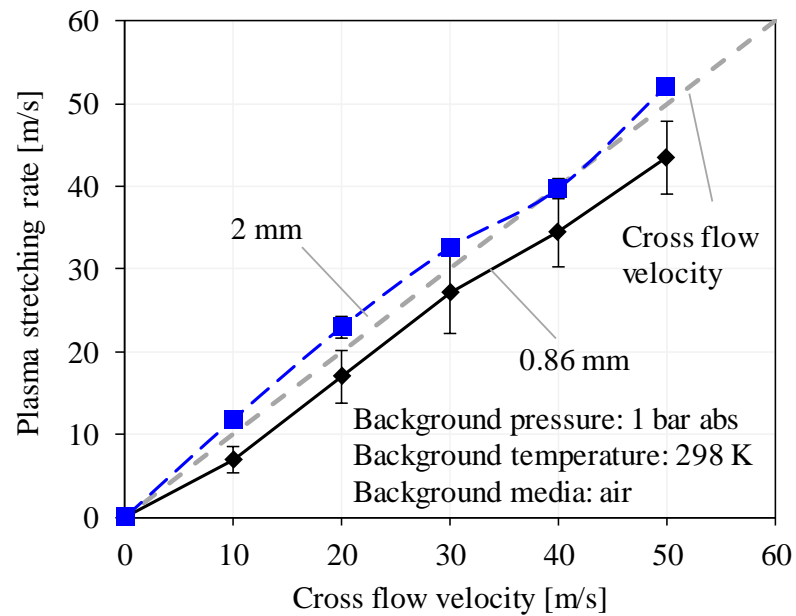


Figure 5-25 Effect of spark gap size on plasma stretching rate

The spark discharge energy and discharge duration with 0.86 mm and 2 mm spark gap sizes are plotted in Figure 5-26. The general trend is similar in the two cases for the electric discharging process, where the spark discharge duration decreases, while the spark discharge energy increases, with the increased air flow velocity. A higher spark discharge energy level and a shorter duration are achieved with a larger spark gap size.

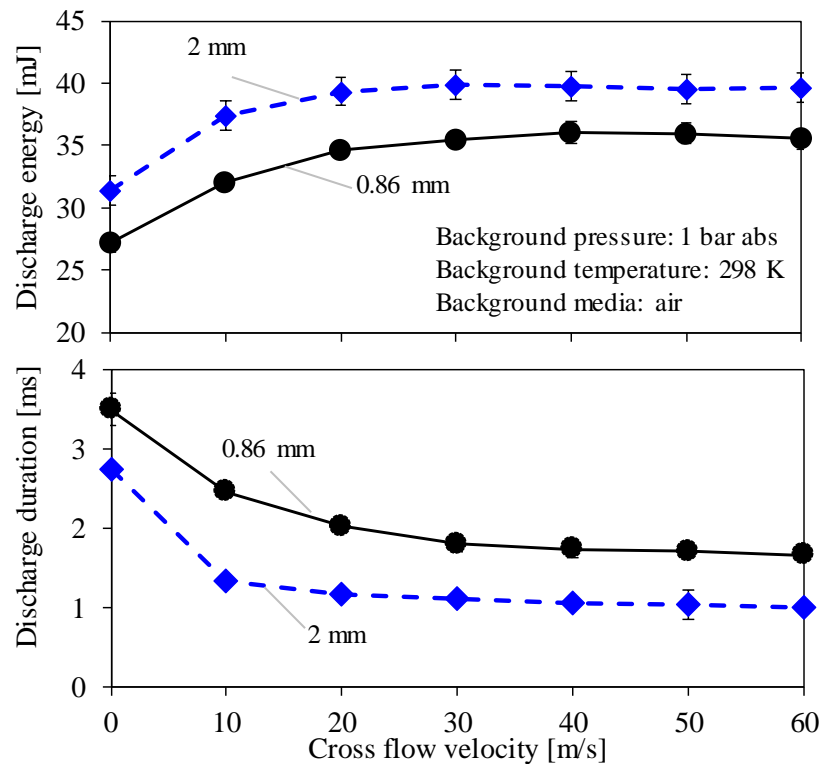


Figure 5-26 Effects of spark gap size on the spark discharge energy and duration

5.5 Effects of air flow on spark discharge process with different discharge current levels

The effects of air flow on the spark discharge with different current levels are analyzed in this section. The experiments are carried out with the controlled air flow bench under ambient background pressure and temperature.

Three spark discharge current levels with a peak current of 150 mA, 80 mA, and 50 mA respectively, are used for the analysis. The three cases of spark events are realized by the

conventional inductive ignition system by changing the charging duration of the primary coil, whereas the hardware configurations are the same. The spark discharge current waveforms are shown in Figure 5-27.

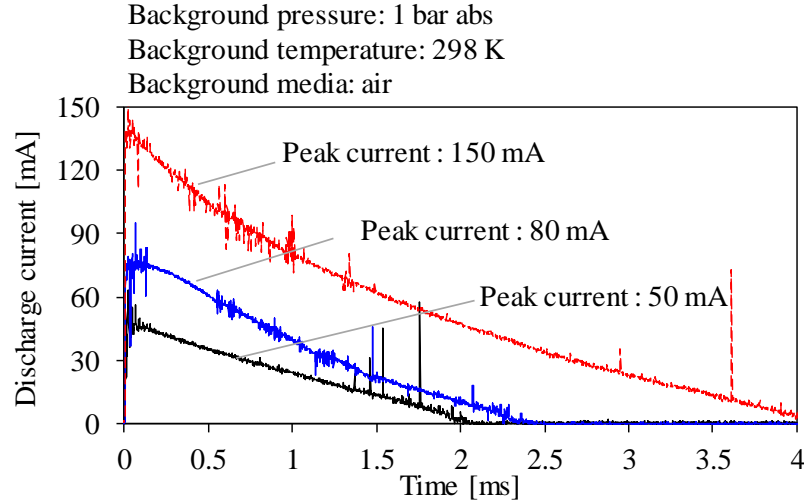


Figure 5-27 Spark discharge current waveforms with increased current levels

5.5.1 Spark discharge energy and discharge duration

The total spark discharge energy and discharge duration change with the increased spark discharge current. In order to compare the impact of the current level on the spark energy and duration, the normalized values are defined in 5-6 and 5-7.

$$\bar{E} = E_{total} / E_{total_quiescent} \quad 5-6$$

$$\bar{t}_{discharge} = t_{discharge} / t_{discharge_quiescent} \quad 5-7$$

Where E_{total} is the total spark discharge energy, $E_{total_quiescent}$ is the total spark discharge energy under quiescent conditions, and \bar{E} is the normalized spark discharge energy with respect to the spark energy under quiescent conditions. $t_{discharge}$ is the spark discharge duration, $t_{discharge_quiescent}$ is the spark discharge duration under quiescent conditions,

and $\bar{t}_{discharge}$ is the normalized spark discharge duration with respect to the duration under quiescent conditions.

The effects of air flow on the spark discharge energy and discharge duration from the three spark strategies are shown in Figure 5-28.

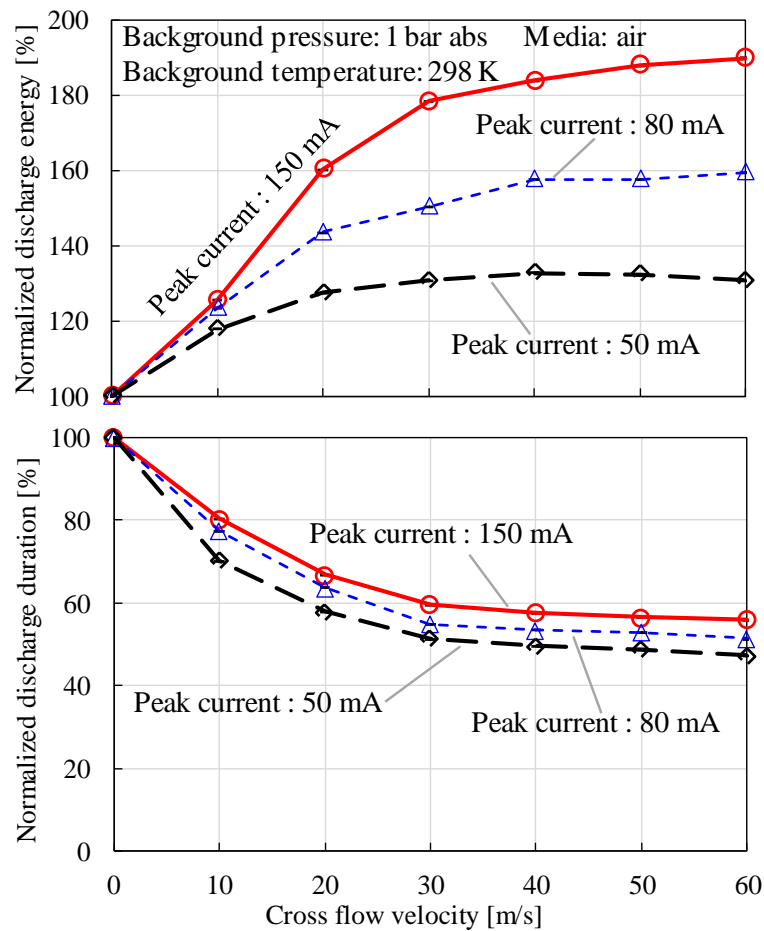


Figure 5-28 Effects of air flow velocity on spark discharge energy and duration with different discharge current levels

5.5.2 Short circuit and restrike frequency

The increase in spark discharge energy is more prominent with a higher discharge current level. As discussed in section 5.2, the increase in the spark gap voltage provides the potential for the increased discharge energy; however, the short circuit and restrike limit

the extendable range for the increase. Figure 5-29 reveals the impact of spark discharge current on the short circuit and restrike frequency. A lower short circuit and restrike frequency is observed with a higher spark discharge current level, which may have contributed to the greater gain in the spark discharge energy when a higher discharge current is available. The spark discharge duration consistently decreases with the increased flow velocity, with a lesser reduction when a higher discharge current is available. The lesser reduction in the spark discharge duration may also be a reason for the more significant spark energy gain with a higher discharge current.

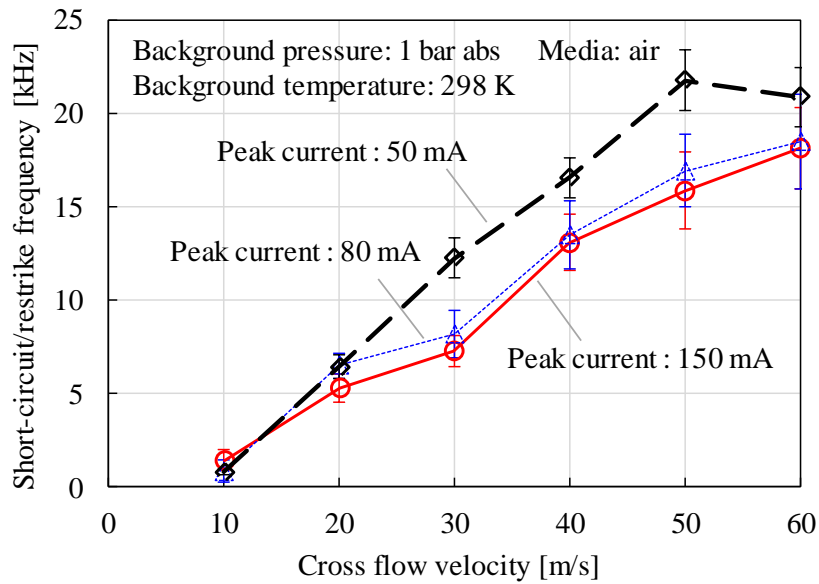
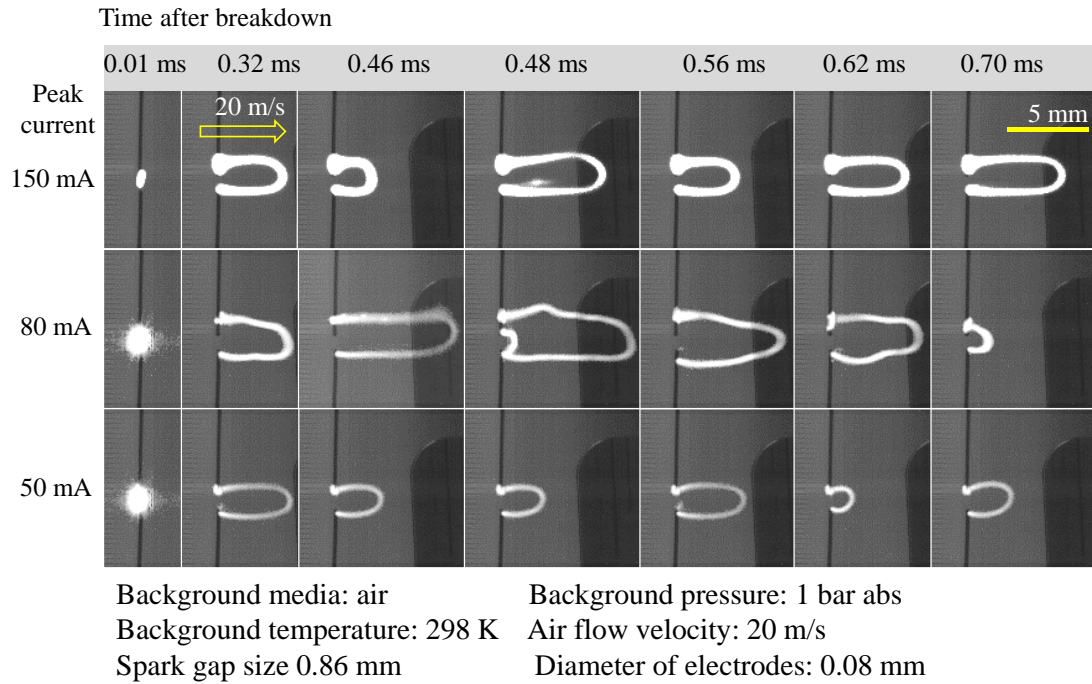


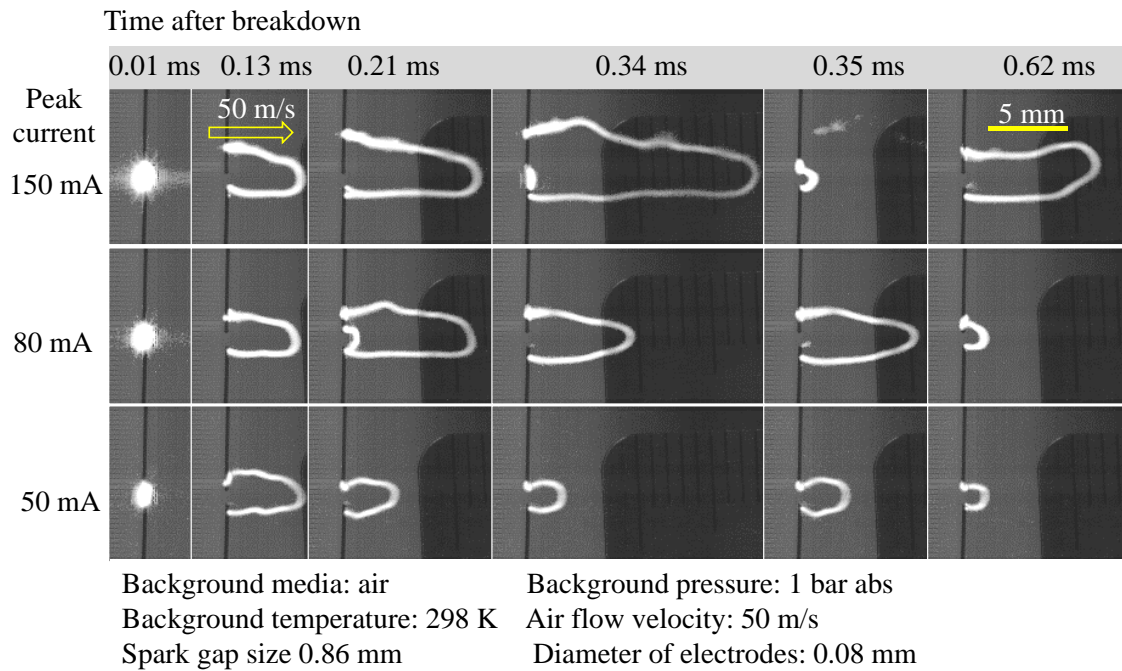
Figure 5-29 Short circuit and restrike frequency with different current level under varied cross-flow velocities

5.5.3 Plasma length and stretching rate

Under a 20 m/s air flow velocity, a longer plasma is observed under a medium spark discharge current level of 80 mA, as shown from the plasma images (Figure 5-30 (a)). The plasma in the 150 mA case is thicker as compared with the other two cases, yet the plasma is not the longest among the three cases. When the air flow velocity increases to 50 m/s, the highest spark discharge current level results in the longest plasma channel, as shown in Figure 5-30 (b).



(a) 20 m/s air flow velocity



(b) 50 m/s air flow velocity

Figure 5-30 Spark plasma images with different spark discharge current level under 20 m/s and 50 m/s air flow

The full process of plasma lengths under the 20 m/s and 50 m/s air flow conditions are plotted, as shown in Figure 5-31. Under an air flow velocity of 20 m/s, the plasma with the highest spark discharge current level is stretched at a slower rate along the timeline, i.e., the slope of the plasma length. The first fully developed plasma length of the 150 mA peak current case is also the shortest among the three, less than 10 mm.

However, when the air flow velocity increases to 50 m/s, the plasma with 150 mA peak discharge current achieves a maximum length of 36 mm, which is the longest among the three cases. The stretching rate is similar in the three cases under 50 m/s air flow, i.e., the slopes of plasma length increase appear identical in the three cases.

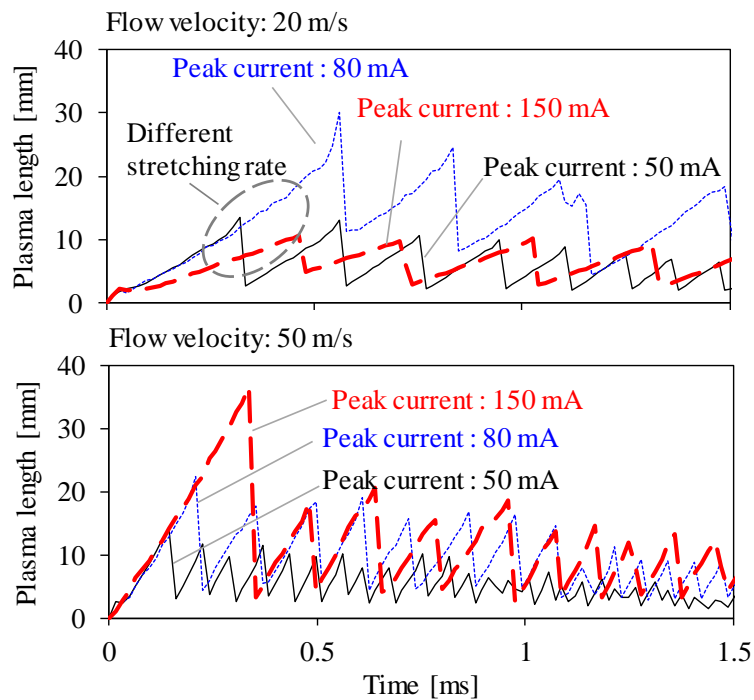


Figure 5-31 Plasma length under 20 m/s and 50 m/s air flow

The plasma stretching rate is calculated and summarized in Figure 5-32. The plasma stretching rate with the highest spark discharge current is lower in comparison to the other two cases when the air flow velocity is lower than 30 m/s. Overall, the stretching rate changes closely on par with the air flow velocity, regardless of the spark discharge current levels.

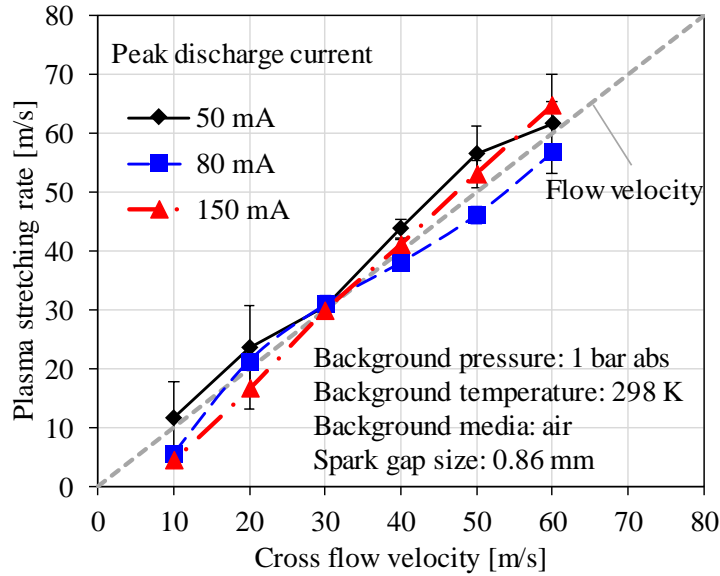


Figure 5-32 Plasma stretching rate at different spark discharge current levels

The maximum plasma length with the three discharge current levels is plotted in Figure 5-33. When the air flow velocity is lower than 40 m/s, the maximum plasma length from the 80 mA case is greater than that from the 150 mA case. When the air flow velocity exceeds 40 m/s, the maximum plasma length of the 150 mA case is the longest among the three peak current cases. The results suggest that a threshold flow velocity exists for the air flow to stretch the plasma channel to its full length. A higher spark discharge current requires a higher threshold velocity to effectively stretch the plasma. For instance, a threshold within 20-30 m/s for the cases of 50 mA and 80 mA; and within 40-50 m/s for the case of 150 mA.

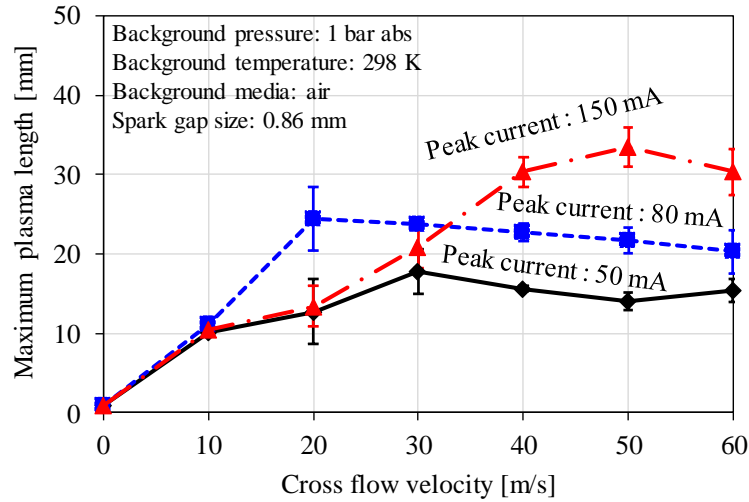


Figure 5-33 Maximum plasma length at different spark discharge current levels

5.6 Impact of air flow on the effective control of different ignition strategies

The impact of air flow on different ignition control strategies is reported in this section. The time scales of the spark discharge event of the ignition strategies are listed in Table 5-1.

Table 5-1 Time scale of the spark discharge events of different spark strategies

	Time scale
High-power	< 1 μ s during the high-power spark discharge
Transient high-current	<40 μ s during the transient high-current spark discharge
Multi-coil	> 0.1 ms
Boosted-current	>0.1 ms

5.6.1 High-power and transient high-current spark

The air flow velocity has minimal impact on the high-power and transient high-current spark discharge, as shown in Figure 5-34 and Figure 5-35. The high power and the transient high-current spark discharge occur in a short time duration, e.g., up to 1 μ s and 40 μ s respectively, which are magnitudes faster than the air flow velocity. For example, under 10 m/s air flow velocity, the conductive particles in the plasma channel can travel up to 0.01 mm during the high-power discharge event, and 0.4 mm during the transient high-current discharge event. The movement of the conductive particles with air is

negligible. Thus, no significant impact is observed on the discharge current and voltage waveforms.

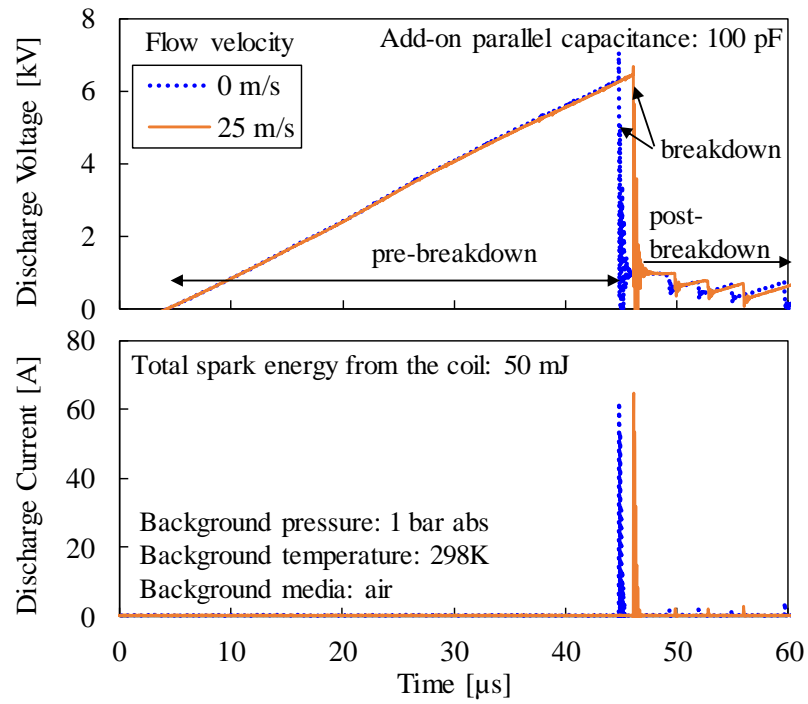


Figure 5-34 Electric waveforms of high-power spark under air flow conditions

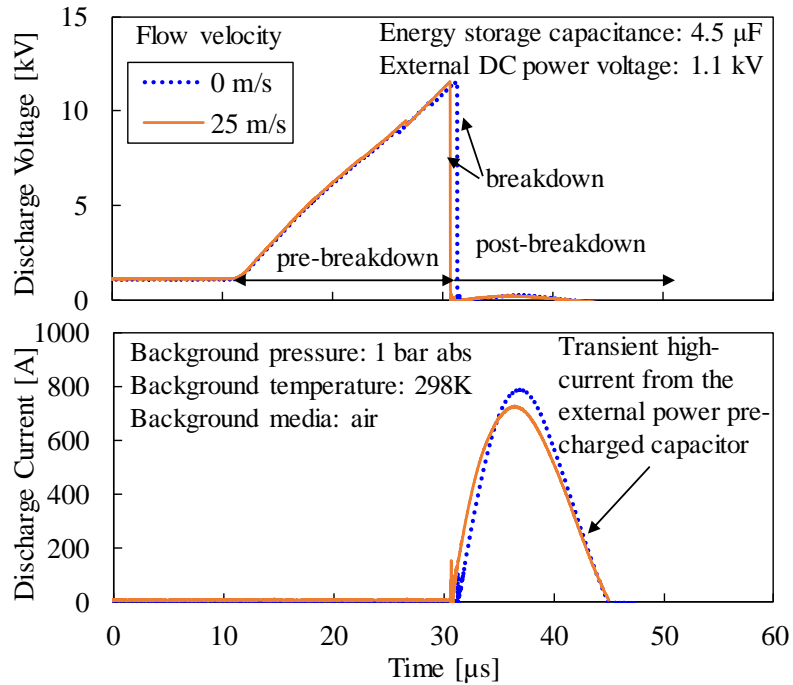


Figure 5-35 Electric waveforms of transient high-current spark discharge under air flow conditions

5.6.2 Multi-coil offset spark

The multi-coil simultaneous spark discharge resembles the spark discharge with a single-coil, albeit with a higher spark discharge current and discharge energy. The impact of air flow on the spark discharge process has been reported in section 5.2. In comparison, the impact of the air flow on the multi-coil spark discharge is more pronounced when the offset strategy is used, as shown in Figure 5-36. The spark discharge duration is progressively shortened pulse by pulse for each coil, due to the air flow effect.

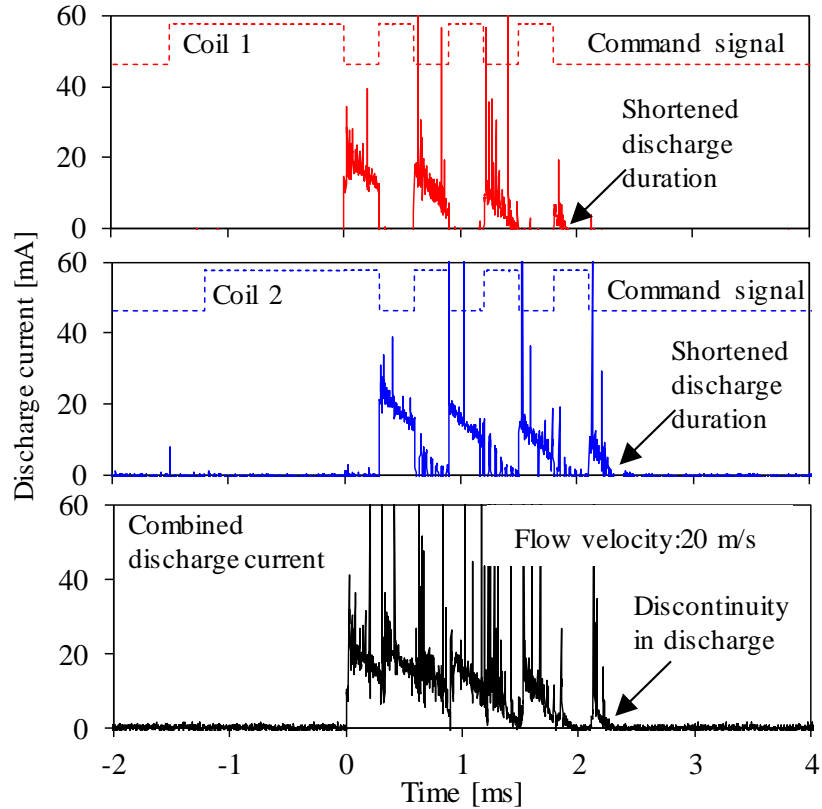


Figure 5-36 Effect of air flow on the dual-coil offset spark discharge

5.6.3 Boosted-current spark

The spark discharge process from the boosted-current ignition strategy is also affected by the air flow. During the spark discharge, the boosted current sets on when a pre-set voltage of the boosted-current module is higher than the voltage across the spark gap, as shown in Figure 5-37. Further details of the working principle of the boosted-current spark discharge have been explained in section 3.3.3.

Under air flow conditions, the spark gap voltage increases due to the stretch of the plasma channel, as shown in Figure 5-38. The spark gap voltage can increase to a value higher than the voltage of the boosted-current module. Adequately high module voltage is required to effectively enhance the plasma channel. Otherwise, the current cannot flow from the boosted-current module to the spark gap under this circumstance. The boosted-current spark discharge can only be resumed when the voltage across the spark gap drops to below

the voltage of the boosted-current module, as marked by shadows in Figure 5-38. Therefore, the boosted-current spark discharge may not be continuous.

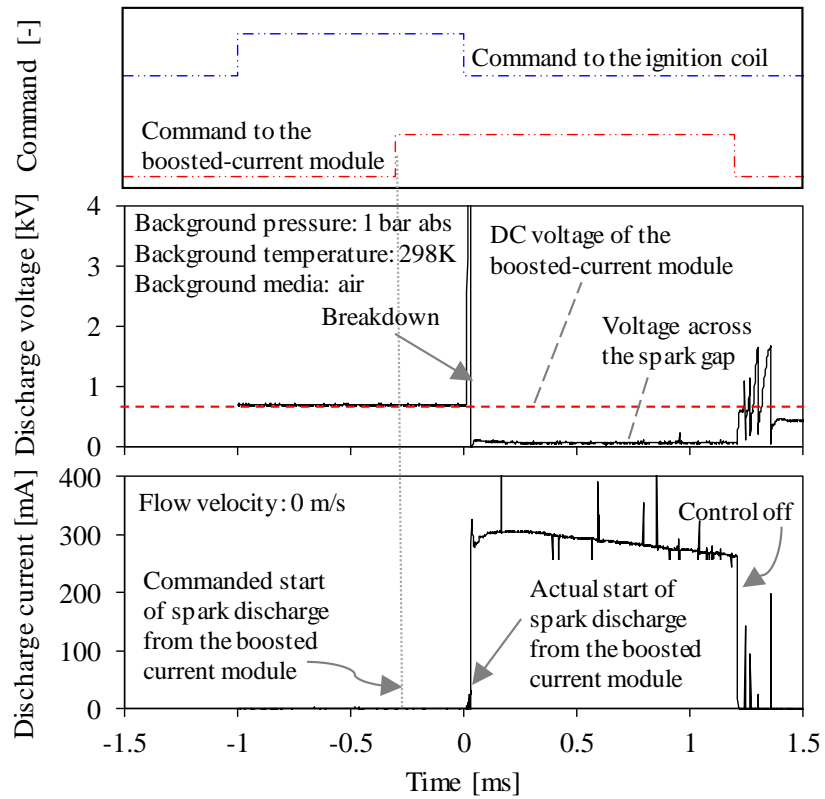


Figure 5-37 Spark discharge current and voltage waveforms of a boosted-current spark under quiescent conditions

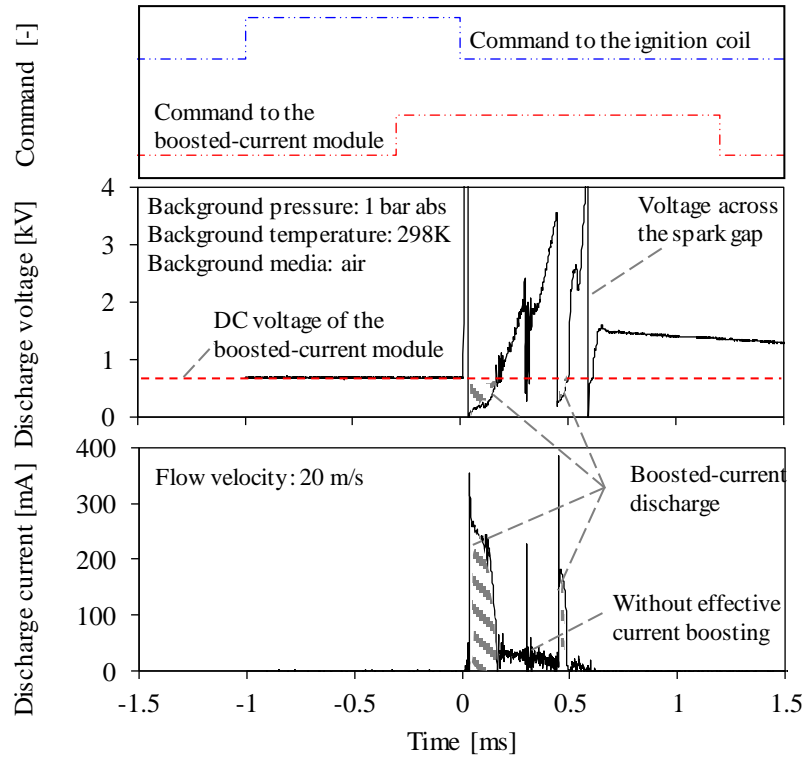


Figure 5-38 Spark discharge current of a boosted-current spark under 20 m/s air flow

A higher voltage in the boosted current module is helpful to maintain a continuous spark discharge under air flow conditions, as shown in Figure 5-39. Owing to the improved spark discharge process, the gain in discharge energy under air flow conditions is also higher when a higher external DC voltage is supplied, as shown in Figure 5-40.

Background pressure: 1 bar abs
 Background temperature: 298K
 Background media: air

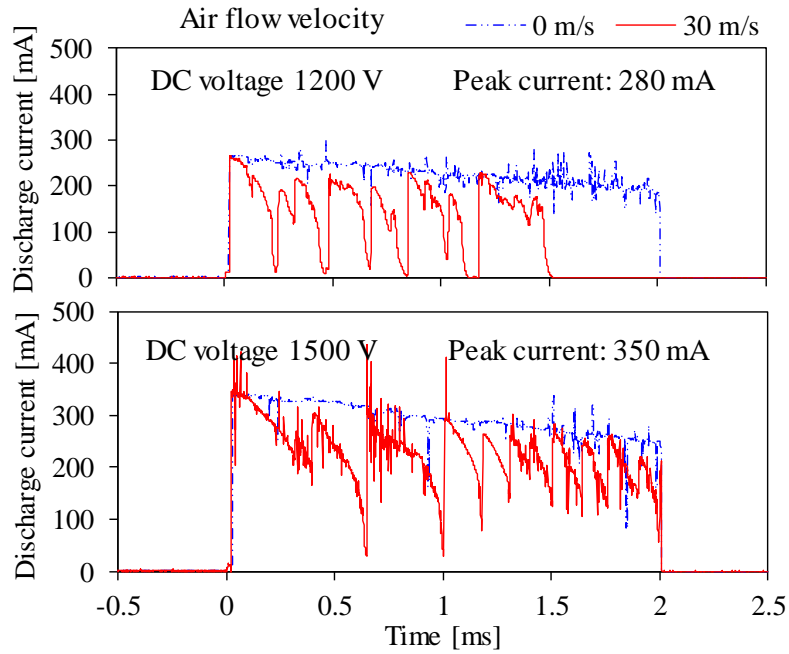


Figure 5-39 Improved spark discharge process of the boosted-current spark with a higher module voltage

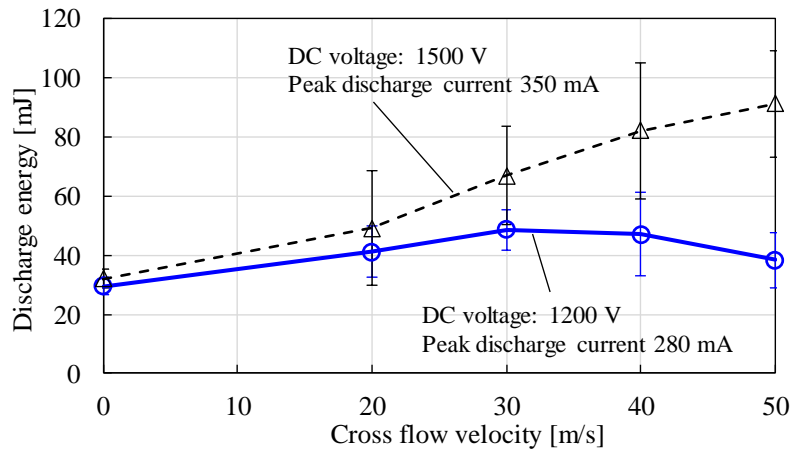


Figure 5-40 Effect of air flow velocity on the spark discharge energy of high-voltage current-boosting module

5.7 Chapter summary

The strength of air flow has a significant impact on the electric waveforms and the plasma channel development of spark discharge during the arc and glow phases; and insignificant impact on the onset of breakdown and capacitor energy release phases, irrespective of structural or add-on capacitors. The air flow commonly results in a longer plasma channel, which increases the plasma resistance. Consequently, a higher spark gap voltage, shorter spark discharge duration, and lower discharge current are observed under air flow conditions. The stretching rate, at which the plasma is elongated by the air flow, closely follows the air flow velocity. The maximum plasma length is related to the discharge current level and the air flow velocity. A larger spark gap size also results in a longer plasma with sufficient discharge voltage and energy. In addition, the short circuit and restrike phenomena are observed under air flow conditions. The frequency of short circuit and restrike increases with the air flow velocity. Under pressurized conditions, the plasma channel is straggled, appearing wandering along a ridge and twisted path.

CHAPTER 6 DIFFERENT IGNITION STRATEGIES ON FLAME KERNEL INITIATION UNDER GASEOUS MIXTURE FLOW CONDITIONS

In this chapter, experimental investigations are carried out to demonstrate the performance of the specifically devised ignition strategies for fuel-lean mixture ignition under controlled mixture flow conditions. The experiments are carried out in the constant volume combustion chamber with a background pressure of 4 bar abs and with gas flow velocities across the spark gap changing from 0 m/s to 35 m/s. Ignition strategies with modulated spark discharge parameters, such as the enhanced spark discharge power, the prolonged discharge duration, and the boosted discharge current, are deployed in the experiments. The spark discharge from a conventional inductive ignition coil is used as a reference for evaluating the performance of such ignition strategies. For simplicity, the combustible gaseous mixtures are referred to as “gas” in the following sections of this chapter.

6.1 Effects of gas flow on flame kernel initiation

The gas motion is deemed critical for the combustion process because of its significance in speeding up the flame propagation. An exemplary case in Figure 6-1 illustrates how gas motion can accelerate the flame propagation, and the pressure increase, during the combustion process. However, in order to benefit from the faster combustion process, the difficulties in the ignition process should be tackled first.

The effects of the gas motion on the ignition process are complex, as shown in Figure 6-2. The combustion is initiated by forming a flame kernel around the spark plasma. The spark discharge energy is transferred to this small volume of the combustible mixture. The chemical energy contained in the fuel molecules is released as the exothermic reaction proceeds. Both the spark discharge energy and the chemical reaction energy of the fuel contribute to the energy required to sustain the flame kernel. More ignition energy is required for lean or diluted mixtures, because less chemical energy is provided by the lean or diluted mixtures. The flame kernel lights up the adjacent unburnt zone when the flame

front propagates toward the remaining unburnt zone. Sufficient exothermic energy is required in the flame front to maintain the desired temperature for the chemical reaction during the flame propagation.

When the ignition is subjected to high-velocity gas flows, the flame kernel formation becomes more difficult. However, the flame surface area increases due to the turbulence interaction, resulting in greater reactive surface areas and enhanced heat transfer between the burnt and the unburnt zones. The larger flame surface area can enhance flame propagation if the energy released from the burning zone is sufficient. Notwithstanding, if the energy released from the burnt zone is insufficient, the larger flame area results in excessive heat loss that eventually leads to a misfired case.

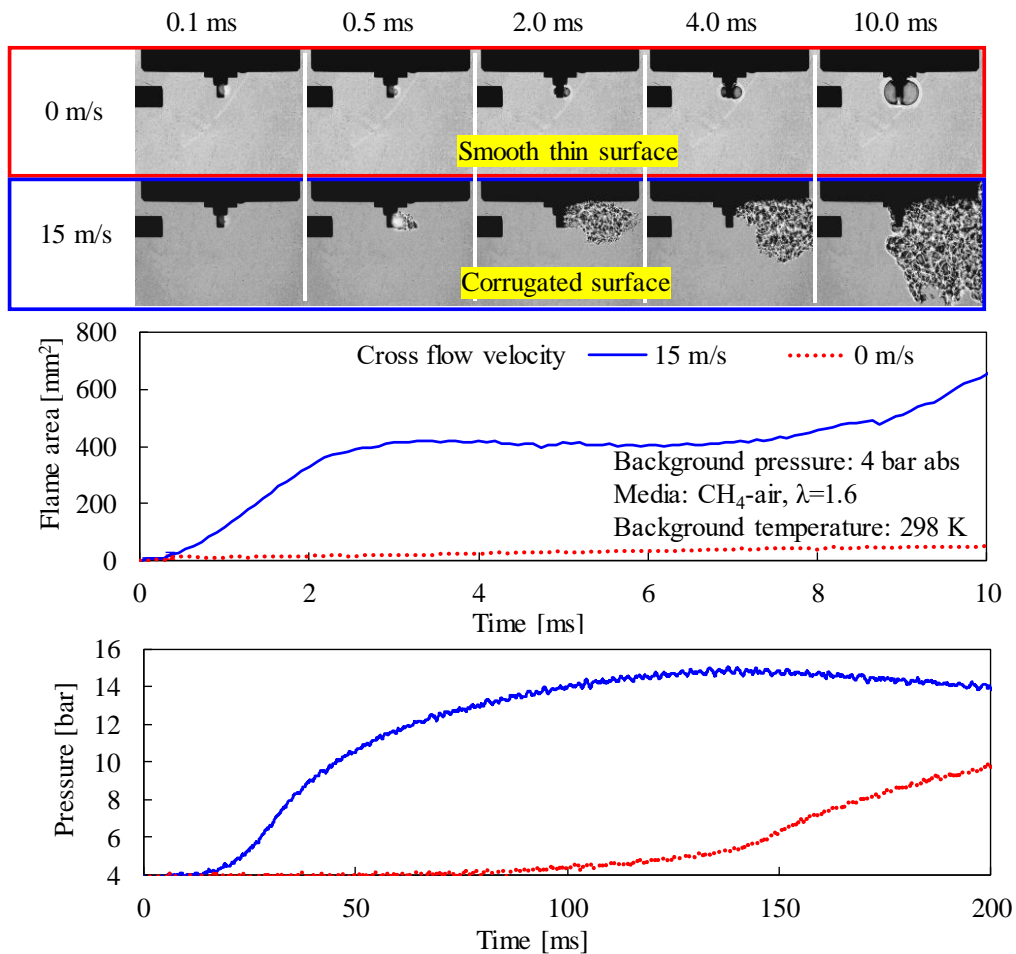


Figure 6-1 Demonstration of enhanced flame propagation by gas motion

Another impact of the gas motion is the stretch of the plasma passage by the gas flow. As the plasma channel bends extensively away from the spark gap, the heat loss of plasma to the electrodes reduces, which is beneficial to succeed ignition. The stretch of the plasma also increases the plasma access region of the combustible mixture. Consequently, a larger flame kernel can be formed. However, contrary to these beneficial effects, the gas flow reduces the specific heating intensity against the heat transfer loss to the mixture prior to forming a sustainable flame kernel. The heat transfer between the flame kernel and the flowing gas increases with the increased gas flow velocity.

For sufficiently strong cross-flow, the early flame region can drift away from the electrodes, appearing like moving at approximately the same velocity as the gas stream. The convection heat transfer between the flame kernel and cold gas stream is less significant under this scenario. However, the flame kernel and early flame is still subjected to the diffusion heat transfer caused by the turbulence [134].

Impacts of flow on the plasma channel

- Prolonged plasma channel
 - Reduced heat transfer loss to the electrodes
 - Increased area for mixture reaction and energy transfer to the combustible gas
- Restrike or short circuit of the plasma
 - Interruption to the energy transfer from the plasma to combustible mixture
 - Possible multiple flame kernels

Impacts of flow on the flame kernel

- Continuous supply of fresh gas
- Drifting of the early flame with flow
- Enlarged flame surface area due to the wrinkles caused by the turbulence
- Enhanced heat transfer from the burnt to the unburnt zone

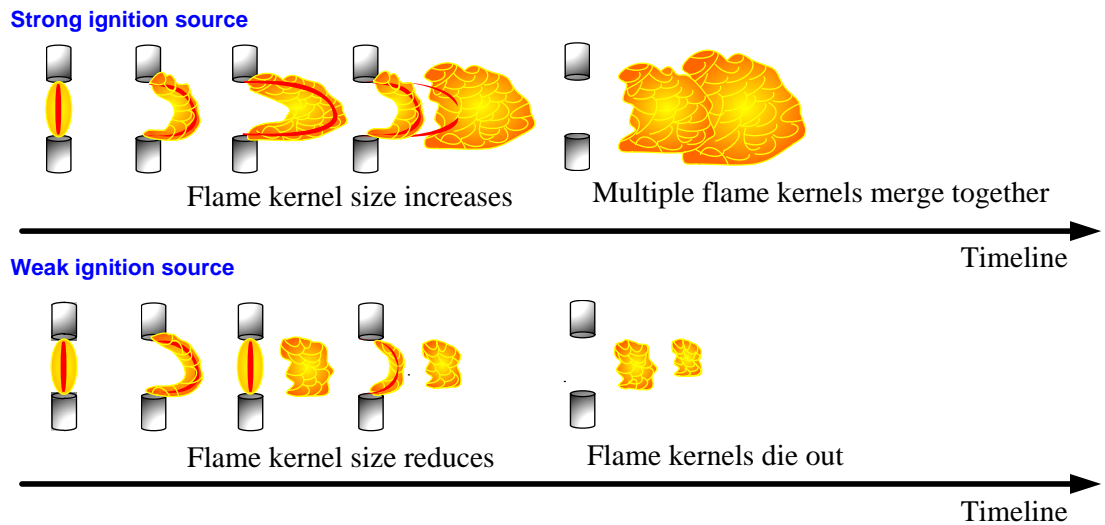


Figure 6-2 Effects of gas flow on spark plasma and flame kernel

The flame kernel formation under quiescent and gas flow conditions are compared in Figure 6-3. The same spark strategy from a conventional inductive coil is used in the two cases, with a peak spark discharge current during the arc and glow phases of around 100 mA, spark duration of about 0.8 ms and 0.5 ms under quiescent and 20 m/s cross flow, respectively.

An approximate spherical flame front progressively propagates outward from the spark gap under quiescent conditions. Under gas flow conditions, the flame kernel forms along the

stretched plasma channel, which is away from the spark gap. Meanwhile, the turbulence effect results in more wrinkles to the flame. The flame kernel grows and expands in the flow field. The flame kernel under gas flow conditions grows larger as compared with the flame kernel formed under quiescent conditions within the same time frame. The quicker flame kernel growth is beneficial for the flame development.

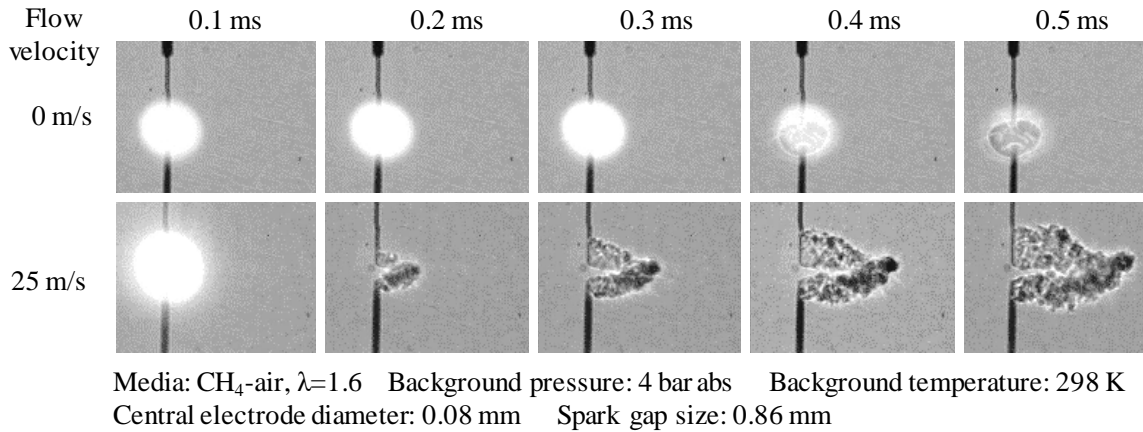


Figure 6-3 Flame kernel formation under quiescent and gas flow conditions

From the analysis of the gas flow impact on the ignition process, with faster gas flow velocity, a shorter time may be required to stretch the plasma channel to the maximum length. More fresh combustible gaseous mixtures can be in contact with the high-temperature ignition source. Consequently, it should take a shorter time to generate a larger flame kernel. However, the excessive gas flow velocity can be detrimental to the flame kernel growth. Figure 6-4 is a demonstration of the gas flow effects on the flame kernel initiation under various air-fuel ratios. The ignition source in these experiments is a spark plasma formed by a conventional inductive coil ignition system, with spark discharge energy around 30 mJ that produces a duration of 3 ms under such quiescent conditions.

The top plot is the $t_{50\%MFB}$ estimated from the combustion pressure trace, as explained in section 3.4.2. The general trend from the combustion of both lean and stoichiometric mixture is that a faster flame propagation speed can be achieved with a higher gas flow velocity, on the condition that the gas flow velocity is within an appropriate range. For the

stoichiometric mixture, the trend persists throughout the tested velocity range of 5 m/s to 35 m/s. However, for the lean mixtures, it is difficult for the flame kernel or early flame to survive under higher gas flow velocities. The shadowgraph images shown at the bottom demonstrate the change in the flame area under 15 m/s flow velocity. For the lean mixture with an excess air ratio of 1.8, though a flame kernel is formed after the spark discharge, it fails to develop into a self-sustained flame kernel under the gas flow conditions.

The lean mixtures have slower flame speed in comparison to that of the stoichiometric mixture so that they need a stronger gas motion to promote the flame propagation. However, the weak flame kernel of a lean mixture makes it a challenging situation for the flame to propagate under strong gas flow. A stronger flame kernel is critical for a successful ignition. The ignition strategy is of great importance to assist the survival of the flame kernel under this circumstance.

The impact of different ignition strategies on the flame kernel growth under flow conditions will be discussed in detail in the following sections.

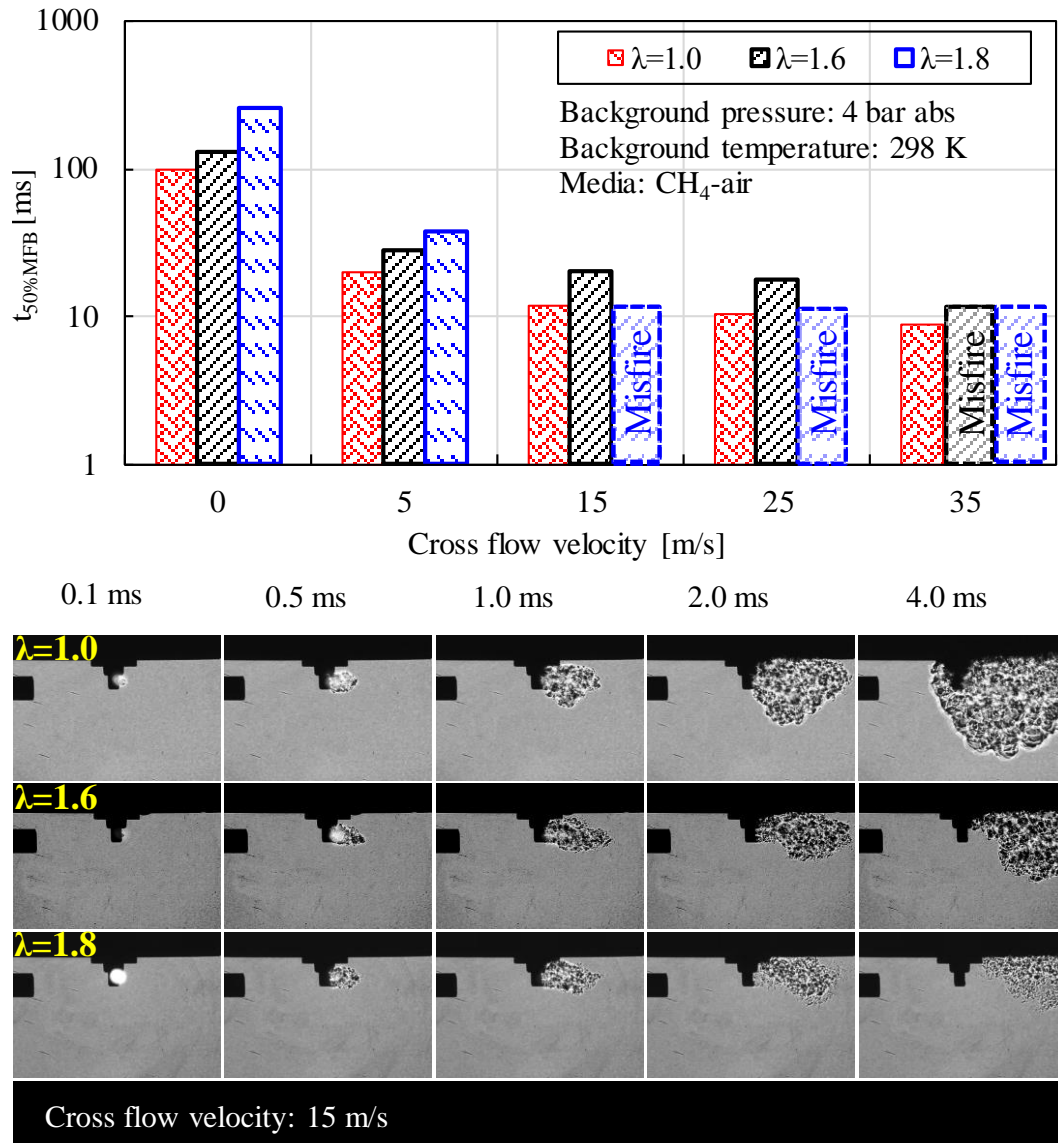


Figure 6-4 Effects of cross-flow velocity on the combustion of lean mixtures

6.2 Effects of enhanced breakdown power on flame kernel initiation

The same high-power ignition strategy as reported in section 4.2 is applied for ignition under gas flow conditions. As discussed in chapter 5, the breakdown phase, along with the capacitor energy release phase, is affected marginally by the gas flow due to the significant difference in their time scales. Hereby, the effects of the gas flow velocity on the high-power spark discharge during the arc and glow phases are shown in Figure 6-5.

When the total spark discharge from the secondary ignition coil is kept constant, the addition of a parallel capacitor allocates more energy to the breakdown phase. As a result, less energy is reserved for the arc and glow phases. Both the gas flow and the added parallel capacitance contribute to the decrease of the spark discharge duration during the arc and glow phases.

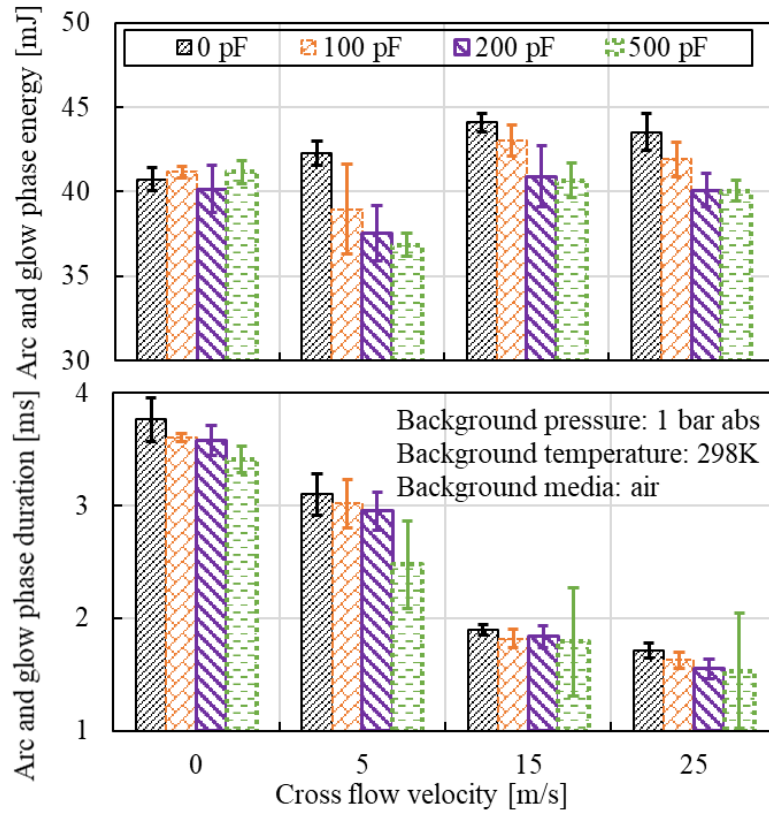


Figure 6-5 Effect of cross-flow velocity on the high-power spark ignition strategy during the arc and glow phases

6.2.1 High-power spark with air as background media

The shadowgraph images of the plasma channel are recorded to show the interactions between the gas flow and the high-power spark (Figure 6-6). The background media is air, so the density gradient purely results from the high-temperature plasma channel. The high-temperature plasma is stretched away from the spark gap. It drifts with the gas flow. Under quiescent conditions, the high-power spark discharge can enhance the turbulence near the

spark gap and expand the high-temperature area. However, the phenomena are not observed under a gas flow velocity of 25 m/s. The flow field enhances the turbulence level, especially during the arc and glow phase discharge, which overshadows the breakdown-enhanced turbulence. Moreover, the increased parallel capacitance shortens the spark discharge duration during the arc and glow phases, which shortens the occurrence of the high-temperature field generated from the spark plasma. The shortened arc and glow spark discharge duration due to the added parallel capacitance may be unfavorable for the flame kernel development.

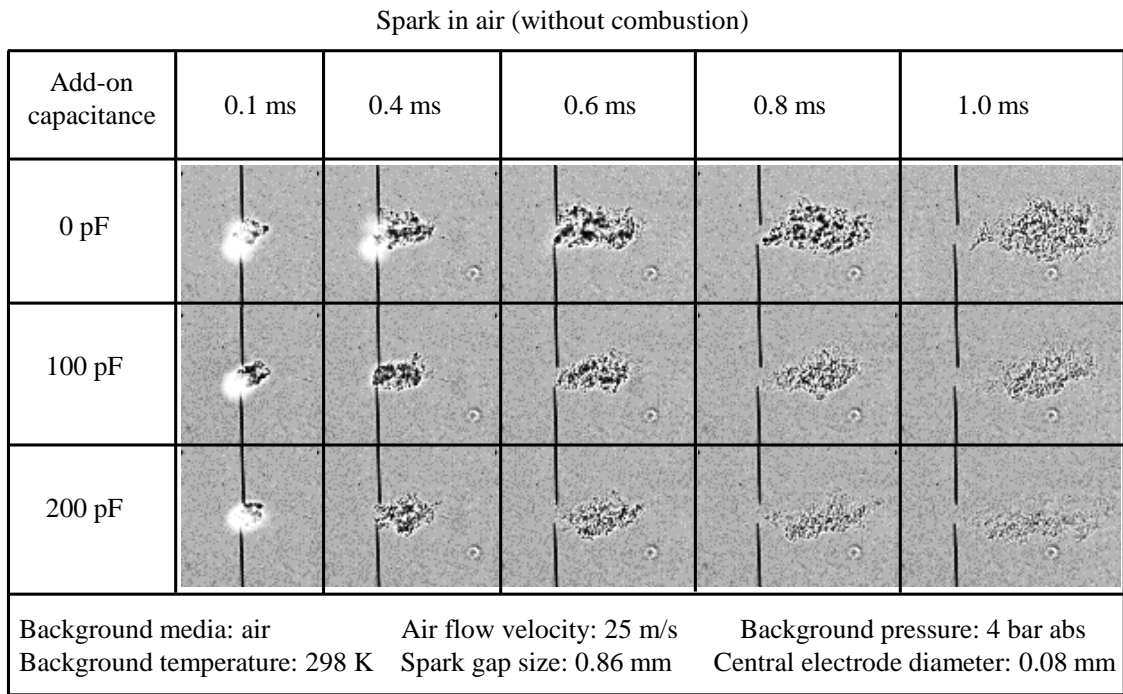


Figure 6-6 Shadowgraph images of the thermal-induced density field by the high-power spark in air under 25 m/s air flow

6.2.2 Impact of high-power spark on ignition of lean mixtures

The combustion test results are shown in Figure 6-7, with the cross-flow velocity of 25 m/s. The experiments are carried out in the optical constant volume chamber shown in Figure 3-2. Methane-air mixture with an excess air ratio of $\lambda=1.6$ is used as both the background gas and flowing gas. The total spark discharge energy in this set of experiments

is controlled at 50 mJ, with different ratios of the energy delivered to the breakdown phase by changing the capacitance levels. The spark energy is supplied by an inductive ignition coil with a charging duration of 4 ms.

The flame kernel that originates from the high-power spark discharge struggles to survive under the gas flow condition. The add-on parallel capacitance enhances the breakdown power at the cost of reduced arc and glow phase energy and duration, which negatively affects the flame kernel development. The benefit of the transient high discharge power is minimal.

The flame area calculated from the shadowgraph images is shown in Figure 6-8. When 200 pF parallel capacitance is used, the flame area demonstrates a declining trend from 4 ms to about 1.7 ms after the ignition. Thereafter, the flame area increases. The reduced flame area is because of the detachment of the flame kernel from the spark plug and the drifting of the flame in the gas flow field. The flame cannot be captured by the shadowgraph images when the flame drifts out of the viewports of the optical window. The flame kernel manages to grow when it travels to some downstream locations and propagates back to the visible region, as can be seen from the increasing flame area after 17 ms. The decrease in the flame area suggests poor sustainability of the flame kernel when the added parallel capacitance is high. The flame area at 5 ms after the breakdown event is used as an indicator to show the sustainability of the flame kernel for further analysis.

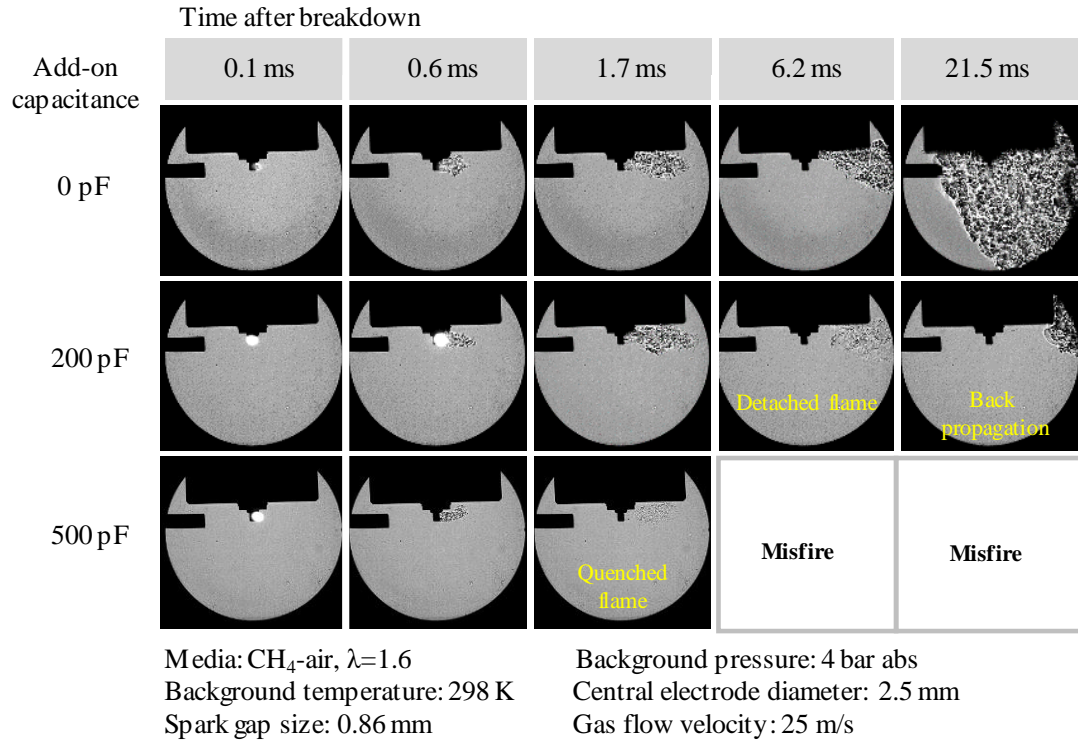


Figure 6-7 Shadowgraph images of flame propagation under 25 m/s gas flow with the high-power spark

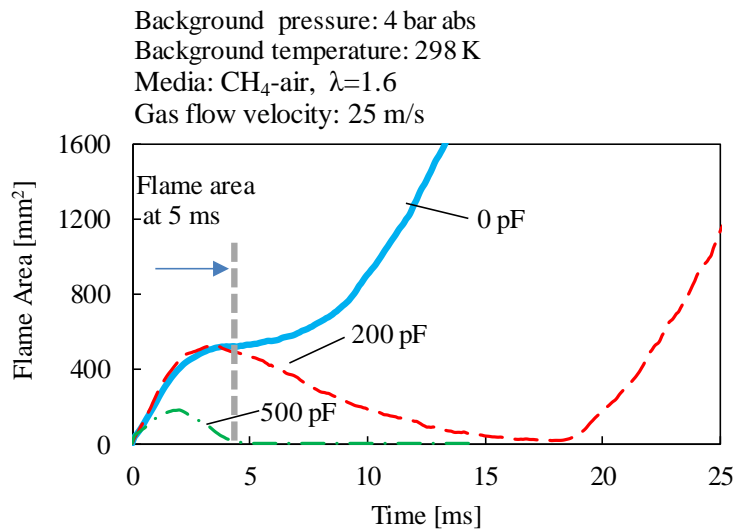


Figure 6-8 Flame area with the high-power spark under 25 m/s gas flow

Four different gas flow velocities, 0 m/s, 5 m/s, 10 m/s, and 25 m/s, are tested to identify the operational boundary of the high-power spark under gas flow conditions. A total spark

energy of 50 mJ is used in the experiments. The same combustion chamber test platform and the same spark strategies are used in the experiments.

The flame areas at 5 ms after the breakdown event in the experiments are shown in Figure 6-9 under the present setup. The high-power spark performs better than the conventional spark when the gas flow velocity is less than 5 m/s. Within this low velocity range, the flame area at 5 ms after the breakdown event increases with the increased parallel capacitance. When the gas flow velocity is increased to 10 m/s, the advantage disappears for the high-power spark with 500 pF parallel capacitance. Misfire cases occur for the 500 pF case when the gas flow velocity is further increased to 25 m/s. The fastest flame propagation speed is observed under a gas flow velocity of 10 m/s for all three capacitance levels. Further increasing the gas flow velocity to 25 m/s reduces the early flame kernel size. The 50 mJ spark energy may not be sufficient to support the flame kernel growth under a 25 m/s gas flow velocity.

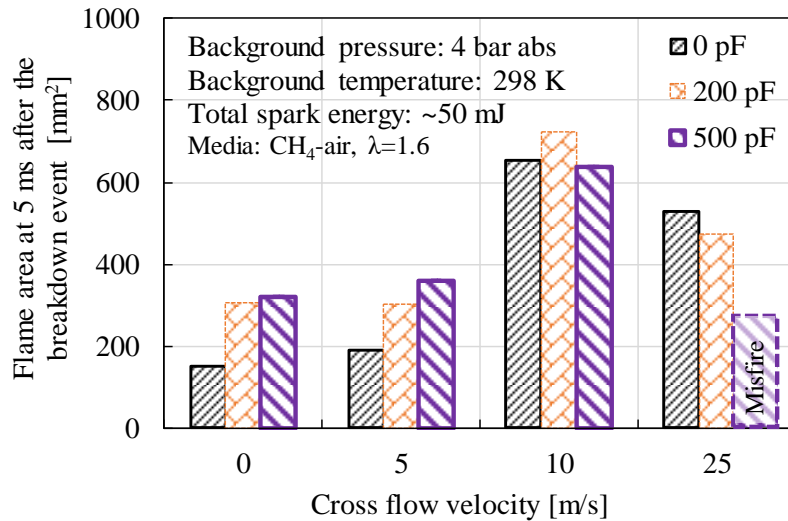


Figure 6-9 Flame area at 5 ms after the breakdown event with the high-power spark under varied cross-flow velocities

To summarize, under the selected experimental conditions, the added parallel capacitance is beneficial for the flame kernel development when the gas flow velocity is below 10 m/s.

However, the high-power spark results in a shorter discharge duration, which adversely affects the ignition process with the enhanced gas flow.

6.3 Effects of transient high-current spark on flame kernel initiation

The measurement results demonstrate that the transient high-current spark has demonstrated strong ignition ability under quiescent conditions. The larger region is produced by the high-current discharge of the large capacitor, as discussed in chapter 4. The performance of the transient high-current spark under gas flow conditions is investigated in this section.

6.3.1 Transient high-current spark with air as background media

First, the density field induced by the transient high-current spark is observed with air as the background media. The high-current surge occurs 2~3 μs after the breakdown event and continues for about 15 μs . The discharge current and voltage waveforms during the transient high-current spark event are shown in Figure 6-10. The spark energy and peak spark current are adjusted by changing the voltage of the DC power supply that charges the energy storage capacitor. The energy delivered from the energy storage capacitor is marked in Figure 6-10. The energy released from the ignition coil in the three cases is about 50 mJ.

The shadowgraph images of the thermal-induced density field are shown in Figure 6-11. The experiments are carried out in the optical combustion chamber under controlled air flow conditions. Even though the thermal impact of the transient high-current spark discharge is also observed under air flow conditions, it is not as profound as that under quiescent conditions.

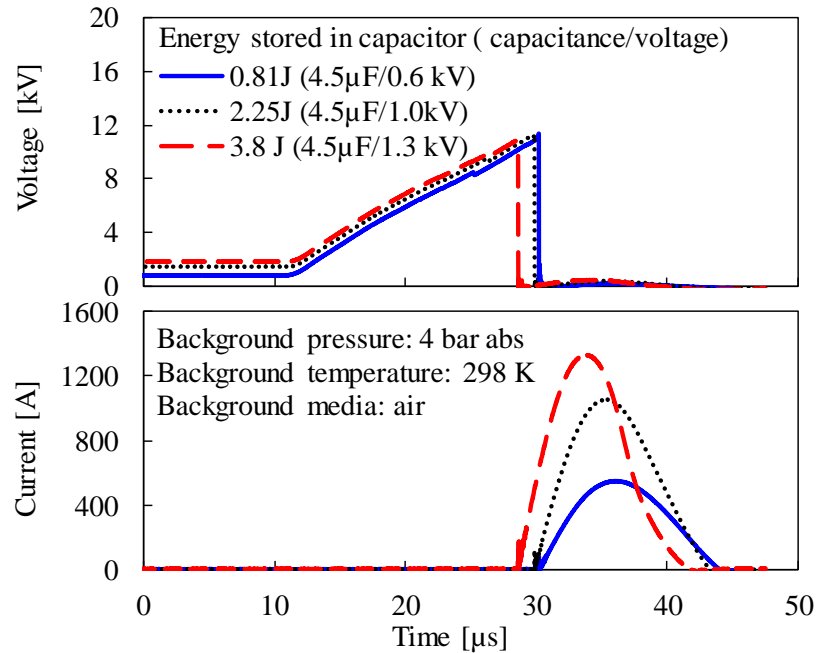


Figure 6-10 Current and voltage waveforms of transient high-current spark

In Figure 6-11, the illumination of the ions resulting from the spark discharge current surge can be observed at 0.02 ms after the breakdown event. The hot plasma-induced high-temperature areas are much larger with the transient high-current spark discharge as compared with that of a conventional spark discharge. The thermal impact persists in the later stage of the spark discharge after the transient high-current spark discharge finishes, as can be seen from the larger high-temperature area in the photos taken at 0.4 ms, 0.6 ms, 0.8 ms, and 1.0 ms after the breakdown event. However, within the range of this investigation, the gas flow effect still dominates during the spark discharge process. Consequently, the difference between the plasma size from a conventional spark and a transient high-current spark is not as significant as that under quiescent conditions.

Spark in air (without combustion)

Case	Capacitance (μF)	DC voltage (kV)	Peak spark current (A)	Energy from transient high-current (mJ)	Energy from the coil (mJ)
1	0	0	0.05	0	50
2	4.5	0.6	550	810	50
3	4.5	1.3	1250	3800	50

Time after breakdown

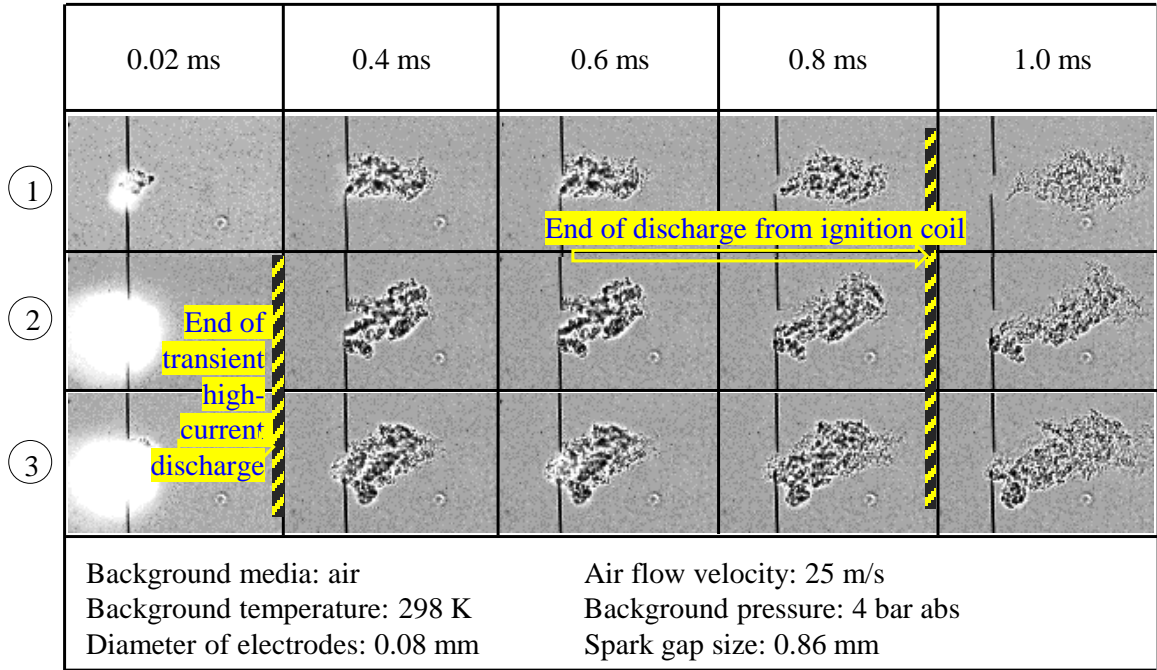


Figure 6-11 Shadowgraph images of the thermal-induced density field by the transient high-current spark discharge in air under 25 m/s air flow

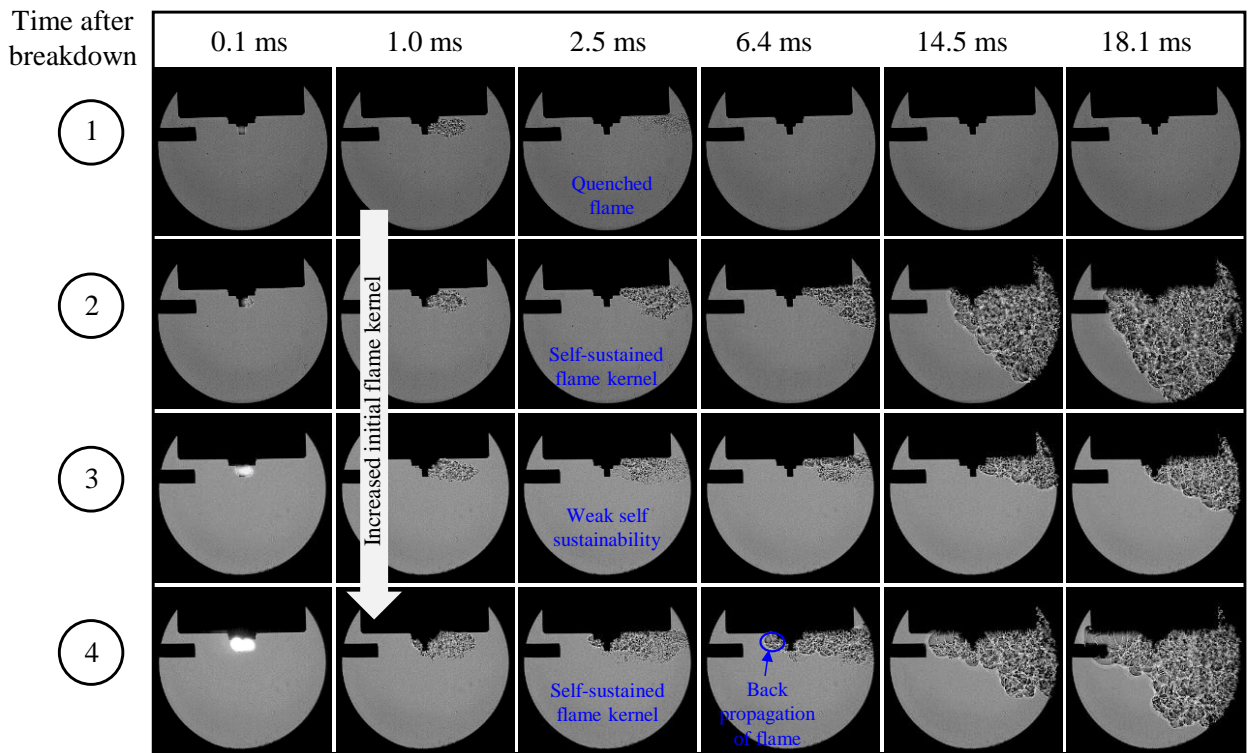
6.3.2 Impact of transient high-current spark on ignition of lean mixtures

Additional experiments demonstrate that the ignition advantage of the transient high-current spark is impaired under flow conditions. The experiments are conducted on the optical chamber under a controlled gas flow velocity of 25 m/s. Methane-air mixture with an excess air ratio of $\lambda=1.6$ is used as both the background gas and flowing gas. Two transient high-current spark discharge cases are compared, listed as case 3 and case 4 in the table shown Figure 6-12. These two cases have a peak discharge current level of 500 A and

1300 A respectively. The transient high-current spark discharge is released once the plasma channel is formed by the ignition coil. To focus on the impact of the transient high-current spark discharge while minimizing the impact of the spark discharge from the ignition coil, the charging duration of the coil is intentionally reduced to a minimum value. The coil can provide enough energy to ensure the breakdown event, yet the spark is not able to ignite the mixture under this condition. The spark discharge energy from the ignition coil is about 10 mJ and the discharge duration is about 0.5 ms, listed as case 1 in the table of Figure 6-12. A conventional spark event with regular spark energy (~50 mJ) is set up as a reference case, listed as case 2. The spark in case 2 has higher discharge energy and longer discharge duration as compared with the spark in case 1. Nevertheless, the energy level and peak spark discharge current in case 2 is significantly lower than that from a transient high-current discharge.

Spark parameters in the experiments

Case No.	Coil energy (mJ)	External capacitor Energy (mJ)	Total discharge duration (ms)	External DC voltage (V)	Peak current (A)	Remarks
1	10	0	0.5	0	0.04	Normal spark
2	50	0	1.1	0	0.08	Normal spark long duration
3	10	810	0.5	600	500	Transient high current spark
4	10	3800	0.5	1300	1250	Transient high current spark



Media: CH₄-air @ $\lambda=1.6$ Background pressure: 4 bar abs Gas flow velocity: 25 m/s
 Background temperature: 298 K Central electrode diameter: 2.5 mm Spark gap size: 0.86 mm

Figure 6-12 Shadowgraph images of flame propagation under 25 m/s gas flow with the transient high-current spark

The ignition energy in case 1 is too low for a successful ignition. The comparison is mainly among cases 2, 3, and 4. The initial flame kernel from the transient high-current spark is larger than that from a conventional spark, as can be seen from the images taken at 1.0 ms after the breakdown event. Though the peak current in case 3 is as high as 500 A, the size of the flame kernel decreases after the initial 2.5 ms. It eventually ignites the mixture successfully, yet at a lower speed. When the spark discharge current is further increased to 1300 A in case 4, the flame can even propagate towards the upstream of the spark plug, suggesting strong self-sustainability of the flame. The flame area in case 2 continuously increases with time, which leads to a self-sustained flame.

The history of the flame area development is shown in Figure 6-13. As the spark discharge durations in the four cases are different (case 2 finishes at 1.1 ms while the other three cases finish at 0.5 ms), the flame areas at the end of spark discharge in each case are marked with a star. The flame area at the end of the spark discharge can represent the combustion performance in the later stage. A larger flame kernel at the end of the spark discharge results in faster flame propagation.

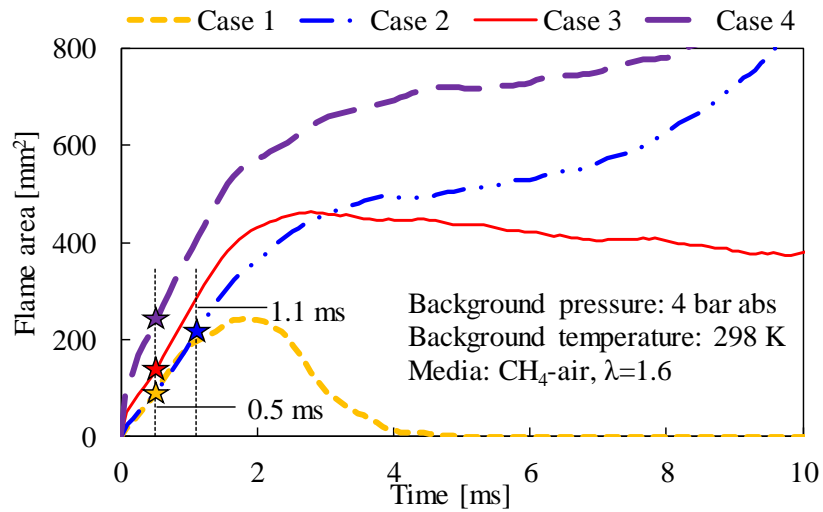


Figure 6-13 Flame area with the transient high-current spark under 25 m/s gas flow

6.3.3 Energy release profile on ignition of lean mixtures

From the above cases of study, the spark discharge energy amount alone cannot decide the ignition performance. Another set of combustion experiments are carried out to study the impact of the energy release patterns on the early flame kernel formation in detail.

A long-duration spark realized by the multi-coil offset spark ignition strategy is applied as a reference case in this comparison. The ignition hardware and control parameters of the two spark strategies are listed in Table 6-1. The spark discharge current and voltage waveforms are shown in Figure 6-14 and Figure 6-15, respectively. For the transient high-current spark discharge, the axis is adjusted to show only the transient high-current part. The actual spark discharge event includes the discharge from the ignition coil, which has a much lower discharge current and a longer discharge duration. The spark gap is formed by a pair of thin needle-electrodes to limit the impact of the electrode shape on the flame kernel development. The thin needle-electrodes also reduce the heat transfer loss to the electrodes.

The energy delivered to the spark gap from both ignition strategies is similar in this comparison, about 140 mJ. The transient high-current spark has a peak current of 140 A. The spark discharge duration of the transient high-current spark is about 20 μ s and the spark discharge from the ignition coil continues for about 0.3 ms under 25 m/s gas flow. The long-duration spark has an average current level of about 100 mA. The peak current during the arc and glow phases can reach about 200 mA. In order to generate similar discharge energy as compared with the transient high-current spark, the discharge duration of the long-duration spark ignition strategy is controlled at 1.17 ms.

External energy storage capacitance (μF)	1.5	Spark energy discharged from the transient high-current module (mJ)	128
DC supply voltage (kV)	0.4	Spark energy discharged from the coil (mJ)	10
Peak spark current (A)	140	Total discharge energy (mJ)	138
Coil discharge duration (ms)	0.3	Transient high-current discharge duration (ms)	0.02

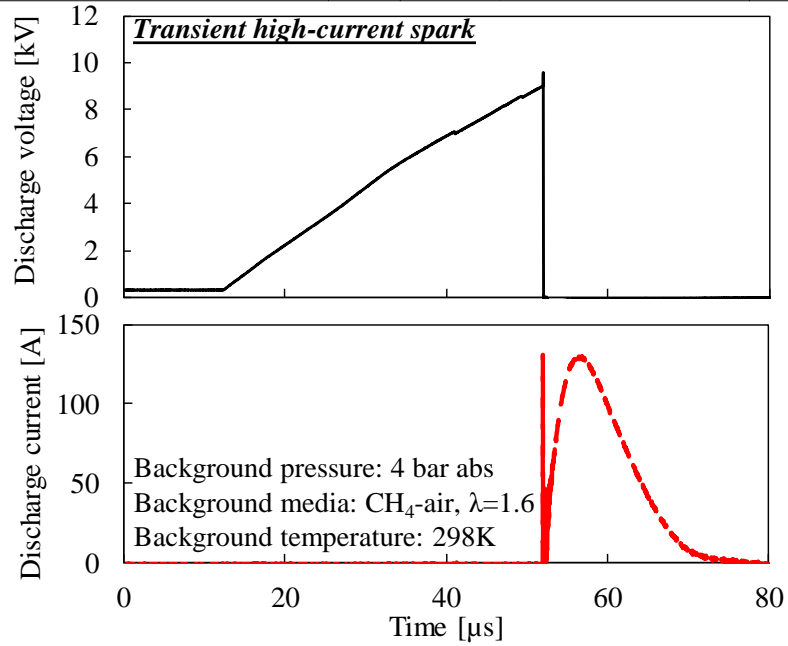


Figure 6-14 Spark discharge current and voltage waveforms of the transient high-current spark discharge

Number of coils	2	Coil discharge duration (ms)	1.17
Peak spark current (mA)	200	Total discharge energy (mJ)	140

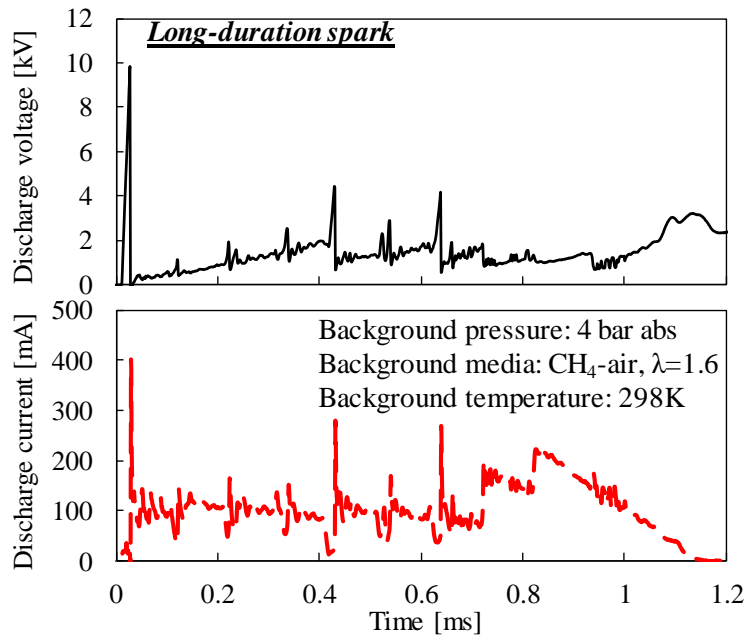


Figure 6-15 Current and voltage waveforms of the long-duration spark discharge

The effectiveness of each of the above two spark strategies is further investigated under various gas flow velocities, from 5 m/s to 35 m/s. The flame kernel and early flame development under a 35 m/s gas flow velocity are shown in the shadowgraph images in Figure 6-16. The images demonstrate the flame kernel development in the first 1.2 ms after the breakdown event. The initial flame kernel of the transient high-current spark discharge strategy is larger than that of the long-duration spark discharge strategy for the first 0.3 ms before the spark discharge finishes in the transient high-current spark. However, the flame kernel initiated by the transient high-current spark gradually becomes weaker. Eventually, the flame diminishes at around 1.2 ms. In contrast, the long-duration spark initiates a smaller flame kernel that keeps increasing in size. By the time the long-duration spark discharge finishes (1.17 ms after the breakdown event), the flame kernel size is significantly larger than the flame kernel initiated by the transient high-current spark discharge. The long-duration spark shows an obvious advantage over the transient high-current spark with a similar energy level in this comparison. Though the transient high-current spark can

initiate a comparatively larger initial flame kernel, the flame kernel is not large enough to release adequate chemical energy to compensate for the heat transfer to the flowing gas. In contrast, it takes a longer time to release the spark discharge energy from the long-duration spark to ignite the combustible mixture. During this time interval, a larger volume of combustible gas is flowing through the spark gap. The combustible gas is in contact with the hot spark plasma channel and ignited. Consequently, a larger flame kernel can be generated.

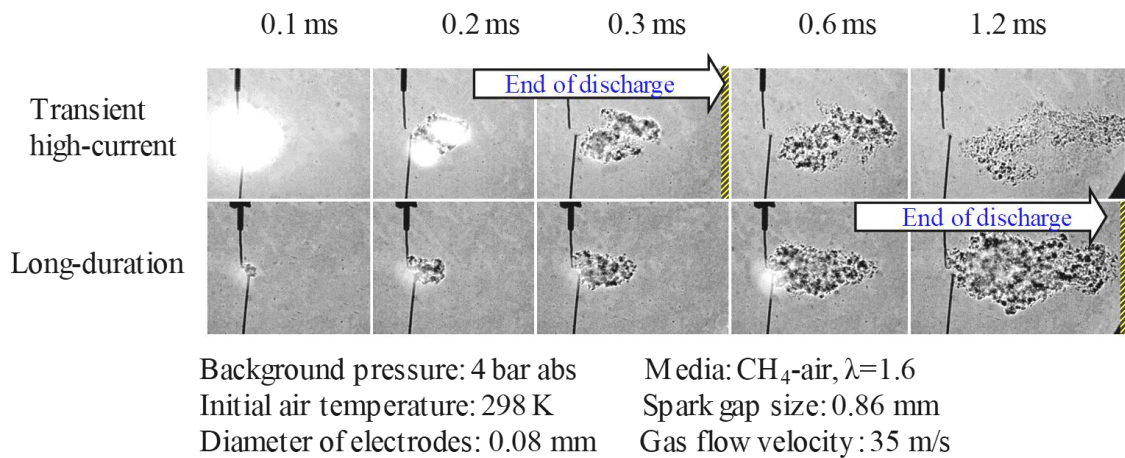


Figure 6-16 Shadowgraph images of the transient high-current and long-duration spark strategies for the flame kernel development under 35 m/s gas flow

The flame areas at the end of the spark discharge with the two strategies under various flow velocities are summarized in Figure 6-17. The long-duration spark has consistently better performance than the transient high-current spark under the tested gas flow conditions as can be seen from the larger flame areas at the end of spark discharge. The improved ignition performance is maintained in the later stage of combustion, as can be seen from the flame area at 3 ms after the breakdown event, shown in Figure 6-18.

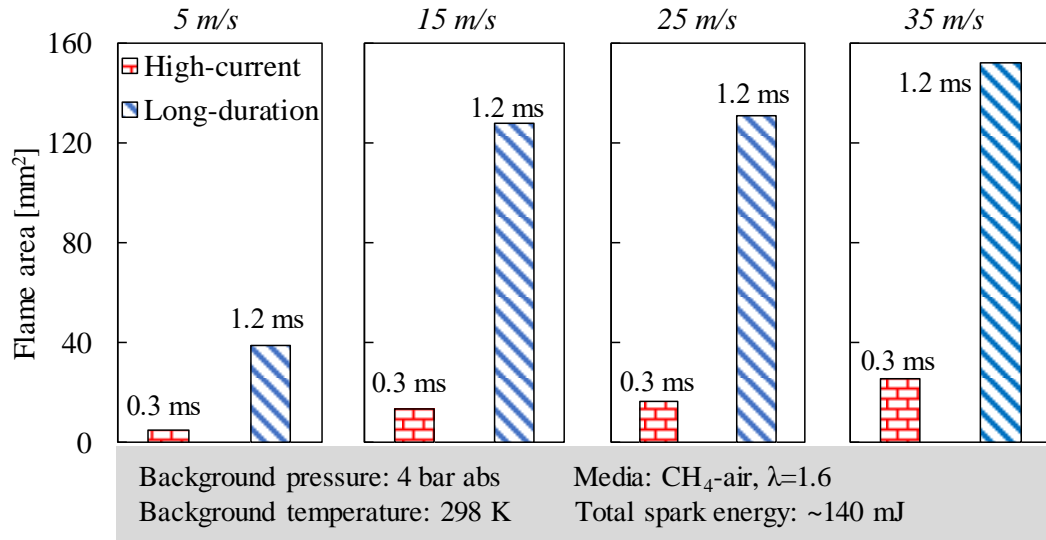


Figure 6-17 Flame area at the completion of the spark discharge process under different cross-flow velocities

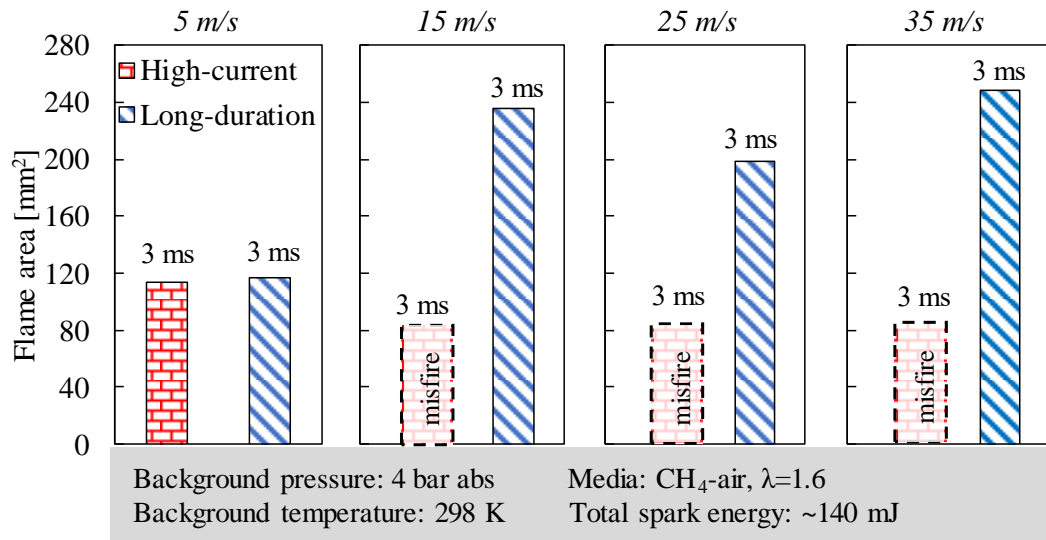


Figure 6-18 Flame area of 3 ms after breakdown under different cross-flow velocities

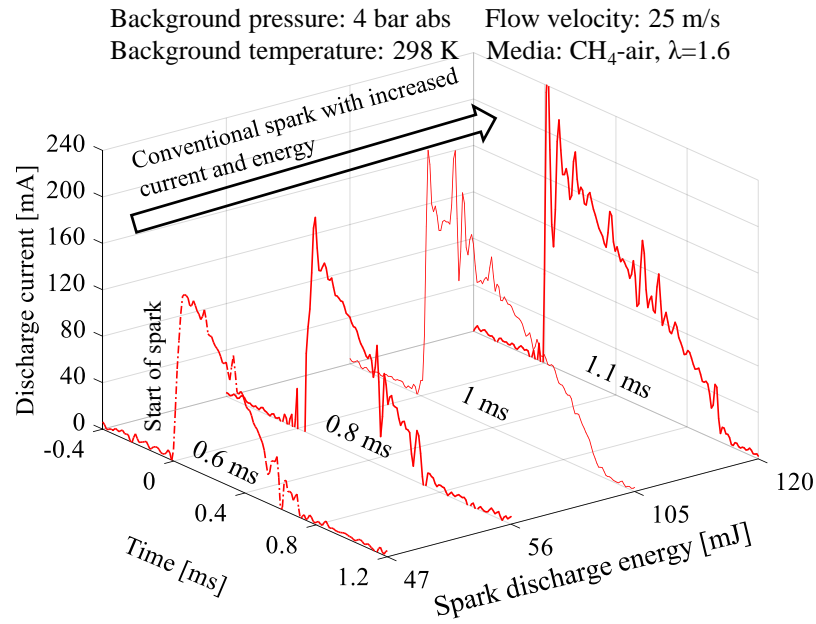
6.3.4 Effects of spark discharge energy levels of the transient high-current and conventional spark on the ignition of lean mixtures

The spark discharge energy (about 140 mJ) in the previous experiments is low for the transient high-current spark ignition strategy. In order to generate considerable thermal

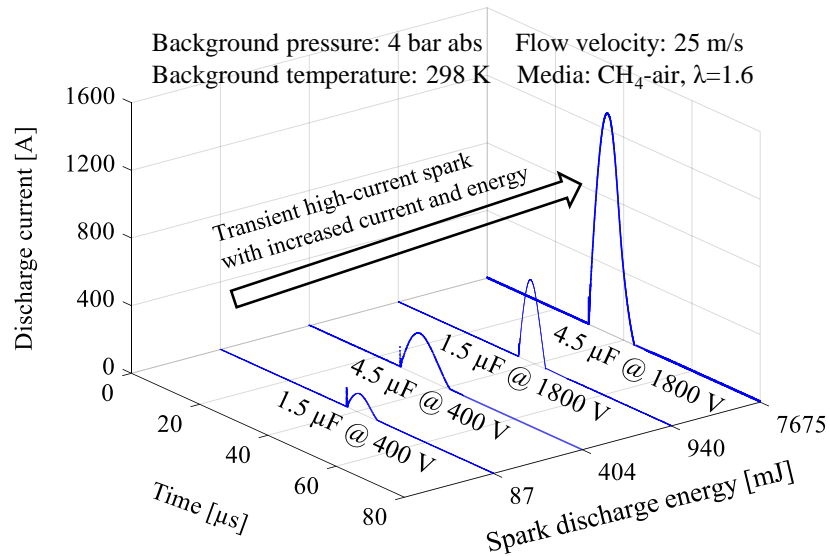
impact, the transient high-current spark requires much higher energy levels. The following experiments have been conducted to further compare the transient high-current spark and the conventional spark at different spark discharge energy levels. The increase in the spark discharge energy of a conventional spark is realized by extending the charging duration to the primary coil. The increase in the transient high-current spark discharge energy is achieved by increasing the voltage of the transient high-current module. The hardware settings and key control parameters for enabling the two spark strategies are listed in Table 6-1. By changing the capacitance of the external energy storage capacitor and the DC voltage that charges the capacitor, the spark discharge energy from the transient high-current spark can be increased from 90 mJ to 7600 mJ, with the peak current increasing from 140 A to 1350 A. The discharge energy and duration from the ignition coil in the transient high-current ignition system is kept constant. For the conventional spark, the discharge energy and discharge duration are adjusted by controlling the charging duration and supply voltage to the primary coil. Discharge energy levels ranging from 47 mJ to 120 mJ with a duration changing from 0.6 ms to 1.1 ms are achieved in the experiments. Selected spark discharge current waveforms are shown in Figure 6-19.

Table 6-1 Characteristics of the spark ignition systems

Transient high-current spark	External energy storage capacitance (μF)	1.5, 4.5
	DC supply voltage (kV)	0.3-1.8
	Peak spark current (A)	140-1350
	Coil discharge duration (ms)	0.5
	Transient high-current discharge duration (ms)	0.007-0.02
	Spark energy from the transient high-current module (mJ)	90-7600
	Spark energy discharged from the coil (mJ)	15
Conventional spark	Number of coils (-)	1
	Supply voltage to the primary coil (V)	12, 24
	Charging duration (ms)	2-6
	Peak spark current during glow phase (mA)	100-240
	Coil discharge duration (ms)	0.6-1.1
	Spark energy discharged from the coil (mJ)	47-120



(a) Spark discharge current waveforms of conventional spark



(b) Spark discharge current waveforms of transient high-current spark

Figure 6-19 Spark discharge current waveforms of the conventional and transient high-current spark

The plot of spark discharge energy versus flame area at the completion of spark discharge with the two strategies is shown in Figure 6-20. With both spark strategies, the flame area

at the end of the spark discharge increases with the increased spark discharge energy. The conventional spark has apparent advantages over the transient high-current spark discharge from an energy consumption point of view. To achieve a similar flame area at the end of spark discharge, the transient high-current spark needs to deliver more than ten times of energy to the spark gap under the tested conditions.

The correlation between the flame area at the end of spark discharge and the flame area at a later time in the combustion process is shown in Figure 6-21. Generally, a larger flame area at the end of spark discharge results in faster flame propagation in the later stage. From this observation, it is confirmed that a conventional spark is a better choice for the ignition under the tested gas flow conditions.

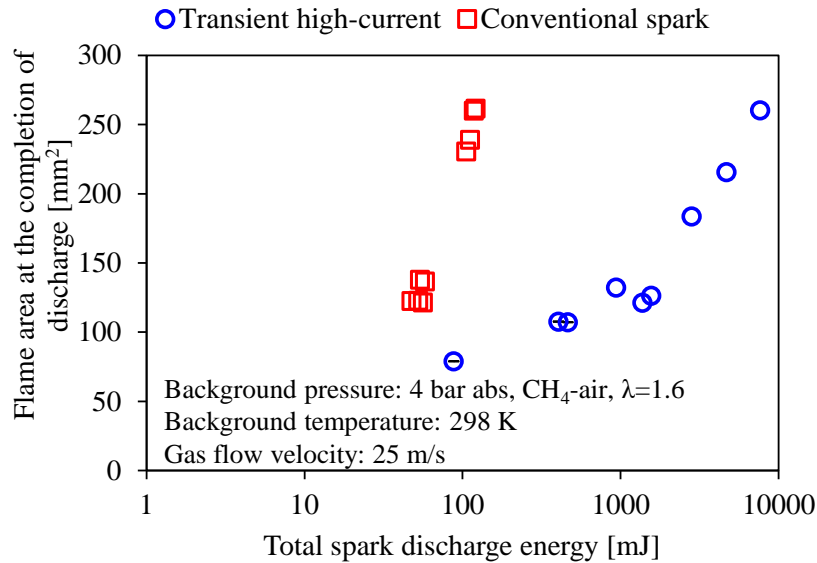


Figure 6-20 Flame area at the completion of spark discharge by the conventional spark and the transient high-current spark under 25 m/s gas flow

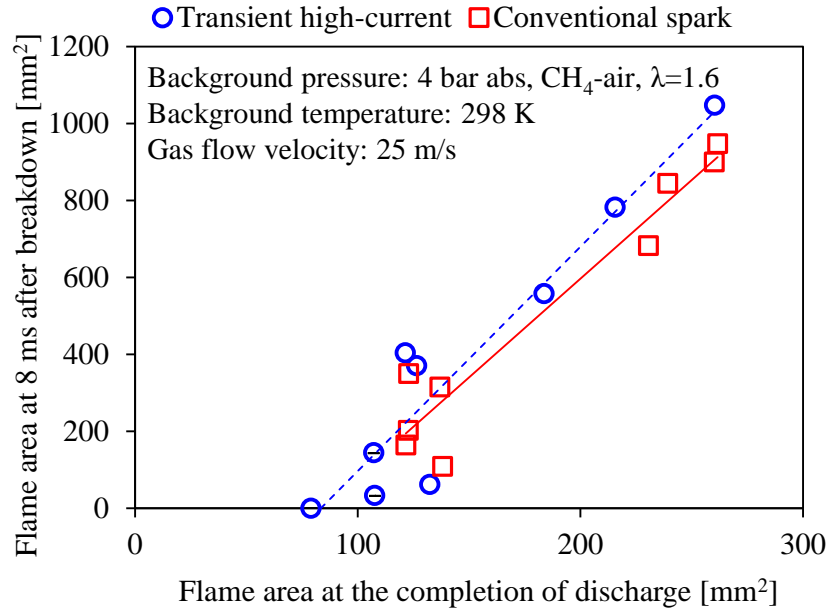


Figure 6-21 Flame area comparison between 8 ms post breakdown and the completion of spark discharge

6.4 Effects of spark glow phase current profile on flame kernel development

The spark discharge current profile during the arc and glow phases has minimal impact on the combustion process under quiescent conditions, as long as the minimum ignition energy is provided, as reported in chapter 4. Under gas flow conditions, however, the amount of spark discharge energy is no longer the single important parameter for the ignition process, which can be seen from the results in section 6.3. The energy release profile also plays an important role in the ignition process. In this section, the impact of the spark glow phase current profiles on the ignition is further investigated with the focus on the spark discharge current and duration during the arc and glow phases.

6.4.1 Effects of varied spark glow phase current profile with equivalent spark energy

Two spark discharge processes with equivalent spark discharge energy levels but different discharge current profiles are compared to demonstrate how the energy release pattern during the arc and glow phases affects the ignition process. The spark discharge current waveforms are shown in Figure 6-22. Case 1 features a low-current spark with a longer discharge duration, while the spark discharge duration in case 2 is shorter but the overall glow phase current level is higher.

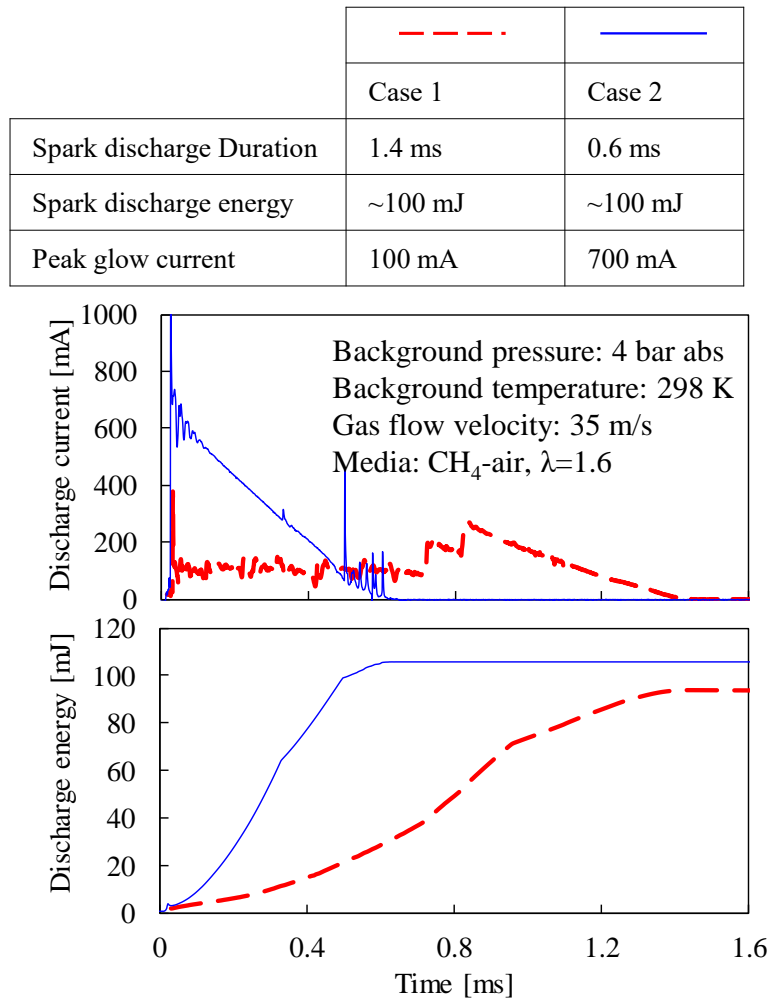
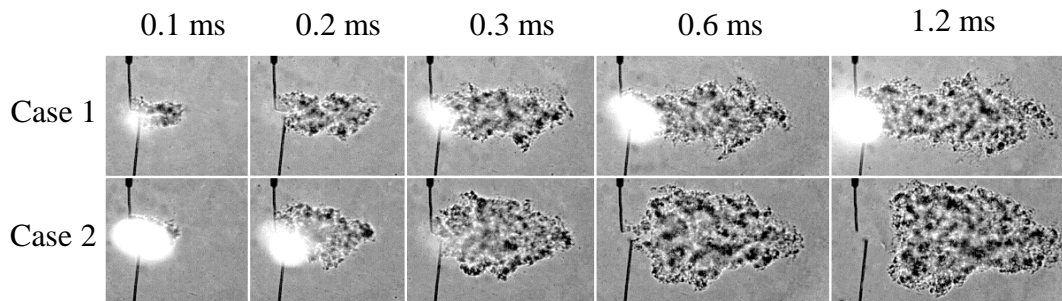


Figure 6-22 Spark discharge current and discharge energy waveforms

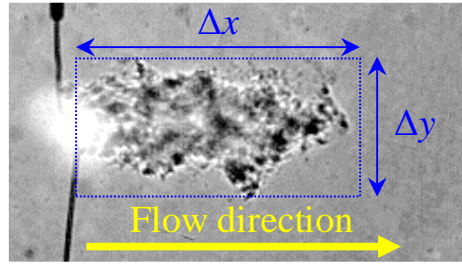
Images of flame area are recorded during the experiments. The flame kernel growth during the initial 1.2 ms with the two spark energy release process under 35 m/s gas flow velocity is shown in Figure 6-23. Two parameters, Δx and Δy , are introduced to better analyze the results. Δx is the stretch of the flame in the gas flow direction, while Δy is the span of the flame perpendicular to the flow direction, as shown in Figure 6-24.

	Case 1	Case 2
Spark discharge Duration	1.4 ms	0.6 ms
Spark discharge energy	~100 mJ	~100 mJ
Peak glow current	100 mA	700 mA
Remarks	Long duration	Conventional



Background pressure: 4 bar abs Media: CH₄-air, $\lambda=1.6$
 Background temperature: 298 K Flow velocity: 35 m/s
 Diameter of electrodes: 0.08 mm Spark gap size: 0.86 mm

Figure 6-23 Shadowgraph images of the flame kernel initiation under 35 m/s gas flow with different spark glow current profiles



Δx : flame propagation in the flow direction

Δy : flame expansion in the perpendicular direction

Figure 6-24 Definition of flame propagation distance in the gas flow direction and perpendicular to the gas flow direction

The flame propagation distances in the two directions, along with the flame area, are shown in Figure 6-25. Δx has similar values for the two ignition strategies under the same gas flow velocity, suggesting that the flame development in the gas flow direction is mainly affected by the gas flow velocity. However, the flame expansion in the y -direction in case 2 is faster than that in case 1. Though the spark discharge of case 2 finishes at 0.6 ms, the trend of the faster expansion in the y -direction is maintained after the completion of spark discharge by the well-established larger flame kernel. The spark discharge in case 1 continues for about 1.4 ms. However, the prolonged duration has a limited contribution to the flame expansion in the y -direction, consequently results in a smaller flame area.

Background pressure: 4 bar abs
 Media: CH₄-air, $\lambda=1.6$

Background temperature: 298 K
 Gas flow velocity: 35 m/s

	Discharge duration	Discharge energy	Peak glow current
□ Case 1	1.4 ms	~100 mJ	100 mA
○ Case 2	0.6 ms	~100 mJ	700 mA

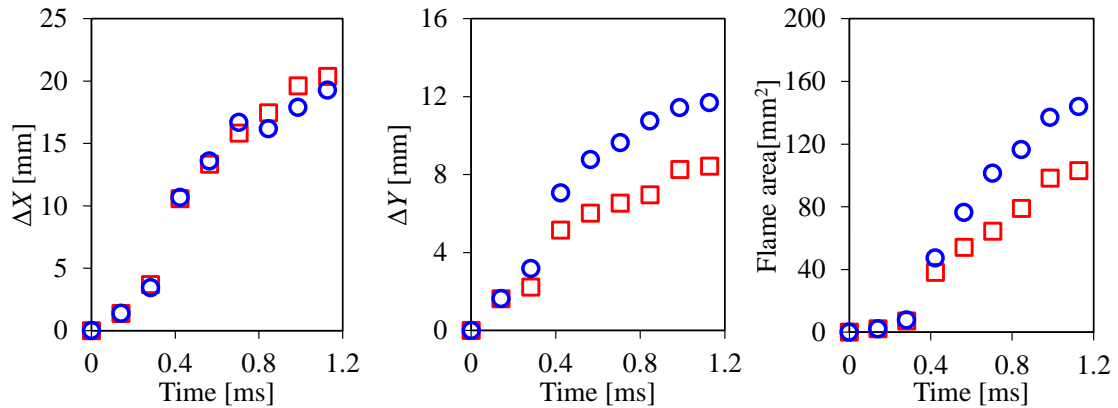
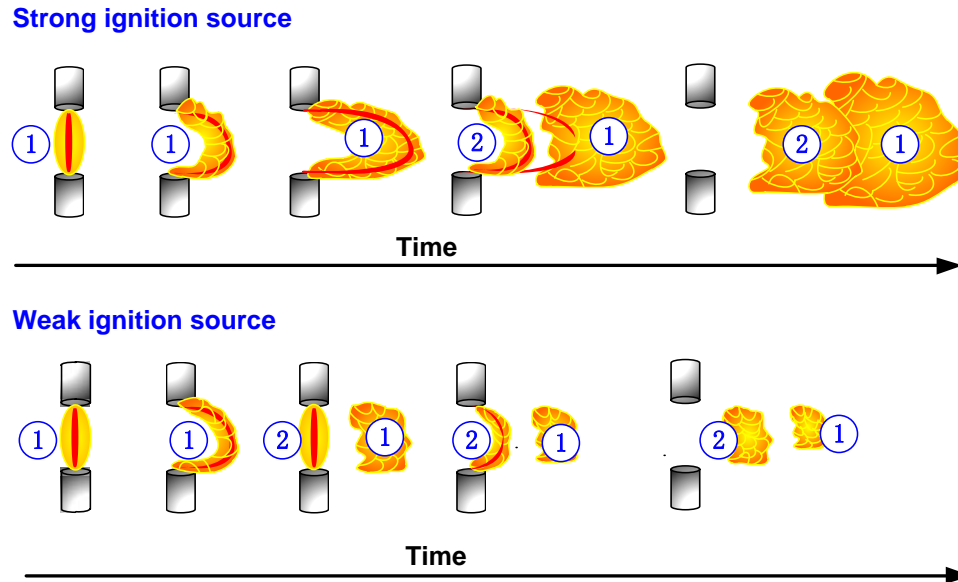


Figure 6-25 Flame propagation distances in different directions and flame areas

The comparison of the ignition performance with the same spark discharge energy yet different current profiles reveals the importance of spark discharge current level on the flame kernel development under high gas flow velocities. As discussed in section 6.1, the increase in gas flow velocity results in increased heat transfer which needs to be compensated by the ignition source for the flame kernel to survive. One of the major differences between the ignition under quiescent and gas flow conditions is the continuous displacement of fresh combustible gas into the flame kernel. The present research depicts the mechanisms of cross-flow on the development of the flame kernel, under different glow energy levels, as illustrated in Figure 6-26.



- ① Flame kernel initiated by the first plasma channel
- ② Flame kernel initiated by the second plasma channel

Figure notes:

Characteristics of ignition under flow conditions:

- Continuous supply of fresh combustible gas
- Drifting of flame with the gas flow
- Possible existence of multiple flame kernels

Figure 6-26 Flame kernel growth under gas flow conditions for different glow energy levels

For illustration purposes, the process is depicted as that the first flame kernel is created by the first plasma channel that is formed in between the spark gap and stretched by the gas flow. A second plasma channel is generated after the first plasma channel is broken off by the gas flow. The second plasma channel creates a second flame kernel. The two flame kernels grow and expand in the gas flow. Eventually, they merge into a larger flame kernel. In contrast, with a weak ignition source, though there are two flame kernels as well, these flame kernels have low sustainability. The flame kernels can not grow and expand to a sufficient size. Consequently, they fail to merge and stay as two separate small flame kernels or even diminish.

The illustration suggests that the flame development under gas flow conditions can be considered as a process consisting of the initiation, growth, and merging of multiple flame kernels during the process of spark discharge. The spark discharge could also be viewed as a combination of multiple segments that are divided by the restrikes or short circuits. After each restrike or short circuit event, the ignited mixture drifts with the gas flow, while the newly formed plasma channel ignites another portion of the combustible gas that is flowing through. Spark event with a higher discharge current is beneficial during the ignition process. The high current reduces the occurrence for short circuits and restrikes, as discussed in chapter 5. The fewer short circuits and restrikes mean that a longer duration can be maintained in each stretch, which ensures a longer time to transfer spark energy to the same portion of the mixture before it drifts away in the gas flow. Besides, the concentration of ions and electrons in the plasma channel increase with the elevated spark discharge current, which may also be beneficial for the ignition.

The impact of the prolonged spark discharge duration in the ignition process is that it can provide more chances for the fresh gas to be in contact with the hot plasma. Nevertheless, the effectiveness of the prolonged duration is effective only if the ignition source is sufficiently strong to form sustainable flame kernels.

6.4.2 Effects of glow phase current level on the flame kernel development

Based on these observations and analyses, further investigations are carried out to study the impact of the spark discharge current levels on the ignition process. Three spark discharge current levels that are enabled by the dual-coil offset strategy and the boosted-current strategy are used in the experiments. The average discharge current levels are 55 mA, 190 mA, and 250 mA, as shown in Figure 6-27. The shadowgraph images of the flame are shown in Figure 6-28.

Spark parameters in the experiments

1	Dual-coil offset spark	Discharge duration (ms)	1.9
		Average discharge current (mA)	50
		Total discharge energy (mJ)	130
		Number of coils (-)	2
2	Boosted current spark	Discharge duration (ms)	1.9
		DC power voltage (kV)	0.78
		Average discharge current (mA)	190
		Total discharge energy (mJ)	170
3	Boosted current spark	Discharge duration (ms)	1.9
		DC power voltage (kV)	1.5
		Average discharge current (mA)	250
		Total discharge energy (mJ)	260
		Number of coils (-)	1

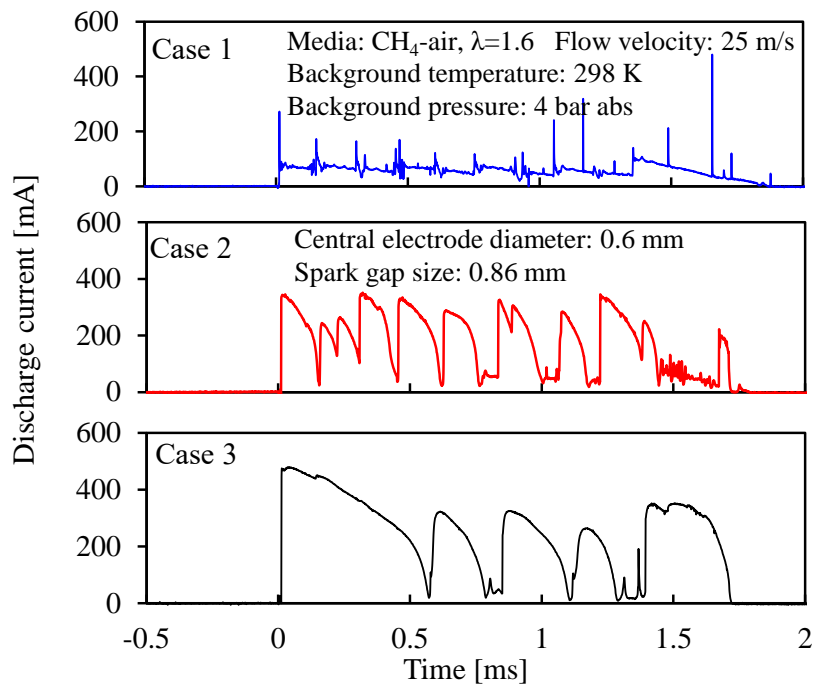


Figure 6-27 Spark discharge current waveforms at different current levels

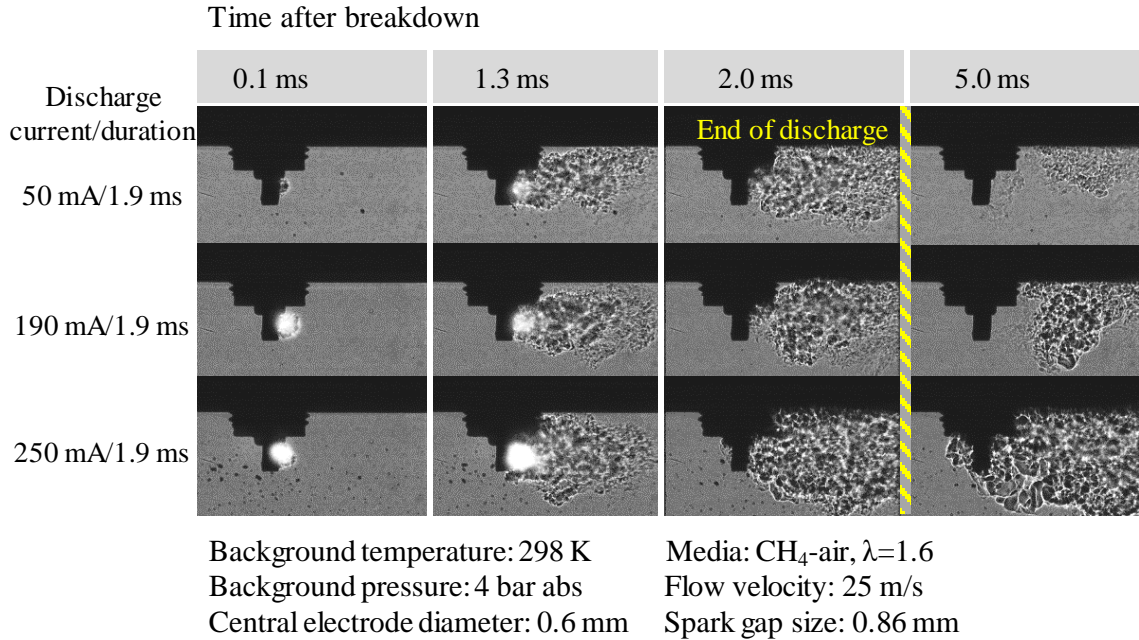
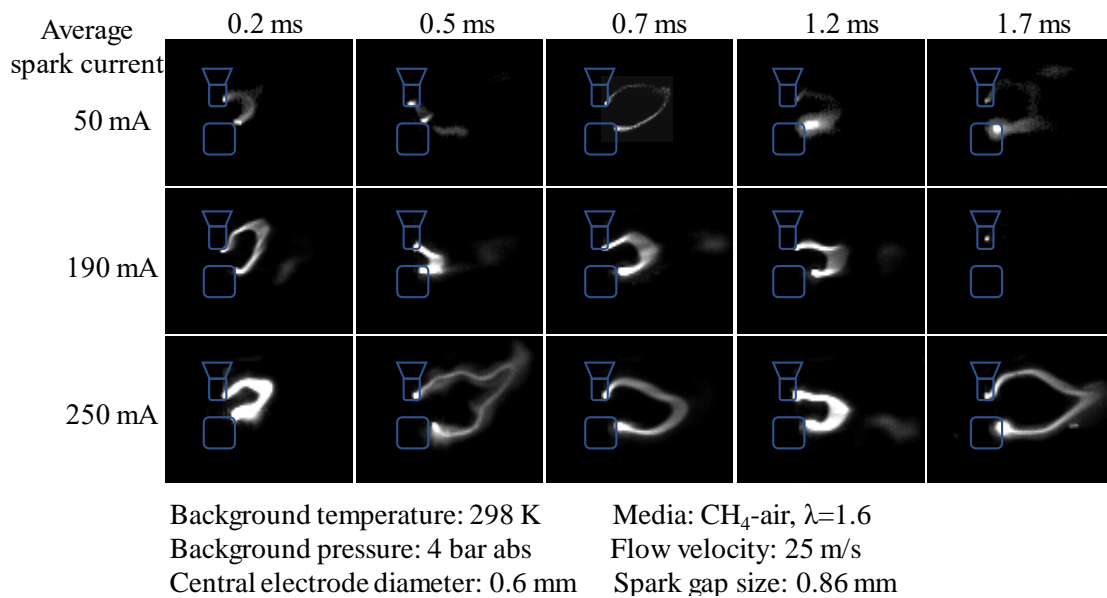


Figure 6-28 Shadowgraph images of the flame propagation with different spark discharge current levels under 25 m/s gas flow

In the initial 2 ms, the flame kernel is attached to the spark plug, which is observed in all three cases. The attached flame kernels are produced by the continuous spark discharge in the first 2 ms. At 5 ms after the breakdown, the flame kernel vanishes in the 55 mA spark discharge current case; the flame kernel is detached from the spark plug by the gas flow in the 190 mA spark discharge current case; while the flame kernel is still attached to the spark plug and thrives when the spark discharge current is 250 mA. The spark plasma images are recorded simultaneously with the flame images, as shown in Figure 6-29. The calculated values of plasma length are shown in Figure 6-30. A longer plasma channel increases the contact area between the plasma and the combustible gas, resulting in a larger flame kernel.



Note: The plasma images are simultaneously recorded with the flame images shown in Figure 6-28.

Figure 6-29 Images of plasma channel with different spark discharge current levels under 25 m/s gas flow

Background temperature: 298 K Media: CH₄-air, $\lambda=1.6$
 Background pressure: 4 bar abs Flow velocity: 25 m/s
 Central electrode diameter: 0.6 mm Spark gap size: 0.86 mm

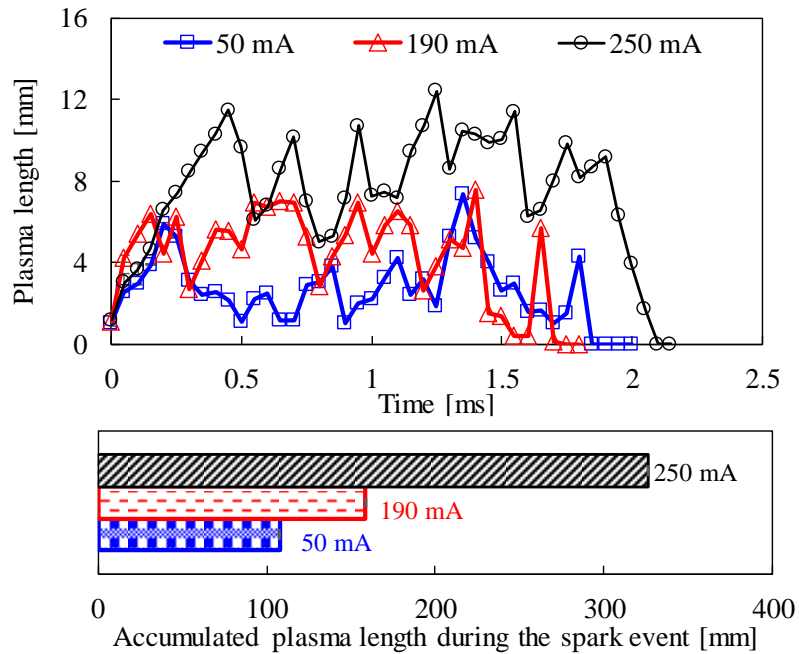


Figure 6-30 Length of the plasma channel at different spark discharge current levels

6.4.3 Effects of glow phase duration on the flame kernel development

More experiments are carried out with different spark discharge durations. The same ignition hardware used in the previous section are used here, with changed discharge duration. The shadowgraph images in Figure 6-31 are taken when 50 mA spark discharge current is used while images in Figure 6-32 are taken with the 250 mA case. For the same spark discharge current, the extension in the discharge duration results in a larger flame area. However, with a lower current level of 50 mA, the flame kernel is weakened by the gas flow once the spark discharge finishes, even with a long spark discharge duration of 3.8 ms. However, with a higher spark discharge current level of 250 mA, a longer discharge duration enables the growth of a larger flame kernel.

The flame areas at 5 ms and 10 ms after the breakdown event are compared to show the ignition ability of various spark strategies, as shown in Figure 6-33. A consistently larger

flame area can be observed with a higher spark discharge current level when the discharge duration is the same. Extending the spark discharge duration is also beneficial for the flame kernel growth, under such lean and high velocity gas flow conditions.

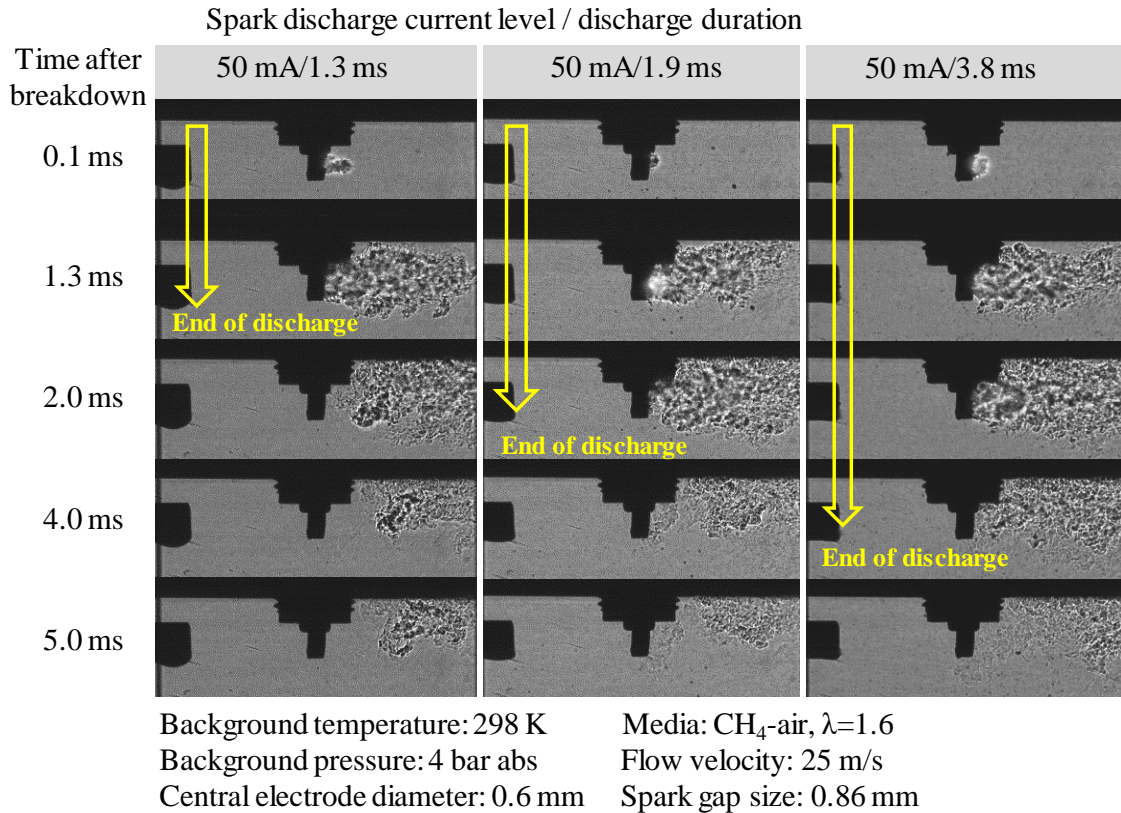


Figure 6-31 Impact of spark discharge duration on flame kernel development (50 mA discharge current)

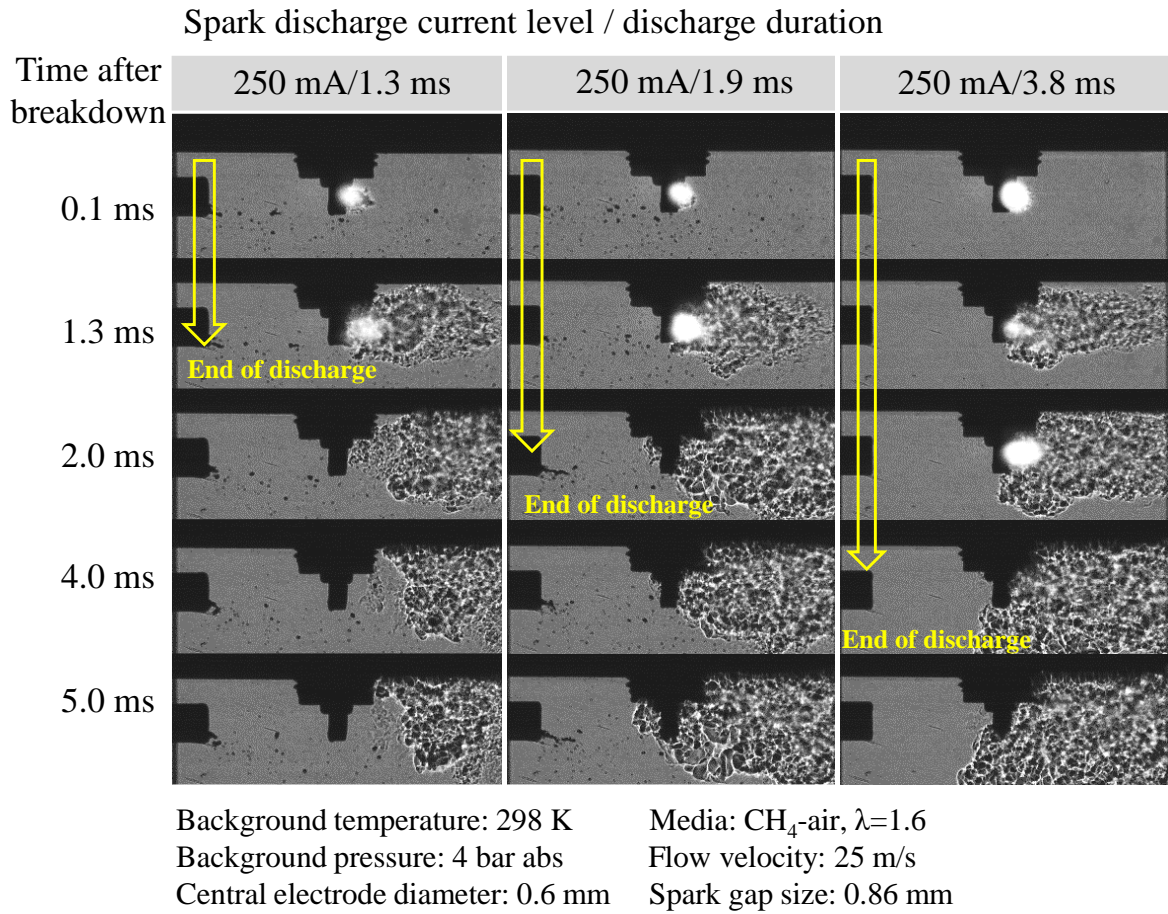


Figure 6-32 Impact of spark discharge duration on flame kernel development (250 mA discharge current)

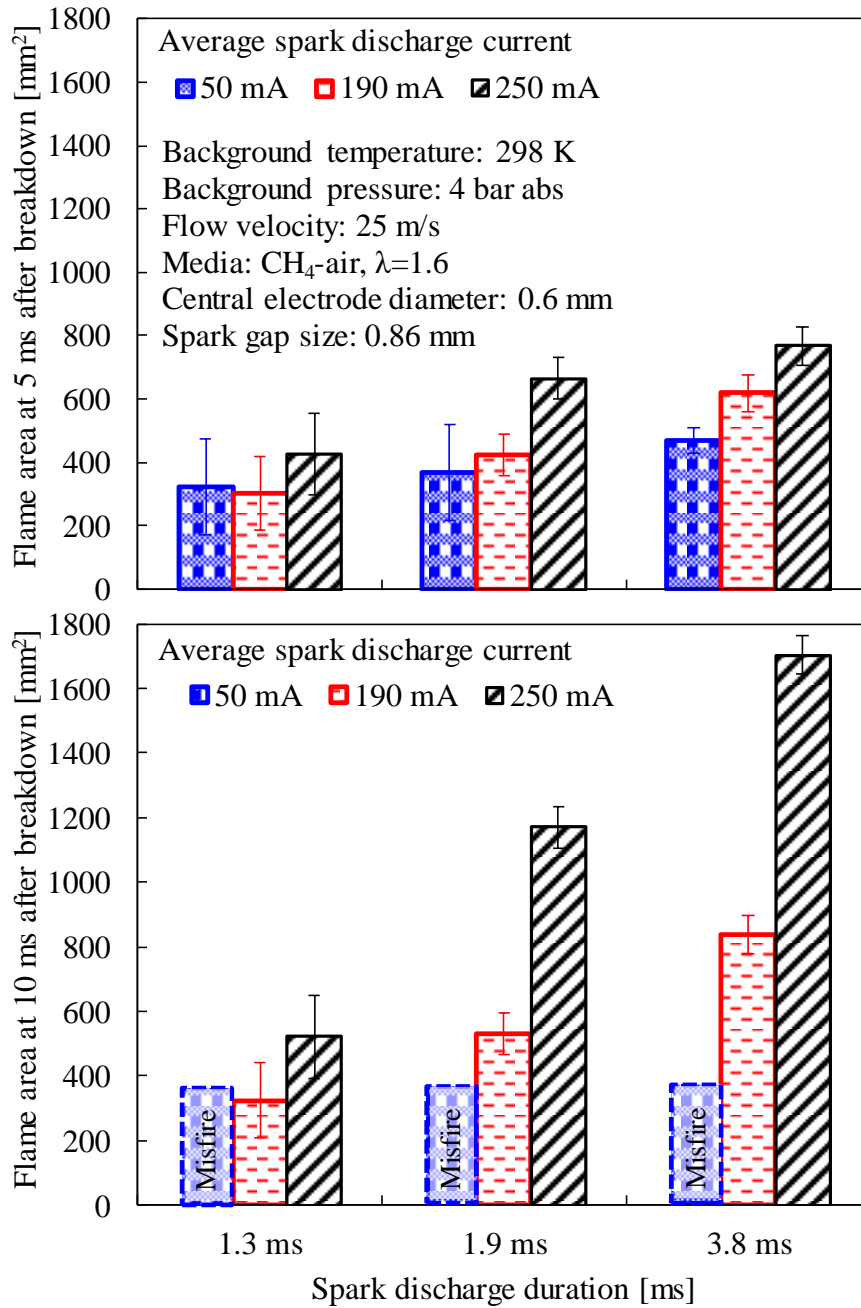


Figure 6-33 Effects of spark discharge current level and discharge duration on flame kernel development

6.4.4 Further considerations of the spark discharge current level and duration

Another observation from the results shown in Figure 6-33 is that similar ignition performance can be achieved either through a spark discharge with a longer discharge duration but lower discharge current, or a spark discharge with a shorter discharge duration but higher discharge current. For instance, a similar flame area is reached at 5 ms with a spark discharge duration of 1.3 ms when the discharge current level is 250 mA, or with a spark discharge duration of 1.9 ms when the discharge current level is 190 mA. The question is then which strategy to use, a long-duration low-current spark, or a short-duration high-current spark? Several constraints need to be considered when designing the spark ignition strategy for internal combustion engine applications.

The spark discharge duration is ultimately limited by the engine speed. Figure 6-34 demonstrates the equivalent crank angles of different spark discharge duration under varying engine speeds. For example, a discharge duration of 5 ms is equivalent to 180°CA for an engine running at 6000 RPM, which is too long for the spark ignition process.

For the selection of spark discharge current level, electrode erosion is one main constraint that will not be discussed in detail here. Another major consideration is the energy transfer efficiency. To demonstrate the impact of discharge current on the spark energy transfer, the spark plasma resistance is calculated. The spark plasma resistance is calculated from 6-1

$$R_{plasma} = V/I \quad 6-1$$

Where R_{plasma} is the plasma resistance, V is the voltage of the spark gap, and I is the spark discharge current.

The resistance of the spark plasma decreases with the increase in discharge current, as shown in Figure 6-35. According to Kirchhoff Circuit Laws [132], the energy delivered to the spark gap is proportional to the resistance of the spark plasma, which also decreases with the increased discharge current. More energy needs to be supplied to the spark plug to

deliver the same energy to the spark gap with a higher spark current. From this perspective, a low spark discharge current level is desirable, on the condition that the spark discharge current is adequately high to support the flame kernel growth in the gas flow.

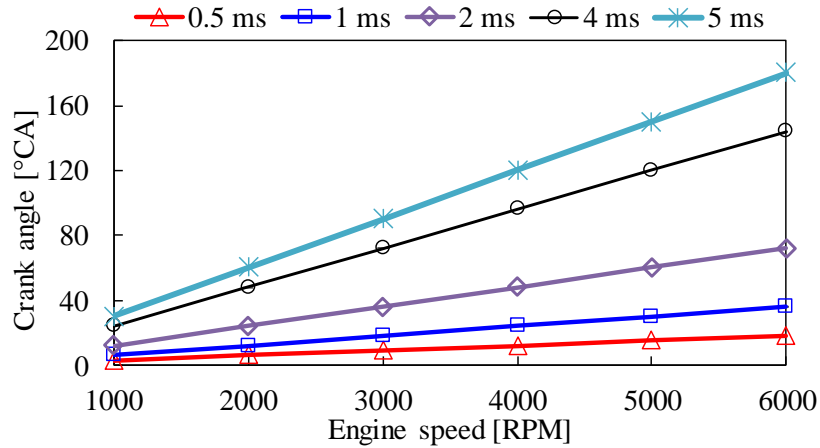


Figure 6-34 Equivalent crank angle of different spark discharge duration under varying engine speeds

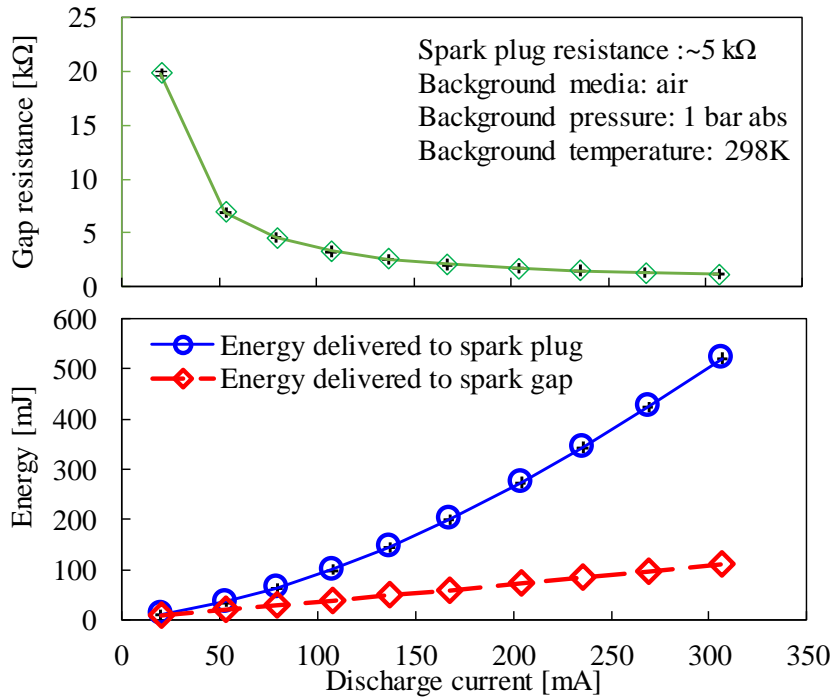


Figure 6-35 Spark gap resistance and energy transfer at different spark discharge current levels

6.5 Chapter summary

In summary of the experimental results, the ignition and flame kernel growth are subject to the strong impact of the flow field. Ignition control strategies with different spark discharge parameters are deployed under various gas flow conditions. The major findings are listed as follows:

- (1) The high-power ignition strategy is beneficial for the ignition of a lean mixture under quiescent and low gas flow velocity (up to 10 m/s), yet it has a negative impact on the ignition under higher gas flow velocity.
- (2) The transient-high current ignition strategy has inferior ignition ability as compared with a long-duration low-current spark when the spark discharge energy is limited to moderate levels.
- (3) A longer spark discharge duration is beneficial for the flame kernel initiation under gas flow conditions, when the current level is above a minimum level.
- (4) A sufficiently high spark discharge current level is beneficial for the flame kernel initiation, especially when the gas flow velocity is extensively high.
- (5) The spark discharge energy amount is not the single most important parameter for the ignition under gas flow conditions. The energy release profile also matters in the ignition process.

CHAPTER 7 CONCLUSION

The primary objective of this research was to study the mechanisms of spark ignition of a lean or diluted fuel-air mixture under gas flow conditions. Effective ignition strategies were configured by controlling the spark discharge parameters via specifically designed ignition circuits. These strategies enabled enhanced spark discharge power, increased spark discharge energy, extended spark discharge duration, and boosted spark discharge current to be facilitated. This made it possible to ignite lean or diluted gaseous fuel-air mixtures in a set of constant volume combustion chambers under controlled gas flow conditions. A complementary objective was to gain insights into how gas flow variations impact different spark parameters, with a view to improving the accuracy of spark ignition models. Accordingly, the interactions between the spark discharge process and the air flow field were investigated under independently controlled air flow velocities. The spark discharge parameters, such as the spark discharge energy, discharge duration, discharge current, discharge voltage, as well as plasma length, were determined and analyzed under varying air flow conditions.

7.1 Conclusions

Several conclusions were drawn from the major findings of the extensive empirical studies undertaken in this research, and these are summarized below:

1. The ignition of a lean combustible mixture under gas flow conditions required both sufficiently high spark discharge current and adequately long spark discharge duration. The former was required to secure the flame kernel growth, especially under high gas flow velocities. A prolonged spark discharge duration effectively enlarged the ignition volume by allowing more combustible gas to be heated by the spark plasma, and consequently increased the chance to generate a larger flame kernel.
2. Spark strategies with transient high discharge power yet short discharge duration was suitable to ignite lean mixtures under quiescent or low gas flow velocities. However,

- prolonged spark discharge durations of adequate current were more effective in generating large flame kernels than sparks with enhanced transient discharge power, under strong gas flows. It was also observed that the transient high-current spark strategy did not perform as well as a conventional spark on equal spark energy under all the tested flow velocity range.
3. The length of the plasma channel increased due to the transportation of conductive particles by the air flow stream. The rate at which the plasma length increased, identified as 'plasma stretching rate', was mainly dependant on the air flow velocity. The maximum length, to which the plasma channel was prolonged, was effected by the air flow velocity and the spark gap size. A maximum length of about 35 mm was observed in this research.
 4. When a spark was discharged under air flow conditions, the discharge duration was reduced due to the increased plasma resistance. The spark discharge energy was changed because of the flow field. The changes in the spark discharge duration and discharge energy were more significant when the air flow velocity increased from 0 m/s to 30 m/s. Further increase in air flow velocity, e.g., from 30 m/s up to 60 m/s, had minimal impact on the spark discharge duration and discharge energy under the tested conditions.
 5. Short circuit and restrike phenomena of the spark plasma were observed under air flow conditions. The frequency of the short circuit and restrike increased with the increased air flow velocity.
 6. The shape of the spark plasma channel became irregular when the background pressure was elevated. Due to this pressure increase, the first short circuit occurred at an earlier stage, provided that the discharge voltage was sufficiently high.
 7. The transient high-power spark and transient high-current spark were not significantly impacted by the magnitude of the air flow, apparently due to the short duration of the discharge process. Conversely, the boosted-current spark and the dual-coil offset spark were subject to great variations in the air flow. It was suggested that these effects were

- due to the increased discharge voltage across the spark gap and the stochastic events of short circuits and restrikes under air flow conditions.
8. The spark discharge power was a major influential factor in the ignition process under quiescent conditions. A high-power spark was beneficial for the flame kernel growth.
 9. When using conventional discharge current levels, the excessive spark discharge current and excessive discharge duration during the arc and glow phases had minimal impact on the flame kernel formation under quiescent conditions, as long as the spark discharge energy was greater than the minimum threshold for a successful ignition.

7.2 Contributions made to the study of spark ignition mechanisms

As guaranteed and successful spark ignition for all gas flow conditions is essential for any future high-efficiency engines, the research work carried out for this dissertation was devoted to the study on the mechanisms of flame kernel growth and the spark discharge process under gas flow conditions through focused and extensive empirical work. The contributions of this work included the following:

1. Modulation of spark discharge parameters was realized through specifically designed ignition circuits and control algorithms. Systematic empirical research was conducted on the effectiveness of spark strategies under controlled background pressure and gas flow conditions. The evaluation of the spark strategies was based on the spark energy that was delivered to the spark gap instead of the coil out energy frequently reported in the existing literature. In addition to the amount of spark energy, the spark discharge current and voltage profiles were measured alongside optical measurements of the flame kernel. This methodology enabled detailed correlations of the spark parameters to the flame kernel growth. A better understanding of how flame kernels grow under gas flow conditions was made possible through these comprehensive measurements.
2. The advantages and shortcomings of various spark strategies under gas flow conditions were discussed based on the experimental results. The experimental work explored a wider range of gas flow conditions as compared with existing results from the literature

- on certain spark strategies, such as the high-power spark and the transient high-current spark.
3. Extensive experiments on the spark discharge under air flow conditions were carried out in this research. The scope of the air flow velocity range was much wider than that reported in previously published research work. The background pressure impact on plasma stretch was also investigated. The effects on maximum plasma length and plasma stretching rate for varying air flow velocities were analyzed. These results could benefit the development of better spark ignition modeling for various gas flow conditions.

7.3 Recommendations for future work

1. The experiments in this research were carried out in a set of constant volume combustion chambers under a background temperature of about 298 K. As temperature is important for both mixture ignition and combustion processes, it would be worthwhile to fully investigate the impact of gas flow on spark discharge and ignition at elevated initial temperatures.
2. Gas flow velocities were shown to influence spark discharge characteristics and flame growth in the constant volume combustion chambers. In Gasoline Direct Injection (GDI) engines the fuel injector, normally located close to the spark plug, will contribute to the mixture motion during the spark ignition process. There is a paucity of empirical data on how the gas flow interactions between the fuel injection technique and in-cylinder bulk mixture motion effect the spark discharge and ignition process. To address this deficiency will require in-depth investigations. Additionally, when a stratified fuel-air mixture is created by the direct fuel injection, the adaptive control of the ignition strategy with changing mixture reactivity under varying gas flow velocities could be beneficial, and such as would also be a meaningful research topic.
3. The impact of spark plug configuration on the ignition performance under gas flow conditions should be studied in more detail. For instance, a longer plasma channel can be achieved with a larger spark gap size. The longer channel is judged to be beneficial

for generating a larger flame kernel. However, the larger spark gap size also results in a shorter spark discharge duration, which impairs the ignition process under gas flow conditions. The overall ignition performance depends on both aspects, which should be studied in greater detail, including to what extent the orientation of the spark plug changes the gas flow characteristics and hence impact the spark discharge and the ignition process.

REFERENCES

1. Ikeya, K., Takazawa, M., Yamada, T., Park, S., and Tagishi, R., "Thermal Efficiency Enhancement of a Gasoline Engine," *SAE International Journal of Engines*, 8(4):1579–1586, 2015
2. Takaki, D., Tsuchida, H., Kobara, T., Akagi, M., Tsuyuki, T., and Nagamine, M., "Study of an EGR System for Downsizing Turbocharged Gasoline Engine to Improve Fuel Economy," *SAE Technical Paper*, 2014-01-1199, 2014
3. Kutlar, O. A., Arslan, H., and Calik, A. T., "Methods to Improve Efficiency of Four Stroke, Spark Ignition Engines at Part Load," *Energy Conversion and Management*, 46(20): 3202–3220, 2005
4. Fischer, M., Kreuziger, P., Sun, Y., and Kotrba, A., "Clean EGR for Gasoline Engines – Innovative Approach to Efficiency Improvement and Emissions Reduction Simultaneously," *SAE Technical Paper*, 2017-01-0683, 2017
5. Alger, T., Gingrich, J., Roberts, C., Mangold, B., and Sellnau, M., "A High-Energy Continuous Discharge Ignition System for Dilute Engine Applications," *SAE Technical Paper*, 2013-01-1628, 2013
6. Jung, D., Sasaki, K., Sugata, K., Matsuda, M., Yokomori, T., and Iida, N., "Combined Effects of Spark Discharge Pattern and Tumble Level on Cycle-to-Cycle Variations of Combustion at Lean Limits of SI Engine Operation," *SAE Technical Paper*, 2017-01-0677, 2017
7. Francqueville, L., and Michel, J.-B., "On the Effects of EGR on Spark-Ignited Gasoline Combustion at High Load," *SAE International Journal of Engines*, 7(4): 1808–1823, 2014
8. Fu, J., Zhu, G., Zhou, F., Liu, J., Xia, Y., and Wang, S., "Experimental Investigation on the Influences of Exhaust Gas Recirculation Coupling with Intake Tumble on Gasoline Engine Economy and Emission Performance," *Energy Conversion and Management*, 127: 424–436, 2016

9. Kolodziej, C. P., Pamminger, M., Sevik, J., Wallner, T., Wagnon, S. W., and Pitz, W. J., "Effects of Fuel Laminar Flame Speed Compared to Engine Tumble Ratio, Ignition Energy, and Injection Strategy on Lean and EGR Dilute Spark Ignition Combustion," *SAE International Journal of Fuels and Lubricants*, 10(1): 82–94, 2017
10. Maly, R.R. and Herweg, R., "Spark Ignition and Combustion in Four-Stroke Gasoline Engines," in *Flow and Combustion in Reciprocating Engines*, pp.1–66, Springer, Berlin, Heidelberg, 2008
11. Ballal, D. R., and Lefebvre, A. H., "The Influence of Flow Parameters on Minimum Ignition Energy and Quenching Distance," *Symposium (International) on Combustion*, 15(1):1473–1481, 1975
12. Sayama, S., Kinoshita, M., Mandokoro, Y., and Fuyuto, T., "Spark Ignition and Early Flame Development of Lean Mixtures under High-Velocity Flow Conditions: An Experimental Study," *International Journal of Engine Research*, p. 146808741774851, 2018
13. Zheng, M., Reader, G. T., and Hawley, J. G., "Diesel Engine Exhaust Gas Recirculation—a Review on Advanced and Novel Concepts," *Energy Conversion and Management*, 45(6): 883–900, 2004
14. Leach, F., Davy, M., and Peckham, M., " Cycle-to-Cycle NO and NO_x Emissions from a HSDI Diesel Engine," *Journal of Engine for Gas Turbines and Power*, 141(8):9, 2018
15. Gan, S., Ng, H. K., and Pang, K. M., "Homogeneous Charge Compression Ignition (HCCI) Combustion: Implementation and Effects on Pollutants in Direct Injection Diesel Engines," *Applied Energy*, 88(3): 559–567, 2011
16. Zheng, M., and Yu, S., "Advanced Ignition Systems for Future Clean Combustion Engines: Review," *Journal of Automotive Safety and Energy*, 6(04): 295, 2015
17. United States Department of Energy, "Fuel Economy Data," [Online]. Available: <https://www.fueleconomy.gov/feg/download.shtml>, [Accessed: 31-Oct-2020]

18. United States Environmental Protection Agency, "EPA Emission Standards," [Online]. Available: <https://www.epa.gov/emission-standards-reference-guide/all-epa-emission-standards>. [Accessed: 31-Oct-2020]
19. Yu, X., Sandhu, N. S., Yang, Z., and Zheng, M., "Suitability of Energy Sources for Automotive Application – A Review," *Applied Energy*, 271, 2020
20. Kühlwein, J., "Driving Resistances of Light-Duty Vehicles in Europe: Present Situation, Trends, and Scenarios for 2025," *communications*, 49(30), 2016
21. Boundy, R.G. and Davis, S.C., *Biomass Energy Data Book: Edition 3* (No. ORNL/TM-2011/43). Oak Ridge National Lab, Oak Ridge, TN, United States, 2010
22. Nobel, D., "Trench blasting with dynamite," *Trench Blasting Guide*, 2006
23. Surampudi, R., Elliott, J., Blosiu, J., Bugga, K., Beauchamp, P., and Cutts, J., "Advanced Energy Storage Technologies for Future NASA Planetary Science Mission Concepts," NASA Jet Propulsion Laboratory, California Institute of Technology, 2018
24. National Research Council, "Technologies and approaches to reducing the fuel consumption of medium-and heavy-duty vehicles," National Academies Press. 2010
25. Yilmaz, M., and Krein, P. T., "Review of Battery Charger Topologies, Charging Power Levels, and Infrastructure for Plug-In Electric and Hybrid Vehicles," *IEEE Transactions on Power Electronics*, 28(5): 2151–2169, 2013
26. Smith, M. and Castellano, J., "Costs Associated with non-Residential Electric Vehicle Supply Equipment: Factors to Consider in the Implementation of Electric Vehicle Charging Stations (No. DOE/EE-1289)," US Department of Energy, 2015 [Online]. Available: <https://trid.trb.org/view/1377403>, [Accessed: 31-Oct-2020]
27. "Learn About Batteries - Battery University," [Online]. Available: https://batteryuniversity.com/learn/article/ultra_fast_chargers, [Accessed: 31-Oct-2020]
28. Davis, S.C., Williams, S.E., Boundy, R.G. and Moore, S., "2016 Vehicle Technologies Market Report." Oak Ridge National Lab, Oak Ridge, United States.

29. Bardasz, E. A., Arters, D. C., Schiferl, E. A., and Righi, D. W., "A Comparison of Gasoline Direct Injection and Port Fuel Injection Vehicles: Part II Lubricant Oil Performance and Engine Wear," SAE Transactions, 108:1007–1021, 1999
30. Ling, H., Xiu, M. Y., Guo, L., and Nan, X., "Dynamic Response of a Three-Way Catalytic Converter," Energy Procedia, 17: 547–554, 2010
31. Zheng, M., Reader, G. T., Wang, D., Zuo, J., Kumar, R., Mulenga, M. C., Asad, U., Ting, D. S.-K., and Wang, M., "A Thermal Response Analysis on the Transient Performance of Active Diesel Aftertreatment," SAE Technical Paper, 2005-01-3885, 2005
32. Mock, P., "CO₂ Emission Standards for Passenger Cars and Light-Commercial Vehicles in the European Union," International Council on Clean Transportation, p. 9, 2013
33. Yang, Z., and Bandivadekar, A., "2017 Global Update: Light-Duty Vehicle Greenhouse Gas and Fuel Economy Standards," International Council on Clean Transportation, p. 36, 2017
34. "The Safer Affordable Fuel-Efficient (SAFE) Vehicles Rule for Model Years 2021–2026 Passenger Cars and Light Trucks," Final rule, Environmental Protection Agency and National Highway Traffic Safety Administration, 2020
35. Cairns, A., Blaxill, H., and Irlam, G., "Exhaust Gas Recirculation for Improved Part and Full Load Fuel Economy in a Turbocharged Gasoline Engine," SAE Technical Paper, 2006-01-0047, 2006
36. Alkidas, A. C. and El Tahry, S. H., "Contributors to the Fuel Economy Advantage of DISI Engines over PFI Engines," SAE Technical Paper, 2003-01-3101, 2003
37. Kumano, K. and Yamaoka, S., "Analysis of Knocking Suppression Effect of Cooled EGR in Turbo-Charged Gasoline Engine," SAE Technical Paper, 2014-01-1217, 2014
38. Potteau, S., Lutz, P., Leroux, S., Moroz, S. and Tomas, E., "Cooled EGR for a Turbo SI Engine to Reduce Knocking and Fuel Consumption," SAE Technical Paper, 2007-01-3978, 2007

39. Reinhart, T. and Megel, M., "An Efficient, Durable Vocational Truck Gasoline Engine," SAE International Journal of Engines, 9(3):1437–1448, 2016
40. Shiga, S., Nakamura, H., Karasawa, T., Yagi, S., Morita, M. and Matsumoto, T., "Effect of Early-Closing of Intake-Valve on the Engine Performance in a Spark-Ignition Engine," SAE Technical Paper, 960585, 1996
41. Leone, T., Christenson, E., and Stein, R., "Comparison of Variable Camshaft Timing Strategies at Part Load," SAE Technical Paper, 960584, 1996
42. Lake, T., Stokes, J., Murphy, R., Osborne, R. and Schamel, A., "Turbocharging Concepts for Downsized DI Gasoline Engines," SAE Technical Paper, 2004-01-0036, 2004
43. Iwamoto, Y., Noma, K., Nakayama, O., Yamauchi, T., and Ando, H., "Development of Gasoline Direct Injection Engine," SAE Technical Paper, 970541, 1997
44. Karl, G., Kemmler, R., Bargende, M., and Abthoff, J., "Analysis of a Direct Injected Gasoline Engine," SAE Technical Paper, 970624, 1997
45. Chevalier, A., Vigild, C., and Hendricks, E., "Predicting the Port Air Mass Flow of SI Engines in Air/Fuel Ratio Control Applications," SAE Technical Paper, 2000-01-0260, 2000
46. Kaiser, M., Krueger, U., Harris, R., and Cruff, L., "Doing More with Less' - The Fuel Economy Benefits of Cooled EGR on a Direct Injected Spark Ignited Boosted Engine," SAE Technical Paper, 2010-01-0589, 2010
47. Hara, S., Nakajima, Y., and Nagumo, S., "Effects of Intake-Valve Closing Timing on Spark-Ignition Engine Combustion," SAE Transactions, 94: 396–405, 1985
48. Teodosio, L., De Bellis, V., and Bozza, F., " Economy Improvement and Knock Tendency Reduction of a Downsized Turbocharged Engine at Full Load Operations through a Low-Pressure EGR System," SAE International Journal of Engines, 8(4):1508–1519, 2015
49. Amann, M., Alger, T., and Mehta, D., "The Effect of EGR on Low-Speed Pre-Ignition in Boosted SI Engines," SAE International Journal of Engines, 4(1):235–245, 2011

50. Kalghatgi, G., "Knock Onset, Knock Intensity, Superknock and Preignition in Spark Ignition Engines," *International Journal of Engine Research*, 19(1): 7–20, 2018
51. Fansler, T. D., Reuss, D. L., Sick, V., and Dahms, R. N., "Invited Review: Combustion Instability in Spray-Guided Stratified-Charge Engines: A Review," *International Journal of Engine Research*, 16(3): 260–305, 2015
52. Zhong, L., Musial, M., Reese, R., and Black, G., "EGR Systems Evaluation in Turbocharged Engines," *SAE Technical Paper*, 2013-01-0936, 2013
53. Grandin, B., and Ångström, H. E., "Replacing Fuel Enrichment in a Turbo Charged SI Engine: Lean Burn or Cooled EGR," *SAE Technical Paper*, 1999-01-3505, 1999
54. Sarikoc, F., Kettner, M., Velji, A., Spicher, U., Krause, A., and Elsaesser, A., "Potential of Reducing the NOX Emissions in a Spray Guided DI Gasoline Engine by Stratified Exhaust Gas Recirculation (EGR)," *SAE Technical Paper*, 2006-01-1261, 2006
55. Wei, H., Zhu, T., Shu, G., Tan, L., and Wang, Y., "Gasoline Engine Exhaust Gas Recirculation – A Review," *Applied Energy*, 99: 534–544, 2012
56. Hoepke, B., Jannsen, S., Kasseris, E., and Cheng, W. K., "EGR Effects on Boosted SI Engine Operation and Knock Integral Correlation," *SAE International Journal of Engines*, 5(2): 547–559, 2012
57. Duchaussoy, Y., Lefebvre, A., and Bonetto, R., "Dilution Interest on Turbocharged SI Engine Combustion," *SAE Technical Paper*, 2003-01-0629, 2003
58. Turner, J. W. G., Pearson, R. J., Curtis, R., and Holland, B., "Effects of Cooled EGR Routing on a Second-Generation DISI Turbocharged Engine Employing an Integrated Exhaust Manifold," *SAE Technical Paper*, 2009-01-1487, 2009
59. Joo, S. M., Alger, T., Chadwell, C., De Ojeda, W., Zuehl, J., and Gukelberger, R., "A High Efficiency, Dilute Gasoline Engine for the Heavy-Duty Market," *SAE International Journal of Engines*, 5(4):1768–1789, 2012
60. Chao, Y., Lu, H., Hu, Z., Deng, J., Wu, Z., Li, L., Shen, Y., and Yuan, S., "Comparison of Fuel Economy Improvement by High and Low Pressure EGR System on a Downsized Boosted Gasoline Engine," *SAE Technical Paper*, 2017-01-0682, 2017

61. Park, C., Lee, S., Kim, C., and Choi, Y., "A Comparative Study of Lean Burn and Exhaust Gas Recirculation in an HCNG-Fueled Heavy-Duty Engine," *International Journal of Hydrogen Energy*, 42(41): 26094–26101, 2017
62. Ibrahim, A., and Bari, S., "A Comparison between EGR and Lean-Burn Strategies Employed in a Natural Gas SI Engine Using a Two-Zone Combustion Model," *Energy Conversion and Management*, 50(12): 3129–3139, 2009
63. Manivannan, A., Porai, P. T., Chandrasekaran, S., and Ramprabhu, R., "Lean Burn Natural Gas Spark Ignition Engine - An Overview," *SAE Technical Paper*, 2003-01-0638, 2003
64. Sjöberg, M., Zeng, W., Singleton, D., Sanders, J. M., and Gundersen, M. A., "Combined Effects of Multi-Pulse Transient Plasma Ignition and Intake Heating on Lean Limits of Well-Mixed E85 DISI Engine Operation," *SAE International Journal of Engines*, 7(4): 1781–1801, 2014
65. Hayashi, N., Sugiura, A., Abe, Y., and Suzuki, K., "Development of Ignition Technology for Dilute Combustion Engines," *SAE International Journal of Engines*, 10(3), 2017
66. VanDerWege, B., Han, Z., Iyer, C., Muñoz, R. *et al.*, "Development and Analysis of a Spray-Guided DISI Combustion System Concept," *SAE Technical Paper*, 2003-01-3105, 2003
67. Blank, H., Dismon, H., Kochs, M., Sanders, M. *et al.*, "EGR and Air Management for Direct Injection Gasoline Engines," *SAE Technical Paper*, 2002-01-0707, 2002
68. Matthias, N., Wallner, T., and Scarcelli, R., "Analysis of Cyclic Variability and the Effect of Dilute Combustion in a Gasoline Direct Injection Engine," *SAE International Journal of Engines*, 7(2): 633–641, 2014
69. Alkidas, A. C., "Combustion Advancements in Gasoline Engines," *Energy Conversion and Management*, 48(11): 2751–2761, 2007
70. Ozdor, N., Dulger, M., and Sher, E., "Cyclic Variability in Spark Ignition Engines A Literature Survey," *SAE Technical Paper*, 940987, 1994

71. Ogata, K., "A High Energy Ignition System for EGR Combustion Engine," SAE Technical Paper, 2017-01-0675, 2017
72. Huang, C. C., Shy, S. S., Liu, C. C., and Yan, Y. Y., "A Transition on Minimum Ignition Energy for Lean Turbulent Methane Combustion in Flamelet and Distributed Regimes," *Proceedings of the Combustion Institute*, 31(1): 1401–1409, 2007
73. Wang, W. Q. and Sun, Z.Y., "Experimental Studies on Explosive Limits and Minimum Ignition Energy of Syngas: A Comparative Review," *International Journal of Hydrogen Energy*, 44(11): 5640–5649, 2019
74. Yu, X., Yu, S., Yang, Z., Tan, Q. *et al.*, "Improvement on Energy Efficiency of the Spark Ignition System," SAE Technical Paper, 2017-01-0678, 2017
75. Merola, S. S., Irimescu, A., Valentino, G., Tornatore, C., Silva, S., Grimaldi, A., and Carugati, E., "Experimental Evaluation of an Advanced Ignition System for GDI Engines," *SAE International Journal of Engines*, 8(5), 2015
76. Yu, X., Yang, Z., Yu, S., Huo, X. *et al.*, "Boosted Current Spark Strategy for Lean Burn Spark Ignition Engines," SAE Technical Paper, 2018-01-1133, 2018
77. Piock, W. F., Weyand, P., Wolf, E., and Heise, V., "Ignition Systems for Spray-Guided Stratified Combustion," *SAE International Journal of Engines*, 3(1): 389–401, 2010
78. Ballal, D. R., and Lefebvre, A. H., "The Influence of Flow Parameters on Minimum Ignition Energy and Quenching Distance," *Symposium (International) on Combustion*, 15(1): 1473–1481, 1975
79. FEDERAL-MOGUL, "All about Ignition Coils," [Online] Available: <https://www.championpowersports.eu/assets/Beru/ti-07-ignition-coils-gb-2013-lowres-0.pdf> [Accessed: 31-Oct-2020]
80. SAE Standard, "Storage Batteries," SAE J537, 2016
81. Melito, M. "Car Ignition with IGBTs," *STMicroelectronics Application Note*, 1999
82. Van Basshuysen, R. and Schäfer, F., "Ignition," in *Internal Combustion Engine Handbook-Basics, Components, Systems and Perspectives*, 2004

83. Maly, R., "Spark Ignition: Its Physics and Effect on the Internal Combustion Engine," In: Hilliard J.C., Springer G.S. (eds) Fuel Economy. Springer, Boston, MA, 91–148, 1984
84. Maly, R., and Vogel, M., "Initiation and Propagation of Flame Fronts in Lean CH₄-Air Mixtures by the Three Modes of the Ignition Spark," Symposium (International) on Combustion, 17(1): 821–831, 1979
85. Herweg, R., and Maly, R. R., "A Fundamental Model for Flame Kernel Formation in S. I. Engines," SAE Technical Paper, 922243, 1992
86. Pashley, N., Stone, R., and Roberts, G., "Ignition System Measurement Techniques and Correlations for Breakdown and Arc Voltages and Currents," SAE Technical Paper, 2000-01-0245, 2000
87. Maly, R., "Spark Ignition: Its Physics and Effect on the Internal Combustion Engine," In: Hilliard J.C., Springer G.S. (eds) Fuel Economy. Springer, Boston, MA, 1984
88. Jacobs, T. J., Camilli, L., and Neubauer, M., "High Power Discharge Combustion Effects on Fuel Consumption, Emissions, and Catalyst Heating," SAE Technical Paper, 2014-01-2626, 2014
89. Rohwein, G. J., "An Efficient, Power-Enhanced Ignition System," IEEE Transactions on Plasma Science, 25(2): 306–310, 1997
90. Yu, S., Xie, K., Yu, X., Han, X. *et al.*, "The Effect of High-Power Capacitive Spark Discharge on the Ignition and Flame Propagation in a Lean and Diluted Cylinder Charge," SAE Technical Paper, 2016-01-0707, 2016
91. Anderson, R., "The Effect of Ignition System Power on Fast Burn Engine Combustion," SAE Technical Paper, 870549, 1987
92. Anderson, R. and Asik, J., "Lean Air-Fuel Ignition System Comparison in a Fast-Burn Engine," SAE Technical Paper, 850076, 1985
93. Pischinger, S. and Heywood, J., "A Study of Flame Development and Engine Performance with Breakdown Ignition Systems in a Visualization Engine," SAE Technical Paper, 880518, 1988

94. Cho, Y., Santavicca, D., and Sonntag, R., "The Effect of Spark Power on Spark-Ignited Flame Kernel Growth," SAE Technical Paper, 922168, 1992
95. Alger, T., Gingrich, J., Mangold, B., and Roberts, C., "A Continuous Discharge Ignition System for EGR Limit Extension in SI Engines," SAE International Journal of Engines, 4(1):677–692, 2011
96. Chiu, J. P., Darden, M. H., Matthews, R. D., Childs, H. E., Faidley, R. W., Zheng, J., Weigand, G., Weldon, W. F., and Nichols, S. P., "Examination of the Factors That Influence the Durability of Railplugs," SAE Technical Paper, 940201, 1994
97. Yubo, G., Guorui, Z. and Xinying X., "Performance of a Plasma Jet Igniter.", SAE Transactions, 89: 246–259, 2013
98. Solomon, A., "Plasma-Jet Ignition of Fuel Sprays in a Rapid Compression Machine," SAE Technical Paper, 880205, 1988
99. Murase, E., Ono, S., Hanada, K., and Nakahara, S., "Plasma Jet Ignition in Turbulent lean Mixtures," SAE Technical Paper, 890155, 1989
100. Modien, R., Checkel, M., and Dale, J., "The Effect of Enhanced Ignition Systems on Early Flame Development in Quiescent and Turbulent Conditions," SAE Technical Paper, 910564, 1991
101. Hall, M., Matthews, R., and Ezekoye, O., "Railplug Ignition Operating Characteristics and Performance: A Review," SAE Technical Paper, 2007-01-1832, 2007
102. Johnston, R., Neuman, J., and Agarwal, P., "Programmable Energy Ignition System For Engine Optimization," SAE Technical Paper, 750348, 1975
103. Brandt, M., Hettinger, A., Schneider, A., Senftleben, H., and Skowronek, T., "Extension of Operating Window for Modern Combustion Systems by High Performance Ignition," in Ignition Systems for Gasoline Engines, M. Günther and M. Sens, Eds. Cham: Springer International Publishing, 26–51, 2017
104. Yu, S., Xie, K., Yu, X., Han, X. *et al.*, "The Effect of High-Power Capacitive Spark Discharge on the Ignition and Flame Propagation in a Lean and Diluted Cylinder Charge," SAE Technical Paper, 2016-01-0707, 2016

105. Dale, J., Smy, P., and Clements, R., "The Effects of a Coaxial Spark Igniter on the Performance of and the Emissions from an Internal Combustion Engine," *Combustion and Flame*, 31: 173–185, 1978
106. Schenk, M., Schauer, F. X., Sauer, C., Weber, G., Hahn, J., and Schwarz, C., "Challenges to the Ignition System of Future Gasoline Engines – An Application Oriented Systems Comparison." *Ignition Systems for Gasoline Engines*, M. Günther, and M. Sens, eds., Springer International Publishing, Cham, pp. 3–25, 2017
107. Suzuki, K., Uehara, K., Murase, E., and Nogawa, S., "Study of Ignitability in Strong Flow Field," *Ignition Systems for Gasoline Engines*, M. Günther, and M. Sens, eds., Springer International Publishing, Cham, pp. 69–84, 2017
108. Weyand, D. P., Lorenz, F., Schilling, D. S., and Hofherr, T., "Adaptive Continuous Spark Ignition as Enabler for High Dilution EGR Operation." 2nd IAV Advanced Ignition Conference At: Berlin, p. 27, 2014
109. Wallner, T., Sevik, J., and Scarcelli, R., "Extending the Lean and EGR Dilute Operating Limits of a Light-Duty GDI Engine Using Alternative Spark-Based Ignition," *Ignition Systems for Gasoline Engines*, M. Günther, and M. Sens, eds., Springer International Publishing, Cham, pp. 489–502, 2014
110. Pilla, G., and de Francqueville, L., "Potential of Innovative Ignition Systems to Stabilize Highly-Diluted GDI Combustion," *Ignition Systems for Gasoline Engines*, M. Günther, and M. Sens, eds., Springer International Publishing, Cham, pp. 489–502, 2014
111. Lindvall, F. C., "A Glow Discharge Anemometer," *Electrical Engineering*, 53(7): 1068–1073, 1934
112. Gardiner, D. P., Wang, G., Bardon, M. F., LaViolette, M., and Allan, W. D., "An Experimental Study of Spark Anemometry for In-Cylinder Velocity Measurements," *Journal of Engineering for Gas Turbines and Power*, 130(4), p. 042801, 2008
113. Kim, J. and Anderson, R., "Spark Anemometry of Bulk Gas Velocity at the Plug Gap of a Firing Engine," SAE Technical Paper, 952459, 1995

114. Ichiyangi, M., Koyama, Y., Sato, Y., and Hishida, K., "Velocity Measurement of Sub-Millimeter-Scale Gas Flow by Spark Tracing Method," *Journal of Thermal Science and Technology*, 8(3):517–532, 2013
115. Shiraishi, T., Teraji, A., and Moriyoshi, Y., "The Effects of Ignition Environment and Discharge Waveform Characteristics on Spark Channel Formation and Relationship between the Discharge Parameters and the EGR Combustion Limit," *SAE International Journal of Engines*, 9(1):171–178, 2016
116. Environics, Inc., "Environics® Series 4040 Computerized Gas Dilution System, " [Online] Available: <https://www.environics.com/products/gas-dilution-system-and-gas-dividers/series-4040/> [Accessed: 31-Oct-2020].
117. National Instruments Corp., "NI 9474 Data Sheet," [Online] Available: https://www.ni.com/pdf/manuals/373974c_02.pdf [Accessed: 31-Oct-2020].
118. National Instruments Corp., "NI 9472 Data Sheet," [Online] Available: https://www.ni.com/pdf/manuals/373509b_02.pdf [Accessed: 31-Oct-2020]
119. Tektronix, Inc., "P6015A High-Voltage Probe," [Online] Available: <https://www.tek.com/datasheet/passive-high-voltage-probes> [Accessed: 31-Oct-2020]
120. Pearson Electronics Inc., "Pearson Current Monitor Model 411," [Online] Available: <http://pearsonelectronics.com/> [Accessed: 31-Oct-2020]
121. Pico Technology Ltd., "PicoScope 4824 Data Sheet." [Online] Available: <https://www.picotech.com/download/manuals/picoscope-4824-data-sheet.pdf> [Accessed: 31-Oct-2020]
122. Dantec Dynamics, "StreamLine Pro CTA system," [Online] Available: https://www.dantecdynamics.com/wp-content/uploads/2019/10/0566_v1_SS_StreamLine-Pro.pdf [Accessed: 31-Oct-2020]
123. SAE Standard, " Ignition System Measurements Procedure," SAEJ973_NOV2020, 2020

124. Michler, T., Toedter, O. and Koch, T., "Spatial and time resolved determination of the vibrational temperature in ignition sparks by variation of the dwell time," *SN Applied Sciences*, 2(7), 2020
125. Zhang, A., Cung, K., Lee, S., Naber, J. *et al.*, "The Impact of Spark Discharge Pattern on Flame Initiation in a Turbulent Lean and Dilute Mixture in a Pressurized Combustion Vessel," *SAE International Journal of Engines*, 6(1): 435–446, 2013
126. Settles, G.S. and Hargather, M.J., "A Review of Recent Developments in Schlieren and Shadowgraph Techniques," *Measurement Science and Technology*, 28(4), 2017
127. Zentgraf, F., Baum, E., Böhm, B., Dreizler, A., and Peterson, B., "On the Turbulent Flow in Piston Engines: Coupling of Statistical Theory Quantities and Instantaneous Turbulence," *Physics of Fluids*, 28(4), 2016
128. Haley, R. and Smy, P., "Electrically induced turbulence-the short duration spark," *Journal of Physics D: Applied Physics*, 22(258), 2000
129. Masuda, R., Sayama, S., Fuyuto, T., Nagaoka, M. *et al.*, "Application of Models of Short Circuits and Blow-Outs of Spark Channels under High-Velocity Flow Conditions to Spark Ignition Simulation," *SAE Technical Paper*, 2018-01-1727, 2018
130. Yu, X., LeBlanc, S., Liu, M., Tjong, J., Zheng, M., (in press) "Spark energy distribution impact on flame kernel initiation and combustion process under lean-burn conditions," 2021 SAE World Congress, 2021
131. Sayama, S., Kinoshita, M., Mandokoro, Y., Masuda, R. *et al.*, "Quantitative Optical Analysis and Modelling of Short Circuits and Blow-Outs of Spark Channels under High-Velocity Flow Conditions," *SAE Technical Paper*, 2018-01-1728, 2018
132. Irwin, J.D. and Nelms, R.M., *Basic Engineering Circuit Analysis (Vol. 900)*. John Wiley & Sons Inc, 2010
133. Yunus, A.C., *Fluid Mechanics: Fundamentals and Applications*. Tata McGraw Hill Education Private Limited, 2010
134. Ballal, D., and Lefebvre, A., "Spark Ignition of Turbulent Flowing Gases," 15th Aerospace Sciences Meeting, American Institute of Aeronautics and Astronautics, Los Angeles, CA, U.S.A, 1977

VITA AUCTORIS

NAME: Zhenyi Yang

PLACE OF BIRTH: Hubei, China

YEAR OF BIRTH: 1986

EDUCATION: University of Windsor
Master of Applied Science
Windsor, Canada, 2015

China Agricultural University
Master of Applied Science
Beijing, China, 2010

China Agricultural University
Bachelor of Engineering
Beijing, China, 2008

LIST OF MY PUBLICATIONS

Articles published in peer-reviewed journals

1. **Yang, Z.**, Yu, X., Zhu, H., Ting, D. S-K., Zheng, M., Effect of Spark Discharge Energy Scheduling on Ignition under Quiescent and Flow conditions, Proceedings of the Institution of Mechanical Engineers, Part D: *Journal of Automobile Engineering*, 234(12): 2878–2891, 2020
2. **Yang, Z.**, Zhu, H., Zheng, M., Ting, D. S-K., Spark Plasma in Different Gas Media under Flow Conditions, *IEEE Transactions on Plasma Science*. 48(1):104-108, 2020
3. Yu, X., Sandhu, N., **Yang, Z.**, Zheng, M., Suitability of Energy Sources for Automotive Application - A Review, *Applied Energy*, 271:115169, 2020
4. Zhu, H., Tan, Q., Yu, X., **Yang, Z.**, Liang, L., Zheng, M., and Reader, G.T., Impact of Spark Plasma Length on Flame Kernel Development under Flow Condition, SAE International *Journal of Advances and Current Practices in Mobility*. 2(4): 2172-2182, 2020
5. **Yang, Z.**, Dev, S., Jeftic, M., Aversa, C., Ravi, A., Ting, D. S-K., Zheng, M., Preliminary Investigation of Exhaust Pressure Waves in a Single Cylinder Diesel Engine and the Impacts on Aftertreatment Sprays, *SAE International Journal of Engines*. 10(2):636-645, 2017
6. Han, X., **Yang, Z.**, Wang, M., Tjong, J. and Zheng, M., Clean Combustion of N-Butanol as A Next-Generation Biofuel for Diesel Engines, *Applied Energy*. 198:347-359, 2017
7. Jeftić, M., **Yang, Z.**, Reader, G.T. and Zheng, M., Fuel Efficiency Analysis and Peak Pressure Rise Rate Improvement for Neat N-Butanol Injection Strategies, Proceedings of the Institution of Mechanical Engineers, Part D: *Journal of Automobile Engineering*, 231(1):50-65, 2016

Peer-reviewed conference papers:

8. **Yang, Z.**, Wang, L., Sandhu, N.S., Yu, X., and Zheng, M., Discharge Current Management for Diluted Combustion under Forced Flow Conditions, SAE Technical Paper 2020-01-

1118, 2020

9. Huang, S., Li, T., Wang, N., Wang, X., **Yang, Z.**, Yu, X. and Zheng, M., Experimental Study on the Characteristics of Short Circuits and Restrikes of Spark Channels, SAE Technical Paper 2020-01-1123, 2020
10. Sandhu, N.S., Yu, X., **Yang, Z.**, Dev, S., Purohit, D., Ting, D. S-K., and Zheng, M., An Investigation of Near-Spark-Plug Flow Field and Its Effect on Spark Behavior, SAE Technical Paper 2019-01-0718, 2019
11. **Yang, Z.**, Yu, X., Yu, S., Han, X., Tan, Q., Chen, G., Chen, X., and Zheng, M., Effects of Spark Discharge Energy Scheduling on Flame Kernel Formation under Quiescent and Flow Conditions, SAE Technical Paper 2019-01-0727, 2019
12. Chang, Y., **Yang, Z.**, Yu, S., and Xu, M., A Study of Energy Enhanced Multi-Spark Discharge Ignition in a Constant-Volume Combustion Chamber, SAE Technical Paper 2019-01-0728 , 2019
13. Zhu, H., Yu, X., **Yang, Z.**, Liang, L., and Zheng, M., Investigation of the Electrical-to-Thermal Energy Transfer Efficiency of Different Discharge Strategies Through Electrical and Calorimetry Measurement, Proceedings of the ASME 2019 Internal Combustion Engine Division Fall Technical Conference. ASME 2019 Internal Combustion Engine Division Fall Technical Conference. Chicago, Illinois, USA. V001T03A015, 2019
14. **Yang, Z.**, Yu, X., Yu, S., Chen, J., Chen, G., Zheng, M., Reader, G., and Ting, D. S-K., Impacts of Spark Discharge Current and Duration on Flame Development of Lean Mixtures Under Flow Conditions. Proceedings of the ASME 2018 Internal Combustion Engine Division Fall Technical Conference. Volume 1: Large Bore Engines; Fuels; Advanced Combustion. San Diego, California, USA. V001T03A032. ASME. <https://doi.org/10.1115/ICEF2018-9771>, 2018
15. Zheng, M., Chen, G., Tjong, J., Li, L., Yu, S., Yu, X. and **Yang, Z.**, Spark-based Advanced Ignition Control for Future Diluted Gasoline Engines, Ignition Systems for Gasoline Engines: 4th International Conference, December 6-7, 2018, Berlin, Germany, 2018
16. Yu, X., **Yang, Z.**, Yu, S., Ting, D., Zheng, M., and Li, L., Boosted Current Spark Strategy for Lean Burn Spark Ignition Engines, SAE Technical Paper 2018-01-1133, 2018

17. Yu, S., Dev, S., **Yang, Z.**, Leblanc, S., Yu, X., Han, X., Li, T., and Zheng, M., Early Pilot Injection Strategies for Reactivity Control in Diesel-ethanol Dual Fuel Combustion, SAE Technical Paper 2018-01-0265, 2018
18. **Yang, Z.**, Han, X., Yu, S., Yu, X., Wang, M., Zheng, M., and Ting, D. S-K., A Fuel Sensitive Ignition Delay Model for Direct Injection Diesel Engine Operating under EGR Diluted Conditions, SAE Technical Paper 2018-01-0231, 2018
19. Yu, S., Yu, X., **Yang, Z.**, Wang, M., Han, X., Tjong, J., and Zheng, M., Ignition Improvement for Ultra-Lean Dilute Gasoline Combustion, SAE Technical Paper 2017-01-2244, 2017
20. Yu, X., **Yang, Z.**, Yu, S., Ives, M., and Zheng, M., Discharge Characteristics of Current Boosted Spark Events under Flow Conditions, ASME 2017 Internal Combustion Engine Fall Technical Conference, Seattle, Washington, USA, 2017
21. Yu, S., Yu, X., **Yang, Z.**, Wang, M., Han, X., Tjong, J., and Zheng, M., Ignition Improvement for Ultra-lean Dilute Gasoline Combustion, SAE International Powertrains, Fuels & Lubricants Meeting, Beijing, China, 2017
22. Zheng, M., Yu, S., Yu, X., and **Yang, Z.**, Spark Distribution to Improve Diluted Gasoline Combustion, The Ninth International Conference on Modeling and Diagnostics for Advanced Engine Systems, Okayama, Japan, 2017
23. Yu, X., Yu, S., **Yang, Z.**, Tan, Q., and Ives, M., Improvement on Discharge Efficiency of Spark Ignition System, SAE Technical Paper 2017-01-0678, 2017
24. Xie, K., Yanai, T., **Yang, Z.**, Reader, G., and Zheng, M., Emission Analysis of HCCI Combustion in a Diesel Engine Fueled by Butanol, SAE Technical Paper 2016-01-0749, 2016
25. **Yang, Z.**, Aversa, C., Ives, M., Divekar, P., Ting, D., and Zheng, M., Hydrogen as a By-product of Diesel Engine Low-Temperature Combustion, Natural Gas and Hydrogen Storage 2015 Symposium & Industry Connector Event, Windsor, Ontario, Canada, 2015
26. Divekar, P., **Yang, Z.**, Ting, D., S-K, Chen, X., Zheng, M., and Tjong, J., Efficiency and Emission Trade-Off in Diesel-Ethanol Low-Temperature Combustion Cycles, SAE Technical Paper 2015-01-0845, 2015

Book chapters

27. **Yang, Z.**, Han, X., Yu, S., Dev, S., *et al.*, Combustion Characteristics and Emissions of Direct Injection Neat n-Butanol in a Compression Ignition Engine, *The Energy Mix for Sustaining Our Future*, Springer Nature Switzerland AG 2019: EAS 2018, SPE, pp. 1–25, 2018

Non-peer-reviewed contributions

28. LeBlanc, S., **Yang, Z.**, Yu, X., Ye, C., Yu, S., and Zheng, M., Effect of Lean and Diluted Conditions on the Combustion Process using Multiple Ignition Strategies, *Proceedings of Combustion Institute – Canadian Section Spring Technical Meeting*, Toronto, Canada, 2018
29. **Yang, Z.**, Dev, S., Bryden, G., Zheng, M., and Ting, D.S-K., Exhaust Pressure Wave and Gas Flow Characteristics in a Single Cylinder Engine System, *Proceedings of Combustion Institute – Canadian Section Spring Technical Meeting*, Waterloo, Canada, 2016
30. Aversa, C., **Yang, Z.**, Tan, Q., Yu, X., Yu, S. and Zheng, M., A Preliminary Investigation on the Ignition Characteristics of a Three-pole Spark Plug under Lean and CO₂ Diluted Conditions, *Proceedings of Combustion Institute – Canadian Section Spring Technical Meeting*, Waterloo, Canada, 2016
31. Bryden, G., Divekar, P., **Yang, Z.**, and Zheng, M., Ignition Delay, Heat Release Profile, and Emission Correlation in Diesel Low-Temperature Combustion, *Proceedings of Combustion Institute – Canadian Section Spring Technical Meeting*, Saskatoon, Saskatchewan, Canada, 2015
32. Jetic, M., **Yang, Z.**, Ting, D., and Zheng, M., An Investigation of the Optimal Post Injection Timing for Diesel Exhaust After-treatment, *Proceedings of Combustion Institute Canadian Section, 2014 Spring Technical Meeting*, Windsor, Ontario, Canada, 2014